HYDROGEL ENGINEERING FOR ENHANCING VASCULARIZATION AND AUGMENTING IMMUNOMODULATION OF ENCAPSULATED MESENCHYMAL STEM CELLS

A Dissertation
Presented to
The Academic Faculty

by

Jose Garcia

In Partial Fulfillment
of the Requirements for the Degree
Doctor of Philosophy in
Bioengineering

School of Mechanical Engineering
Georgia Institute of Technology
August 2018

HYDROGEL ENGINEERING FOR ENHANCING VASCULARIZATION AND AUGMENTING IMMUNOMODULATION OF ENCAPSULATED MESENCHYMAL STEM CELLS

Approved by:

Dr. Andrés J. García, Advisor
School of Mechanical Engineering
Georgia Institute of Technology

Dr. Robert Guldberg
School of Mechanical Engineering
Georgia Institute of Technology

Dr. Edward Botchwey
Department of Biomedical Engineering
Georgia Institute of Technology

Dr. Alberto Fernandez-Nieves
School of Physics
Georgia Institute of Technology

Dr. W. Robert Taylor
School of Medicine
Emory University School of Medicine

Date Approved: 5/18/2018

To my family, for their love and unending support

ACKNOWLEDGEMENTS

I would like to thank all the educators who I have had the privilege to learn from over the years. My education did not start when I entered my PhD and I hope that it won't end when I leave. Every teacher I've had has brought me to this point in one way or another. I'd like to especially thank Dr. Benjamin Fregly, my biomechanics professor at my undergraduate institution, the University of Florida. Dr. Fregly may not know this, but he was the one who convinced me to apply for a PhD program. I had thought for many years, since high school, that I had wanted to be a professor but it was ultimately my conversations with Dr. Fregly that convinced me to go for it. Dr. Fregly is an inspirational teacher who always made himself available to his students and truly and visibly cared that they learned. I will always be grateful for having the opportunity to take his class and learn from him. I'd like to thank Dr. Brian Sorg for being my first research advisor as an undergraduate. His willingness to take me on and let me screw up while I learned how to properly do bench-work set me up to succeed in my PhD. I'd like to also thank Dr. Raymond Kozikowski for being my PhD mentor as an undergraduate. I probably screwed up more experiments than I helped but I'm grateful for his tutelage and mentorship. I'd also like to thank my committee members for their invaluable input throughout the process. I'd like to thank Dr. Robert Guldberg for keeping me sharp on the bone aspects of my project, to Dr. Botchwey and Dr. Taylor for our interesting conversations and insights about the role of the immune system on the various aspects of my project and to Dr. Fernandez-Nieves for

ensuring the roots of the entire hydrogel project, that is, the mechanical and physical properties of the gels themselves, never left our sights.

I would like to thank the entire Garcia lab for all the support they have given me throughout my time here. From the science talks and discussion we would have in lab trying to figure out a problem to the happy hour and social events, I definitely could not have finished this without the help of all of them.

To the older students and those who graduated before me and all the post-docs, thank you for setting up a fantastic environment for me to grow in. I'd like to thank Dr. Amy Clark for taking me under her wing when I first started and for showing me the ropes. While we both had our frustrations regarding a certain peptide which will go unnamed here, being able to discuss issues with her definitely made it a little more bearable. Thank you to Dr. Christopher Johnson for telling me I had to go to the emergency room after I cut myself in surgery. Seriously though, thank you for being a fantastic lab-mate and someone I could confide in regarding whatever problem I was having in lab. Both Amy Clark and Chris Johnson were the best surgical assistants anyone could ask for and the best sounding boards for generating multiple ideas and I'm incredibly grateful for that fact. Efrain Cermeño – What can I say? Whatever I say to you now, I can say in our next stop after graduate school where we'll be working together. I'm very excited we got to know each other throughout graduate school and excited for that to continue after we leave. I'd like to thank Dr. Devon Headen for encouraging me to think as an engineer. In a lab full of

biology, his truly engineering mindset was a fantastic resource to bounce ideas off and learn from. I'd like to also thank Ted Lee for arguably being the most eclectic guy I've ever met. His demeanor always pushed me to learn more and pull the trigger in whatever idea we had concocted up. Thank you to Dr. Apoorva Salimath for all the fun times we've had both in and out of lab and for being dog park buddies! Asha Shekaran, Nduka Enemchukwu, and Stacie Gutowski – I didn't overlap too much with them all too much all but thank you for being exemplary senior graduate students when I first started and for being great role models for how science should be done.

To all the younger students and those coming after me, thank you for keeping me from devolving into a crotchety old man. I'd like to especially thank Ricardo Cruz and Dennis Zhou for providing me an ample sounding board for generating ideas. I'd also like to thank my friends in other labs at Georgia Tech for making the PhD experience more enjoyable. To the characters in the Guldberg lab, especially Albert Cheng and Brennan Torstrick – we might have been able to get a lot more done in graduate school had we not sat together in the lair, but the time we spent together kept the lair a fun and stimulating environment.

I'd like to especially thank my advisor, Dr. Andrés García. I remember when I first was looking at graduate schools, I was confused by the difference between Bioengineering and Biomedical Engineering at Georgia Tech and so I e-mailed the Bioengineering chair at the time noting also that I was interested in the research being conducted in his lab.

Within a day (I believe, given how rapid Dr. García responds to e-mails), I got an e-mail from him saying he'd be happy to talk on the phone. His willingness to spend time talking to a random student that day is a testament to what I've discovered over the past 6 years: his passion for teaching and mentoring. I know that Dr. García has a deep passion for this and for his science as I've been the one to test it from time to time. Times inevitably got rough over the past 6 years with countless experiments going sideways, more than a handful of pivoting projects and a graduate student who, at times, found it cathartic to butt heads. Through it all however, Dr. García kept pushing me and our projects further and further and never gave up. Many people state how the lessons learned in graduate school persist regardless if one ever touches a pipette ever again. I hope that the determination and problem-solving that I learned from Dr. García are one of those lessons that persist.

Last but not least, I'd like to thank my family for all their support throughout not only these past 6 years but from childhood. My parents always told me that education was the most important thing to have and that with a strong education, I could do anything. This obviously would send a child's eyes rolling but as I grew older, I learned to appreciate this value they instilled in me and that without, I would certainly not be writing this thesis. My parents also instilled in me the idea that you need to find what you love to do no matter what the situation is and strive to be the best at it. I remember my father telling me at one point "If you love to be a garbage man, just be the best garbage man there is". This too would send my eyes rolling, but now I see the value in such an idea. Over the past 6 years, I at times lost sight of this goal, this process of finding what I loved to do. Remembering

what my parents instilled in me though would always correct my viewpoint. I know at times, my sister and I made parenting a little difficult, but I am forever thankful for the time, energy and love my parents have put into raising us. I'd also like to thank my sister Cristina. Coming in as an undergraduate at the University of Florida, she showed me the ropes of being in college and helped get me started on a great undergraduate experience which inevitably led me here. Thank you for being a great big sister and I'm looking forward to officially welcoming Brian into the family!

I'd also like to thank my wife Emily. A PhD inevitably has its ups and downs and Emily has helped me through every trough and every peak this process has given me. One of the lessons this process has taught me is to balance the different aspects of my life, both work and home. This didn't occur instantaneously though and there were many times where the failure of experiments would find their way home. Thank you for being my rock and my confider in such times. Thank you also for supporting me when I had the wild idea of pursuing a career path following my PhD that seemed so completely tangential to what I had been doing for the past years. I could never have finished my PhD without my wife and this degree is as much hers as it is mine.

And lastly, I'd like to dedicate my thesis to my late grandfather who passed away only a few months prior to my thesis defense. When he was younger, he started his doctoral studies at the University of Michigan but for personal reasons, had to leave it prior to completion. During the past few years, although in failing health, he would always tell me

to power through my studies and to finish no matter what happened. Thank you grandpa. I finished.

TABLE OF CONTENTS

LIST OF FIGURES

LIST OF SYMBOLS AND ABBREVIATIONS

PEG	Polyethylene-glycol
IFN-γ	Interferon-gamma
HUVEC	Human umbilical vein endothelial cells
μCT	Microcomputed tomography
CD	Cluster of Differentiation
TGF-β	Transforming growth factor-beta
BMP	Bone morphogenic protein
PDGF	Platelet derived growth factor
ROCK	RhoA kinase
PMMA	Poly(Methylmethacrylate)
ECM	Extracellular matrix
TNF-α	Tumor necrosis factor-alpha
VEGF	Vascular endothelial growth factor
PDGF-β	Platelet derived growth factor - β
MLR	Mixed lymphocyte reaction
PGE2	Prostaglandin E2
COX2	Cyclooxygenase-2
GvHD	Graft vs Host Disease
IBD	Inflammatory bowel disease
1-MT	1-methyl-tryptophan

SUMMARY

Since the discovery of adult human mesenchymal stem cells in the late 1900's, the potential of utilizing these cells in the clinic for cell-therapy applications has been an ever-present goal. Unfortunately, clinical trials using these cells have garnered lackluster results with a high degree of variability in patient outcome and in many cases no difference between patients who received these adult stem cell or placebo. Various factors account for such results including the inability to properly control cell presence via the routine method of intravenous administration, the inability to control cell phenotype once the cells are injected into the patient and the harsh microenvironment cells are injected into. Biomaterials can provide solutions for these factors through engineering scaffolds to present needed signals to both encapsulated stem cells and the surrounding microenvironment. The objective of this project is to engineer bioartificial hydrogels presenting specific signals in the form of integrin-specific ligands and covalently-bound proteins to enhance vascularization and mesenchymal stem cell activity and efficacy in wound and disease models.

We investigated the application of these bioarticifial hydrogels towards two different goals: 1) to enhance vascularization and bone regeneration in a critical size bone defect and 2) to enhance immunomodulation of encapsulated stem cells. For the first aim, cell-mediated degradable poly(ethylene) glycol-based (PEG) hydrogels were functionalized with the vasculogenic protein, vascular endothelial growth factor (VEGF),

along with one of two types of adhesive peptides, either the $\alpha_2\beta_1$ integrin-targeting 'GFOGER' peptide or the mainly $\alpha_v\beta_3$ integrin-targeting 'RGD' peptide. These hydrogels were implanted within a murine segmental bone defect and bone repair monitored via microcomputed tomography and vascularization assessed via vessel perfusion. We hypothesized that incorporation of VEGF and different peptides would result in a differential effect on vascularization which would enhance both stem cell therapy and bone repair. For our second goal, we synthesized PEG-based hydrogels functionalized with a tethered form of the protein interferon-gamma (IFN-γ), a protein known to enhance the immunomodulatory properties of hMSCs. The capacity for these hMSC-laden hydrogels to modulate immune responses was tested *in vitro* with monocytes and T-cells before assessing the platform in a colonic wound model. We hypothesized that covalent tethering of this protein onto hydrogels would result in enhanced immunomodulation by encapsulated stem cells which would translate into more rapid wound resolution.

For our first goal, we found that hydrogels presenting the $\alpha_2\beta_1$ ligand 'GFOGER' resulted in enhanced vascularization of bone defects compared to hydrogels presenting the $\alpha_v\beta_3$ ligand 'RGD' in the absence of vasculogenic protein. For our second goal, we found that hydrogels functionalized tethered IFN-γ enhanced the immunomodulatory properties of encapsulated hMSCs which led to enhanced tissue resolution in a colonic wound model. Together, our findings elucidate novel ways to enhance adult stem cell efficacy and further the applicability of these cells in clinical settings.

CHAPTER 1. SPECIFIC AIMS

1.1 Introduction:

Human mesenchymal stem cells (hMSCs) are a widely studied cell type that are now in over 493 ongoing or completed clinical trials according to the database of the National Institutes of Health [1]. HMSCs are attractive for regenerative medicine applications due not only to their ability to differentiate down several lineages but also their immunomodulatory activities and their beneficial paracrine effects [2-4]. Indeed, while various studies have investigated how MSCs contribute directly to regeneration of tissue through differentiation [5-7], more recent studies have focused instead on the ability of hMSCs to curtail and control the microenvironment through paracrine signaling and immunomodulation as can be seen in their utilization in multiple autoimmune diseases [8]. Regardless of the mechanism(s) of action, successful application of hMSCs in the clinic faces hurdles including issues related to sourcing and procurement, as well as challenges on issues related to the actual efficacy of the cell-therapy [9, 10].

In terms of efficacy, hMSC therapy is fraught with problems relating to poor survival, retention and engraftment of hMSCs *in vivo*, and donor-to-donor variability [10]. Twoissues that lead to poor outcomes on these various metrics is the large number of cells that die upon implantation and the inability to control the cells once implanted *in vivo*. In many applications that infuse donor hMSCs intravenously for example, once the cells are

delivered, there is little that clinicians can do to control the fate of the transplanted cells. In many cases, infusion or implantation of MSCs results in the majority of MSCs dying shortly after implantation due, at least in part, to a lack of vascularization. Additionally, having the ability to control the hMSCs or their microenvironment once implanted would allow researchers the ability to manipulate the cells in order to increase their efficacy toward various clinical outcomes. To this end, biomaterials can be used as a cell delivery and encapsulation vehicle precisely to engineer the microenvironment in which both the stem cell resides as well as to control its interaction with the recipient system. Whereas biomaterials have been used in recent years for this purpose, there remains a lack of understanding of what specific cues and signals the host tissue and encapsulated hMSCs need embedded within the biomaterial in order to enhance the efficacy of different cell therapies. The two main ***objectives*** of this project are thus to 1) understand the interplay of integrin-binding peptides and the vasculogenic factor VEGF within a biomaterial to increase vascularization and bone regenerationwithin a critical-size bone defect and 2) engineer a biomaterial with an tethered inflammatory protein to enhance the immunomodulatory properties of encapsulated hMSCs. Our ***hypothesis*** for the two objectives are respectively 1) functionalization of polyethylene glycol (PEG) hydrogels with different integrin-specific peptides and VEGF will modulate vascularization and associated bone regeneration and 2) functionalization of PEG hydrogels with a recombinant engineered interferon-gamma (IFN-γ) will enhance the immunomodulation

of hMSCs and thus enhance their efficacy for treating colonic wounds. These objectives will be accomplished through the following two aims:

1.2 Specific Aim 1: Engineer hydrogels functionalized with integrin-specific peptides and vascular endothelial growth factor (VEGF) to investigate the interplay between these two factors on vascularization and bone regeneration of a murine segmental defect.

We will utilize two different synthetic peptides exhibiting varying integrin-binding specificity: the fibronectin-derived RGD peptide for mainly $\alpha_v\beta_3$ binding or the collagen-mimetic GFOGER peptide for $\alpha_2\beta_1$ binding. These peptides will be incorporated into hydrogels by covalently tethering them to a 4-arm poly (ethylene) glycol-maleimide (PEG-MAL) macromer through Michael-type addition. VEGF will also be tethered onto the macromer through similar Michael-type addition of its free cysteine. Macromers will then be cross-linked together with bi-cysteine presenting protease-degradable synthetic peptides. With this platform in place, we will initially test the bioactivity of the tethered VEGF through *in vitro* studies on its proliferative and network-forming effect on human umbilical vein endothelial cells (HUVECs). After we have proven the retention of the tethered VEGF's bioactivity, we will implant these hydrogels within a murine critical-size radial segmental bone defect and monitor longitudinal bone regeneration through microcomputed tomography (μCT). Vascularization will also be analyzed via μCT analysis of MicroFil perfusion and histological techniques. We hypothesize that integrin-specific

hydrogels functionalized with VEGF will have differential effects on vascularization of the defect and thus lead to differential bone regeneration.

1.3 Specific Aim 2: Engineer covalently bound IFN-γ hydrogels to increase immunomodulatory properties of encapsulated hMSCs for the treatment of colonic wounds.

We will utilize the PEG hydrogel platform described in Aim 1 to test the ability for covalently tethered interferon gamma (IFN-γ) to modulate the immunomodulatory properties of encapsulated MSCs. We will encapsulate hMSCs into the hydrogel and analyze how tethered IFN-γ influences hMSC polarization into an immunomodulatory state by both flow cytometric analysis of specific markers as well as paracrine cytokine secretion. We will then analyze the ability for bound IFN-γ to modulate hMSC-based CD4+ T-cell proliferation and monocyte and macrophage polarization. We hypothesize that bound IFN-γ will differentially regulate encapsulated hMSC immunomodulatory properties. Based on these preliminary results, we will select the hydrogel formulation most suitable for increasing the immunomodulatory properties of encapsulated hMSCs and investigate how the selected conditions influence the efficacy of the biomaterial construct for treating colonic wounds in immunodeficient mice. We will induce colonic wounds in mice through a custom-engineered colonoscope device that allows for precise tearing of the epithelial layer. Colonic wounds will be induced through this method followed by injection of the aforementioned hydrogel formulations into the wound area. Efficacy of

treatment will be assessed through the following parameters: 1) wound closure over the course of 14 days through colonoscope assessment; 2) cytokine analysis of surrounding tissue for pro- and anti-inflammatory markers; 3) histological assessment of the wound area at 14 days for signs of wound resolution.

1.4 Significance

This work is significant as it elucidates novel ways to engineer biomaterials to enhance the efficacy of adult stem cells in disease models. Current use of stem cells in the clinical is largely restricted to systemic infusion in which localization as well as control of microenvironmental cues is absent. Through the research presented here, we show how engineering the microenvironment surrounding mesenchymal stem cells through biomaterials engineering approaches, we can significantly alter and shape stem cell phenotype.

CHAPTER 2. LITERATURE REVIEW*

*Partly adapted from Garcia, JR. and A.J. Garcia, *Biomaterial-mediated strategies targeting vascularization for bone repair.* Drug Deliv Transl Res, 2016 6(2): 77-95 [11]

2.1 Characterization of human mesenchymal stem cells (hMSCs)

By definition, stem cells are cells that exhibit two distinct properties: 1) the ability for self-renewal and 2) the ability to differentiate into other cell phenotypes or the characteristic known as multipotent (or pluripotent). Human mesenchymal stem cells were first discovered in the middle to late half of the 20th century by Friedenstein and colleagues through observation of a subset of isolated bone marrow cells that rapidly adhered to tissue culture plastic and exhibited a fibroblast-like appearance [12-14]. Since this initial discovery, many more parameters have been identified aimed at providing a general guideline for researchers to conclusively label a cell as a mesenchymal stem cell. According to the International Society for Cellular Therapy (ISCT), human mesenchymal stem cells must meet three main criteria: 1) Adherence to plastic 2) a specific antigen profile and 3) differentiation potential to three main lineages, namely, osteogenic, adipogenic and chondrogenic lineages [15]. In regards to the specific antigen profile, MSCs must be positive for cluster of differentiation (CD) markers CD105, CD73 and CD90 while lacking expression for CD45, CD34, CD14, CD79α and HLA-DR [15].

As described before, hMSCs were first isolated from bone marrow and thus initial studies centered on bone marrow as the primary source of hMSCs [3, 16, 17]. Due to various issues including the difficulty in procuring bone marrow, other sources of human adult or neonatal tissue such as umbilical cord blood, dental pulp, Wharton's jelly and placenta among other sites have been analyzed for the presence of mesenchymal stem cells [18-22]. Notably however, the most common source of MSCs aside from bone marrow has become adipose tissue due to both the presence of MSCs as well as the relative ease in procuring the tissue as adipose tissue is normally discarded in many elective surgeries [23]. While MSCs from each of these sources exhibit the criteria for definition of a mesenchymal stem cell described previously, recent studies have noted that the cells from these sources can have differences in phenotype. Kern *et al* discovered that MSCs isolated from umbilical cord blood exhibited significantly higher potential for proliferation and population doubling compared to MSCs isolated from bone marrow and adipose tissue but failed to differentiate into adipose tissue [24]. In addition to tests for proliferation and differentiation, other studies have focused on functional effects on other cell types. Puissant and colleagues compared the ability for either bone marrow-derived or adipose-derived MSCs to inhibit the proliferation of lymphocytes in co-culture and found that both cell types halted proliferation at similar levels [25]. Yoo and colleagues affirmed this finding and added that umbilical cord blood-derived and Wharton's jelly-derived MSCs also inhibit lymphocyte proliferation to similar levels as bone marrow-derived and adipose-derived cells [26]. Overall, while much research has been done on comparing different

sources of MSCs for both their ease of procurement as well as their functionality, as MSCs increasingly make their way into clinical use, more studies will have to be done regarding their efficacy in the various disease models.

2.2 Bone repair and use of hMSCs

2.2.1 Epidemiology and mechanisms of bone repair

In the United States alone, there is an estimated 7.9 million fractures that occur annually costing over $21 billion [27]. Of the 7.9 million annual fractures, approximately 5-10% exhibit either delayed or impaired healing and a further 15% of these continue on to the point of non-union where the broken bone does not fully heal [28]. For patients in which their fracture exhibits impaired healing, this can translate into higher medical costs as well as a lower standard of living. Because of this, there is a demand for research into methods and treatments that can increase the success rate for bone healing.

The process of bone healing is highly orchestrated one that falls into two categories: endochondral and intramembranous ossification. Endochondral ossification, the process through which all long and load-bearing bones in the body are generated and is characterized through development by a cartilage intermediary, initiates through migration and differentiation of mesenchymal stem cells (MSCs) into chondrocytes in part through activation and suppression of the transcription factors Sox9 and β-catenin, respectively [29]. Differentiated chondrocytes then proliferate under the control of the Sox9

transcription factor, and ultimately undergo hypertrophy through activation of Runx2 followed by apoptosis following secretion of collagen and proteoglycans. Prior to apoptosis, these hypertrophic chondrocyte cells secrete a synchronized cascade of chemokines and cytokines that recruit endothelial cells and associated vasculature. The invading vasculature then allows for recruitment of osteoclasts, which subsequently remove the cartilaginous matrix and allow for osteoprogenitors to migrate to and deposit calcium and bone matrix into the remnants of the matrix [30]. While osteoprogenitors originate from the same cell type as the initial chondrocytes that laid down the cartilaginous matrix, early activation of the transcription factor Runx2 in the absence of Sox9 followed by upregulation of osterix, alkaline phosphatase and osteopontin cause MSC differentiation down the osteogenic lineage [31].

Throughout this process, the spatiotemporal regulation of growth factor activity provides necessary cues for proper skeletogenesis. Notably, vascular endothelial growth factor A (VEGF) along with the family of bone morphogenetic proteins (BMPs) and fibroblast growth factors (FGFs) are central to this process. Initially, BMP 2, 4, 7 and 9 all aid in the initiation of chondrocyte differentiation and cartilage development; deletion of these growth factors leads to gross absence of most skeletal components [32, 33]. Once chondrocytes begin to undergo hypertrophy, their VEGF mRNA expression increases with subsequent secretion of the protein resulting in elevations in the proliferative capacity of nearby chondrocytes as well as inducing vascular invasion into the ischemic cartilaginous region [34-36]. Blocking the activity of VEGF through soluble VEGF receptors impairs

angiogenesis, ossification and results in massive cell death in chondrocytes, whereas reverting this blocking treatment restores normal bone formation [34-36]. Coinciding with this increase of locally secreted VEGF, expression of FGF18 is increased and acts as a negative regulator of chondrocytic proliferation through FGF receptor 3 (FGFR3) [37]. Mice lacking either the *Fgf18* or *Fgfr3* gene exhibit heightened levels of chondrocyte proliferation and associated lower levels of osteogenic differentiation from invading MSCs into the ossification front. The fact that VEGF increases the proliferation of chondrocytes while the presence of FGF18 counteracts this process indicates a tightly regulated process in which it has been postulated that VEGF expression is controlled through activation of FGFR3 [38].

In contrast to endochondral ossification, intramembranous ossification forms bone without a cartilage intermediary and is the mechanism by which all flat bones, including the cranial and clavicle bones, are formed [39]. In this process, MSCs directly differentiate into osteoblasts and secrete bone matrix into the surrounding ECM. Prior to their differentiation, MSCs destined to become osteoblasts begin to condense at the area of ossification with various FGFs being highly expressed in center of ossification [40]. Following condensation, spatiotemporal concentrations of BMP2, BMP4, and BMP7 activate the expression of Runx2 which acts as a transcription for further osteogenic differentiation [41]. Expression of late-markers for differentiation including osteocalcin and osteopontin requires the initial activation of Runx2. In regards to vascularization, the spatiotemporal expression of angiogenic factors such as VEGF and HIF-2α direct

surrounding blood vessels to invade the mesenchymal condensation near the time of initial ossification [42]. As ossification occurs surrounding the blood vessels, the mesenchymal stem cells not involved in ossification at the time migrate outward. Blood vessels continue to extend toward these migrating cells with mineralization occurring near these sprouting vessels [42].

2.2.2 Use of mesenchymal stem cells for bone repair

Due to their ability to differentiate down an osteogenic lineage, MSCs have long been recognized as a clinically relevant cell for bone regenerative applications. In 1998, Bruder *et al.* implanted bone-marrow isolated mesenchymal stem cells within a hydroxyapatite carrier into femoral defects in rats and found that implantation of these cells increased the strength of regenerated bone compared to vehicle only controls [43]. In that same year, Bruder and colleagues also demonstrated efficacy of autologous mesenchymal stem cells when applied within the larger canine animal model [44]. Since then, many more studies have been conducted in which mesenchymal stem cells within a carrier were utilized to treat bone defects [45-48]. While MSCs were known to undergo osteogenic differentiation *in vitro*, throughout these initial studies, it was unknown whether delivered MSCs underwent osteogenic differentiation once implanted within the defect site. In a recent study however, Vila *et al.* demonstrated, using a dual-luciferase tracking system in which MSCs were transduced to express luciferase driven by constitutive and osteocalcin (OC)-responsive promoters, that MSCs implanted into calvarial defects in mice greatly

upregulated their expression of osteocalcin, a late-marker for osteogenic differentiation [49].

Whereas multiple studies have demonstrated MSCs being efficacious in regenerating bone in multiple models, it is worthy to note that there are various studies showing the opposite effect. Niemeyer *et al.* conducted a study in which autologous MSCs were implanted within ceramic scaffolds in a rabbit calvarial defect. The researchers found no difference in the mechanical strength of regenerated bone between groups containing the autologous MSCs and acellular scaffolds [50]. Seebach and colleagues also demonstrated in a rat femoral defect model that beta-tricalcium phosphate scaffolds loaded with bone-marrow derived MSCs had no difference in bone volume and ultimate load compared to acellular beta-tricalcium phosphate scaffolds [51]. In another study, Zou *et al* showed that MSCs delivered within a gelatin sponge had no effect on either bone volume or bone mineral density compared to acellular gelatin implants in a rat calvarial defect [52]. Altogether, these studies and others [53] show that over a range of bone defect models, assessment metrics and delivery vehicles for the MSCs, there remains a large discrepancy over the efficacy of MSCs and the overarching question remains as to if MSCs meaningfully and significantly enhance bone repair.

2.2.3 Factors affecting MSC efficacy in bone repair

With the discrepancies in MSCs for bone repair in mind, it is important to understand the underlying factors that affect the efficacy of MSC therapy. It is useful to

break down the factors into categories for ease of analysis. In any of these experiments, there are 4 main categories to consider: 1) the quality of cells being used prior to implantation 2) the method and material for cell delivery 3) the model and surgical procedure and 4) what occurs in the implant following the surgery. While much can be discussed regarding the first three categories described, specifically the quality of cells used as there has been enormous amount of research recently going into looking at the vast differences bona fide MSCs have from batch to batch, we will focus on the fourth category described: understand what occurs to MSCs post-implantation and discuss how engineering the material used to deliver the cells can potentially lead to enhanced efficacy of cells once implanted. In this section, we will be focusing on two major issues regarding stem cell use once implanted: 1) the hostile environment present in damaged tissue in which MSCs are implanted and how that affects MSC viability and 2) the lack of control once MSCs are implanted. For the latter case, we will explore the different cues, both chemical and physical, that cells sense that affect their phenotype. We will end this section by discussing how biomaterials can be made to address these two issues.

2.2.3.1 Oxygen and nutrient deprivation following injury

Many types of tissue defects and injury but specifically bone defects exhibit a difficult environment for cells to grow. In many cases of injured bone in which non-union occurs and intensive therapy is necessitated, the local vascular network has been destroyed [54]. This lack of blood vessels penetrating into the area causes ischemic conditions that in

turn increase the chance of a delayed-union occurring [55]. MSCs delivered into ischemic environments have been noted to exhibit increased levels of cell death compared to MSCs in more normoxic environments [56]. Indeed, studies that have tracked the retention of MSCs in bone defects through bioluminescence and constitutively expressed luciferase show that within 1-2 weeks of MSC implantation, a vast majority of the cell signal is absent [48, 57, 58]. The lack of MSC survival in bone defects thus poses a potentially large factor in limiting the efficacy of MSCs for bone repair.

2.2.3.2 Cues for directing stem cell phenotype: Chemical

Another issue when delivering MSCs into bone defects is the inability to control cell fate and phenotype once delivered. *In vitro,* stem cells are routinely manipulated using growth factors or cytokines added to the media. The semi-known environment inherent in the *in vitro* experiment allows for a high degree of user-defined control of stem cell phenotype. *In vivo* however, the lack of control over the microenvironment as well as the complicated interplay between endogenous and exogenously delivered cells results in an extreme lack of control over the delivered stem cell phenotype. To this end however, multiple studies have investigated the different cues that control stem cell fate with the potential utilization of these cues to direct cell phenotype *in vivo*. External cues can be grouped into two broad categories: 1) chemical and 2) physical cues. Chemical cues can be defined as any cue in the form of a soluble factor such as a small molecule drug or biologic factor while physical cues can be defined as any interaction that translates into a

mechanical stimulus on the cell, usually through the form of mechanotransduction molecules such as integrins. While chemical cues can be added to media for *in vitro* purposes, utilizing chemical cues to direct cell fate *in vivo* requires different strategies.

One strategy used has been to load known amounts of growth factor or cytokines into a stem cell-laden scaffold and investigate how the release kinetics and dose of the growth factor affect encapsulated cell phenotype. This technique has been successfully used in a variety of studies looking at the differentiation of MSCs down chondrogenic and osteogenic lineages through encapsulation of both MSCs and various proteins including transforming growth factor-beta (TGF-β), dexamethasone and bone morphogenic protein (BMP) [59-63]. A different take on this strategy is to somehow tether, through covalent interactions or otherwise, a prescribed molecule or biologic of interest directly onto the scaffold. Rather than having the drug or protein of interest release through strictly diffusion, this deviation allows for a higher degree of control based on the engineering of the tethering itself. Nuttelman *et al.* has demonstrated that covalently tethering dexamethasone, a powerful factor in osteogenic differentiation of MSCs, onto the PEG backbone of a PEG-based hydrogel increases the osteogenic differentiation of encapsulated MSCs [64]. In lieu of covalently tethering a molecule onto a scaffold, controlling the presence and kinetics of a growth factor through binding domains is also a viable option. Martino and colleagues engineered a fragment of fibronectin that held both an integrin-binding domain and a growth factor-binding domain [65]. Through this approach, the researchers showed that they could alter MSC differentiation through encapsulation of

MSCs into this scaffold along with either platelet derived growth factor (PDGF)-BB or BMP-2 [65].

2.2.3.3 Physical cues for directing stem cell phenotype: Stiffness

In addition to chemical cues, physical cues have also been explored as a potential lever in inducing and altering MSC phenotype *in vivo*. It is important to make the distinction that while physical cues fundamentally translate into mechanical stimulus on a cell, the breadth of research in this topic span three broad categories: 1) stiffness of a material 2) topography and 3) ligand-specific interactions on a cell. The relationship of stiffness to the differentiation potential of a mesenchymal stem cell was first observed in 2006 in a seminal paper by Adam Engler and Dennis Discher [66]. In the study, Engler and colleagues seeded MSCs on substrates spanning stiffness values from 0.1 to 40 kPa and found that the cells on different stiffness substrates exhibited significantly different expressions of lineage-specific proteins [66]. On soft substrates, MSCs tended to express proteins consistent with a neurogenic phenotype while on stiff substrates, MSCs exhibited proteins consistent with an osteogenic phenotype. Since this finding, future studies have also shown other adult stem cells to act in a similar manner [67]. For example, muscle stem cells exhibit differences in proliferation and differentiation when seeded on substrates of different stiffness [68]. For many years, the molecular mechanism behind the ability of a cell to 'feel' its underlying matrix was not completely understood. A recent study however posed a theory that cells sense matrix rigidity through integrin binding dynamics [69]. On

soft substrates, the underlying ECM deforms easily which causes the force-loading rate on the integrin bond to be low. This thus causes the unbinding of the integrin-ECM bond to be based on the intrinsic unbinding rate rather than an excessive force load ripping the bond. On high stiffness substrates in contrast, the high force-load rate causes an increase in integrin-ECM bond breakage that creates a reinforcement phenomena where additional integrins are recruited to the site through force-induced conformational changes in cytoskeletal proteins or mechanostabilization of integrin-clusters [70-72].

2.2.3.4 Physical cues affecting stem cell phenotype: topography

In addition to stiffness, topography has also been shown to have a significant effect on MSC phenotype and differentiation. The general idea behind topography influencing cell phenotype revolves around the finding that cell shape is a significant factor in cell function. One of the first observations of this phenomena was in 1978 when Folkman and Moscona regulated cell shape through changing the adhesivity of tissue culture plastic [73]. The different cell shape resulting from the differences in adhesivity were then correlated with DNA synthesis [73]. Future work has built on this premise through a variety of techniques including micropatterning cell adhesive areas onto a surface and engineering surfaces with different topographical cues such as grooves or roughness [74-77]. Similar to the other mammalian cell types used in the preliminary studies of cell shape, MSCs also show a dependence of cell shape on their function and phenotype. Through micropatterning techniques on a planar surface, MSCs restricted to an adhesive 'island' size of 1024 μm^2

showed a significantly greater degree of adipogenic differentiation than osteogenic differentiation while MSCs on an adhesive island size of 10,000 μm^2 showed a greater degree of osteogenic differentiation than adipogenic differentiation [78]. This observation was further attributed to the increased activity of RhoA and RhoA kinase (ROCK) in spread cells on the larger islands than unspread cells on the smaller islands [78]. Rather than patterning adhesive moieties on planar surfaces, surface engineering of topographical cues such as grooves, troughs and roughness also exhibits a significant effect on MSC phenotype. Dalby *et al.* demonstrated that MSCs cultured on randomized poly(methyl methacrylate) (PMMA) nanopatterns showed significantly increased amount of osteogenic markers compared to ordered nanopatterns of the same material [79].

2.2.3.5 Physical cues for directing stem cell phenotype: Integrin-ECM interactions

The previous two physical cues discussed, that of stiffness and topography, are in theory, non-discriminatory in relationship to the specific cell-matrix interaction molecules. That is, the stiffness or topography alterations one makes may not favor a certain type of integrin-ECM interaction. The last type of physical cue discussed will be that of specifically engineering a material to activate a predetermined set or class of integrin molecules. We will discuss here the following two topics related to integrins: 1) what are integrins and how are they classified and 2) how do integrins function.

Integrins consist of one of the key classes of molecules that mechanically link the cell to its matrix. Integrins are classified as heterodimeric transmembrane glycoproteins

consisting of a α- and β- subunit brought together through non-covalent interactions [80]. While there are 8 β subunits and 18 α subunits, together, they can form 24 distinct integrins (Fig. 1) [81]. These 24 distinct integrins can be further categorized by either the types of cells that express the integrins at appreciable levels or the main ligand molecule binding the integrin. In the former case, integrin expression on a specific subset of cells results in differential population adhesion based on the cell types in the population. This is the case for the β2 subunit which is mainly found on leukocytes and is an important regulator of extravasation of the cells from the blood stream to regions to regions of inflammation [82, 83]. By solely isolating the β2 subunit to a class of cells, non-leukocytes are prevented from attaching to and interacting with ligands found on the endothelial surface. Another method of classifying integrins can be via the specific protein ligand(s) through which the integrins mainly bind to. There are a variety of ligands found in the ECM including collagen, fibronectin, fibrinogen and vitronectin as well as many others that have been extensively studied to discover which integrins bind to which ligands and with what affinity [84]. It is important to note that most integrins can bind to several ECM proteins. The combination of the number of distinct integrin pairs, the differing affinities each integrin has to a variety of ligands and the differential expressions on subsets of cells creates a system where virtually every cell is uniquely affected by its environment.

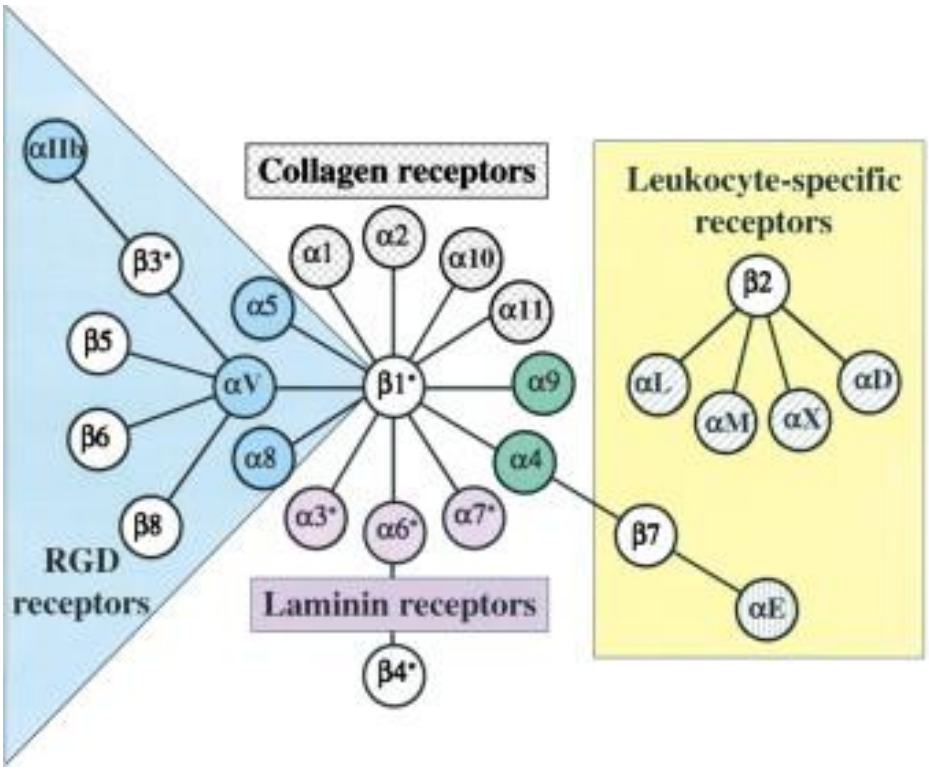

Figure 1: Integrin family as classified by different subpopulations of cells expressing each integrin. Adapted from [81].

As a class of adhesion molecules, integrins function in a similar fashion to one another in that they adhere to and exert forces on the extracellular matrix (ECM) that in turn get translated into biochemical signalling inside the cell [85]. The method in which this happens occurs through two dynamic and related processes termed “outside-in signalling” and “inside-out signalling” [86-88]. To understand outside-in signalling, it is important to understand the structure of integrins. Integrins consist of large extracellular domain and a smaller intracellular domain which, by itself, is devoid of catalytic activity [89]. Upon presentation of a ligand in the extracellular space, integrins bind to the ligand and begin forming a cluster [90]. The clustering of intracellular domains enables the generation of a focal adhesion which is a conglomerate of adaptor proteins including talin, paxillin, vinculin and focal adhesion kinase (FAK) [91, 92]. These adaptor proteins have binding sites for the cytoskeletal actin filaments as well as a myriad of phosphorylation that initiate downstream signalling [93, 94]. Thus, outside-in signalling involves the transmissions of signals from outside the cell (ECM ligands) into biochemical signals through the integrin. In contrast, inside-out signalling involves altering the extracellular domain conformation of integrins and thus their affinity to ECM ligands. For conformational changes to be induced on the extracellular portion of integrins, it must start at the intracellular domain which, as noted above, is devoid of catalytic activity. Thus, inside-out signalling necessarily must proceed through the adaptor proteins that bind to the intracellular domain. One of these important adaptor proteins that contribute to inside-out signalling is talin. Prior to activation, talin is in an autoinhibited ‘closed’ formation and

prevented from associating with integrins [95, 96]. Upon cleaving of the closed formation through a variety of potential pathways, talin is released from its closed conformation and integrin and cytoskeletal binding sites become accessible [95]. Binding of talin to the cytoplasmic tail of β integrin subunits has been subsequently shown to induce a conformational change in the extracellular portion of the integrin and increase its affinity [97]. Other proteins such as the proteins within the kindlin family have also been identified as important regulators of inside-out signalling and integrin activation through a similar process as talin [98, 99]. While the intricacies of inside-out signalling are still being elucidated, an important question is that of what signals or pathways activate the adaptor proteins that then activate integrins? Research into this has shown that there exists an incredibly interwoven state of crosstalk between integrins and growth factor receptors and receptor tyrosine kinases [100]. This crosstalk can occur through either downstream pathways activated by cytokines or through direct interaction of integrins with the membrane-bound growth factor receptors. In the former case, various growth factors and cytokines such as those found in serum and specifically epidermal growth factor (EGF), insulin-like growth factor-1, and tumor necrosis factor alpha (TNF-α) have been identified as altering the affinity state of integrins [101-104]. Importantly, VEGF has also been implicated in altering the affinity state of integrins and thus consists of a potential lever through which growth factors and integrin activation can work together to achieve a desired outcome [105, 106]. Crosstalk also occurs directly between growth factor receptors and integrins which in turns can affect both the affinity of integrins to ECM ligands as well as

the affinity of the growth factor receptor to its substrate. Receptors for platelet derived growth factor-β (PDGF-β) and VEGF for example localize with the β_3 subunit upon which activation of the β_3 subunit potentiates resultant VEGF-induced cellular functions [107-109]. Given the clearly interwoven state of crosstalk between growth factors and specifically that of VEGF and integrins, it is clear that further elucidation and utilization of this crosstalk is merited.

2.2.4 Role of biomaterials in enhancing MSC efficacy

To reiterate the main takeaway from this section, MSC use in bone repair is hampered for two main reasons: 1) the hostile environment within damaged tissue in which MSCs are implanted and 2) the lack of appropriate control over cell phenotype once MSCs are delivered into a defect. Biomaterials have been explored as avenues to solve these two issues. In this section, we will explain the state of the biomaterials field as it pertains to these two problem areas.

2.2.4.1 Role of biomaterials in enhancing MSC efficacy: vascularization

As stated earlier, tissue injury results in the destruction of a vascular network and thus the limited availability of necessary nutrients. To confront this issue, biomaterials have been engineered to address two main problems: 1) supplying necessary nutrients, notably oxygen, to delivered cells in the short-term and 2) supplying necessary signals to induce and enhance vascular remodelling in the damaged area over a longer temporal period. In

the former strategy, biomaterials have been engineered to generate oxygen to supply encapsulated cells through either the use of peroxides or perfluorocarbons [110-112]. Pedraza and colleagues engineered polydimethylsiloxane (PDMS) disks containing calcium peroxide which, when exposed to aqueous solutions, generate oxygen through the reaction between the peroxide and water [113]. The researchers tested this platform with pancreatic islets and showed that the oxygen-generating biomaterial significantly decreased hypoxia-induced islet death compared to the non-oxygen-generating biomaterial [113]. Specifically within a bone radial defect, Kimelman-Bleich *et al.* demonstrated that BMP-2-expressing MSCs resuspended in a hydrogel supplemented with oxygen-generating perfluorotributylamine exhibited heightened early-term cell survival and enhanced bone mineral density compared to cells in a hydrogel lacking the oxygen-generating compound [114]. Notably however, the researchers showed that at one week post-implantation, there ceased to be differences in cell number between the oxygen-generating and non-oxygen-generating group and that while differences arose in bone mineral density, there were no differences in bone volume [114]. The lack of differences between cell numbers at longer time-points may signal the need for the biomaterial to supply signals to enhance vascularization at longer temporal time-points.

This thus brings us to our second point: biomaterials that supply signals to enhance the speed at which vascular remodelling takes place within damaged tissue and specifically bone. One of the most widely used approaches for the induction of vascular invasion is delivery of angiogenic and osteogenic growth factors. The growth factors VEGF, FGF2,

BMP2, BMP7, PDGFB and TGFB1 have all been explored to increase the early onset of vascular invasion with the most prominently utilized growth factor being VEGF [115]. VEGF is a potent angiogenic/vasculogenic growth factor and exerts its effects through interacting with two receptor tyrosine kinases, VEGFR1 (otherwise known as Flt1) and VEGFR2 (otherwise known as Flk1) [116]. Activation of these receptors in endothelium causes destabilization of the junctions holding endothelial cells in order to facilitate angiogenesis. Once broken down, VEGF acts as a chemotactic factor as well as signals for the proliferation of endothelial cells. One of the first studies investigating VEGF for bone regeneration showed in a fracture model in mice that treatment with a soluble VEGF receptor blocking endogenous VEGF activity impaired new bone formation [117]. Additionally, when VEGF was continuously delivered to critically-sized bone defects in rabbits over the course of seven days via a subcutaneously implanted osmotic pump, significant bone regeneration was observed in comparison to no VEGF treatments. One of the drawbacks with this study, however, was the supraphysiological doses of VEGF required to induce bone regeneration as high microenvironmental concentrations of VEGF results in the formation of aberrant and leaky neovasculature [118, 119].

To optimally control the kinetics and distribution of therapeutic protein release and subsequently lower the total delivered dose, biomaterials have been engineered to achieve tailored and sustained delivery profiles. A common strategy is absorbing and entrapping growth factors within biomaterial scaffolds synthesized with pore sizes that would dictate growth factor release. Entrapment of VEGF into β-TCP scaffolds exhibited increased

invasion of microvasculature and osseointegration in a murine calvarial defect [120]. Similarly, incorporation of VEGF into a PLGA scaffold followed by coating with bioactive glass showed increased infiltration of blood vessels with an increase in bone mineral density in a rat calvarial defect compared to scaffolds without VEGF [121].

The effectiveness of therapeutic proteins depends heavily in the spatial and temporal microenvironmental concentrations of the protein(s). This delivery profile in turn is controlled by the total dose incorporated within a material, the kinetics of release, and the persistence and stability of the protein. In most therapies, including those in which therapeutic proteins are absorbed or incorporated into materials without any covalent or affinity-mediated tethering, release kinetics are defined by non-specific interactions between the protein and the material. Scaffold porosity, adsorption parameters, and affinity to the scaffold control the release of these proteins. In this sense, the kinetics of protein release can be thought of as a 'materials-driven process' with the advantage being that one can precisely engineer a material, by regulating pore size for example, to fit a distinct release profile. The issue, however, is that this process is independent on the particular protein-material pair and the surrounding biological environment. To engineer biomaterials to effectively deliver therapeutic proteins, it may be beneficial to consider how these growth factors are typically presented in tissue repair.

Following vascular injury, platelets, neutrophils, and macrophages respond to the injury and lay down a provisional fibrin-rich matrix with embedded growth factors [122].

As matrix metalloproteinases (MMPs) work to degrade this provisional matrix, ECM-bound growth factors are released and dictate the appropriate course of action for surrounding cells to heal the wound and revascularize the region [123]. It is this spatiotemporal control of MMP activity followed by the spatial regulation of growth factor concentration by ECM degradation and presentation that, among other factors, controls proper wound revascularization. Mimicking this ECM-embedding strategy can prove useful in aptly controlling angiogenic growth factor presentation within bone defects.

A ground-breaking study by Hubbell and colleagues demonstrated the engineering of a completely synthetic scaffold in which BMP2 had been entrapped within an MMP-sensitive hydrogel and used to regenerate bone within an orthotopic model [124]. *In vitro*, hydrogels exhibited BMP2 release kinetics which were highly dependent on gel degradation with 90% of the protein being retained in a saline solution whereas addition of the proteolytic MMP-2 induced 100% protein release. BMP2-loaded MMP-sensitive hydrogels also exhibited significantly higher bone healing in rat calvarial defects compared to hydrogels without MMP-sensitivity as well as those without BMP2. Further work has even shown that MMP-sensitive BMP2-loaded synthetic hydrogels exhibit higher bone regeneration in a critically-sized defect compared to the current clinical standard of a BMP2 loaded absorbable collagen sponge [125]. This biomaterial platform has also been used for vascularization applications through incorporation of angiogenic proteins [126, 127]. Covalently conjugating VEGF onto a PEG-diacrylate matrix results in increased tubule formation by endothelial cells cultured on top of the gels compared to conditions

with VEGF in the media indicating the importance of controlled growth factor presentation [128]. *In vivo*, delivering VEGF through covalent tethering to a protease-degradable PEG-maleimide matrix increases therapeutic re-vascularization in both hind limb ischemia and myocardial infarction models [129, 130]. Importantly, the VEGF-incorporated matrix increases the survival and function of transplanted islets thus showing promise for other cellular therapies [131].

A conceptually different strategy but one that still relates to the controlled presentation of growth factors is that of tethering heparin or other growth factor binding domains onto implantable materials. A highly negatively charged sulfated molecule, heparin exhibits the ability to bind to numerous angiogenic and osteogenic growth factors including VEGF, FGF, PDGF, and BMP2 through their heparin-binding domains. Scaffolds containing the covalently-bound heparin attempt to mimic the ECM by controlling the presentation and activity of growth factors through an affinity-based system [132, 133]. Heparin-bound BMP2 has been shown to induce elevated levels of ALP activity and increase proliferation in C2C12s compared to soluble BMP2 [134]. Taking a step further, certain materials can be chemically sulfated in order to bind to growth factors with the same or even higher affinity as heparin itself with sulfated alginate exhibiting enhanced FGF2-mediated vasculogenesis *in vivo* [135]. In lieu of heparin, Hubbell's group has pioneered the use of short protein fragments having precisely controlled cell and growth factor binding sites. By engineering a recombinant fibronectin fragment to contain fibrin-binding, integrin-binding and growth-factor binding sequences, Martino *et al*.

demonstrated that delivery of this fragment within a fibrin construct along with nominal levels of BMP2 and PDGF-BB significantly increased bone healing in a rat calvarial defect compared to fibrin constructs lacking the protein fragment [65]. Additionally, delivering VEGF and PDGF-BB within fragment-functionalized fibrin matrices enhanced skin wound healing in diabetic mice through increased angiogenesis. Further work in this area has resulted in isolation of a domain found on placenta growth-factor-2 that binds strongly to ECM proteins [136]. Inclusion of this domain onto VEGF, PDGF-BB, and BMP2 resulted in increased angiogenesis in an induced murine skin wound as well as elevated bone healing in a calvarial defect.

In addition to tissue-demanded kinetics control, covalently or affinity-based tethering of growth factors can potentially increase their half-lives compared to their unconjugated form, although this is system-dependent on the site of immobilization and the ability for interactions to still exist with specific epitopes [137-139]. To date however, no study has investigated materials in which controlled, tissue-demanded release of angiogenic growth factors have been applied in the context of bone regeneration leaving the field open to further materials engineering.

2.2.4.2 Role of biomaterials in enhancing MSC efficacy: Integrins

As stated earlier, integrins can profoundly affect cell phenotype based on the downstream pathways that are activated following integrin binding to the ECM. Furthermore, activation of different integrins can elicit differential activation of these

downstream pathways [140]. MSCs, for example, have been observed to undergo enhanced osteogenic differentiation upon binding and activation of the $\alpha_2\beta_1$ integrin that binds to type I collagen [141]. Because of this, biomaterial scaffolds have been engineered to activate only a certain repertoire of integrins in the hopes of being able to control cell phenotype. Importantly, a concerted effort has been placed on identifying and recognizing minimal integrin binding motifs on large ECM proteins to allow for modification of surfaces for cell-binding. In 1984, Pierschblacher and Ruoslahti first discovered the amino-acid sequence RGD as a minimal binding domain on fibronectin and postulated its presence in other proteins [142]. Since then, multiple other peptide sequences derived from proteins have been identified as binding domains such as the peptide sequences termed 'GFOGER' and 'IKVAV' for collagen and laminin respectively [143-145]. Specifically for bone, Wojtowcz *et al.* demonstrated that when the $\alpha_2\beta_1$-binding peptide GFOGER is coated on polycaprolactone (PCL) scaffolds and implanted into a critical-size defect in rat femurs, the coated scaffolds elicited enhanced bone regeneration compared to both non-coated scaffolds and empty controls [146]. Integrin-functionality has also been explored for use in vascularization. Endothelial cells undergoing angiogenesis abundantly express the $\alpha_v\beta_3$ integrin and treatment with an $\alpha_v\beta_3$ blocking antibody has been shown to abrogate tumor vascularization in small animal models [147, 148]. The successful use of integrin-blocking antibodies for inhibiting tumor vascularization and tumor growth in small animal models paved the way for integrin-blocking antibodies to be used in several clinical trials although limited anti-tumor efficacy was noted [149, 150]. Interestingly, while much attention has

been placed on limiting vascularization through blocking integrins, little to no attention has been paid to augmenting vascularization for tissue regeneration purposes through integrin strategies. Specifically for vascularization, the VEGF receptor, VEGFR-2, and the β_3 exhibit a type of synergism in which VEGFR-2 activation induces β_3 phosphorylation which consequently induces VEGFR-2 phosphorylation and activation of downstream angiogenic signalling [151]. Utilization of this synergism by providing a material that has both VEGF as well as is functionalized to bind preferentially to the β_3 integrin subunit could function as a potential vascularization strategy.

2.3 Mesenchymal stem cells for immunomodulation

As stated earlier, hMSCs have two general groups of properties: 1) These cells exhibit the ability to differentiate down osteogenic, chondrogenic and adipogenic lineages, but have also been claimed to differentiate into other cell types including muscle and endothelial lineages [3, 152-154] and 2) hMSCs secrete a repertoire of factors distinct from other cells and that has been noted to aid in inducing a pro-resolution phase after inflammation or injury [155]. Initial work with MSCs noted that MSCs had the capacity to repair damaged or destroyed tissue notably in bone. Because of their differentiation potential, there was debate that this could be a result of direct differentiation of the cells into osteoblasts which would then regenerate the bone. In a 2005 study, Taguchi and colleagues induced femur fractures in mice followed by an infusion of GFP-labelled bone marrow cells [156]. Three to five weeks following fracture, researchers found GFP- and

osteocalcin-dual positive cells within the callus and hypothesized that the infused bone marrow cells directly differentiated into osteoblasts within the defect thus contributing to its regeneration [156]. More recently however, mounting evidence points to a more indirect process of MSC-based tissue regeneration where these cells act as a modulatory player throughout the inflammatory and restorative process. In this section, we will discuss three topics regarding MSC-immunomodulation: 1) what properties do MSCs exhibit and how are they pertinent to immunomodulation, 2) chronic inflammatory and auto-immune disease models in which MSCs have been employed, and 3) issues with current approaches and how can new technologies alleviate these issues.

2.3.1 Properties of MSCs for immunomodulation

Properties of MSCs for immunomodulation can be separated into two broad categories: 1) the secretion of soluble factors and 2) contact-dependent factors. MSCs secrete a repertoire of soluble factors that are involved in immunomodulation including interleukin-6 (IL-6), prostaglandin E2 (PGE2), indoleamine-pyrrole 2,3-dioxygenase (IDO), transforming growth factor-β (TGF-β), IL-10, VEGF, M-CSF as well as a variety of CCLs and CXCLs [157-159].

2.3.1.1 Soluble factors: Indoleamine-pyrrole 2,3-dioxygenase (IDO)

Indoleamine-pyrrole 2,3-dioxygenase (IDO) is an enzyme that constitutes the rate-limiting step in the metabolism of tryptophan to kynurenine [160, 161]. Early studies in

IDO and its role in modulation of immune cells discovered that select subsets of antigen-presenting cells (APCs) express IDO and have significant immunomodulatory effects on T-cells [162]. Dendritic cells and macrophages that co-express CD123 and CCR6 have enhanced IDO activity which correlates with reduction in T-cell proliferation *in vitro* [163]. Multiple groups have since affirmed that MSCs also express IDO under certain conditions and that MSC-secreted IDO expression is correlated with reductions in activated T-cell proliferation when MSCs are co-cultured with activated T-cells [164-166]. Moreover, this suppression of proliferation is at least in part due to MSC-secreted IDO activity as addition of an IDO inhibitor restores proliferation of the treated T-cells [164, 167]. MSC-based IDO also plays a role in the regulation of natural killer (NK) cells. When MSCs were co-cultured with isolated NK cells, the proliferation and cytotoxicity of the NK cells was significantly reduced while addition of an IDO inhibitor partially restored NK activity [168]. Interestingly, previous studies have argued that IDO is in fact not important for MSC-based immunomodulation, instead arguing that it is inducible nitric oxide synthase (iNOS). Ren *et al.* treated MSCs with an IDO inhibitor and found no effect on splenocyte proliferation while iNOS activity did correlate with lower T-cell proliferation with Sato and colleagues affirming this as well [169, 170]. Further elucidation into this paradox revealed species differences in immunomodulation with mouse MSCs utilizing iNOS and human MSCs using IDO to suppress immune responses [171]. This ‘devil in the details’ underscores the risk in drawing conclusions from dissimilar studies as well as the importance of utilizing human cells for clinical relevance. Importantly, for MSCs to exhibit significant IDO

activity, the cells must first be activated by the presence of pro-inflammatory factors, the most important being interferon gamma (IFN-γ) [172]. The process of activating MSCs to express IDO through incubation with IFN-γ is known as 'licensing' [173]. While activated T-cells and other immune cells secrete IFN-γ to then activate MSCs, licensing MSCs with IFN-γ prior to co-culturing with immune cells enhances the MSC's immunosuppressive activities by not only blocking T-cell proliferation, as un-licensed MSCs do, but also ameliorating T-cells' effector functions [174]. Furthermore, IDO activity within MSCs is significantly different among different MSC donors, thus implicating a need for augmenting IDO activity to ensure a higher portion of MSC batches can elicit a biological effect [175].

2.3.1.2 Soluble factors: Prostaglandin E2

Prostaglandin E2 (PGE2) is a small-molecule product of the metabolism of arachidonic acid by cyclooxygenases, COX-1 and COX-2 [176]. While COX-1 is constitutively expressed, COX-2 expression is highly dynamic with increased expression occurring via concerted actions of specific cytokines and growth factors within pro-inflammatory environments [177]. While COX-2 can significantly increase presence of PGE2 in inflammatory environments, the degradation of PGE2 is also tightly controlled by two metabolic enzymes 15-hydroxyprostaglandin dehydrogenase and 15-keto-prostaglandin-13-reductase [178]. PGE2 has a short half-life *in vivo*, approximately seven minutes in whole blood, signifying that the concentration of PGE2 is highly regulated

based on the activity of both COX-2 as well as the two metabolic enzymes governing its degradation [179]. PGE2 exerts its effect through an array of G-protein coupled receptors designated EP1, EP2, EP3 and EP4 receptors which subsequently activate cAMP, PI3K, and Rho downstream pathways depending on which EP receptor is activated [180]. Regarding its role in MSC-related immunosuppression, PGE2 has been implicated in a similar role as that of IDO. When licensed with IFN-γ, hMSCs significantly increase their secretion of PGE2 [181, 182]. T-cells cultured without MSCs but with increasing concentrations of exogenously added PGE2 exhibit a dose-dependent decrease in their proliferation similar to that of when MSCs are placed in co-culture [181]. In addition to having the ability to suppress T-cell proliferation, MSC-secreted PGE2 is also implicated in inducing a $CD4^{+}Foxp3^{-}$ regulatory T-cell phenotype while inhibiting a T-helper 17 cell differentiation [183, 184]. The effect of MSCs on NK cells, as discussed earlier being at least partially affected by IDO, is also dependent on PGE2 as treatment with a COX-2 inhibitor restores NK cell proliferation and effector function [185]. An effect of PGE2 not noted for IDO is the inhibition of dendritic cell differentiation from monocytes [186]. When co-cultured with MSCs, human-derived monocytes in dendritic cell differentiation media show significantly less dendritic cell differentiation compared to monocytes cultured without MSCs. Furthermore, when the co-cultures were treated with a COX-2 inhibitor, the dendritic cell differentiation is restored even in the presence of MSCs [186]. A common theme that can be seen here and repeated throughout this section is the multitude of MSC-related pathways through which immune suppression can occur.

2.3.1.3 Soluble factors: IL-6

Interleukin-6 is a pleiotropic cytokine secreted by a variety of cells including MSCs. While MSCs secrete basal levels of IL-6, this secretion is, similar to PGE2 and IDO, increased when pro-inflammatory cytokines are present in the MSC microenvironment [187]. Similar to PGE2, IL-6 has been implicated in the inhibition of monocyte-derived dendritic cell differentiation [188]. When MSCs were incubated with purified monocytes under dendritic cell differentiation conditions, as seen in other studies, the differentiation of monocytes was prevented as analyzed through the ratio of CD1a+ to CD14+ markers. When an anti-IL-6 neutralizing antibody was added however, the differentiation of dendritic cells was partially restored [188]. Further studies concluded that this MSC-secreted IL-6 effect also holds for CD34+-derived dendritic cell differentiation [189]. M-CSF was also implicated in these same studies as an important factor in inhibiting dendritic cell differentiation [188, 189]. A proposed mechanism for this effect is that the IL-6 secreted by MSCs induces monocytes to upregulate the secretion of IL-10 which in turn acts in an autocrine fashion to halt the dendritic cell differentiation process [190].

2.3.1.4 Soluble factors: Macrophage colony stimulating factor (M-CSF)

Macrophage colony stimulating factor (M-CSF) is a cytokine constitutively expressed by a variety of cells in the body including MSCs [191]. M-CSF is commonly used to differentiate bone marrow cells into macrophages eliciting an anti-inflammatory phenotype [192]. These macrophages tend to express high levels of the anti-inflammatory

cytokine IL-10 as well as CCL2 compared to macrophages cultured in granulocyte macrophage colony-stimulating factor which tend to elicit a more inflammatory phenotype [193]. Because of this, MSC-secreted M-CSF secretion has been studied as a conduit for its role in immunosuppression. As stated earlier, groups that concluded IL-6 to have an important factor in regulating the differentiation of monocytes to dendritic cells also found M-CSF to have a similar effect as well [188, 189]. When MSC / monocyte co-cultures were treated with a neutralizing antibody toward M-CSF, monocytes partially regained their differentiation potential toward dendritic cells. Importantly, neutralizing both IL-6 and M-CSF allowed monocytes to regain their differentiation potential to a greater extent than neutralizing either factor individually. On a related note, MSC-secreted M-CSF plays a crucial role in the ability for MSCs support hematopoiesis *in vitro* [194].

2.3.1.5 Soluble factors: CCL2 / Monocyte chemoattractant protein -1

CCL2, otherwise known as monocyte chemoattractant protein-1, is also a cytokine secreted by MSCs and implicated in their role of immunomodulation. MSC-secreted CCL2 has been shown to inhibit immunoglobulin production from differentiated B cells in both *in vitro* and *in vivo* models [195].

2.3.1.6 Contact-dependent factors: PD-L1 (B7-H1)

In addition to the various soluble cytokines that have been implicated to play a role in MSC-based immunomodulation, there are various contact-dependent mechanisms that

have been studied and proposed to enhance the anti-inflammatory phenotype of MSCs. This was first identified *in vitro* when transwells were used to separate MSC culture from the T-cells. While MSCs on transwells still retained their ability to suppress activated T-cell proliferation, it was significantly less potent than cells in direct contact with the T-cells [196, 197]. One of the hypothesis following this finding was that the soluble factors necessary for immunosuppression, namely nitric oxide, had short half-lives and thus needed to be in close proximity to the immune cells [170]. However, when it was discovered that nitric oxide was used by mouse MSCs rather than human MSCs and the transwell effect was still noted in human MSCs, this hypothesis was partially ruled out. A recent study noted that MSCs regulate T-cell suppression through IDO-independent pathways, notably through cell-cell contact and the programmed death pathway [198]. MSCs express high levels of membrane-bound B7-H1 molecule otherwise known as programmed death ligand-1 (PD-L1) when licensed with IFN-γ. When these licensed MSCs are co-cultured directly with T-cells and siRNA directed at PD-L1, the MSC-based immunosuppression of T-cell proliferation is significantly reduced [198]. Future experiments showed that this regulation by B7-H1 is independent of the IDO pathway as inhibiting IDO activity had no effect on the cell-cell contact inhibition. Together, the presence of both soluble and cell-cell contact mediated pathways as well as the multitude of independent pathways for MSC-based immunomodulation contributed to the notion of MSCs being a useful tool for treatment of chronic and autoimmune diseases.

2.3.2 Research advances in MSC immunomodulation

Because of their role in immunomodulation, MSCs have been proposed as a candidate for cell therapy in a variety of preclinical disease models including colitis, graft vs host disease (GvHD), arthritis, autoimmune encephalomyelitis, type 1 diabetes, lupus and many more [169, 199-204]. Of particular note however are the disease models in which a number of clinical trials have and are being conducted to ascertain the efficacy of MSC therapy, notably acute GvHD and inflammatory bowel disease (IBD).

Acute Graft vs Host Disease (aGvHD) is a condition following hematopoietic stem cell transplantation (HSCT) where donor T-cells become activated by the host system due to the preparative regime and begin damaging host tissue, usually within the gastrointestinal tract, the skin and liver [205]. Following allogenic HSCT, up to 14% of recipients will develop severe aGvHD with a third of these patients not responding to steroid therapy leading to a dismal prognosis for survival [206]. MSCs have been proposed as a way to treat steroid-resistant aGvHD with over 30 studies either completed or underway (www.clinicaltrials.gov). Le Blanc and colleagues found that out of 55 patients having severe aGvHD that received an infusion of MSCs, 30 had a complete response while the other 25 had either a partial or no response to MSC therapy [207]. Those that did not respond had a mortality rate of 72% within the first year after treatment. The complete responders had a lower mortality rate but of the 30 that responded, 11 had died within the first year from transplantation-related issues [207]. Another clinical study by Resnick and colleagues found similar results in which responders to MSC infusion therapy had a significantly lower mortality rate at 6 months post infusion compared to non-responders

[208]. However, only 17 of 50 patients showed a complete response with the rest showing either partial or no response. These and other trials show a similar pattern in that the fraction of patients exhibiting a complete response, while exhibiting much higher survival rates, is approximately half of total patients receiving therapy [209]. Other trials meanwhile cast doubt on the efficacy of MSCs to treat aGvHD altogether. A phase III clinical trial for using MSCs for treatment of steroid-refractory GvHD failed to meet an overall response rate better than placebo control [210]. We will discuss some of the important issues and paradoxes in MSC efficacy following the discussion on IBD.

MSC-based therapy in clinical trials have also been used for treating IBD. IBD, including Crohn's disease and ulcerative colitis, is an autoimmune disease where overactive T-cells within the intestine react with surrounding tissue ultimately leading to excessive inflammation and damage causing detrimental effects on quality of life [211, 212]. To date, 22 clinical trials using MSCs as a treatment for Crohn's disease are either completed or ongoing with results similar to that of GvHD, notably, that while MSC therapy can improve patient outcome, only a limited portion of patients respond to the therapy (www.clinicaltrials.gov). In a phase I clinical study, out of 9 patients exhibiting refractory Crohn's disease and given two doses of MSC therapy, 3 patients showed positive response to the treatment while another three needed surgery due to disease progression [213]. In another phase II clinical study, out of 15 patients exhibiting refractory Crohn's disease, although the overall disease score was significantly reduced with administration of MSCs for group as a whole, the patient improvement was only noted in 7 of the 15

patients [214]. In a phase III randomised double-blind clinical trial, Panés and colleagues found that out of 107 patients receiving MSC infusion therapy to treat their refractory Crohn's disease, 53 patients achieved remission compared to 36 out of 105 patients in the placebo group [215]. Overall, as was seen in the GvHD cases, treatment with MSCs seems to enhance patient outcome but only in a portion of the total patient group, in some cases less than half. The cause of this can be traced to one of two factors: 1) patient factors or 2) treatment factors. While patient factors are vitally important and much research is being conducted on ascertaining which patients might be most beneficial for which therapies, we will limit our discussion to treatment-related factors and point out how these can be enhanced with recent research advances.

2.3.3 Augmenting treatment-related factors for enhanced patient outcomes

Whereas other factors are certainly in play, one of the main factors that can affect the efficacy of cell therapy is the state in which the cells that are infused are at. In other words, the efficacy of cell therapy relies on the ability of the infused cells to impart a desired effect. In terms of immunomodulation, this translates into increasing the anti-inflammatory nature of MSCs. As stated earlier, one of the ways MSCs show enhanced immunomodulation *in vitro* is through licensing and this notion continues for preclinical studies. Polchert *et al.* found that mice exhibiting GvHD injected with MSCs pre-treated with IFN-γ showed significant improvements in GvHD scores compared to those injected with MSCs that were not pre-treated [216]. This is also seen in models of induced colitis

where MSCs stimulated to augment IDO activity prior to injection showed enhanced efficacy in mice compared to MSCs that were not pre-stimulated [217, 218]. Another potential issue with the anomalies posed by the mixed clinical trial results is potentially in the heterogeneity of the cell sources itself. Donor variability and the immunomodulatory capacity of MSCs from different sources are known to exist [175]. A recent study however shows that while differences were seen at basal states in between different MSC batches, once the cells were licensed with inflammatory factors, all cells elevated their immune inhibitory capacities to similar levels [219].

MSCs that are licensed prior to use *in vivo* thus show signs of higher efficacy than those that are not. However, two issues arise with this approach: 1) the length of activation and 2) the complexity of clinical translation. In terms of the former, while licensing MSCs increases their immunomodulatory capabilities, once MSCs are removed from an environment presenting IFN-γ, their immunomodulatory capability decreases significantly [220]. To alleviate this issue, various groups have attempted to continuously license MSCs through either genetic modification or continuous presentation of IFN-γ within a biomaterial [220, 221]. Approaches focused on continuous presentation of IFN-γ though do not currently control the release of IFN-γ thus posing a risk for use *in vivo* to potentially augmenting the deleterious effect of additional IFN-γ. Furthermore, genetic modification of MSCs faces significant translation and regulatory barriers. In terms of the second issue, that of complexity of clinical translation, the act of needing to culture cells ex vivo for manipulation prior to injection has been the death knell for various companies. Engineering

a biomaterial scaffold that can continuously present encapsulated MSCs with a licensing agent in a controlled fashion can eliminate the need to culture cells ex vivo, improve the clinical translatability of MSC therapy and augment MSC efficacy for improved patient outcome.

CHAPTER 3. AIM 1: INTEGRIN-SPECIFIC HYDROGELS FUNCTIONALIZED WITH VEGF FOR VASCULARIZATION AND BONE REGENERATION

Adapted from:

Garcia JR, Clark AY, Garcia AJ. *Integrin-specific hydrogels functionalized with VEGF for vascularization and bone regeneration in critical-size bone defects*. J. Biomedical Materials Research A. 2016. 104(4): 889-900 [222]*

3.1 Abstract:

Vascularization of bone defects is considered a crucial component to the successful regeneration of large bone defects. Although vascular endothelial growth factor (VEGF) has been delivered to critical-size bone defect models to augment blood vessel infiltration into the defect area, its potential to increase bone repair remains ambiguous. In this study, we investigated whether integrin-specific biomaterials modulate the effects of VEGF on bone regeneration. We engineered protease-degradable, VEGF-loaded polyethylene glycol (PEG) hydrogels functionalized with either a triple-helical, $\alpha_2\beta_1$ integrin-specific peptide (GFOGER) or an $\alpha_v\beta_3$ integrin-targeting peptide (RGD). Covalent incorporation of VEGF into the PEG hydrogel allowed for protease degradation-dependent release of the protein while maintaining VEGF bioactivity. When applied to critical-size segmental defects in

* chosen as 2016 Student Award for Outstanding Research by Society for Biomaterials

the murine radius, GFOGER-functionalized VEGF-free hydrogels exhibited significantly increased vascular volume and density and resulted in a larger number of thicker blood vessels compared to RGD-functionalized VEGF-free hydrogels. VEGF-loaded RGD hydrogels increased vascularization compared to VEGF-free RGD hydrogels, but the levels of vascularization for these VEGF-containing RGD hydrogels were similar to those of VEGF-free GFOGER hydrogels. VEGF transiently increased bone regeneration in RGD hydrogels but had no effect at later time points. In GFOGER hydrogels, VEGF did not show an effect on bone regeneration. However, VEGF-free GFOGER hydrogels resulted in increased bone regeneration compared to VEGF-free RGD hydrogels. These findings demonstrate the importance of integrin-specificity in engineering constructs for vascularization and associated bone regeneration.

3.2 Introduction:

Vascularization is a crucial factor in bone development as well as the repair of bone defects [11, 223, 224]. In the developing skeleton, long bones are formed through endochondral ossification which involves the invasion and sprouting of blood vessels into the intermediate cartilage tissue followed by osteoprogenitor cell migration and mineralization of the cartilaginous anlage [30]. Blocking infiltration of blood vessels into the cartilage tissue causes enlarged hypertrophic zones associated with incomplete and delayed onset of ossification and suboptimal bone formation [225]. In terms of bone repair, large bone defects arising from trauma or cancer resection suffer from poor vascularization

and impaired healing [226]. Co-induction of a tibial fracture and vascular injury in the form of hind limb ischemia in a mouse model increases the chances of a non-union compared to the fracture alone [55]. Anti-angiogenic treatment to inhibit the initial revascularization response following a critical-size segmental defect also results in lower levels of bone formation and a higher prevalence of non-union [117]. Although current gold-standards of autografts and allografts are extensively used in the clinic, these constructs are significantly limited by donor-site morbidity, supply, bioactivity and risk of infection [227]. Additionally, the revascularization of these grafts remains limited without micro-surgical procedures which often results in high degrees of local tissue morbidity [228, 229]. Therefore, incorporating cues to augment the vascularization response can greatly enhance the efficacy of these treatments while diminishing their limitations.

Vascular endothelial growth factor (VEGF) has routinely been delivered to increase vascularization *in vivo*. By interacting with two main tyrosine kinase receptors, VEGFR1 and VEGFR2, VEGF destabilizes existing blood vessel walls and allows endothelial cells to proliferate and migrate in the direction of highest VEGF concentration [116]. VEGF is instrumental in bone development as blocking VEGF activity results in reduced angiogenesis, massive chondrocyte death and severely under-developed bone [34, 35]. However, in terms of bone repair, the efficacy of exogenous VEGF in increasing vascularization and associated bone regeneration remains ambiguous. One of the first studies utilizing VEGF for bone treatment demonstrated that continuous delivery of VEGF to a rabbit critical-size defect through a subcutaneously implanted osmotic pump resulted

in increased bone formation compared to no VEGF treatment [117]. Subsequent efforts have focused on engineering scaffolds to deliver VEGF through more practical methodologies. VEGF incorporated into β-tricalcium phosphate and PLGA scaffolds increased blood vessel invasion and bone formation in critical-size defects [120, 121]. Other reports, however, have shown VEGF to induce minimal bone formation despite enhanced blood vessel formation [230-234].

Synergistic interactions between VEGF receptors and integrin adhesion receptors provide signals regulating vascularization. For example, blocking antibodies against the α_2 subunit of the collagen-binding $\alpha_2\beta_1$ integrin inhibits VEGF-dependent endothelial cell chemotaxis [235]. Consistent with these results, deletion of the β_1 integrin subunit using the Cre-lox system negatively impacts angiogenic sprouting [235]. VEGF has also been shown to upregulate endothelial cell surface expression of $\alpha_2\beta_1$ [236]. In addition to the $\alpha_2\beta_1$ integrin, the $\alpha_v\beta_3$ integrin plays a central role in angiogenesis and vascularization [147, 237, 238].

While the mechanism of integrin-dependent angiogenesis remains unclear, antagonists to $\alpha_v\beta_3$ have been used to prevent abnormally active angiogenesis within tumors as activated endothelium within these environments exhibit greatly enhanced expression of $\alpha_v\beta_3$ [239-243]. Extensive cross-talk also exists between $\alpha_v\beta_3$ and VEGF as expression of VEGF is in part induced through $\alpha_v\beta_3$ ligation, clustering and association of the β_3 subunit

with phosphorylated p66 Shc [106]. The β_3 subunit is also involved in the activation of VEGFR2 in response to VEGF [105, 151].

Because of the interplay between VEGF and integrins $\alpha_2\beta_1$ and $\alpha_v\beta_3$, the objective of this study was to investigate whether presentation of integrin-specific peptides within a hydrogel in combination with exogenous VEGF modulates vascularization and bone formation in a murine segmental bone defect model. We synthesized protease-degradable poly(ethylene glycol)-based hydrogels functionalized with VEGF and either the collagen I-mimetic $\alpha_2\beta_1$-targeting GFOGER peptide or the fibronectin-derived $\alpha_v\beta_3$-targeting RGD peptide. We then implanted these constructs within critical-size murine radial bone defects and evaluated blood vessel formation and newly formed bone tissue. Based on previous studies showing that GFOGER-functionalized biomaterials promote osteoblastic differentiation *in vitro* [244] and enhance osseointegration of metal implants in rat tibiae [245], we hypothesized that VEGF-functionalized GFOGER hydrogels would increase vascularization and subsequent bone regeneration compared to VEGF-functionalized RGD hydrogels.

3.3 Materials and Methods:

3.3.1 PEG hydrogel synthesis and VEGF release kinetics

Four-arm maleimide-end functionalized PEG macromer (PEG-MAL 20 kDa MW, Laysan Bio, >95% purity) was functionalized with recombinant human VEGF-A165

(Invitrogen) for 15 min at room temperature in 10 mM HEPES buffer pH=7.4 followed by functionalization with either GFOGER peptide, GGYGGGP$(GPP)_5$GFOGER$(GPP)_5$GPC (AAPPTec), or RGD peptide (GRGDSPC) (AAPPTec). Functionalized macromers were cross-linked using the bi-cysteine peptide VPM (GCRDVPMSMRGGDRCG) (AAPPTec). The PEG-MAL hydrogels were synthesized to obtain a final concentration of 1.0 mM adhesive peptide and 10 µg/mL VEGF unless otherwise noted. The concentration of cross-linker used for the synthesis of each hydrogel was calculated by matching the number of cysteine residues on the cross-linker to the number of residual maleimides on the PEG-MAL macromer following adhesive peptide and VEGF functionalization. Hydrogels were allowed to gel at 37°C for 15 min before swelling in PBS. For verification of VEGF tethering to the PEG-MAL macromer, the VEGF-PEG-MAL product was run on SDS-PAGE gel followed by protein visualization with Sypro Red (Life Technologies) staining.

To assess VEGF release kinetics, VEGF was labelled with NHS-AlexaFluor 488 (Life Technologies), purified, and incorporated into hydrogels as described. Hydrogels were incubated in either PBS or 50 µg/mL collagenase (Worthington Biomedical). At specified time points, supernatant was collected and analyzed for fluorescence.

3.3.2 Rheology

To examine the effect of adhesive peptide and VEGF incorporation on the rheological properties of hydrogels, the storage and loss moduli of hydrogels were assessed by dynamic

oscillatory strain and frequency sweeps performed on a MCR 302 stress-controlled rheometer (Anton Paar, Austria) with a 9 mm diameter, 2° cone and plate geometry. The hydrogels were synthesized as described and loaded between the cone and plate, after which the measuring system was lowered to a 39 μm gap. Initial strain amplitude sweeps were performed at an angular frequency of 10 rad s^{-1} to determine the linear viscoelastic range of the hydrogel. Oscillatory frequency sweeps were then used to examine the storage and loss moduli (ω= 0.5-100 rad s^{-1}) at a strain of 1%.

3.3.3 Bioactivity of PEGylated VEGF

Human umbilical vein endothelial cells (HUVECs, Lonza) were grown in complete endothelial growth media EGM-2 (Lonza). Cells were synchronized in growth factor-free basal media (EBM-2, Lonza) with 1% fetal bovine serum (FBS) for 8 hours followed by addition of soluble VEGF, VEGF-conjugated PEG-MAL macromer, or control (VEGF-free) media for 48 hr. Cell metabolic activity was measured using CellTiter 96 AQueous One Solution Cell Proliferation Assay (Promega). To assess the activity of endothelial cells on VEGF-functionalized hydrogels, GFOGER-modified hydrogels were synthesized with or without incorporated VEGF. HUVECs were seeded at 10,000 cells/cm^2 and incubated for 4, 8 or 15 hours. Samples were fixed in 3.7% paraformaldehyde, stained with AlexaFluor 488-conjugated phalloidin and DAPI, and imaged on a Nikon C2 confocal microscope. Endothelial cell network length and cell numbers were quantified using a custom macro in ImageJ.

3.3.4 3D endothelial cell network formation

To study 3D endothelial cell network assembly, a co-culture of GFP-expressing HUVECs (Angioproteomie) and mouse embryo 10T1/2 cells (ATCC) was used. GFP-expressing HUVECs and 10T1/2 cells were resuspended in media and encapsulated in PEG-MAL hydrogels presenting either GFOGER or RGD at final cell densities of 4 $x10^6$ cells/mL for 10T1/2 cells and 15 $x10^6$ cells/mL for HUVECs. For gels containing VEGF, gels were incubated in EGM-2 media without supplemented VEGF. For gels synthesized without VEGF, gels were incubated in EGM-2 media with or without soluble VEGF. The cell-laden hydrogels were cultured for 48 hours, rinsed, and fixed in 3.7% paraformaldehyde. GFP-expressing HUVECs were imaged on a Nikon C2 confocal microscope and 3D network formation analyzed using a custom ImageJ macro.

3.3.5 Bone defect surgery

A critical-size bone defect model in the mouse radius was used to evaluate bone formation as previously described [246]. All animal experiments were performed with the approval of the Georgia Tech Animal Care and Use Committee within the guidelines of the Guide for the Care and Use of Laboratory Animals. C57BL/6J wild-type male mice (8-10 weeks old, Jackson Laboratories) were anesthetized under isoflurane and fur was removed from the right forelimb. Prior to surgery, mice were administered a single dose of slow-release buprenorphine for pain relief. The right forelimb was then swabbed with chlorohexidine and alcohol, and a 1.5 cm incision was made in the skin. Muscle tissue

surrounding the ulna and radius was dissected away, and a 2.5 mm complete excision in the radius was made using a custom-built bone cutter. A 4-mm long polyimide sleeve with laser machined holes containing 3.0 µL of hydrogel was carefully inserted over the ends of the defect. The incision was then closed using Vicryl sutures. Mice were monitored post-surgery for lethargy, weight loss, normal eating habits and signs of distress.

3.3.6 µCT angiography

Animals were euthanized by CO_2 inhalation at 8 weeks post-surgery. Radiopaque contrast agent-enhanced µCT angiography was performed using a protocol modified from Phelps *et al*. [129]. Briefly, an incision was made across the lower abdomen of the mouse followed by a continuing incision up the midline of the mouse exposing the entire abdominal cavity. The thoracic cavity was cut to carefully expose the heart. A butterfly needle was inserted into the left ventricle followed by cutting of the lower vena cava. Mice were then sequentially perfused with saline, 10% neutral buffered formalin, saline and lead chromate-based radiopaque contrast agent at a 30:60:10 v/v mixture of MV-122 Yellow:MV-diluent:MV curing agent (Microfil MV-122, Flow Tech). Samples were kept at 4°C overnight to allow the contrast agent to polymerize, and the forearms were then incubated for 72 hours in Krajian decalcification solution (Ricca Chemical), rinsed with PBS and scanned using a µCT50 scanning system (7 µm resolution, 55 kVp, 145 µA, Scanco Medical).

3.3.7 Immunohistochemistry

Following euthanasia by CO_2 inhalation, the ulna and radius were excised and fixed in 10% neutral-buffered formalin, decalcified using Krajian decalcification solution, processed for paraffin embedding and embedded in paraffin wax. Sections (5 µm thick) were deparaffanized and incubated in antigen retrieval solution (10 mM sodium citrate buffer, pH=6.0) overnight at 60°C. Sections were then stained with either rabbit anti-endomucin or rat anti-CD31 antibodies overnight at 4°C followed by secondary staining with AlexaFluor 488- and AlexaFluor 555-conjugated goat antibodies for 1 hour at room temperature. Sections were imaged on a Nikon C2 confocal microscope.

3.3.8 VEGF & FGF-2 secretion

Human mesenchymal stem cells (hMSCs, Texas A&M University) were grown in α-MEM containing 16% FBS, 2 mM L-glutamine, 100 U/mL penicillin and 100 µg/mL streptomycin. HMSCs were encapsulated in VEGF-free integrin-specific hydrogels as previously described at a concentration of 5 $x10^6$ cells/mL and cultured for 24 hours in growth media. After 24 hours, the media was exchanged for osteogenic media (growth media with 10 nM dexamethasone, 20 mM Na-β-glycerolphosphate, and 50 µM L-ascorbic acid 2-phosphate). After 7 days in culture, the conditioned media was collected and assayed for VEGF and FGF-2 levels using ELISA (Life Technologies, USA).

3.3.9 µCT imaging of bone formation

In vivo μCT imaging was performed on anesthetized mice using a VivaCT imaging system (Scanco Medical) at a voltage of 55 kVp and a current of 142 μA. Mice were centered such that the 2.5 mm radial defect was scanned within a 3.2 mm scan length window. Bone volume was evaluated as previously described [246]. Briefly, 2D slices were contoured to solely include the radius followed by application of a Gaussian filter (sigma=1, support=1, threshold= 540 mg HA/ccm). While 3D reconstructions displayed the full 3.2 mm scanned length, only the middle 2.0 mm of the defect was analyzed for bone volume.

3.3.10 Statistics

Error bars on graphs represent SEM. Comparisons among multiple groups was performed by one-way analysis of variance (ANOVA) with post-hoc Tukey tests. Comparisons between two groups were done through a *t*-test in GraphPad Prism 6. A *p* value of <0.05 was considered significant.

3.4 Results

3.4.1 Synthesis and characterization of VEGF-releasing PEG-MAL hydrogels

We engineered hydrogels based on a maleimide-functionalized 4-arm PEG macromer which allows for peptide tethering onto the polymer precursor via a Michael-type addition reaction between the terminal-maleimide group and free thiols present on the biomolecules. Subsequent reaction with bi-cysteine cross-linking peptides (VPM) containing a protease

cleavage site resulted in the formation of an insoluble cross-linked PEG hydrogel network sensitive to protease degradation (Fig. 2A). Prior to cross-linking, the PEG-MAL macromer was functionalized with VEGF. The VEGF-functionalized macromer was further reacted with either the RGD or GFOGER cell adhesion peptides in order to investigate the coupled effects of biomaterials-based VEGF delivery and integrin-specificity on vascularization and bone regeneration. By design, covalent incorporation of VEGF onto the hydrogel backbone provides for cell-demanded release of VEGF as the construct degrades and the surrounding tissue invades. Covalent tethering of VEGF to the PEG-MAL macromer was verified through an expected increase in molecular weight for VEGF reacted with PEG-MAL polymer on SDS-PAGE (Fig. 2B).

To determine the kinetics of VEGF release from integrin-specific hydrogels *in vitro*, VEGF was fluorescently labelled and incorporated into RGD- or GFOGER-functionalized hydrogels. Hydrogels subjected to collagenase treatment degraded within the first 48 hours and released 100% of the incorporated VEGF (Fig. 2C). We note that the collagenase concentration used was selected to fully degrade the gel by 2-3 days and does not reflect *in vivo* protease-dependent degradation [246, 247]. In contrast, hydrogels incubated in PBS remained intact and, following an initial burst release due to hydrogel swelling, retained approximately 70% of the loaded VEGF over a period of 5 days. To investigate whether adhesive peptide or VEGF incorporation influences the hydrogel's mechanical properties, we performed dynamic oscillatory rheological testing to assess the storage (G') and loss (G'') moduli of the different hydrogel conditions (Fig. 2D). Importantly, no significant

differences in moduli were detected among the hydrogel conditions tested (average storage and loss moduli equal to 160 ± 6.3 and 8.1 ± 0.69 Pa, respectively).

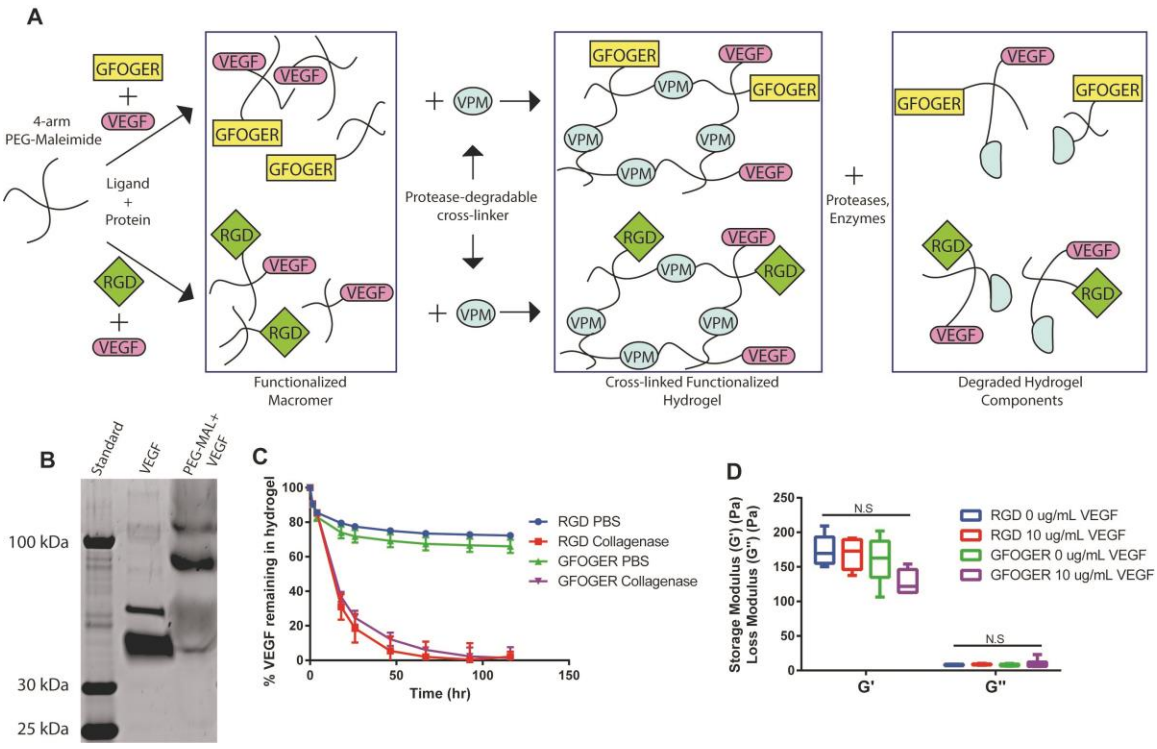

Figure 2: Protease-degradable integrin-specific PEG-MAL hydrogels for degradation-dependent release of covalently-tethered VEGF. (A) Schematic detailing PEG-MAL synthesis, stoichiometric ligand functionalization and growth factor incorporation. (B) Gel electrophoresis of VEGF and PEG-MAL+VEGF demonstrating increased MW of VEGF tethered onto PEG-MAL macromer. (C) VEGF release profile from integrin-specific hydrogels treated in PBS or collagenase as measured through fluorescence (Mean ± SEM N=4). (D) Rheological properties of integrin-specific hydrogels measured through storage and loss moduli from dynamic oscillatory frequency tests (Box-whisker plot show min-max, N= 6) N.S., not significant.

3.4.2 Bioactivity of PEGylated and hydrogel-tethered VEGF

We next investigated the bioactivity of VEGF tethered to the PEG-MAL macromer. HUVECs cultured in media containing either PEG-MAL-conjugated or unmodified VEGF displayed similar dose-dependent responses in metabolic activity over the course of 48 hours (Fig. 3A). This result indicates that VEGF tethered to the PEG-MAL macromer retains bioactivity and that the PEG macromer does not interfere with VEGF-dependent signaling.

We further examined the bioactivity of VEGF tethered to hydrogels by assessing the proliferation and network formation of endothelial cells cultured on top of hydrogels with either VEGF-tethered or VEGF-free hydrogels. GFOGER-functionalized hydrogels supported cell adhesion regardless of VEGF incorporation (Fig. 3B). By 8 and 15 hours after seeding, endothelial cells adhering to VEGF-containing hydrogels exhibited elevated levels of network formation compared to hydrogels lacking VEGF (Fig. 3B-C). By quantifying the number of nuclei, we also found a significant increase in the number of endothelial cells on VEGF-containing hydrogels compared to VEGF-free gels (Fig. 3D). Taken together, these results show that tethering VEGF to the PEG-MAL macromer either in soluble form or after incorporation into a hydrogel network maintains the bioactivity of VEGF in regards to endothelial cell activity.

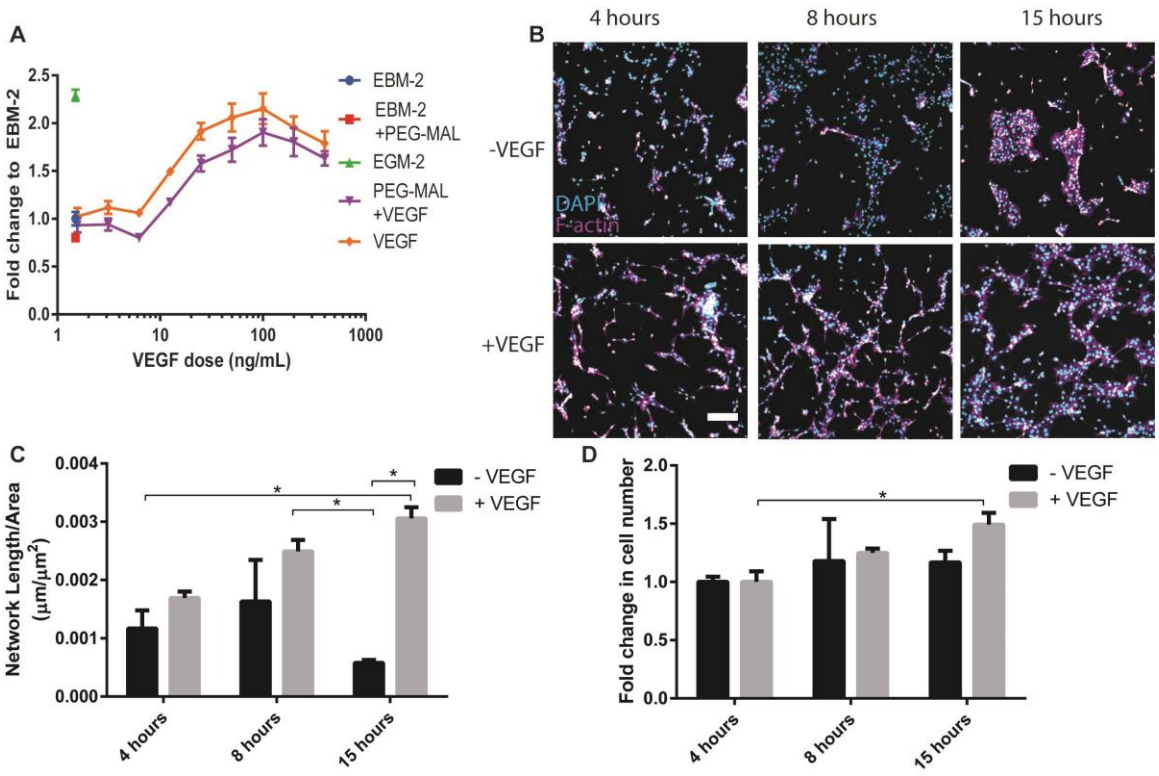

Figure 3: Bioactivity of PEGylated VEGF. (A) Endothelial cell metabolic assay for VEGF vs. PEG-MAL-VEGF (Mean ± SEM n=6). (B) Images of endothelial cell networks on top of GFOGER-functionalized hydrogels either functionalized with (VEGF) or lacking VEGF (Control) over 15 hours (Scale bar = 200μm, DAPI=cyan, F-actin=magenta). (C) Quantification of endothelial cell network length measured through custom ImageJ macro. (Mean ± S.E.M n=4) (D) Quantification of endothelial nuclei count (Mean ± S.E.M n=4) * $p<0.05$.

3.4.3 Integrin-dependent 3D endothelial cell tubulogenesis

After confirming the biological activity of PEGylated VEGF, we examined the effect of different integrin ligands in conjunction with VEGF presentation on the vasculogenic response to these materials. We used a model for 3D vascular tubulogenesis consisting of GFP-expressing HUVECs encapsulated with 10T1/2 cells, which act as a supporting pericyte-like cell, in hydrogels functionalized with either the GFOGER or RGD adhesive peptide. For both adhesive peptides, endothelial cells encapsulated within VEGF-free hydrogels and cultured in VEGF-free media exhibited minimal tubulogenesis as the cells remained largely rounded and failed to form protrusions to adjacent cells (Fig. 4A). In contrast, endothelial cells cultured in the presence of soluble VEGF in the media showed increased network formation in both RGD and GFOGER hydrogels (Fig. 4B). Importantly, VEGF-containing hydrogels cultured in VEGF-free media displayed enhanced endothelial cell-based network formation compared to hydrogels in VEGF-free conditions for both RGD- and GFOGER-functionalized hydrogels (Fig. 4B). For GFOGER-functionalized hydrogels, VEGF containing hydrogels exhibited similar levels of increased network formation compared to that of GFOGER-functionalized hydrogels cultured in VEGF-containing media. VEGF-containing RGD-functionalized hydrogels displayed elevated network formation compared to RGD hydrogels in VEGF-free conditions and RGD hydrogels cultured in media with VEGF (Fig. 4B). Taken together, the data demonstrates that hydrogels containing VEGF induce similar levels of endothelial cell tubulogenesis *in*

vitro compared to soluble VEGF present in the media. Furthermore, this increase in tubulogenesis is independent of the adhesive peptide presented in the hydrogel.

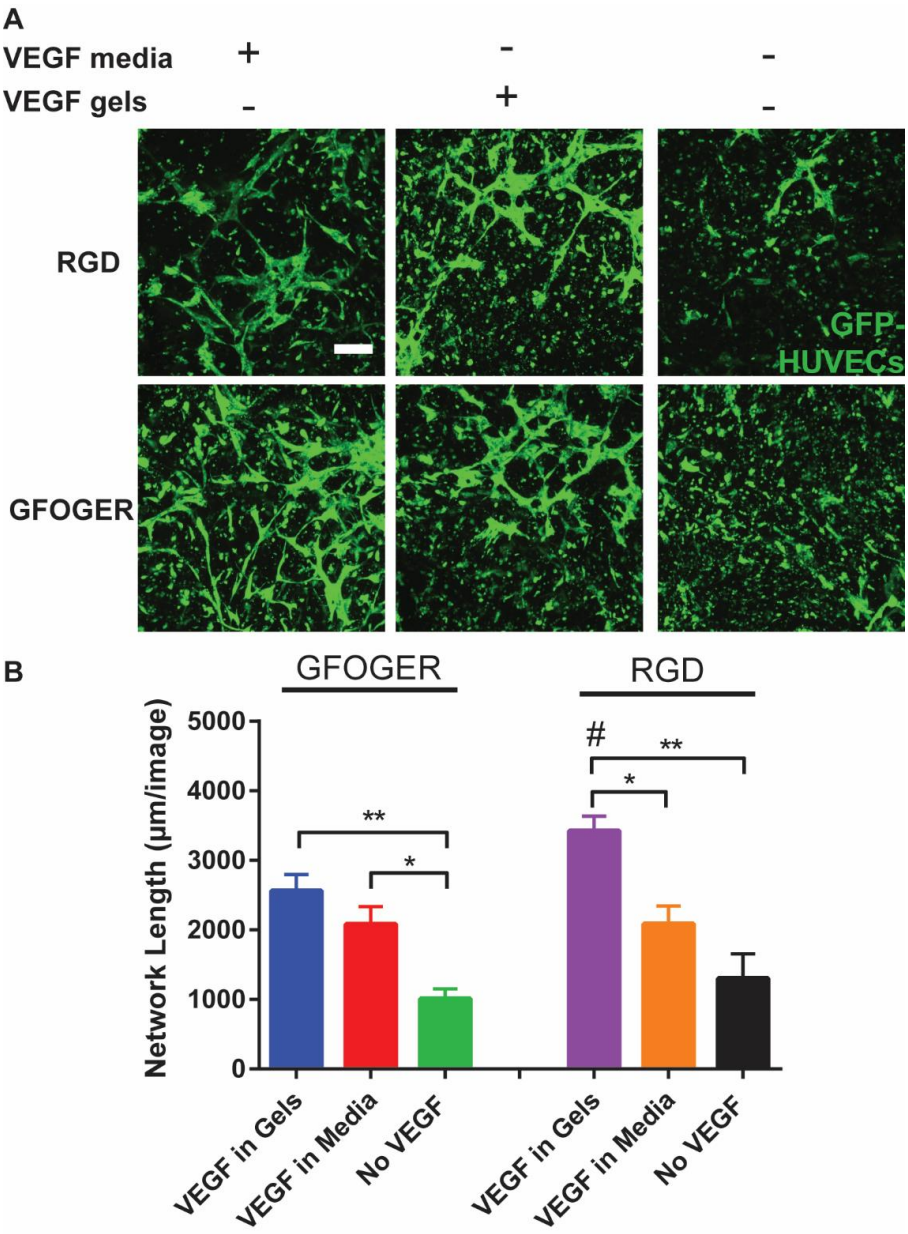

Figure 4: Integrin-specific hydrogels demonstrate VEGF-dependent increases in 3D endothelial cell network formation. (A) Projected Z-stack images of GFP-HUVECs cultured in either media containing VEGF, hydrogels containing VEGF or VEGF-free

conditions for 3 days (scale bar = 200 µm). (B) Quantification of 3D network length in varying conditions (Mean ± S.E.M N=5). *$p < 0.05$, ** $p < 0.01$.

3.4.4 VEGF-free GFOGER hydrogels enhances vascularization over VEGF-free RGD hydrogels

We evaluated the potential of VEGF-functionalized hydrogels presenting integrin-specific peptides to enhance vascularization in a murine critical-size radial bone defect model. We tested two different VEGF doses (50 and 250 ng, referred to as low and high doses, respectively) as well as hydrogels lacking VEGF (0 ng) for both RGD and GFOGER-functionalized hydrogels. Hydrogels of each condition were gelled within polyimide tube sleeves engineered with laser-machined holes to improve cell infiltration and nutrient transport across the sleeve walls. The hydrogel-containing sleeves were then implanted into 2.5 mm long unilateral murine radial defects and evaluated for vascular morphometric parameters within the bone defect area at 8 weeks via micro-computed tomographic (μCT) analysis of a perfused radiopaque polymer (Fig. 5A). Importantly, this technique measures functional vasculature connected to the host vasculature as the radiopaque polymer is perfused through the left ventricle and exits out the inferior vena cava to perfuse the vasculature. VEGF-free, RGD hydrogels exhibited very low levels of vascularization (Fig. 5A). With low and high doses of VEGF, RGD hydrogels exhibited significantly increased vessel number as well as significantly decreased vessel spacing denoting a higher density of vessels for both VEGF doses (Fig. 5C-D). Low doses of VEGF also significantly increased the total blood vessel volume and resulted in higher frequency of both small diameter (25-50 μm) and larger diameter vessels (80-100 μm) compared to VEGF-free RGD hydrogels (Fig. 5B, E).

Remarkably, VEGF-free GFOGER hydrogels displayed significantly increased vascularization across all quantified parameters (vessel volume, number and spacing) compared to VEGF-free RGD hydrogels (Fig. 5B-D). The levels of vascularization present within VEGF-free GFOGER hydrogels were equivalent to those of VEGF-containing RGD hydrogels. Furthermore, at high VEGF doses, while GFOGER and RGD hydrogels showed similar levels of vascular number and spacing, GFOGER hydrogels demonstrated elevated levels of total vascular volume compared to those of RGD hydrogels. The high levels of vascularization exhibited in GFOGER hydrogels were insensitive to delivery of both low and high doses of exogenous VEGF as shown by the equivalent levels of vessel volume, spacing, and number (Fig. 5B-D). Whereas no differences were seen in these parameters, high doses of VEGF did increase the frequency of larger diameter vessels for GFOGER hydrogels compared to VEGF-free and low VEGF dose conditions (Fig. 5F). Taken together, the μCT vascular analysis shows that for growth-factor free conditions, RGD hydrogels result in poor vascularization; however, addition of VEGF to these hydrogels increases vascularization of these bone defects. In contrast, GFOGER hydrogels show elevated levels of vascularization regardless of delivery of exogenous VEGF. The observation that VEGF-free GFOGER hydrogels show significantly increased vascularization compared to VEGF-free RGD hydrogels and similar levels of vascularization compared to low dose VEGF-delivering RGD hydrogels emphasizes the importance of integrin-specificity in these biomaterials. By simply functionalizing

scaffolds with differing integrin-specific ligands, robust increases in vascularization can be achieved.

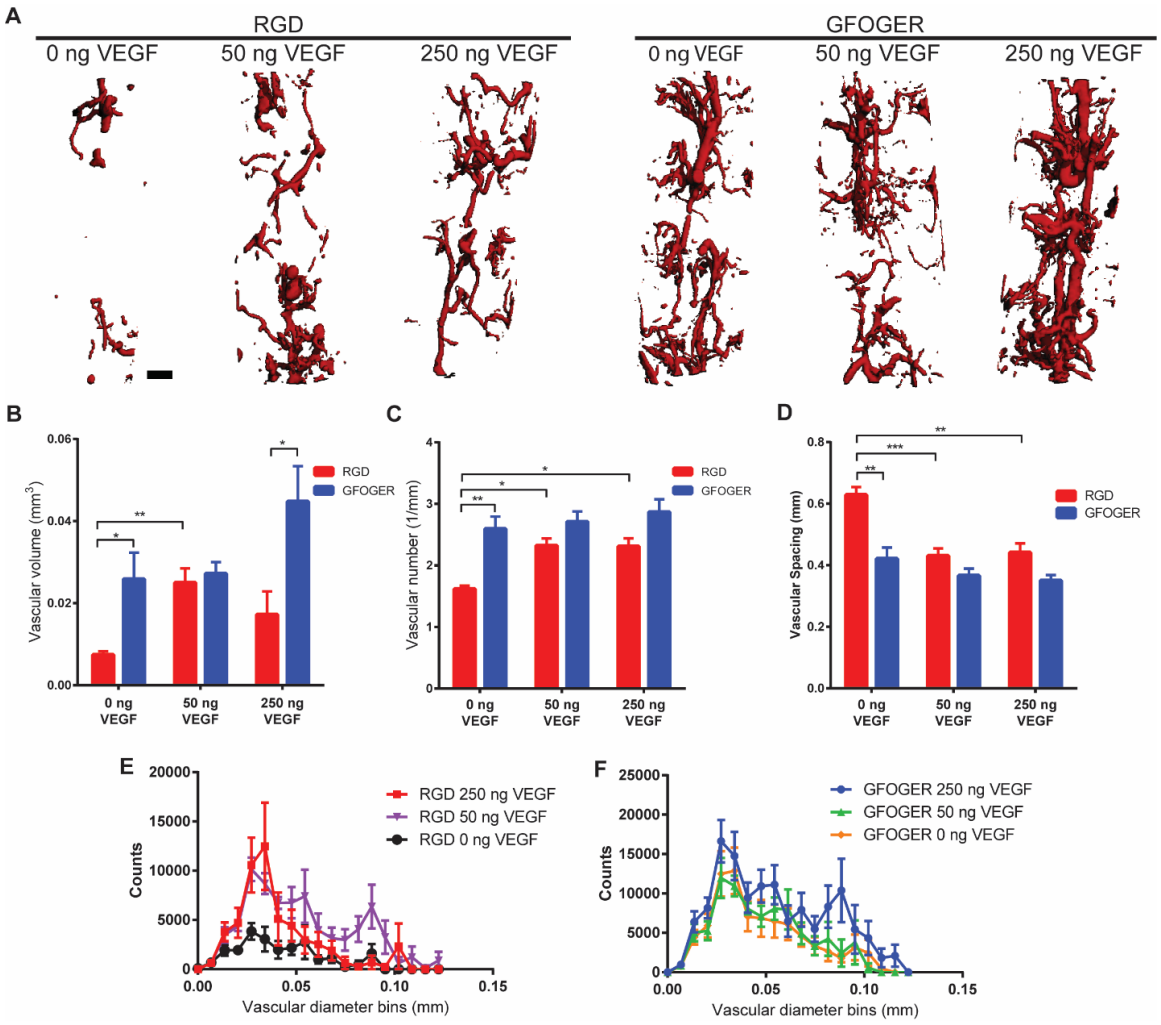

Figure 5: Vascularization of bone defects. (A) Representative 3D reconstructions of vascular structures within the bone defect for different adhesive peptides and VEGF doses (scale bar = 200 µm). (B, C, D) Vascular volume, number and spacing in bone defect respectively. (E, F) Vascular diameter histogram indicating blood vessel size distribution. (Mean ± S.E.M n=5-8) *$p < 0.05$, **$p < 0.01$, ***$p < 0.001$.

We also performed immunostaining for CD31 and endomucin, which are specific markers for endothelial cells within capillary networks [248] (Fig. 6). RGD hydrogels having low and high doses of VEGF exhibited increased levels of CD31 and endomucin staining compared to VEGF-free RGD hydrogels. The staining also showed the presence of larger diameter vessels in the low dose group compared to the high dose group and VEGF-free gels, in agreement with the μCT vascular analyses. GFOGER hydrogels displayed robust staining for CD31 and endomucin independent of the VEGF dose. The histological analysis is fully consistent with the μCT results showing VEGF dose-dependent increases in endothelial markers for RGD hydrogels and no VEGF-dependence in GFOGER hydrogels, underscoring the importance of integrin-specificity in the vascularization response to these biomaterials.

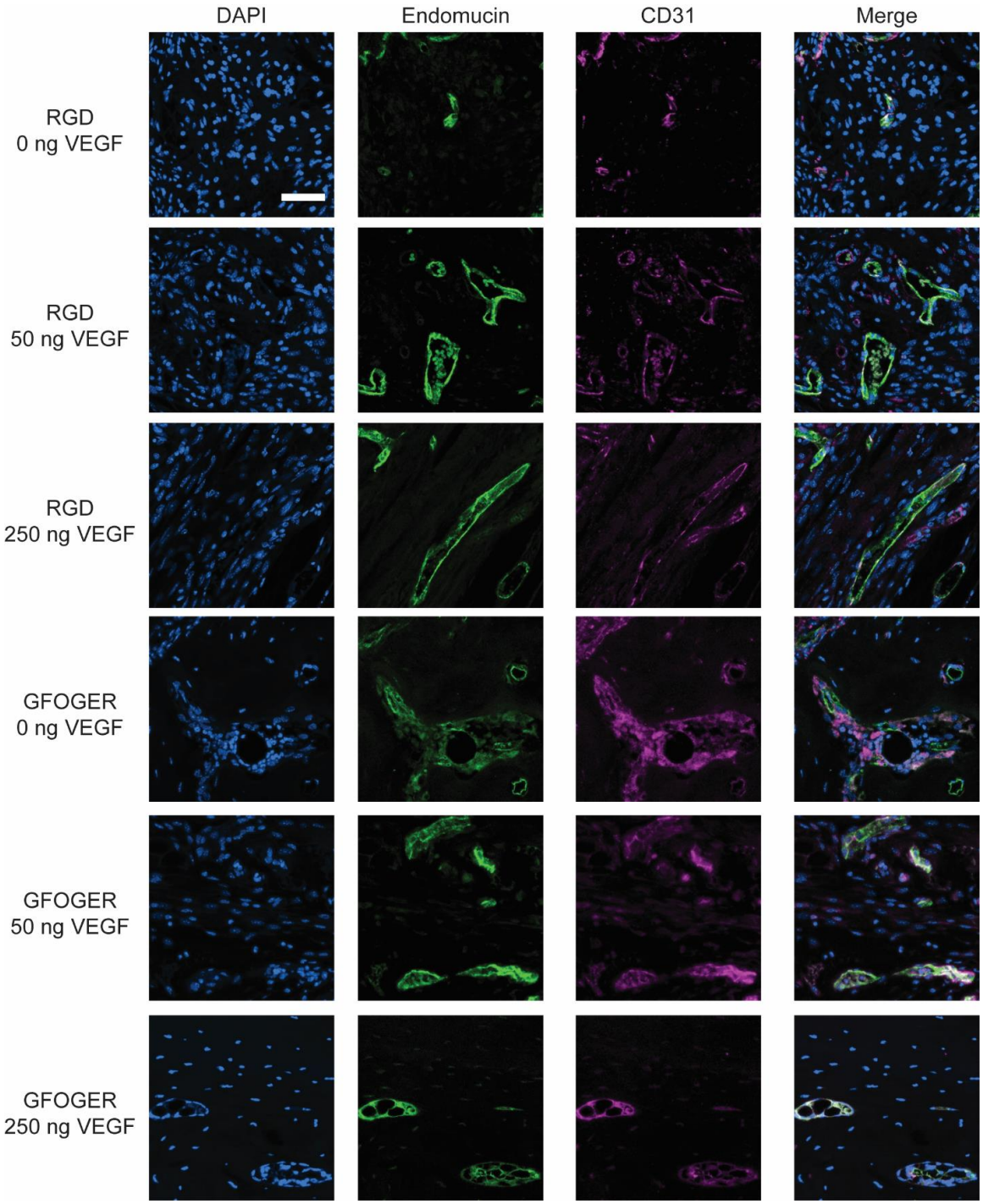
DAPI
Endomucin
CD31
Merge
RGD
0 ng VEGF
RGD
50 ng VEGF
RGD
250 ng VEGF
GFOGER
0 ng VEGF
GFOGER
50 ng VEGF
GFOGER
250 ng VEGF

Figure 6: Representative images of endomucin and CD31 staining in bone defect samples. (scale bar = 50 μm).

3.4.5 Effects of integrin-specificity on vascsulogenic protein secretion by MSCs

A major finding from the *in vivo* vascularization study is the enhancement in vascularization for defects treated with GFOGER-functionalized hydrogels compared to RGD-presenting gels. The network formation assay showed no differences in endothelial cell tubulogenesis between these two integrin-specific ligands (Fig. 4). Therefore, we investigated whether integrin binding specificity could influence the vasculogenic potential of non-endothelial cells such as mesenchymal stem cells (MSCs). During bone repair, MSCs secrete paracrine factors that increase the recruitment and proliferation of endothelial cells to form functional neovessels [249, 250]. Due to the influx of MSCs and osteoprogenitors immediately after bone injury [251], we speculated that differential integrin binding could result in differences in secreted factors by MSCs. We thus investigated the effect of integrin-specificity on the secretion of angiogenic proteins from MSCs encapsulated within GFOGER or RGD-functionalized hydrogels. Integrin-specific hydrogels containing human MSCs were cultured in osteogenic media for 7 days after which the conditioned media was analyzed through ELISA for VEGF and FGF-2 levels. Conditioned media from GFOGER hydrogels showed a significantly elevated concentration of VEGF when compared to that of RGD hydrogels (Fig. 7A). The GFOGER-dependent upregulation in angiogenic factor secretion was specific to VEGF, as secretion of FGF-2 was below the limit of detection of the assay for both GFOGER and RGD hydrogels (Fig 7B). These results demonstrate that MSCs cultured within hydrogels presenting the $\alpha_2\beta_1$-specific GFOGER secrete higher levels of VEGF compared to that of

MSCs cultured in RGD hydrogels. This finding provides an explanation for the enhancements in vascularization observed in bone defects treated with GFOGER-functionalized hydrogels compared to defects treated with RGD-presenting hydrogels.

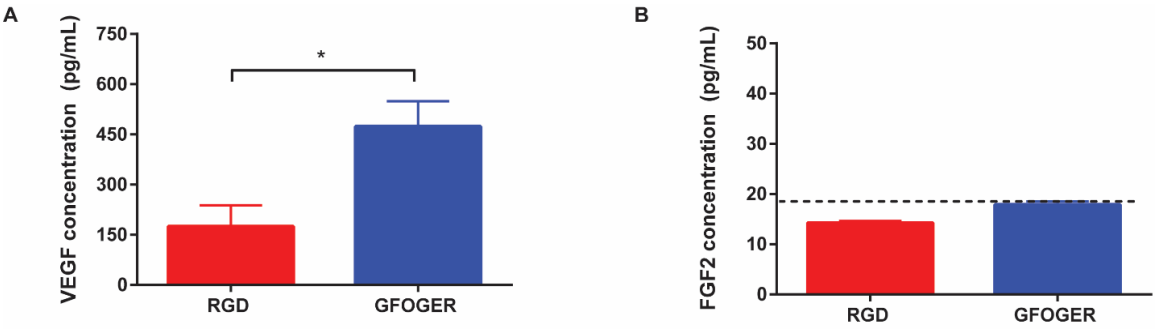

Figure 7: hMSCs encapsulated within GFOGER-functionalized hydrogels exhibit enhanced secretion of VEGF compared to hMSCs encapsulated within RGD-functionalized hydrogels. (A, B) Quantification of VEGF or FGF-2 in the supernatant of hMSCs encapsulated within integrin-specific hydrogels in osteogenic differentiation conditions (Mean ± S.E.M n=4). Dotted line indicates reliable limit of detection. *$p < 0.05$.

3.4.6 Effect of VEGF-delivering hydrogels on bone repair

We next analyzed the effects of VEGF delivery within integrin-specific hydrogels on the repair of non-healing bone defects. Hydrogel conditions and surgical procedures were consistent with the vascularization study, and bone healing was evaluated by μCT at 4 and 8 weeks post-surgery. Bone defects treated with VEGF-free GFOGER-modified hydrogels exhibited 3-4 fold higher bone volume compared to those treated with VEGF-free RGD-modified hydrogels at 4 and 8 weeks post-surgery (Fig. 8B,D). For GFOGER hydrogels, VEGF had no significant effect on bone formation at 4 and 8 weeks post-surgery, consistent with the vascularization analyses. For RGD hydrogels, low doses of VEGF significantly increased bone volume at 4 weeks, whereas high doses of VEGF showed similar levels of bone volume compared to VEGF-free RGD hydrogels. However, by 8 weeks post-surgery, there were no differences among VEGF-containing and VEGF-free RGD hydrogels (Fig. 8B, D). These results demonstrate that in VEGF-free conditions, GFOGER hydrogels exhibit significantly increased bone formation compared to RGD hydrogels. Additionally, although increases in vascularization are noted, especially within RGD hydrogels, delivery of exogenous VEGF does not enhance bone repair in this murine critical-size defect for either integrin-specific hydrogel.

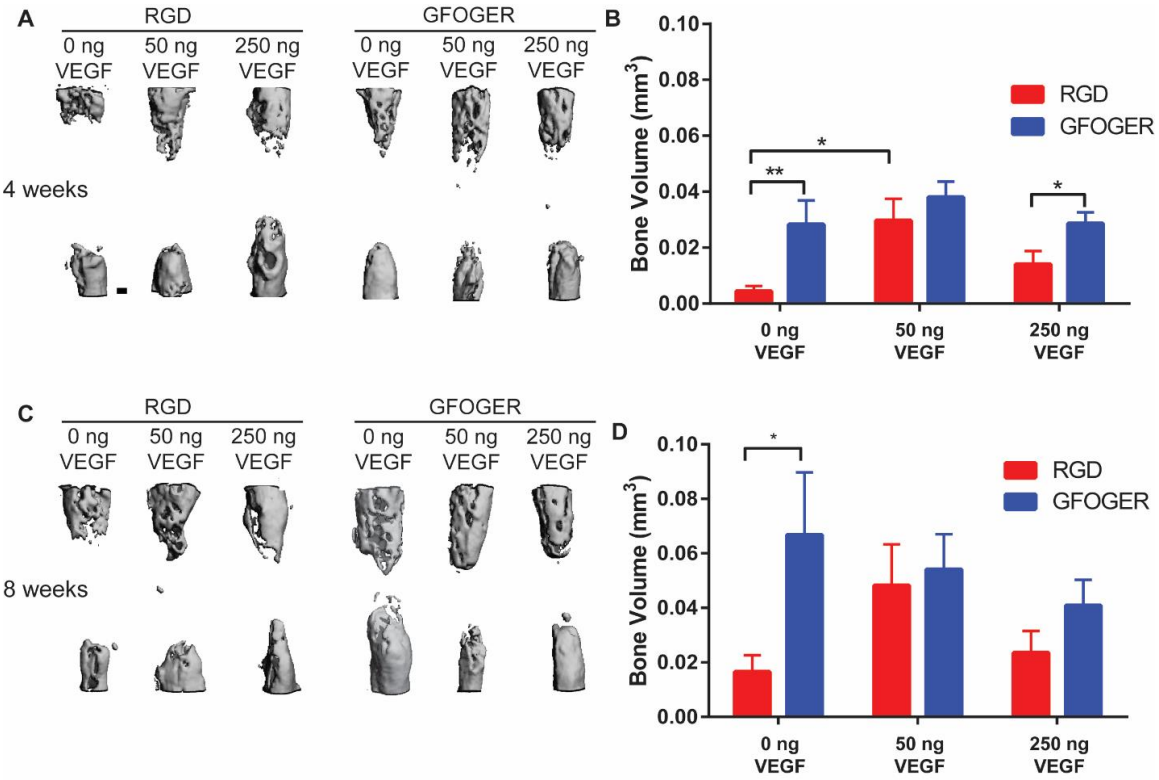

Figure 8: Bone volume for bone defects treated with VEGF-containing hydrogels. (A, C) Representative 3D reconstructions of radial defect at 4 and 8 weeks respectively with differing ligand and VEGF doses (scale bar = 200 μm). (B, D) Quantification of bone volume of defects at 4 and 8 weeks respectively. (Mean ± S.E.M n=7-9) *$p < 0.05$, ** $p < 0.01$.

3.5 Discussion

Non-healing bone defects and fractures represent a serious clinical problem with over 1 million surgical procedures necessitating bone grafts performed annually in the USA alone and costing over $5 billion [252]. While the creation of a functional vascular network is considered a crucial factor in successful regeneration of bone defects, it is still unclear whether delivery of vasculogenic factors such as VEGF enhances bone repair [117, 121, 230, 253]. Additionally, while the role that integrins play in the progression of angiogenesis in tumors has been of particular interest recently [254], the ability of integrin binding to direct vascularization in the context of biomaterial-directed tissue repair has not been investigated. In this study, we examined whether incorporation of VEGF into synthetic hydrogels functionalized with either the $\alpha_2\beta_1$ integrin-targeting GFOGER ligand or the RGD peptide that mainly binds to $\alpha_v\beta_3$ integrin modulates both the vascularization and bone regeneration of critical-size bone defects.

Controlled and sustained delivery of VEGF constitutes an important parameter in the design of the hydrogel. In the strategy described here, VEGF is covalently tethered to the hydrogel precursor thus allowing for high retention efficiency once cross-linked. The protease-sensitive nature of the cross-linked material provides for controlled release of VEGF based on cell-mediated invasion and degradation of the hydrogel. This system results in a positive feedback loop *in vivo* where VEGF initiates cell invasion which subsequently causes further release of VEGF. Another crucial parameter when designing

a growth-factor based release system is retaining the biological activity of the protein. For delivery vehicles based on the encapsulation of proteins within solid matrices such as microparticles, the bioactivity of the protein is likely reduced [255]. In the described system, VEGF remains in a hydrated state throughout gelation. Furthermore, the conjugation of the PEG macromer to free thiols within VEGF does not affect the protein's biological activity as endothelial cells exhibited heightened 3D network formation when encapsulated within VEGF-tethered hydrogels compared to those in VEGF-free conditions.

Whereas no differences were observed for *in vitro* endothelial network formation between integrin-specific hydrogels, significant differences were observed in the vascularization of bone defects *in vivo* for hydrogels presenting different adhesive peptides. For VEGF-free conditions, GFOGER-functionalized $\alpha_2\beta_1$-targeting hydrogels exhibited significantly increased vascular volume and density compared to RGD-functionalized $\alpha_v\beta_3$-targeting hydrogels. This difference may be attributed to multiple factors. Activation of the $\alpha_2\beta_1$ integrin has been reported to increase osteogenic activity resulting in increased pro-angiogenic signals as osteoblasts and osteoprogenitors secrete large quantities of VEGF to support the survival and proliferation of surrounding endothelial cells [256-258]. This observation potentially explains the findings that VEGF-free GFOGER-functionalized hydrogels produce higher bone regeneration *in vivo* compared to VEGF-free RGD-functionalized hydrogels. Additionally, while the $\alpha_v\beta_3$ integrin has often been implicated in angiogenesis, more recent studies have shown that the role of this integrin in

vascularization is context-dependent [259]. Depending on the environment, cell type, and which molecules the integrin interacts with, the $\alpha_v\beta_3$ integrin can play either a pro- or anti-angiogenic role [260-262].

For hydrogels incorporating VEGF, RGD hydrogels exhibited increases in blood vessel volume, number and density within the bone defect area compared to VEGF-free controls. This result is consistent with the well-established cross-talk between the β_3 integrin subunit and VEGFR2. Mutation of the cytoplasmic tail of the β_3 integrin results in impaired interactions with VEGFR2 which leads to inefficient phosphorylation of the dimerized VEGFR2 complex [151]. Downstream activation of FAK and JNK signaling pathways from VEGFR2 activity is also dependent on the co-activation of the $\alpha_v\beta_3$ integrin [263]. The ability for RGD hydrogels to activate the $\alpha_v\beta_3$ integrin could thus cause heightened sensitivity to the presence of VEGF within the defect microenvironment. In contrast, the level of vascularization for GFOGER-functionalized hydrogels was independent of VEGF dose, with VEGF-free as well as low and high doses of VEGF exhibiting high levels of vascularization. Notably, when MSCs were encapsulated within GFOGER hydrogels *in vitro*, the cells exhibited increased secretion of VEGF compared to those encapsulated within RGD hydrogels. This finding provides an explanation as to why *in vivo* vascularization in GFOGER hydrogels was elevated and insensitive to exogenous VEGF as the interaction between the hydrogel and invading MSCs may provide abundant levels of endogenous VEGF. Overall, the finding that VEGF-free, GFOGER hydrogels show elevated levels of *in vivo* vascularization compared to VEGF-free, RGD hydrogels and

similar levels of vascularization compared to VEGF-containing RGD hydrogels is noteworthy. The ability for integrin-specificity alone to instruct and guide levels of vasculogenesis and regulate biological activity of vasculogenic proteins highlights the importance of exploiting integrin-specificity in regenerative medicine applications. With the expensive and often significant regulatory issues associated with growth factor therapies, the ability to engineer scaffolds to reduce or completely eliminate the need for growth factors through simple functionalization techniques can greatly enhance the clinical efficacy of future regenerative medicine constructs.

In addition to differences in vascularization for the integrin-specific hydrogels, integrin specificity also played a role in the regeneration of bone within the critical-size defects. VEGF-free, GFOGER-functionalized hydrogels exhibited higher bone repair at both 4 and 8 weeks in comparison to VEGF-free RGD-presenting hydrogels. Addition of VEGF however had no effect on bone formation at 8 weeks indicating that exogenously delivered VEGF is not sufficient to repair critical-size bone defects in this model. This conclusion does not rule out an important role for VEGF in bone repair. On the contrary, endogenous VEGF is necessary for bone repair as treatment with VEGF blocking antibodies inhibits the healing of bone defects [117]. Furthermore, mice lacking the $VEGF_{165}$ and $VEGF_{188}$ isoforms show abnormal vascular patterning along with significant decreases in trabecular bone volume and bone growth [264]. However, in terms of delivering exogenous VEGF to regenerate bone defects, studies demonstrate conflicting results with some reports showing enhanced bone formation while others showing no effect

after delivery of VEGF [120, 121, 230, 231, 265, 266]. The inconsistencies between these reports could be related to the *in vivo* model, scaffold, or delivery kinetics. Exploration into strategies utilizing VEGF in conjunction with other stimuli such as other growth factors (e.g., BMP-2), further scaffold engineering, cell therapy or gene therapy could enhance its effects.

3.6 Conclusion

While endogenous VEGF is known to be essential to osteogenesis, the ability of exogenously delivered VEGF to significantly repair bone defects remains ambiguous. In this study, we investigated whether integrin-specific biomaterials could constitute a crucial, yet, up to now, unexplored role in vascularization and osteogenesis in bone defects. VEGF-free GFOGER-presenting hydrogels exhibited significantly increased vascularization and bone formation in a non-healing segmental bone defect compared to RGD-functionalized hydrogels. Furthermore, RGD-presenting hydrogels exhibited exogenous VEGF dose dependent increases in vascularization. Nevertheless, addition of VEGF to these hydrogels did not enhance bone repair in this bone defect model. This study demonstrates interplay between biomaterial integrin specificity and VEGF in tissue vascularization.

CHAPTER 4. AIM 2: IFN-γ FUNCTIONALIZED HYDROGELS FOR ENHANCED MSC-BASED IMMUNOMODULATION

4.1 Abstract

Human mesenchymal stem cells have recently garnered attention for their ability to treat a variety of chronic inflammatory diseases such as inflammatory bowel disorders due in part to their immunomodulatory properties. Treating hMSCs with IFN-γ prior to administration has been shown to augment these immunomodulatory properties. However, the *ex vivo* manipulation of these cells severely limits their clinical potential due to the prolonged handling and associated heightened cost and regulatory hurdles. In this study, we engineered a hydrogel with covalently tethered IFN-γ that can interact with encapsulated hMSCs to increase their immunomodulatory properties and thus avoid the need for *ex vivo* manipulation. Following verification of successful tethering of IFN-γ onto our scaffold, we found that hMSCs encapsulated within tethered IFN-γ hydrogels had significantly increased expression of indoleamine 2,3-dioxygenase (IDO) and programmed death ligand-1 (PD-L1) as well as increased expression of a variety of cytokines. Moreover, hMSCs within these IFN-γ bound hydrogels exhibited a potent ability to halt activated T-cell proliferation and monocyte-derived dendritic cell differentiation compared to hMSCs that were pre-treated with IFN-γ and control hMSCs. Importantly, hMSCs encapsulated in tethered IFN-γ hydrogels significantly accelerated healing of mechanically-induced

colonic wounds in mice. Altogether, this novel methodology of licensing hMSCs with IFN-γ can significantly increase both the efficacy and translatability of these cells into the clinic.

4.2 Introduction

Human mesenchymal stem cells (hMSCs) are a type of multipotent stromal cell that, in addition to having an ability to differentiate into a variety of cell types including bone, cartilage and fat, exhibit potent immunomodulatory capabilities [152, 267-269]. *In vitro*, co-culturing MSCs with activated T-cells or monocytes leads to reduced proliferation of T-cells and an inhibition of monocyte-derived dendritic cell differentiation, respectively [164, 186]. HMSCs have also been shown to have potent inhibitory effects on other immune cell types ranging from natural killer cells to B cells [168, 270]. The effects seen *in vitro* also extend to *in vivo* applications as hMSCs have been shown to have significant effects on ameliorating a range of autoimmune diseases in pre-clinical models of graft vs host disease (GvHD), experimental colitis and experimental autoimmune encephalomyelitis [8, 271-273]. With the observed success in pre-clinical models, hMSCs have been utilized in clinical trials for treating Crohn's disease as well as steroid-refractory acute GvHD but with varying levels of success. In a phase II clinical study of refractory Crohn's disease, although the overall disease score was significantly reduced with administration of hMSCs for group as a whole, the patient improvement was only noted in 7 of 15 patients [214]. For GvHD, Le Blanc and colleagues found that out of 55 patients having severe aGvHD that received an infusion of MSCs, 30 had a complete response while

the other 25 had either a partial or no response to MSC therapy [207]. Overall, these studies as well as others point to the notion that while hMSC therapy aids in the amelioration of autoimmune diseases, but the effect is only seen in approximately half of patients, thus leaving vast room for improvement [208, 215].

In order to enhance the efficacy of stem cell-therapy, it is necessary to understand the underlying mechanisms of hMSC-based immunomodulation. While the exact molecular mechanisms of how hMSCs generate such a potent response are still being elucidated, evidence points to the necessity for hMSCs to be activated with a pro-inflammatory stimulus, notably interferon-gamma (IFN-γ), in order to elicit their immunomodulatory activities, a term known as 'licensing' [172, 274]. This has been confirmed by the observation that by either co-culturing hMSCs with IFN-γ deficient immune cells or using antibodies to neutralize IFN-γ, hMSCs lose the ability modulate immune cell phenotype [216, 275]. Once licensed with IFN-γ, hMSCs elicit their immunomodulatory effects by the IFN-γ-induced upregulation of various immunomodulatory factors including indoleamine 2,3-dixygenase (IDO), programmed death ligand-1 (PD-L1), prostaglandin E2 (PGE2), CCL8, CXCL9 and CXCL10 among many others [276, 277].

Importantly, the timing and duration of licensing are crucial and it has been shown that licensing hMSCs prior to co-culture or use *in vivo* enhances their immunomodulatory capabilities [278]. Whereas activated T-cells secrete IFN-γ, licensing hMSCs with IFN-γ

prior to co-culture with activated T-cells results in both inhibited T-cell proliferation and T-cell effector functions, while hMSCs that were not licensed prior to co-culture only inhibited T-cell proliferation [174]. Furthermore, licensing hMSCs prior to infusion into mice with GvHD results in enhanced hMSC-based suppression of the GvHD compared to that of un-licensed hMSCs [216]. Duijvestein and colleagues also showed that delivering pre-licensed hMSCs significantly reduced the severity of experimental colitis in a murine model compared to un-licensed hMSCs [279]. From a translatability standpoint however, pre-licensing hMSCs raises serious concerns due to the significant cost and logistics necessary for such processing. *Ex vivo* manipulation, for example, runs into countless issues such as creating an efficient manufacturing process which complies with GMP standards and regulation [280, 281]. Furthermore, the increased cost necessary with manual or even automated processing presents a key burden that has contributed to the bankruptcy of many companies offering cell therapy [282]. Generating a solution that bypasses the need for such processing would potentially enhance the translatability and efficacy of stem-cell therapy.

Engineered biomaterials offer the potential for a solution to the need of *ex vivo* manipulation through scaffolds that can provide necessary cues to encapsulated cells. Through either covalent tethering or non-covalent affinity interactions, various groups have engineered scaffolds that bind proteins and other factors for either influencing encapsulated cells or interacting with the local microenvironment once implanted *in vivo* [65, 283-285]. We have previously shown that covalently tethering vascular endothelial

growth factor onto a poly(ethylene) glycol-based hydrogel significantly increases encapsulated endothelial cell tubulogenesis as well as induces increased vascularization *in vivo* compared to non-functionalized hydrogels [127, 131, 222]. There has been very little research done, however, in engineering a scaffold to license encapsulated hMSCs and enhance their immunomodulatory capabilities. Thus, the objective of this study was to engineer a scaffold exhibiting a covalently-bound form of IFN-γ for providing a persistent licensing cue for activation of hMSCs. We hypothesize that hMSCs encapsulated within this scaffold will elicit enhanced immunomodulation on immune cells *in vitro* as well as enhance the regeneration of colonic wounds in a mouse model. This data will provide much needed insight on whether biomaterials in conjunction with protein cues can act as an effective licensing agent and suitable for use in pre-clinical inflammatory models.

4.3 Materials and Methods:

4.3.1 Cell culture

All human cell isolation and culture procedures were performed following IRB-approved protocols. Human mesenchymal stem cells were acquired from the NIH Resource Center at Texas A&M University and grown in MEM-α containing 16% fetal bovine serum (FBS), 2 mM L-glutamine and 100 U/mL penicillin/streptomycin (ThermoFisher, MA). Human CD4+ T-cells were purified from frozen leukapheresis samples from Emory University through negative selection with a CD4 T-cell isolation kit according to the manufacturer's instructions (Biolegend, CA). Human monocytes were purified from

peripheral blood mononuclear cells (PBMCs). Briefly, peripheral blood was diluted 1:1 with PBS containing 2% FBS after which the peripheral blood mononuclear cells (PBMCs) was separated via density gradient centrifugation (specific gravity: 1.077 g/mL, Stemcell Technologies, Canada). The isolated PBMCs were washed and subjected to monocyte purification using the EasySep human monocyte isolation kit (Stemcell Technologies, Canada) according to the manufacturer's instructions. All cell culture was conducted at 37 ºC in a 5% CO_2 atmosphere.

4.3.2 PEG hydrogel synthesis and IFN-γ functionalization

Four-arm maleimide-end functionalized PEG macromer (PEG-4MAL 20kDa MW, Laysan Bio, AL, >95% purity, >95% end-functionalization) was functionalized with IFN-γ engineered to express a surface-exposed cysteine at amino acid position 103 (Boulder Biotechnology, CO) [286] for one hour at room temperature in phosphate buffered saline at pH=7.4. The macromer was further functionalized RGD peptide (GRGDSPC) (Genscript, NJ). The functionalized macromers were cross-linked using a mixture of the bi-cysteine peptide VPM (GCRDVPMSMRGGDRCG) (Genscript, NJ) and dithiothreitol (Sigma-Aldrich, MO). The PEG-4MAL hydrogels were synthesized to obtain a final concentration of 1.0 mM RGD peptide and a concentration of 25 μg/mL IFN-γ unless otherwise noted. The concentration of cross-linker used for the synthesis of each hydrogel was calculated by matching the number of cysteines in the cross-linking solution to the number of residual maleimides following complete macromer functionalization. In certain

experiments, the cysteine-variant IFN-γ was substituted for the non-cysteine-containing human recombinant IFN-γ (Biolegend, CA). Cysteine-expressing IFN-γ functionalized into the PEG-4MAL hydrogel is termed 'cys-IFN-γ hydrogels' whereas non-cysteine-expressing IFN-γ mixed into the PEG-4MAL hydrogel precursor is termed 'IFN-γ hydrogels'. In experiments where cells were encapsulated in hydrogels, a pre-determined number of cells were mixed with the functionalized macromer followed by cross-linking. Hydrogels were allowed to gel at 37 ºC for 10 minutes before swelling in either PBS or complete cell culture media if cells were encapsulated in the hydrogel. Functionalization of the cysteine-expressing IFN-γ onto PEG-4MAL was determined through protein gel electrophoresis on an SDS-PAGE gel followed by protein visualization with Sypro Ruby according to manufacturer's instructions (ThermoFisher, MA)

4.3.3 IFN-γ release kinetics

To assess IFN-γ release kinetics from hydrogels, hydrogels were synthesized with either cys-IFN-γ or IFN-γ. Hydrogels were incubated in PBS for 4 days with supernatant collected at specified time points, snap-frozen and stored at -80ºC. At day 4, the PBS from all wells was removed and replaced with fresh PBS with a subset of wells having hydrogels having cys-IFN-γ, receiving PBS with 50 μg/mL collagenase (Worthington Biochemical, NJ). Supernatants were collected at specified time points for an additional 3 days, snap-frozen and stored at -80ºC. At the end of the experiment, samples were thawed and the concentration of IFN-γ assessed via ELISA (Biolegend, CA).

4.3.4 Bioactivity of cys-IFN-γ

HMSCs were plated onto 24-well tissue culture plastic plates at a density of 10,000 cells/cm^2. Four hours after seeding, various forms of IFN-γ were added to the cultures at a concentration of 50 ng/mL. After four days in culture, the conditioned media was collected and frozen at -80ºC. HMSCs were trypsinized, fixed, permeabilized and subjected to flow cytometric analysis on a BD Accuri C6 flow cytometer for expression of IDO and PD-L1. Conditioned media was analyzed for secreted proteins using a custom Luminex kit (R&D Systems, MN).

4.3.5 Cys-IFN-γ in hydrogel-encapsulated hMSC culture

HMSCs were encapsulated in hydrogels containing cys-IFN-γ, IFN-γ or no IFN-γ as described above at a concentration of 5 x 10^6 cells/mL. After four days in culture, conditioned media was collected and frozen at -80ºC. Hydrogels were then degraded by incubation in 1 mg/mL collagenase in PBS for 30 minutes at 37 ºC. Cells were collected and subjected to flow cytometric analysis for expression of IDO and PD-L1. Conditioned media was analyzed for various proteins using a custom Luminex kit (R&D Systems, MN).

4.3.6 IDO activity / kynurenine assay

Tryptophan is converted to kynurenine through IDO activity [287]. Kynurenine was quantified using a protocol previously described [288]. Briefly, 150 µL of conditioned media after four days of culture in specified conditions was collected and mixed with 50

µL of 30% trichloroacetic acid. This solution was then heated to 50 ºC for 10 minutes. Solutions were then vortexed and centrifuged at 10,000g for 5 minutes. 75 µL of supernatant samples were mixed with 75 µL of Ehrlich's reagent and incubated for 10 minutes. Absorbance was then read at 492 nm.

4.3.7 T-cell proliferation assay

HMSCs (1 x 10^6 cells/mL) were encapsulated in hydrogels (20 µL) with cys-IFN-γ, IFN-γ, or no IFN-γ. For the pre-licensed group, hMSCs on tissue culture plastic were stimulated with IFN-γ for 48 hours prior to encapsulation in no IFN-γ hydrogels. To simulate *in vivo* applications in which a sink environment is present, cys-IFN-γ and IFN-γ hydrogels were washed two times over the course the first 24 hours following hydrogel synthesis. Following 48 hours of hMSC-hydrogel culture, CD4+ T-cells purified from PBMCs were resuspended in RPMI 1640 supplemented with 10% FBS, 2 mM L-glutamine, 10 mM cell-culture grade HEPES and 100 U/mL penicillin/streptomycin. CD4+ T-cells (100,000) were added to each well in a 96 well plate and stimulated with 2 µL of Dynabeads (ThermoFisher, MA). HMSC-encapsulated hydrogels were then transferred to the wells containing the CD4+ T-cells and co-cultured for an additional 4 days. Eight hours prior to the end of culture, EdU was added to the media. At the end of 4 days, hydrogels were removed from the co-culture, T-cells were collected, fixed and permeabilized. T-cells were stained for DAPI and EdU that was incorporated into the T-cells upon proliferation was stained by using a Click-iT EdU kit (ThermoFisher, MA) according to manufacturer's

instructions. Stained T-cells were imaged using a Nikon C2 confocal microscope and the proliferation of T-cells as quantified by taking the ratio of EdU+/total cells was performed using a custom ImageJ macro. In certain experiments, 1-methyl-L-tryptophan (1-MT) (Sigma-Aldrich, MO) was used to inhibit IDO activity. In these experiments, 1-MT was added to the media at the start of co-culture at a concentration of 1.0 mM 1-MT. The T-cells were subjected to the same EdU staining protocol as described above.

4.3.8 Monocyte-derived dendritic cell differentiation assay

HMSCs were encapsulated in cys-IFN-γ, IFN-γ or no IFN-γ hydrogels (20 μL) at a concentration of 2.5 x 10^6 cells/mL. For the pre-licensed group, hMSCs on TCP were stimulated with IFN-γ for 48 hours prior to encapsulation in no IFN-γ hydrogels. To simulate *in vivo* applications in which a sink environment is present, cys-IFN-γ and IFN-γ hydrogels were washed two times over the course the first 24 hours following hydrogel synthesis. Hydrogels were cultured in this manner for 48 hours. Following 48 hours of hMSC-encapsulated hydrogel culture, purified human monocytes were isolated from peripheral blood and monocytes (500,000) were added into wells of a 24-well plate. Monocytes were cultured in RPMI 1640 supplemented with 10% FBS, 2 mM L-glutamine, 100 U/mL penicillin/streptomycin, 50 ng/mL GM-CSF (Biolegend, CA) and 20 ng/mL IL-4 (Biolgend, CA). HMSC-encapsulated hydrogels were then transferred to the wells containing monocytes and co-cultured for 5 days with media changes every 2-3 days. At day 5, 100 ng/mL lipopolysaccharide (LPS) (Sigma-Aldrich, MO) was added to each well

to induce maturation of dendritic cells. Cells were cultured for an additional 48 hours after which the monocytes were gathered and subjected to flow cytometric analysis for CD1a, CD14, CD80 and CD86 on a BD Accuri C6 flow cytometer. In certain experiments, 1-methyl-L-tryptophan (1-MT) (Sigma-Aldrich, MO) was utilized to inhibit IDO activity. In these experiments, 1-MT was added to the media at the start of co-culture at a concentration of 1.0 mM 1-MT. The differentiated monocytes were subjected to the same flow cytometric analysis as described above.

4.3.9 Subcutaneous hydrogel injections

All animal experiments were performed with the approval of the Georgia Tech Animal Care and Use Committee within the guidelines of the Guide for the Care and Use of Laboratory Animals. NOD SCID gamma (NSG) male mice (8-10 weeks old, Jackson Laboratories) were anesthetized under isoflurane and fur removed from the dorsal back. The skin was swabbed with chlorohexidine and alcohol. The entire dorsal back was divided into four separate quadrants. 50 µL hydrogel solutions or hMSCs in saline were injected via a 31g syringe needle into each of the four quadrants. Mice were monitored post-injection for lethargy, weight loss, normal eating habits and signs of distress. After 3 days post-injection, mice were euthanized via CO_2 inhalation. Hydrogels and the tissue surrounding the injection site were explanted via a 10 mm radius biopsy punch and immediately frozen at -80ºC. To analyze cytokines, samples were mixed with tissue extraction buffer (100 mM Tris, 150 mM NaCl, 1mM EDTA, 0.05% Triton X-100, 0.5%

sodium deoxycholate) and protease inhibitors (ThermoFisher, MA). Total protein content and cytokine analysis was performed via a BCA assay and Luminex assay respectively according to manufacturer's instructions.

4.3.10 Colonic wound surgery and injections

All animal experiments were performed with the approval of the University of Michigan Animal Care and Use Committee within the guidelines of the Guide for the Care and Use of Laboratory Animals and in accordance with the US Department of Agriculture (USDA) Animal and Plant Health Inspection Service (APHIS) regulations and the National Institutes of Health (NIH) Office of Laboratory Animal Welfare (OLAW) regulations governing the use of vertebrate animals. Colonic wounds were induced in a method similar to previously published protocols [289]. Briefly, male (8 weeks old) NOD-SCID IL2Rg-null (NSG) mice (Jackson Laboratory) were anaesthetized by intraperitoneal injection of a ketamine (100 mg/kg)/xylazine (10mg/kg) solution. A high-resolution miniaturized colonoscope system equipped with biopsy forceps (Coloview Veterinary Endoscope, Karl Stortz) was used to biopsy-injure the colonic mucosa at 5 sites along the dorsal artery. Wound size averaged approximately 1 mm^2. 50 µL hydrogel injections were performed 1 day following wounding with the aid of a custom-made device comprising a 29-gauge needle connected to a small tube. Endoscopic procedures were viewed with high-resolution (1,024 x 768 pixels) live video on a flat-panel color monitor. Each wound region was digitally photographed at day 1 and day 5 and resulting wound images for which the wound

area was calculated by a blinded observer using ImageJ. Results for one mouse were averaged through quantification of the five colonic wounds/injections per mouse.

4.3.11 Statistics

Unless otherwise noted, error bars on graphs represent SEM. Comparisons among multiple groups was performed by one-way analysis of variance (ANOVA) with post-hoc Tukey tests if data did not have significant differences in standard deviation. Data with significant differences in standard deviation were subject to log transformation after which post-hoc Tukey test performed. All statistics were performed in Graphpad Prism version 6. A p value of <0.05 was considered significant.

4.4 Results

4.4.1 IFN-γ functionalization onto PEG-MAL and release kinetics

We engineered hydrogels based on a maleimide-functionalized 4-arm PEG (PEG-4MAL) macromer which allows for facile covalent tethering of proteins exhibiting a surface-accessible cysteine. Further reaction of the PEG-4MAL with a protease-degradable bicysteine peptide results in an insoluble and cross-linked PEG-based hydrogel sensitive to protease degradation (Fig. 9A). Native human IFN-γ has no cysteine present in its amino

acid sequence and thus no ability to conjugate onto a PEG-MAL macromer through a maleimide-cysteine reaction without addition of other linking reagents. To circumvent this, we utilized an IFN-γ variant that is genetically engineered to express a surface-available cysteine residue at amino acid position 103 [286]. To verify that this variant could be functionalized onto a PEG macromer, protein gel electrophoresis was performed (Fig. 9B). The cysteine-expressing IFN-γ (cys-IFN-γ) that was not functionalized with PEG-MAL and instead mixed with PBS exhibited a distinct single band at approximately 17 kDa as expected. When the IFN-γ was reacted with PEG-MAL macromer (20 kDa), no band is seen at the 17 kDa and instead the band is shifted to greater than 30 kDa indicating successful conjugation. To further verify the tethered nature of this cys-IFN-γ, we also performed a release assay in which either cys-IFN-γ or IFN-γ was incorporated into hydrogels (Fig. 9C). Native IFN-γ does not have a cysteine and thus cannot be covalently conjugated to PEG-4MAL and therefore not tethered into the hydrogel. Upon synthesis, hydrogels were placed in PBS and samples removed at specified time-points for analysis by ELISA. Non-tethered IFN-γ exhibited a significant ~62% burst release after only 2 hours followed by complete release by 18 hours. In contrast, cys-IFN-γ that was functionalized onto the PEG-MAL prior to gelation released ~10% of total incorporated IFN-γ after 2 hours and after 4 days, still retained approximately 65% of total incorporated protein. To show that this retention is dependent on hydrogel degradation as the IFN-γ is tethered to the polymeric backbone, at 4 days, a subset of cys-IFN-γ hydrogels were incubated in 50 μg/mL of collagenase in PBS. The addition of collagenase caused

degradation of the hydrogel through the degradable cross-linkers over the course of the following three days and resulted in complete cys-IFN-γ release. Together, the protein gel electrophoresis and release results verify that the cys-IFN-γ can be chemically conjugated onto the PEG-MAL macromer and subsequently tethered into a formed hydrogel.

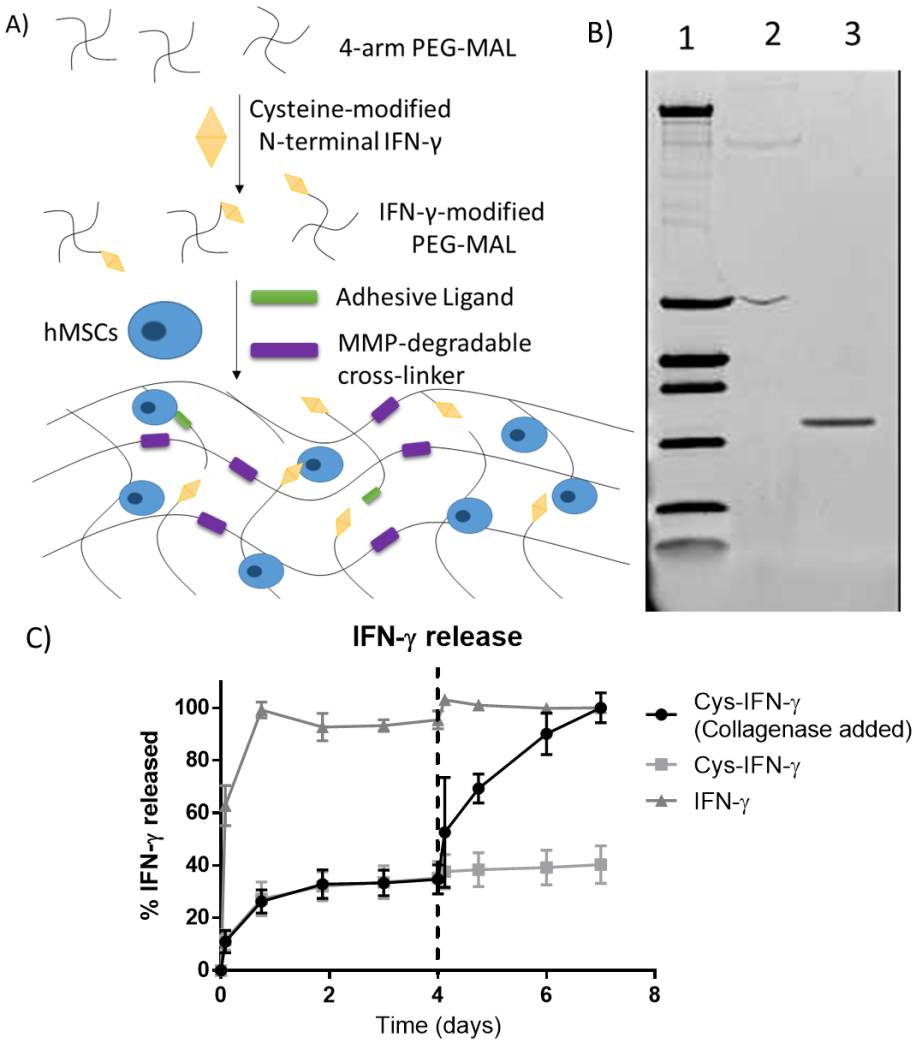

Figure 9: Tethering of IFN-γ onto PEG-4MAL hydrogels and degradation-dependent release. (A) Schematic representing cytokine functionalization with adhesive ligand, hMSC and protease-degradable cross-linker incorporation. (B) Protein gel electrophoresis with functionalized IFN-γ onto PEG-4MAL. Lane 1) protein ladder, lane 2) Cys-IFN-γ with PEG-4MAL, lane 3) Cys-IFN-γ with PBS. (C) Cys-IFN-γ release kinetics as measured

by ELISA. All groups were incubated in PBS until 4 days at which point collagenase (50 μg/mL) was added to the respective group. N=5. Error bars ± SEM.

4.4.2 Biological activity of PEGylated IFN-γ

To assess whether biological activity is affected by the chemical conjugation of the cys-IFN-γ onto PEG-4MAL, hMSCs were plated on tissue-culture plastic wells and incubated in cell culture supplemented with either cys-IFN-γ + PEG-4MAL, the cys-IFN-γ without PEG-4MAL, native IFN-γ, PEG-4MAL without IFN-γ or no additives. HMSCs exposed to native IFN-γ exhibit upregulated IDO and PD-L1 activity as well as secrete differing levels of cytokines [174, 175, 290]. To determine whether the biological activity of both the cys-IFN-γ as well as its PEG-4MAL conjugated state, we performed flow cytometric analysis for IDO and PD-L1 activity as well as assessed certain cytokine concentrations through a custom Luminex kit. hMSCs incubated with cys-IFN-γ + PEG-4MAL, cys-IFN-γ without PEG-MAL, or native IFN-γ all showed significantly increased levels of IDO and PD-L1 activity as assessed by median fluorescence intensity (MFI) compared to hMSCs incubated with PEG-4MAL or with cell culture media alone (Fig. 10A,B). Importantly, there were no significant differences in the MFI of IDO or PD-L1 among hMSCs exposed to either the cys-IFN-γ + PEG-4MAL, the cys-IFN-γ or native IFN-γ, indicating that the cys-IFN-γ has similar biological activity to the native protein and that further conjugation also does not hinder its activity. Furthermore, upon analysis of the conditioned media, concentrations of multiple secreted cytokines were noted to be

significantly different among the tested groups. Specifically, concentrations of IL-6, CXCL10, CCL2, CCL8, and M-CSF were all significantly increased while VEGF was significantly decreased in all forms of IFN-γ treated conditions compared to groups not treated with IFN-γ (Fig. 10C-H). No significant differences were noted between cys-IFN-γ + PEG-4MAL, cys-IFN-γ or native IFN-γ for IL-6. cys-IFN-γ + PEG-4MAL did show significant decreases in CXCL10, CCL2, VEGF, CCL8 and M-CSF compared to cys-IFN-γ without PEG-4MAL and native IFN-γ, but these levels were higher than levels for inactive controls.

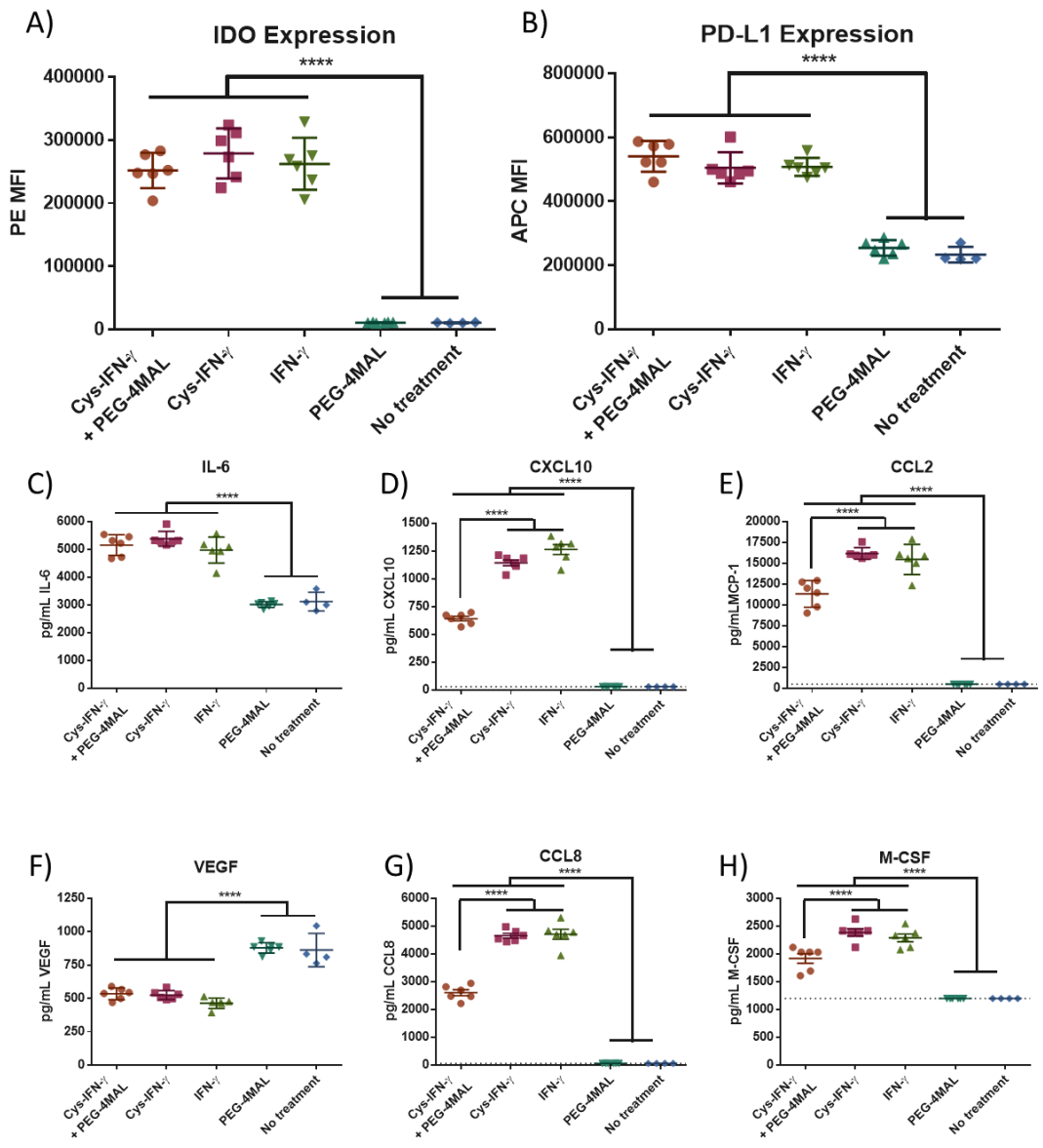

Figure 10: hMSCs on tissue culture plastic exhibit significant changes in marker expression and secretome when incubated with IFN-γ in all forms compared to hMSCs without IFN-γ. HMSCs were incubated with either cys-IFN-γ + PEG-4MAL, cys-IFN-γ, native IFN-γ,

PEG-4MAL or with no treatment. Following 4 days, hMSCs were stained for (A) IDO and (B) PD-L1 and subjected to flow cytometry. Conditioned media was analyzed for concentrations of various proteins including (C) IL-6, (D) CXCL10, (E) CCL2, (F) VEGF, (G) CCL8 and (H) M-CSF. Dotted lines signify limit of detection for specific protein. N=6. Error bars ± SEM. One-way ANOVA **** $p < 0.0001$.

4.4.3 HMSC phenotype in hydrogels with tethered IFN-γ

Following verification of the biological activity of PEG-4MAL-conjugated IFN-γ on hMSCs seeded on tissue-culture plastic, we examined whether cys-IFN-γ hydrogels modulated the phenotype of hydrogel encapsulated-hMSCs. HMSCs were encapsulated in hydrogels having doses of cys-IFN-γ ranging from 0-25 μg/mL. Following 4 days in culture, MSCs were subjected to flow cytometric analysis for IDO and PD-L1 (Fig. 11A). The expression of PD-L1 decreased as concentration increased from 0 to 5 μg/mL but then increased from 5 to 25 μg/mL. Notably, IDO expression increased significantly with increasing cys-IFN-γ concentration in a dose-dependent fashion. We also verified that increased IDO expression as seen determined by flow cytometric analysis correlated with IDO activity by measuring the concentration of kynurenine, the product of tryptophan after its catalysis by IDO (Fig. 11B).

After this dose-dependent study, we sought to understand how the polymer density of the hydrogel influences the expression of IDO and PD-L1. HMSC-encapsulated hydrogels of differing polymer densities ranging from 4% to 10% were synthesized with a constant 25 μg/mL concentration of cys-IFN-γ. Following 4 days in culture, MSCs were subjected to flow cytometric analysis for expression of IDO and PD-L1 (Fig. 12A, B). Whereas no differences were noted for PD-L1 expression, MSCs within 10% PEG weight hydrogels exhibited significantly lower levels of expression of IDO compared to those in 4%, 6% and 8% hydrogels. Given the results of both the dose study and the mechanical

properties study, we chose to focus on 6% hydrogels with a 25 μg/mL IFN-γ dose in subsequent *in vitro* experiments.

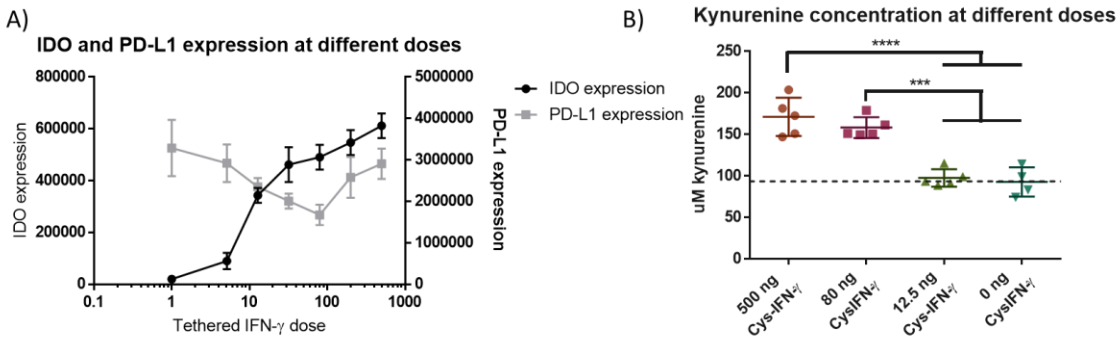

Figure 11: IDO and PD-L1 expression are functions of cys-IFN-γ dose. (A) HMSCs were encapsulated within 20 µL 6% PEG weight hydrogels having differing doses of cys-IFN-γ and placed in 1 mL of media. After 4 days in culture, hMSCs were stained for IDO and PD-L1 and subject to flow cytometric analysis. N=3-5. Error bars ± SEM (B) Conditioned media at select doses was tested for kynurenine concentration to verify correlation of IDO expression with IDO activity. Dotted line signifies concentration of kynurenine in hMSC media. N=4-5. Error bars ± SEM One-way ANOVA *** $p<0.001$, **** $p<0.0001$.

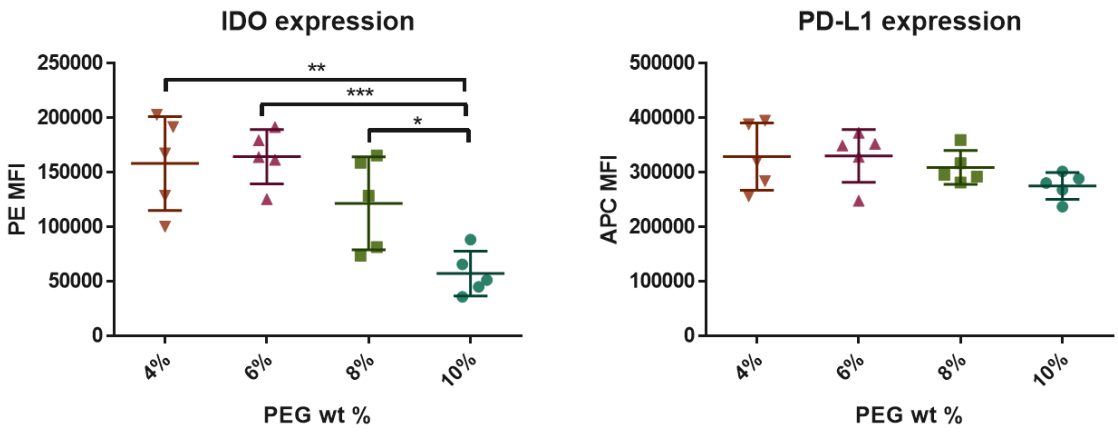

Figure 12: IDO is a function of PEG weight percent. HMSCs were encapsulated within 20 µL hydrogels of varying PEG weight percentages and 500 ng cys-IFN-γ. After 4 days in culture, hMSCs were stained for IDO and PD-L1 and subject to flow cytometric analysis. N=5. Error bars ± SEM. One-way ANOVA * $p<0.05$, ** $p<0.01$, *** $p<0.001$, **** $p<0.0001$.

4.4.4 Transient licensing of IFN-γ hydrogels compared to cys-IFN-γ hydrogels

While cys-IFN-γ exhibits the ability to license hMSCs within our hydrogel construct, we further explored whether tethering significantly increased licensing duration compared to a non-tethered form of IFN-γ. HMSCs were encapsulated in hydrogels with either cys-IFN-γ, IFN-γ or no IFN-γ. Following encapsulation, hydrogels were washed throughout the first 24 hours to simulate sink conditions present *in vivo.* Hydrogels were then cultured for an additional 3 days after which the hydrogels were degraded, conditioned media collected for cytokine analysis and hMSCs stained for IDO and PD-L1 followed by flow cytometric analysis (Fig. 13A,B). HMSCs encapsulated in IFN-γ hydrogels exhibited significantly increased IDO and PD-L1 expression compared to control hMSCs. Importantly however, hMSCs encapsulated in cys-IFN-γ hydrogels showed significantly increased IDO and PD-L1 expression compared to hMSCs encapsulated in IFN-γ hydrogels as well as control hMSCs. Additionally, analysis of conditioned media showed that hMSCs encapsulated in cys-IFN-γ hydrogels secreted increased levels of CXCL10, CCL2, CCL8, M-CSF and CXCL9 compared to hMSCs encapsulated in either IFN-γ hydrogels or hMSCs encapsulated in hydrogels without IFN-γ licensing (Fig. 14 A-J).

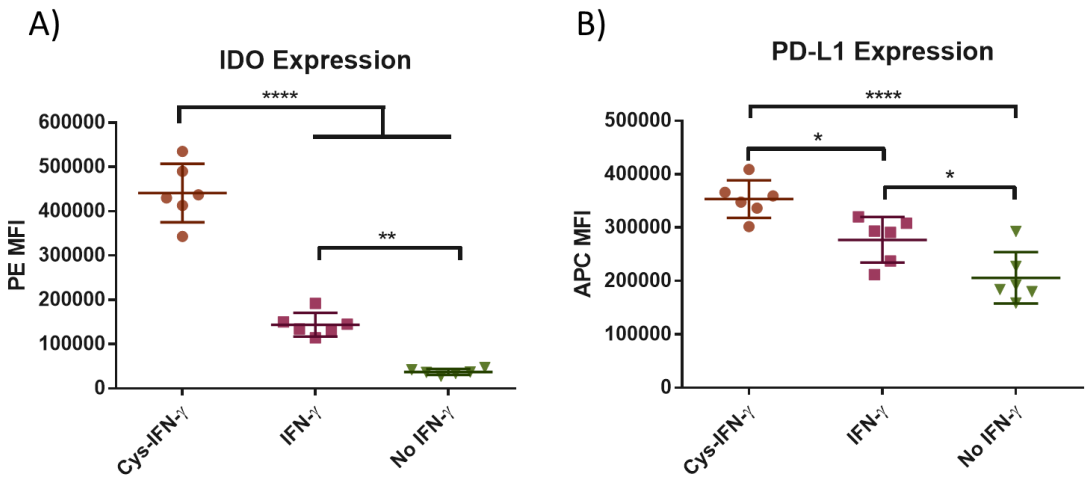

Figure 13: IDO and PD-L1 expression of hMSCs in hydrogels with cys-IFN-γ and IFN-γ. Following 4 days of culture, hMSCs in hydrogels with either cys-IFN-γ, IFN-γ or no IFN-γ were stained for (A) IDO and (B) PD-L1 and subjected to flow cytometric analysis. N=6 separate hydrogel with 5000 hMSCs analyzed per hydrogel. Error bars ± SEM. One-way ANOVA. * $p<0.05$, **** $p<0.0001$.

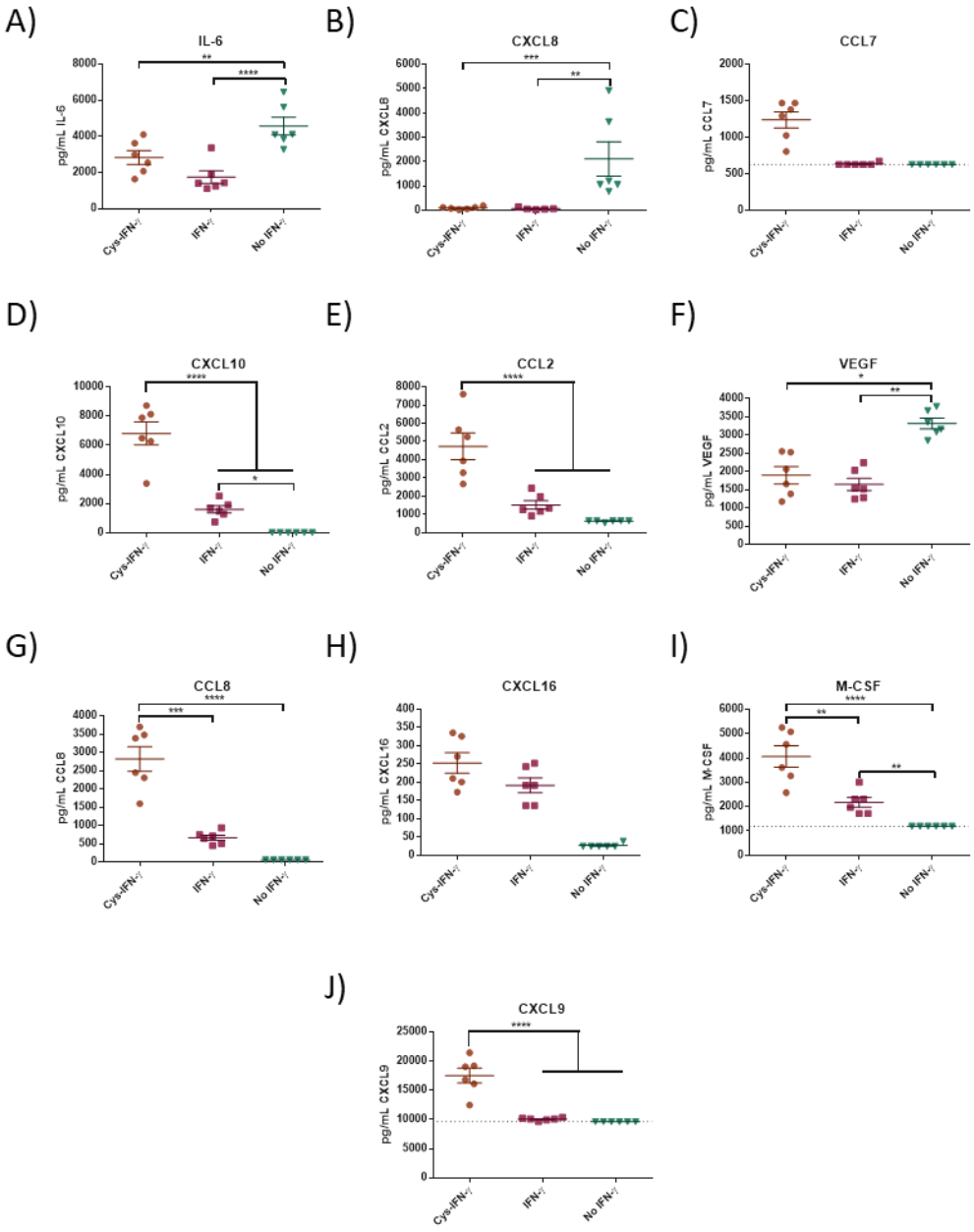

Figure 14: Cytokine analysis of conditioned media. Conditioned media of hMSCs encapsulated in hydrogels with either cys-IFN-γ, IFN-γ or no IFN-γ was analyzed for (A)

IL-6, (B) CXCL8, (C) CCL7, (D) CXCL10, (E) CCL2, (F) VEGF, (G) CCL8, (H) CXCL16, (I) M-CSF and (J) CXCL9. N=6. Error bars ± SEM. One-way ANOVA. * *p<0.05, ** p<0.01, *** p<0.001, **** p<0.0001*.

4.4.5 HMSCs encapsulated in cys-IFN-γ hydrogels significantly inhibit T-cell proliferation via an IDO-dependent mechanism

HMSCs have been noted to elicit immunomodulatory properties on a variety of immune cell types. Notably, hMSCs significantly reduce the proliferation of activated T-cells when co-cultured together [164]. Given the significant effect that cys-IFN-γ has on encapsulated hMSCs compared to hMSCs encapsulated in IFN-γ hydrogels, we next assessed whether cys-IFN-γ hydrogels could augment the inhibitory effect of hMSCs on T-cell proliferation (Fig 15). HMSCs were encapsulated in hydrogels with either cys-IFN-γ, IFN-γ, or no IFN-γ. Additionally, we wanted to further test the functional ability for hMSCs encapsulated in cys-IFN-γ hydrogels to hMSCs licensed with IFN-γ prior to utilization in therapy as is routinely done. Thus, in a separate group, hMSCs were encapsulated in hydrogels without IFN-γ and incubated in media having 500 ng/mL native IFN-γ. HMSCs in cys-IFN-γ and IFN-γ hydrogels were washed twice within 24 hrs following encapsulation to simulate a sink effect *in vivo*. These hydrogels were then incubated with activated CD4+ T-cells and co-cultured for 4 days after which the T-cells were stained for EdU and CD3 to examine proliferation and verify their T-cell phenotype, respectively (Fig. 15). Activated T-cells cultured solely with Dynabeads (to activate T-cells) showed a similar high degree of proliferation compared to activated T-cells cultured with a cys-IFN-γ hydrogel without hMSCs indicating that the presence of the cys-IFN-γ hydrogel by itself has no effect on T-cell proliferation (Fig. 16). Furthermore, these two groups showed significantly greater levels of T-cell proliferation compared to all groups

having IFN-γ. Importantly however, T-cells incubated with hMSCs in cys-IFN-γ hydrogels exhibited significantly lower levels of proliferation compared to T-cells cultured with hMSCs in IFN-γ hydrogels, indicating augmented immunomodulatory properties for tethered IFN-γ over non-tethered forms. There were no differences in T-cell proliferation for T-cells incubated with hMSCs in cys-IFN-γ hydrogels or hydrogels with pre-licensed hMSCs.

We further assessed the mechanism behind this inhibitory effect. Thus, hMSCs were encapsulated in cys-IFN-γ hydrogels and co-cultured with T-cells (Fig. 17A). An IDO inhibitor, 1-methyl-tryptophan (1-MT), was either added or excluded from the media. After 4 days, T-cells that were incubated with hMSCs encapsulated in cys-IFN-γ hydrogels without 1-MT exhibited significantly reduced proliferation compared to T-cells cultured in the same conditions with 1-MT (Fig. 17B). Importantly, T-cells cultured with 1-MT either with or without hMSCs showed no difference in their proliferation denoting that the addition of 1-MT completely inhibited the anti-proliferative effect of licensed hMSCs in the co-culture. This complete abrogation of anti-proliferative effect indicates that IDO is a critical regulator of the anti-proliferative activities of hydrogel-encapsulated hMSCs.

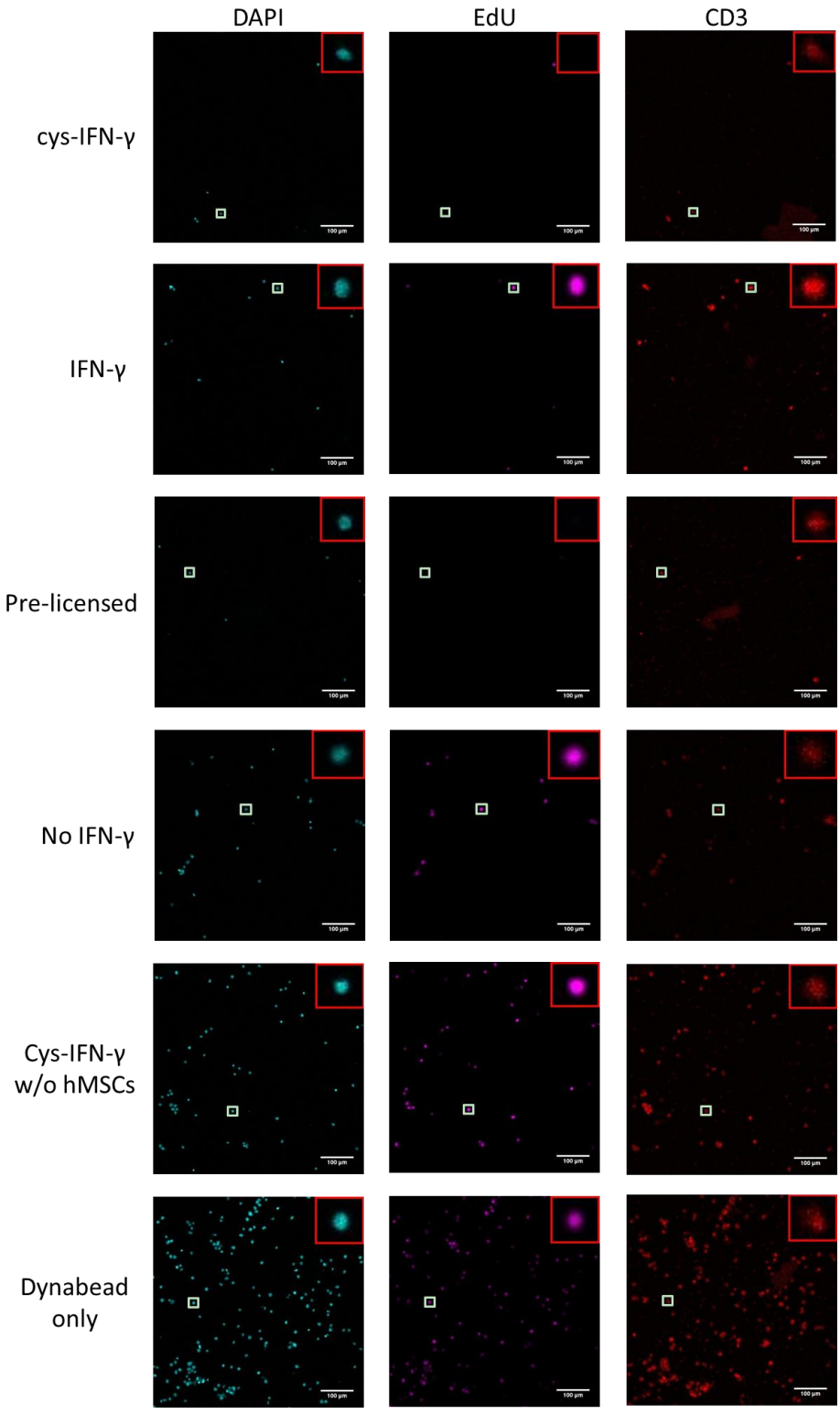
DAPI
EdU
CD3
cys-IFN-γ
IFN-γ
Pre-licensed
No IFN-γ
Cys-IFN-γ
w/o hMSCs
Dynabead
only

Figure 15: Representative images of fluorescence microscopy images of proliferating T-cells stained for DAPI, EdU and CD3. Scale bars = 100 µm.

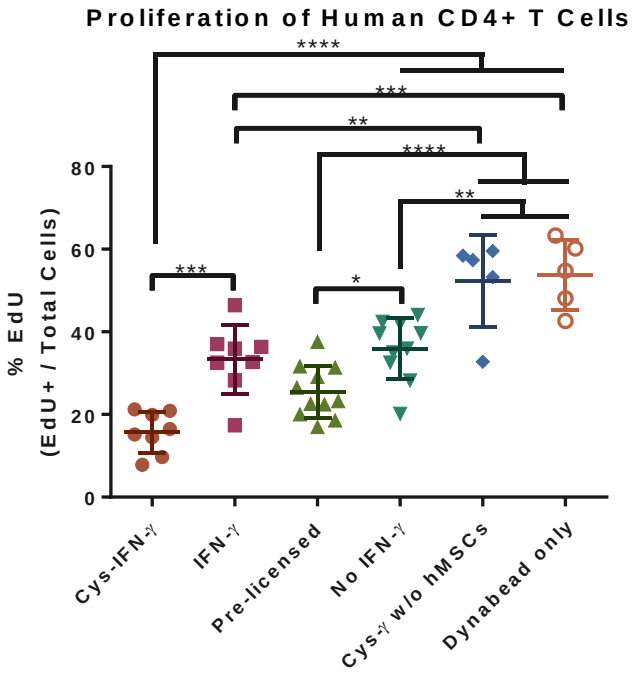

Figure 16: Quantification of proliferating T-cells. HMSCs encapsulated within cys-IFN-γ hydrogels significantly reduce activated CD4+ T-cell proliferation. Untreated or pre-licensed hMSCs were encapsulated within cys-IFN-γ, IFN-γ or no IFN-γ hydrogels and co-cultured with activated CD4+ T-cells for 4 days. T-cell proliferation was assessed via EdU incorporation. Graph shows samples from two independent experiments. N= 5-8 separate wells with quantification of >100 T-cells per well. Error bars ± SEM. One-way ANOVA * $p<0.05$.

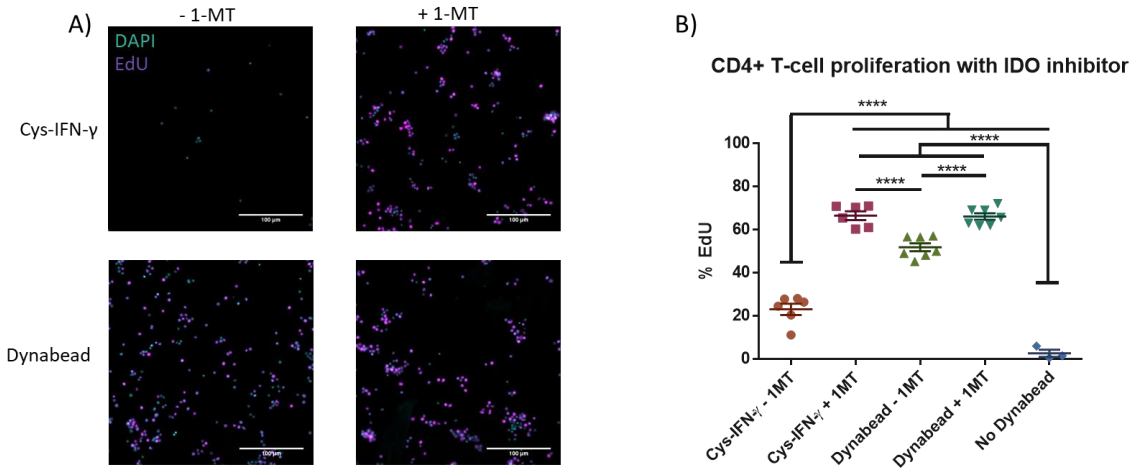

Figure 17: T-cell proliferation with IDO inhibitor. (A) Representative images of fluorescence microscopy images of proliferating T-cells with or without IDO inhibitor. Scale bars = 100 µm. (B) Quantification of proliferating T-cells. N= 6-7 separate wells with quantification of > 100 T-cells per well. Error bars ± SEM. All quantification of proliferating T-cells was performed via custom ImageJ macro. One-way ANOVA. **** *p<0.0001*.

4.4.6 HMSCs encapsulated in cys-IFN-γ hydrogels significantly inhibit monocyte-derived dendritic cell differentiation via a primarily IDO-dependent method

In addition to inhibiting T-cell proliferation, hMSCs have been noted to inhibit the differentiation of monocytes into dendritic cells *in vitro* [186]. We thus assessed whether cys-IFN-γ hydrogels could augment the inhibition of dendritic cell differentiation (Fig. 18A). Untreated or pre-licensed hMSCs were encapsulated within cys-IFN-γ, IFN-γ, or no IFN-γ hydrogels and co-cultured with peripheral blood purified CD14+ monocytes. These cells were co-cultured in dendritic cell differentiation conditions for 5 days. Mature dendritic cell differentiation was performed by addition of 100 ng/mL LPS for an additional 2 days. Following complete differentiation, monocytes were stained for the monocyte marker CD14, the dendritic cell marker CD1a and maturation markers CD80 and CD86. Monocytes cultured in the absence of hMSCs exhibited significantly greater dendritic cell differentiation compared to monocytes co-cultured with hMSCs as quantified by the percentage of CD1a+/CD14- cells (Fig. 18A). Monocytes cultured with hydrogels having untreated hMSCs, pre-licensed hMSCs or hMSCs encapsulated in IFN-γ hydrogels showed no differences in their dendritic cell differentiation. Importantly however, monocytes cultured with hMSCs encapsulated in cys-IFN-γ hydrogels showed a significant reduction in their dendritic cell differentiation compared to monocytes cultured with all other hMSC conditions and IFN-γ. Furthermore, monocytes cultured with hMSCs encapsulated in cys-IFN-γ hydrogels exhibited significantly greater expression of maturation markers CD80 and CD86 compared to monocytes cultured in all other conditions tested (Fig. 18B, C).

These results show that hMSCs in cys-IFN-γ hydrogels exhibit significantly upregulated ability to inhibit monocyte-derived dendritic cell differentiation compared to either hMSCs not exposed to IFN-γ or hMSCs in IFN-γ hydrogels.

We next investigated the mechanism of action for this effect and conducted an experiment where monocytes were co-cultured with either hMSCs in cys-IFN-γ hydrogels or alone with the addition of either an IDO inhibitor (1-MT), a PGE2 inhibitor (NS-398), or both. Following 7 days in dendritic cell differentiation conditions, the monocytes were collected, stained for CD1a and CD14 and subjected to flow cytometric analysis (Fig. 19). Without the addition of IDO or PGE2 inhibitor, monocytes co-cultured with hMSCs in cys-IFN-γ hydrogels exhibited less dendritic cell differentiation compared to those without hMSCs. Monocytes co-cultured in the hMSC condition and cultured with the IDO or PGE2 inhibitor exhibited more dendritic cell differentiation compared to vehicle only controls. Monocytes with the IDO inhibitor exhibited more dendritic cell differentiation than those with the PGE2 inhibitor indicating IDO to be the dominant mechanism halting dendritic cell differentiation.

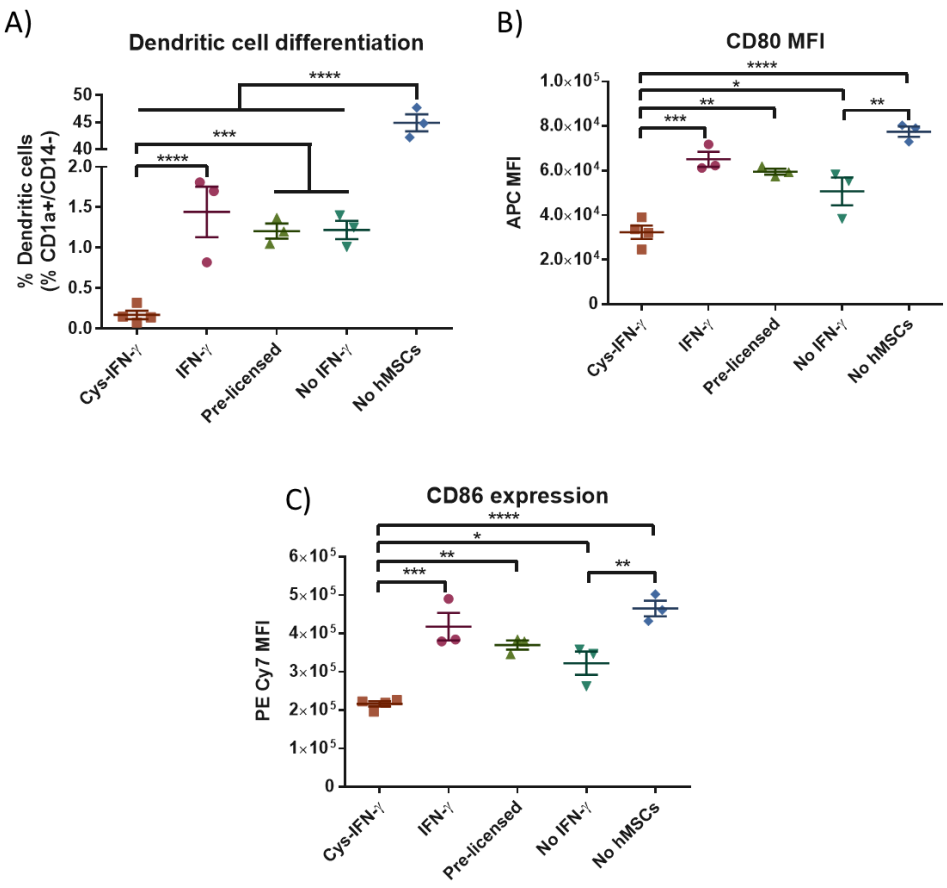

Figure 18: hMSCs in cys-IFN-γ hydrogels inhibit dendritic cell differentiation. (A) Percentage of dendritic cells in monocyte culture after 7 days differentiation as defined by CD1a+ / CD14- by means of FMO controls. Median fluorescence intensity for markers (B) CD80 and (C) CD86. N=3-4 separate wells with 20,000 cells analyzed per well. Error bars ± SEM. One-way ANOVA * $p<0.05$, ** $p<0.01$, *** $p<0.001$, **** $p<0.0001$.

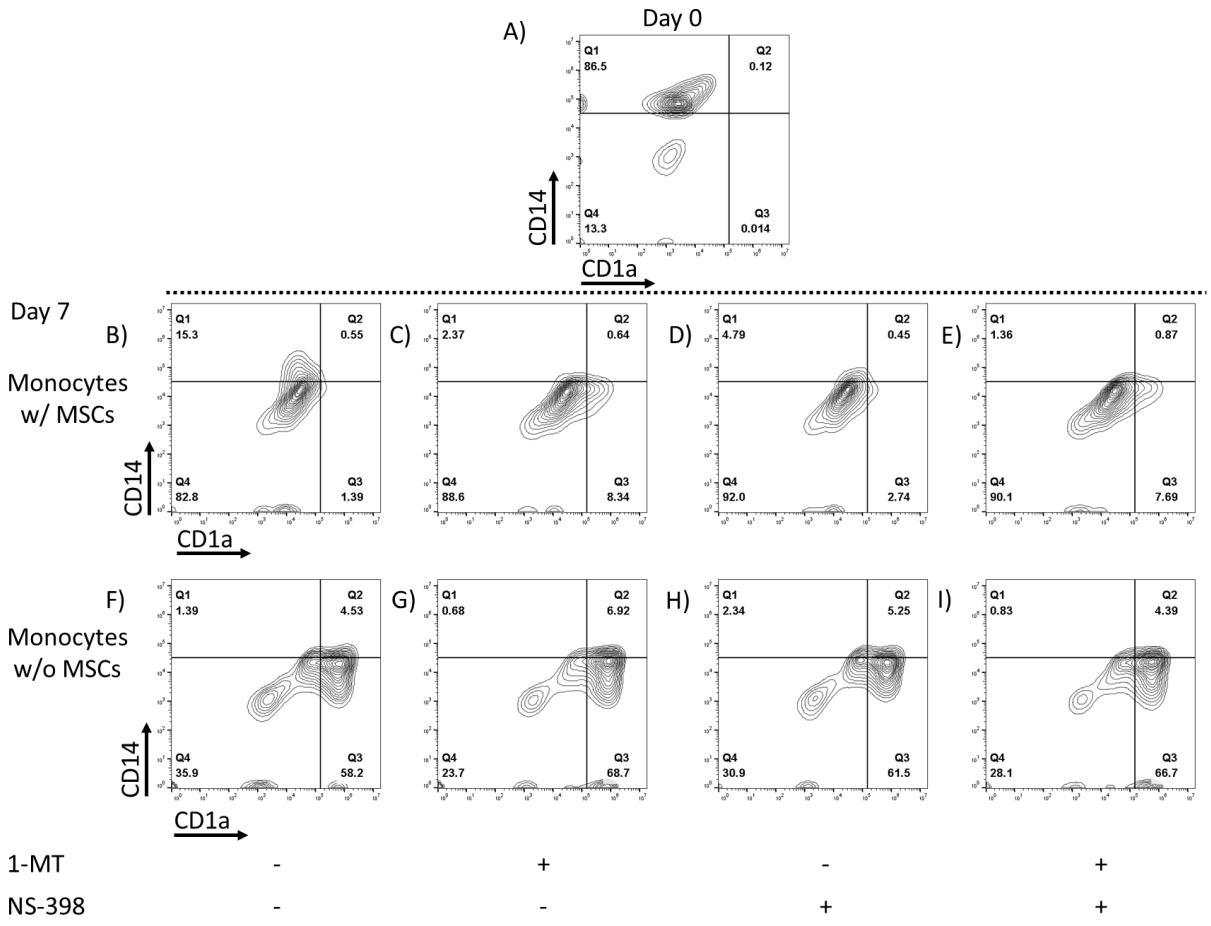

Figure 19: hMSC-based inhibition of monocyte differentiation is dictated primarily through IDO: (A) Isolation of monocytes from peripheral blood at day 0 resulted in 86.5% of cells displaying the CD14+ / CD1a- monocyte phenotype. After 7 days in dendritic cell differentiation conditions either (B-E) with or (F-I) without co-culturing with hMSCs encapsulated within IFN-γ tethered hydrogels and with or without IDO or PGE2 inhibitors 1-methyl tryptophan (1-MT) or NS-398 respectively.

4.4.7 HMSCs in cys-IFN-γ hydrogels exhibit differential cytokine expression in a murine subcutaneous environment compared to pre-licensed hMSCs

Because we observed enhanced hMSC-based immunomodulation on cells from both myeloid and lymphoid lineages when hMSCs were encapsulated in cys-IFN-γ hydrogels compared to other forms of IFN-γ activation, we explored whether cys-IFN-γ hydrogels could augment hMSC immunomodulation *in vivo*. For this experiment, we utilized a murine subcutaneous model in which human cytokine analysis was performed 3 days after hMSC-encapsulated hydrogels were injected into immunocompromised mice. HMSCs were encapsulated within cys-IFN-γ hydrogels or within hydrogels without IFN-γ. We also encapsulated pre-licensed hMSCs which were incubated in 500 ng/mL IFN-γ for 48 hours prior to subcutaneous injection. These groups were injected in the subcutaneous space of the dorsum of mice. After 3 days post-injection, tissue explants were analyzed for a panel of human cytokines via a Luminex assay. Two-way hierarchical clustering of the 14 cytokines assessed showed distinct groupings among experimental conditions (Fig. 20). Furthermore, by performing canonical correlation analysis, distinct groupings are seen with larger separation between hMSCs in cys-IFN-γ hydrogels and other hMSC groups compared to pre-licensed hMSCs and hMSCs not treated with IFN-γ (Fig. 21). Individual cytokine analysis also revealed significant differences among tested groups (Fig. 22). In particular, it is interesting to note that for certain specific cytokines including IL-6 and VEGFA, the trends opposed were opposite of that measured *in vitro.* This can be explained by the potential increased amount of interactions and feedback loops

with differing cell types present *in vivo* compared to our *in vitro* system. That said however, it is worthy to note that many other cytokines that have been implicated in hMSC-based modulation of immune cell reaction such as M-CSF and MCP-1 follow similar trends seen *in vitro*.

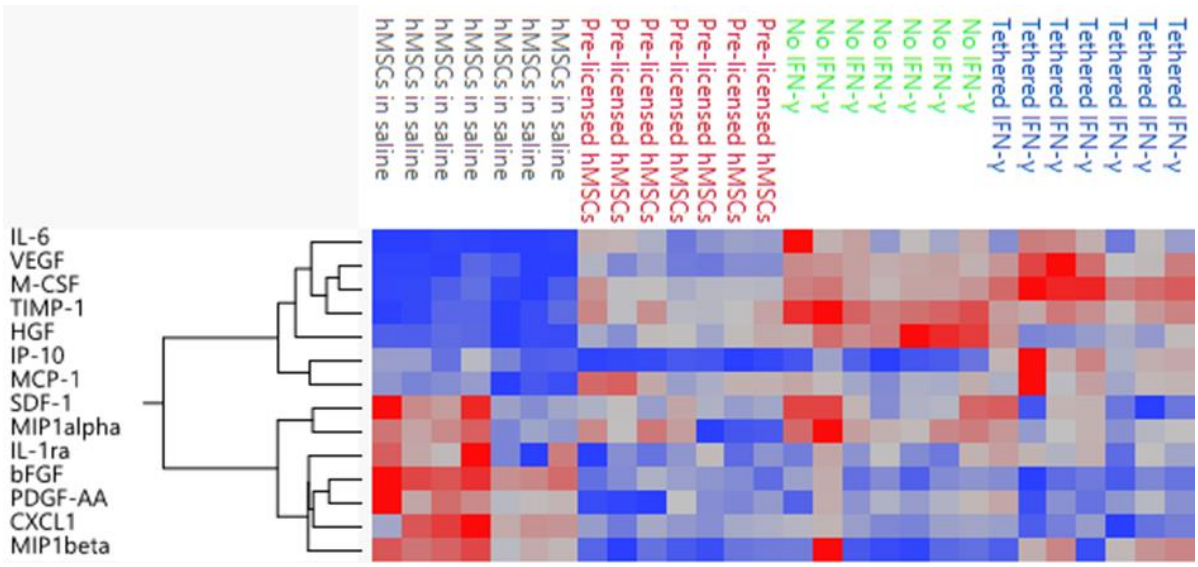

Figure 20: Two-way hierarchical clustering analysis

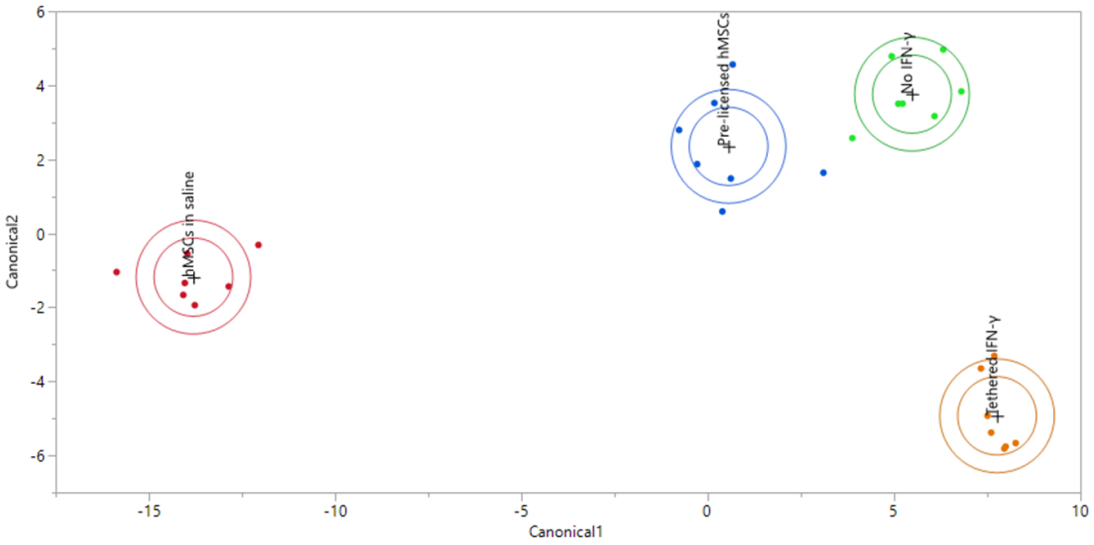

Figure 21: Canonical correlation analysis

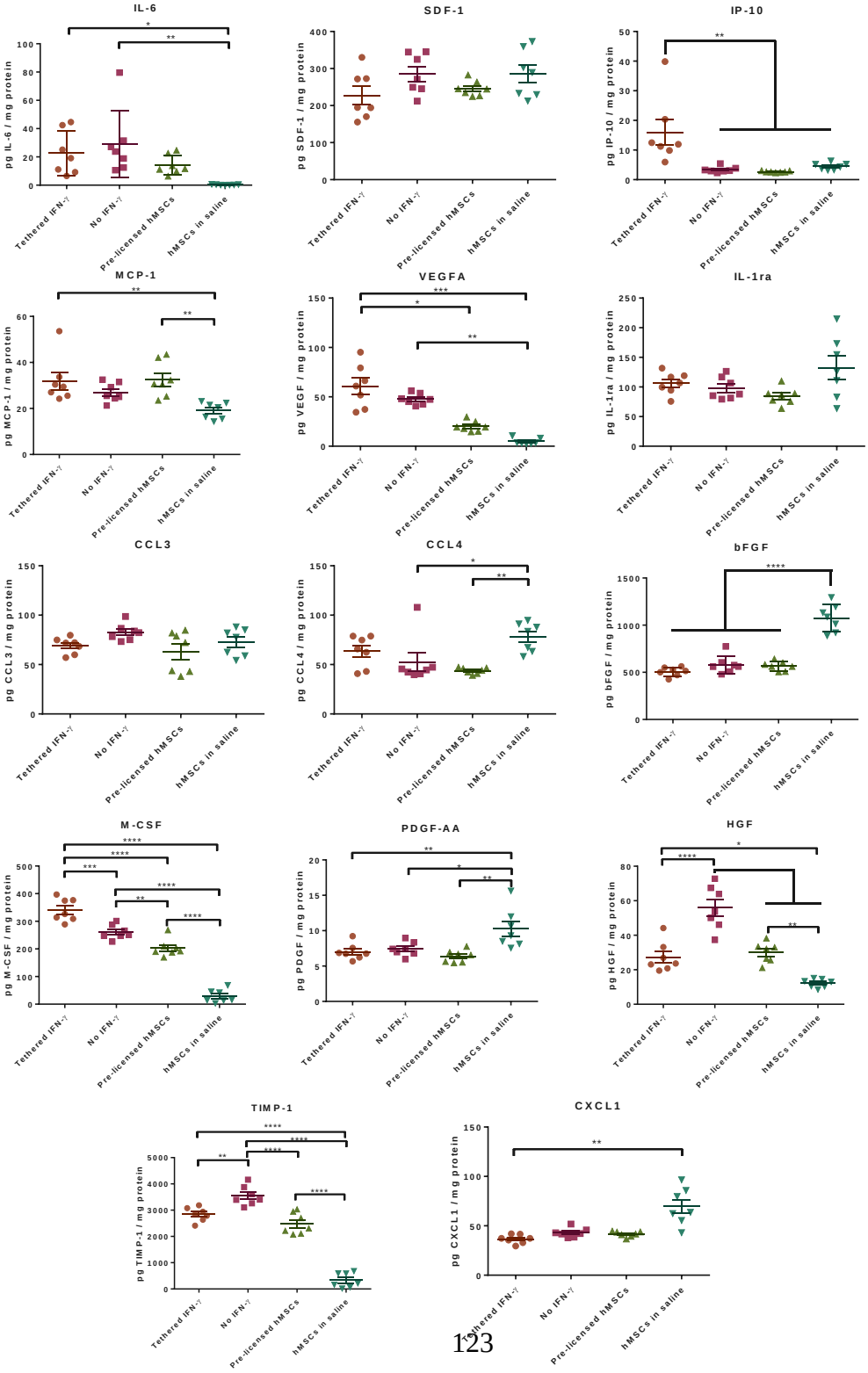
IL-6
pg IL-6 / mg protein
SDF-1
pg SDF-1 / mg protein
IP-10
pg IP-10 / mg protein
MCP-1
pg MCP-1 / mg protein
VEGFA
pg VEGF / mg protein
IL-1ra
pg IL-1ra / mg protein
CCL3
pg CCL3 / mg protein
CCL4
pg CCL4 / mg protein
bFGF
pg bFGF / mg protein
M-CSF
pg M-CSF / mg protein
PDGF-AA
pg PDGF / mg protein
HGF
pg HGF / mg protein
TIMP-1
pg TIMP-1 / mg protein
CXCL1
pg CXCL1 / mg protein
Tethered IFN-γ
No IFN-γ
Pre-licensed hMSCs
hMSCs in saline

Figure 22: Individual cytokine analysis from tissue extraction. N=7. Error bars ± SEM One-way ANOVA * $p<0.05$, ** $p<0.01$, *** $p<0.001$, **** $p<0.0001$.

4.4.8 HMSCs in cys-IFN-γ hydrogels accelerate healing of colonic wounds

Following our findings that hMSCs within cys-IFN-γ hydrogels show a different cytokine profile compared to either pre-licensed or untreated hMSCs within a subcutaneous model, we examined the use of hMSCs encapsulated within cys-IFN-γ hydrogels within a more functional model. The use of hMSCs toward treating inflammatory diseases in clinical trials has rapidly grown in recent years with Crohn's and other inflammatory bowel diseases consisting a large portion of the conditions being treated [291]. In addition, previous literature suggests that licensing hMSCs with IFN-γ can significantly augment the regenerative effects of cell therapy in pre-clinical colitis models [221]. We thus tested whether hMSCs encapsulated within cys-IFN-γ hydrogels could significantly enhance regeneration of intestinal mucosal wounds. A preliminary pilot experiment demonstrated that hMSCs within cys-IFN-γ hydrogels accelerated the regeneration of colonic wounds compared to either controls where no treatment was injected or to wounds where cys-IFN-γ hydrogels without hMSCs were injected (Appendix C). This pilot experiment demonstrates that colonic wounds in control animals without hMSCs do not heal as well as when hMSCs are delivered. This allows for future experiments to drill deeper on the question of whether hMSCs in cys-IFN-γ hydrogels outperform non-licensed or pre-licensed hMSCs since the control group of no cells is already proved to be ineffectual.

We thus conducted a larger scaled experiment where we focused on the issue of hMSC efficacy in healing colonic wounds. HMSCs were encapsulated within either cys-

IFN-γ hydrogels or no IFN-γ hydrogels and injected at the site of mechanically induced mucosal wounds in the distal colon of mice. Additionally, we incorporated a group where hMSCs in saline were injected at the wound site. We also had a group, termed the control group, where un-cross-linked hydrogel components in saline were injected at the wound site. Five days post-injury, wound closure was assessed via a murine colonoscope and quantified. No differences in wound closure were noted between control mice and mice injected with hMSCs either in no IFN-γ hydrogels or in saline alone. However, hMSCs that were encapsulated within cys-IFN-γ hydrogels exhibited significantly higher levels of wound closure at day 5 post-injury than control mice (Fig. 23).

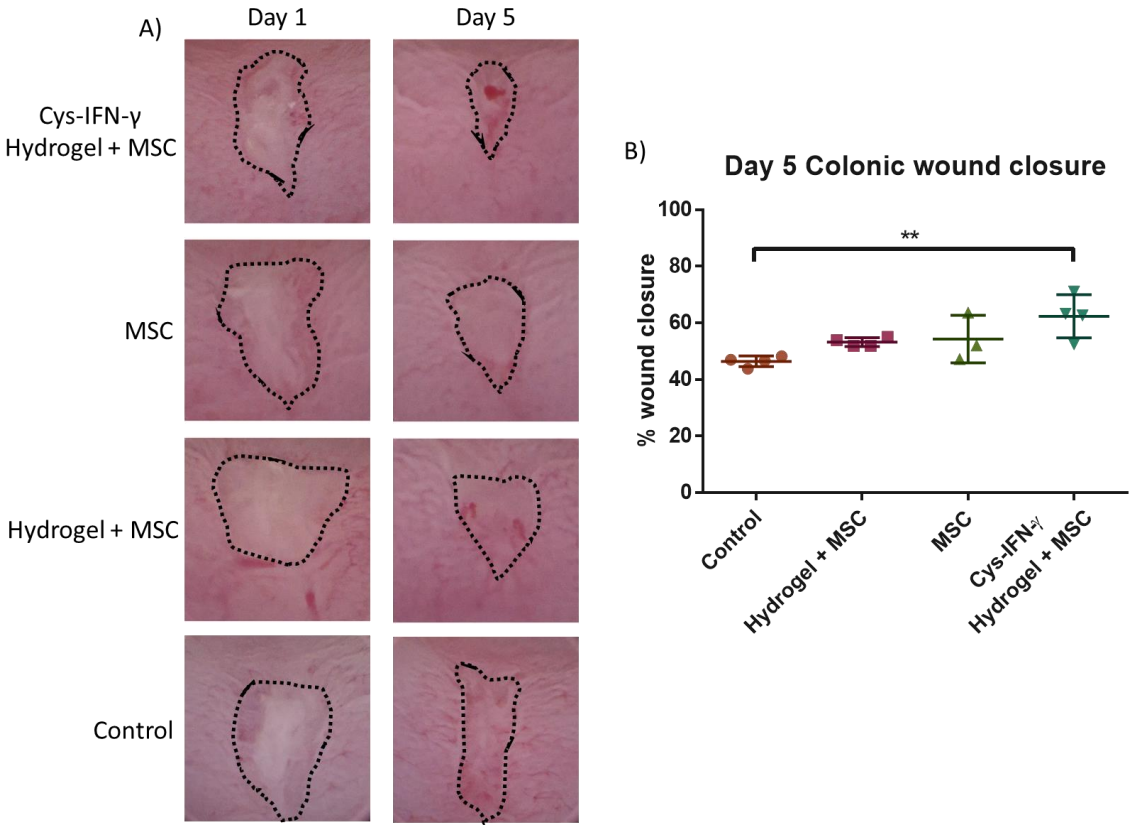

Figure 23: Regeneration of colonic wounds. (A) Representative images of colonic wounds at day 1 and day 5 after implantation. (B) Quantification of colonic wound closure at day 5 post-injury. Error bars ± SEM. One-way ANOVA ** $p<0.01$.

4.5 Discussion

With the impetus for cell therapies to be translated into the clinic, human mesenchymal stem cells have become a widely researched cell type with utilization in nearly 500 clinical trials [1]. While these cells were initially touted for their differentiation potential, recent evidence including their potential for treating inflammatory diseases such as graft vs host disease and Crohn's disease point to their effects being due principally to their immunomodulatory properties [292, 293]. Nonetheless, the success of these clinical trials in treating inflammatory diseases is mixed with approximately half of all patients who were administrated hMSCs showing little to no improvement [207, 208, 214, 215]. This points to a need for increasing the efficacy of stem cell based therapy and specifically, increasing the immunomodulatory properties of hMSCs. Licensing hMSCs with IFN-γ has been noted to increase their immunomodulatory properties within both *in vitro* and *in vivo* systems [294]. However, the need for *ex vivo* manipulation of hMSCs with IFN-γ raises considerable concerns including the presence of increased costs, clearing regulatory hurdles and establishing rigorous and reliable cell handling practices that all negatively affect clinical translation [280]. Engineering a biomaterial that can license hMSCs without the need for *ex vivo* manipulation can significantly enhance the translation of stem cell therapy.

In this study, we engineered a novel methodology for licensing hMSCs by functionalizing a PEG-based hydrogel scaffold with a biologically active form of IFN-γ.

To assess the functionality and efficacy of our platform, we tested two general concepts: 1) whether the scaffold modification elicited a response onto scaffold-encapsulated hMSCs and 2) whether the effect imparted onto the hMSCs generated a secondary effect onto other cell types, specifically immune cells. For the former concept, hMSCs encapsulated within the modified hydrogel exhibited similar or increased expression of both cell-licensing markers IDO and PD-L1 compared to hMSCs that were pre-licensed with IFN-γ. For the latter concept, hMSCs encapsulated within modified hydrogels showed a potent ability to hinder both activated T-cell proliferation and monocyte-derived dendritic cell differentiation. Importantly, the monocyte hindrance imparted by hMSCs encapsulated within IFN-γ-modified hydrogels was greater than that of encapsulated hMSCs that were licensed with unbound IFN-γ prior to co-culture. This increased effect for the bound form could potentially be due to the increased duration of licensing as the bound IFN-γ form is present throughout the co-culture period while the unbound IFN-γ is removed prior to co-culture as a simulation for how this treatment would be translated into the clinic. In addition to the increased duration, the bound form of IFN-γ presumably results in higher microenvironmental concentrations of IFN-γ surrounding the encapsulated hMSCs compared to the unbound form. This notion elicits the possibility for future studies investigating whether lower doses of cys-IFN-γ could be utilized thus furthering the applicability of clinical use.

In addition to the *in vitro* results, the cytokine data gathered from the subcutaneous experiment further corroborate the notion that hMSCs within hydrogels containing bound

IFN-γ imparts a more significant effect than pre-licensed hMSCs. Through canonical correlation analysis of the cytokine data, it was observed that pre-licensed hMSCs exhibited a more similar cytokine signature to un-treated hMSCs than hMSCs within cys-IFN-γ hydrogels. On an individual cytokine basis, hMSCs within cys-IFN-γ hydrogels showed significantly higher levels of the cytokine macrophage colony stimulating factor (M-CSF), which is known to skew monocytes toward an anti-inflammatory phenotype. Furthermore, within a functional model, hMSCs encapsulated in cys-IFN-γ hydrogels exhibited significantly higher levels of wound closure compared to controls as well as untreated hMSCs. This finding supports the notion that the effects imparted by this methodology of licensing hMSCs elicits a functional response *in vivo*. It remains unclear however the mechanisms behind the increased regeneration. Further studies are needed to understand how such licensing affects the cellular and molecular cascades within the affected area in order to further increase the efficacy of the therapy. While the levels of healing in the hMSC + cys-IFN-γ hydrogel group can be described as relatively modest compared to that of control groups, it is important to recognize that model carries some limitations. For one, the colonic wounds in control mice which received only saline injections exhibited approximately 47% wound closure by day 5. This indicates that even with no treatment, the wound heals by itself. Future experiments utilizing a more rigorous chronic inflammatory model would provide more information as to the efficacy of the cell therapy.

4.6 Conclusion

While hMSCs have been recently used for treating inflammatory diseases in clinic trials, their scale use is limited by issues with efficacy and *ex vivo* manipulation. In this study, we engineered a novel way to license hMSCs by covalently tethering IFN-γ within hMSC-encapsulated hydrogels. HMSCs within bound IFN-γ hydrogels exhibited significantly increased IDO activity compared to un-treated hMSCs as well elicited either equal or greater ability to hinder immune cell proliferation and differentiation compared to pre-licensed hMSCs. Furthermore, in a functional colonic wound model, hMSCs within tethered IFN-γ hydrogels exhibited significantly enhanced healing compared to untreated hMSCs. This study demonstrates the ability for covalently bound IFN-γ to enhance the immunomodulatory properties of hMSCs and enhances the clinical translatability of licensing hMSCs.

CHAPTER 5. FUTURE CONSIDERATIONS

5.1 Vascularization and bone healing with human mesenchymal stem cells

We have observed that integrin-specific hydrogels significantly impact the level of vascularization within a bone defect depending on the specific ligand the hydrogel is functionalized with (Chapter 3). Preliminary experiments in which integrin-specific and VEGF-functionalized hydrogels were encapsulated with hMSCs and delivered within the bone defect however showed no effect from either the integrin-specificity or the presence of VEGF on stem cell number in the defect as assessed via bioluminescence tracking (Appendix A). Future work to resolve this issue can revolve around ascertaining the cause of stem cell death and engineering the material to enhance short-term survival of hMSCs. The rationale for implanting hydrogels functionalized with VEGF was to improve the vascularization of the surrounding tissue, thereby increasing oxygen and nutrient availability to enhance implanted cell survival. However, the model used consists of a defect where the total diameter of the wounded bone is < 1 mm. This raises the possibility that the wound itself may not be under hypoxic stress. Future work may include inducing a wound followed by observation of hypoxic conditions through commercially available products such as hydroxyprobe. If hypoxic conditions exist, the presence of VEGF may not provide sufficient vascularization within a timespan immediately following surgical

implantation. Thus, work in which VEGF functionalization is combined with approaches aimed at enhancing cell survival in the short-term such as an oxygen-generating material within the hydrogel construct could increase the efficacy of the cell-based therapy.

Preliminary experiments also showed that neither integrin-specificity nor VEGF functionalization onto hMSC-laden hydrogels had effects on vascularization or bone regeneration within the bone defect model (Appendix A). One potential reason for this dichotomy between the results with and without cells is the difference of immune-based parameters between experiments incorporating hMSCs and those without. Experiments without hMSCs were performed in C57 mice which have fully functioning immune systems while experiments with hMSCs were performed in immunodeficient mice. Mounting evidence points to the importance of the immune system in the successful resolution of bone defects [295]. The effect integrin-specificity has within a bone defect may be in part due to immune cell interactions which would be absent within immunodeficient mice. Utilizing human mesenchymal stem cells within humanized mice, which exhibit a fully functional immune system, will be required to definitively ascertain the role of the immune system on our hydrogel construct and increase the relevance of the findings.

5.2 Immunomodulation by MSCs

In Aim 2 of this thesis, we engineered a PEG hydrogel in which IFN-γ was covalently bound to the hydrogel backbone. The bound form of IFN-γ retained its biological activity

and was able to interact with hMSCs to enhance their immunomodulatory properties both *in vitro* and *in vivo*. There are multiple directions that this research can continue forth to. Maintaining with the inflammatory bowel disease model, further studies can be performed understanding how our platform compares to the current gold standard consisting of pre-licensing the cells with IFN-γ prior to implantation. While our platform can theoretically avoid the use of *ex vivo* manipulation thus enhancing its clinical translation, it would be important to understand how a persistent IFN-γ signal *in vivo* compares to an IFN-γ stimulus prior to treatment in a functional manner. Additionally, one area that can be explored is that of the mechanism of action underlying the increased regeneration noted in the colonic wound model. *In vitro* results noted that both T-cells and monocytes are affected by licensed hMSCs; however, the inflammatory and regenerative signals following injury involve a complex cascade of events which make it difficult to properly and precisely carry interpretation from *in vitro* studies into *in vivo* scenarios. Flow cytometric-based phenotyping of the wound at different time-points following colonic injury and hydrogel injection would provide insight into the cellular environment. This analysis could also provide insight into the polarization of the various cells to indicate whether a shift into an anti-inflammatory state occurs. Once the mechanism of action is understood, it is also plausible to move into more clinically relevant models of inflammatory bowel disease rather than that of a mechanically induced colonic injury. There are a variety of knock-out murine models where colitis spontaneously occurs including IL-10 knockout and IL-2 knockout as well as many transgenic models that also

emulate colitis. While knockouts can result in colitis, the systemic effects of knockout can limit the interpretation of results and so a transgenic model where colitis can be selectively induced provide more relevant models. A soluble B7.2 transgenic model results in mice that are genetically engineered to express a soluble form of B7.2 Ig Fc under the control of a liver-specific promoter which results in colitis with large inflammatory cell infiltration [296].

In addition to staying with an inflammatory bowel disease centered focus, the findings of this Aim can also extend to other applications. Graft vs host disease (GvHD) is another chronic inflammatory disease in which MSCs have been utilized in clinical trials to treat patients. Similar to treating Crohn's disease, MSCs that are pre-licensed with IFN-γ show an enhanced ability to ameliorate the effects of graft vs host disease in preclinical models compared to hMSCs that are untreated prior to *in vivo* delivery [216]. Preliminary experiments are currently being conducted within our lab to assess whether MSCs delivered within a PEG scaffold can treat murine GvHD compared to MSCs that are delivered intravenously. If the results from that study show that administration of MSCs to a confined area *in vivo* can also treat GvHD compared to systemic treatment, it could allow for further investigation into whether IFN-γ bound hydrogels could be used for that application.

The results shown in this thesis can also point to venturing outside utilization of IFN-γ entirely while retaining the underlying theme of engineering a biomaterial scaffold that

allows for increasing the immunomodulatory of encapsulated cells. A recent study showed that MSCs that were pre-treated with IL-1β significantly ameliorated the development of colitis in a dextran sulfate sodium model compared to untreated MSCs [218]. In a similar fashion as IFN-γ, hydrogels can be engineered to have bound forms of IL-1β to augment MSC activity. Following this logic, more complex systems can be developed where multiple cytokines are incorporated into biomaterial scaffold for the purpose of enhanced encapsulated cell efficacy. This can also be combined with other technology that is aimed to induce recruitment of endogenous cells. In this model, a specific cytokine can be included and made to release from the scaffold to allow for recruitment of endogenous cells while other tethered and bound forms of cytokines are present to train and activate the cells for a specific purpose.

APPENDIX A: HMSC-ENCAPSULATED INTEGRIN-SPECIFIC HYDROGELS FOR VASCULARIZATION AND BONE REGENERATION OF CRITICAL-SIZE DEFECTS

A.1 Summary

Following the results acquired from Chapter 3, namely that integrin-specificity and VEGF-incorporation had a significant effect on vascularization, we wanted to probe whether these two parameters could affect vascularization and viability of delivered hMSCs in the murine bone defect model. Our hypothesis was that differential vascularization induced by these two parameters would result in differential hMSC viability and thus induce changes in bone regeneration. To test this, we transduced hMSCs to constitutively express a red firefly luciferase construct to enable *in vivo* tracking within the critical-size bone defect. We then encapsulated hMSCs within integrin-specific hydrogels that were either functionalized with RGD or GFOGER as well as with different doses of VEGF. We conducted longitudinal bioluminescence tracking of hMSCs as well as vascularization and bone regeneration analysis through μCT. Our results showed that neither integrin-specificity nor VEGF had an effect on hMSC viability, vascularization of the defect or bone regeneration.

A.2 Luciferase-expressing MSCs for in vivo tracking

HMSCs were transduced to constitutively express a tdtomato / red firefly luciferase construct for purposes of *in vivo* tracking within the critical-size defect model. Transduction efficiency of hMSCs was tested assessing tdtomato+ cells via flow cytometry

(data not shown). The linearity of bioluminescent signal against cell number was tested by seeding the transduced hMSCs into 24 well plates at differing concentrations (Fig. 24). Saturating concentrations of luciferin were added to the media and bioluminescent signal was acquired by IVIS Spectrum CT. Bioluminescent signal was then plotted against cell number and linear regression analysis performed. Linear regression analysis shows an R-squared value of 0.9917 indicating that bioluminescent signal correlates linearly with cell number.

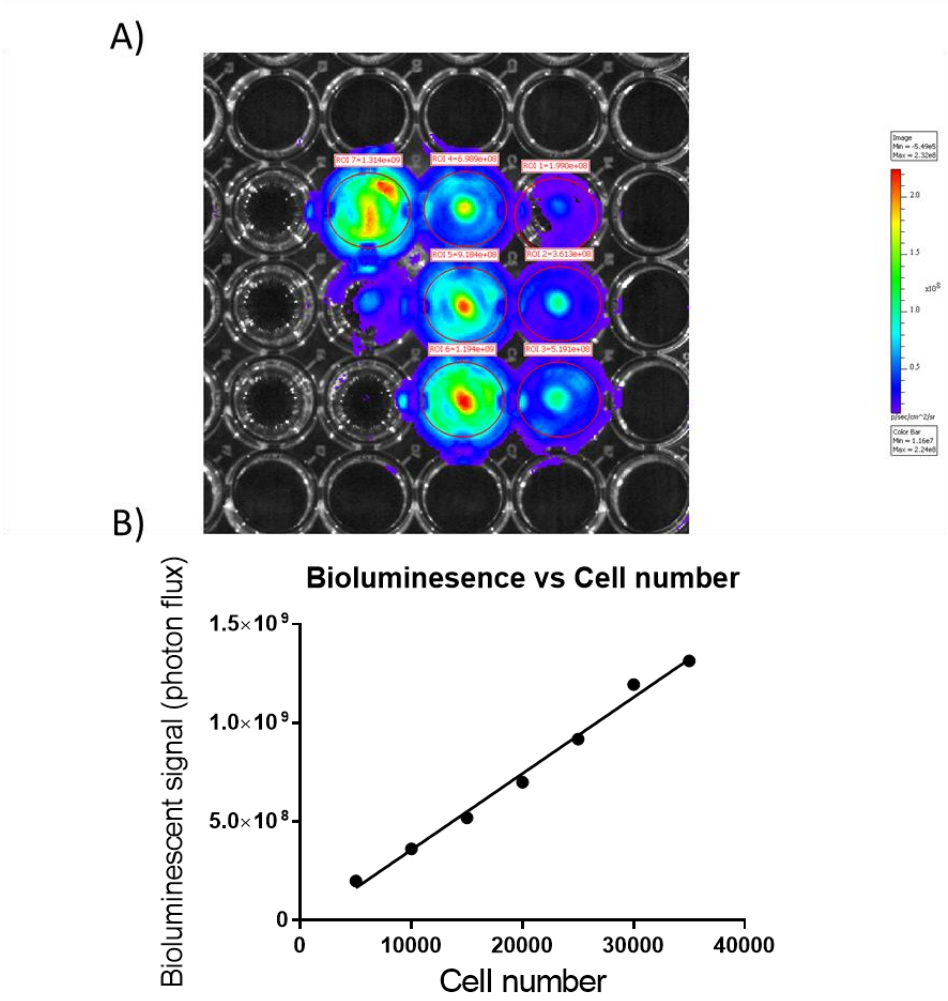

Figure A1: Bioluminescent signal against cell number. A) Different numbers of hMSCs expressing constitutive red firefly luciferase were seeded in a 24 well plate and saturated concentrations of luciferin added to each well. B) Quantification of bioluminescent signal vs cell number with linear regression analysis. R-squared value of the linear regression equals 0.9917

A.3 Longitudinal hMSC number within a critical-size defect are independent of hydrogel-based integrin-specificity and VEGF incorporation

Given that both integrin-specificity and VEGF had significant effects on vascularization and bone regeneration in acellular hydrogels, we were interested in understanding how integrin-specific hydrogels incorporating VEGF could enhance hMSC therapy. The first experiment we wanted to perform was that of hMSC survival with altering these two factors, integrin-specificity and VEGF incorporation. Following confirmation that bioluminescent signal correlates linearly with hMSC number, we encapsulated hMSCs within either GFOGER-functionalized or RGD-functionalized hydrogels with or without 50 ng VEGF. These hydrogels were then implanted within murine critical-size defects and bioluminescence tracking performed for 6 weeks post-implantation (Fig. 25). Quantification of bioluminescent flux showed no significant differences between GFOGER- or RGD-functionalized hydrogels at all time points tested. There was also no significant differences seen between hydrogels functionalized with or without VEGF. Notably, all groups showed a consistent trend where bioluminescent signal increased until 7 days post-implantation followed by a drop at 14 days to approximately 10% of implanted bioluminescence intensity. This low level of bioluminescence persisted until 6 weeks post-implantation.

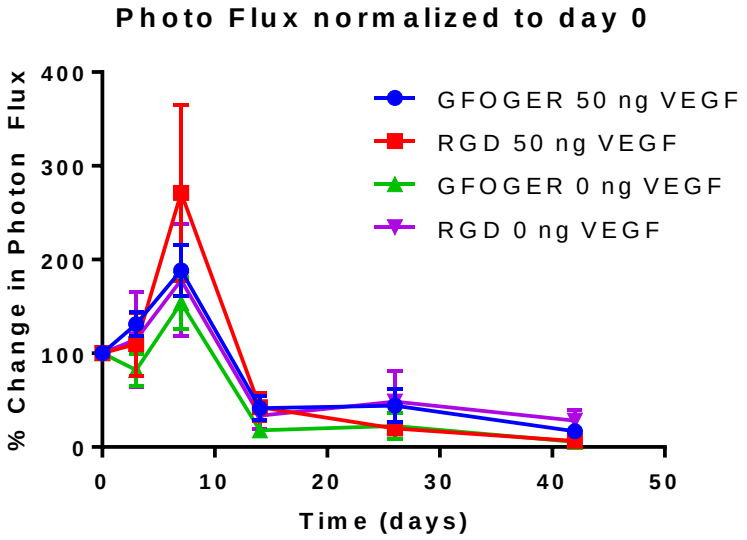

Figure A2: Longitudinal *in vivo* bioluminescent tracking of hMSCs. Bioluminescent signal quantified as photon flux normalized to day 0. N=8-9. Error bars ± SEM. One-way ANOVA

A.3 Vascularization of hMSC-encapsulated integrin-specific hydrogels functionalized with VEGF

While no differences were noted in cell number over 6 weeks post-implantation, hMSCs are known to impart effects at short time points as seen through our immunomodulation studies. Because of this, we wanted to see whether integrin-specificity or VEGF incorporation had an effect on vascularization in hMSC-encapsulated hydrogels. HMSCs were encapsulated in either GFOGER- or RGD- functionalized hydrogels and in hydrogels functionalized with or without 50 ng VEGF. The hydrogels were implanted

within critical-size bone defects and after 8 weeks post-implantation, mice were euthanized and blood vessels perfused with Microfil for μCT based imaging of blood vessels surrounding the defect area (Fig. 26). Four parameters for vascularization quantification were defined: vascular volume, vascular number, vascular thickness and vascular spacing. No differences were found in these four parameters between either GFOGER- or RGD-functionalized hydrogels or between hydrogels functionalized with or without 50 ng VEGF.

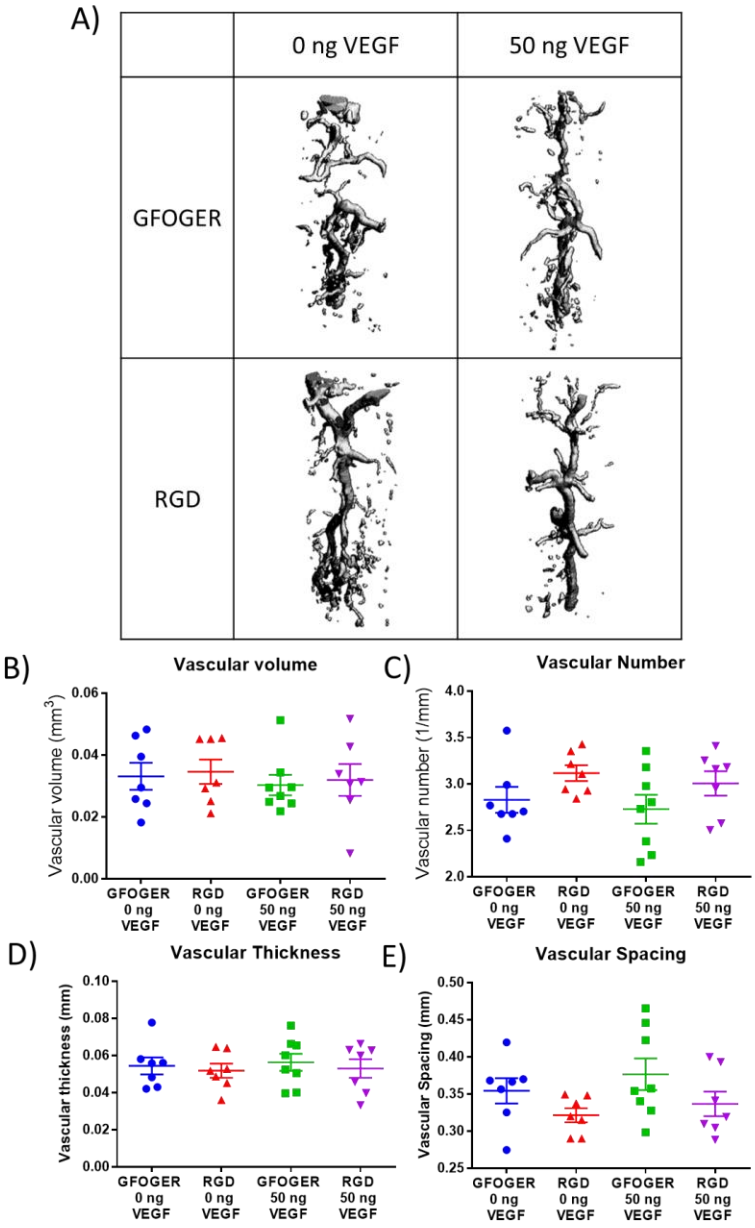

Figure A3: Vascularization of hMSC-encapsulated hydrogels is independent of integrin-specificity or VEGF incorporation. A) Representative images of vascularization of defects at 8 weeks post-implantation as assessed by Microfil µCT imaging. Quantification of (B)

vascular volume, (C) vascular number, (D) vascular thickness and (E) vascular spacing. N=6. Error bars ± SEM. One-way ANOVA

A.4 Bone regeneration of hMSC-encapsulated hydrogels is independent of integrin-specificity and VEGF functionalization

While no differences were noted for vascularization between hMSC-encapsulated GFOGER- and RGD-functionalized hydrogels or between VEGF incorporating or VEGF-free hydrogels, we wanted to see if any differences were present in bone regeneration. We conducted two different experiments to assess bone regeneration. The first experiment consisted of hMSCs encapsulated in either GFOGER- or RGD-presenting hydrogels functionalized with either 0 or 50 ng VEGF. For the second experiment, we wanted to increase our dose of VEGF to test whether a higher dose of VEGF would elicit a more pronounced response. We thus encapsulated hMSCs within either GFOGER- or RGD-presenting hydrogels functionalized with either 0, 50 or 250 ng VEGF. These hydrogels were then implanted within critical-size defects. At 4 and 8 weeks post-implantation, bone regeneration within the defect was assessed via μCT imaging. (Fig. 27). For both experiments, no significant differences were noted between GFOGER- or RGD-functionalized hydrogels at any dose of VEGF.

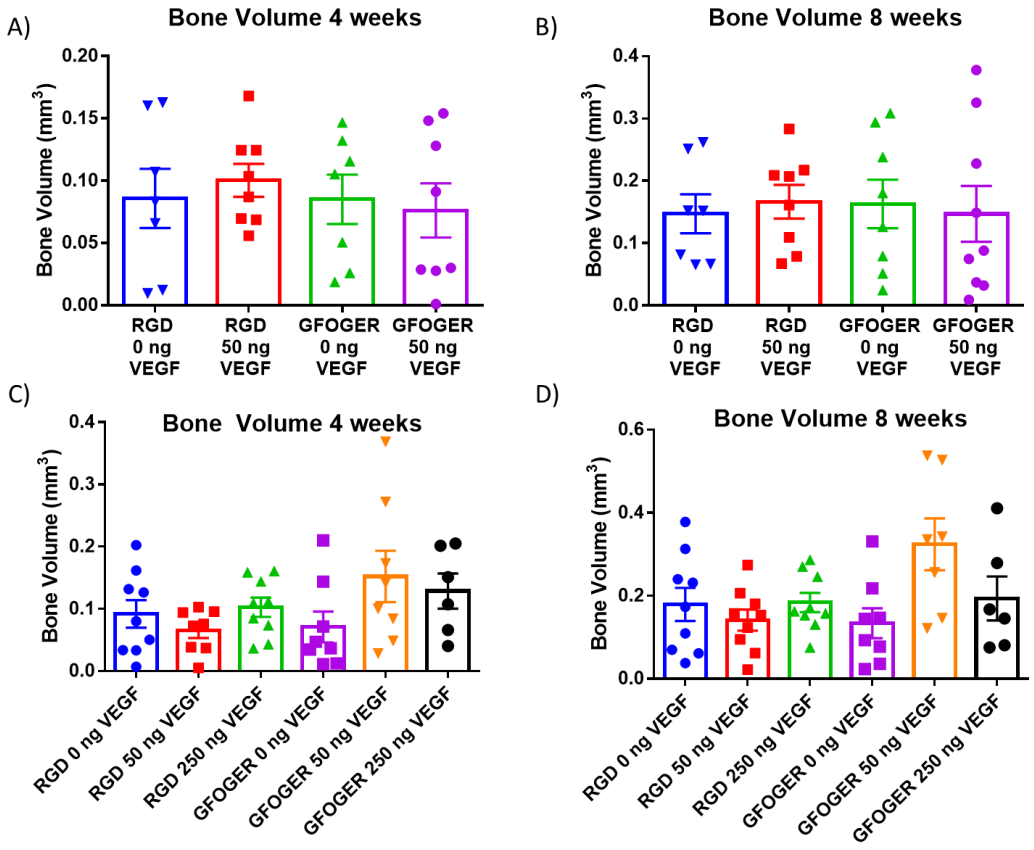

Figure A4: Bone regeneration in hMSC-encapsulated hydrogels is independent of integrin-specificity or VEGF incorporation. Quantification of bone regeneration within a murine critical-size defect for two independent experiments. Panels (A) and (B) represent bone volume quantification at 4 and 8 weeks respectively for one experiment and panels (C) and (D) represent bone volume quantification at 4 and 8 weeks respectively for a second independent experiment respectively. N=6-9 for both experiments. Error bars ± SEM. One-way ANOVA.

APPENDIX B: EFFECTS OF ADHESIVE PEPTIDE FOR IMMUNOMODULATION OF ENCAPSULATED HMSCS

B.1 Summary

In addition to understanding how integrin-specificity affected vascularization and bone regeneration within a murine bone defect, we also wanted to understand if the incorporation of ligands affect hMSC immunomodulatory properties. Previous literature, as discussed in Chapter 4, noted that hMSCs exhibit a potent anti-proliferative effect on activated T-cells, that this effect is cell dose-dependent and that the effect is modulated by soluble molecules. We thus chose to probe the notion that ligand can differentially modulate hMSC immunomodulation by investigating whether hMSCs encapsulated within either adhesive RGD or non-adhesive RDG functionalized hydrogels exhibited differential effects on activated T-cell proliferation. Our results showed that hMSCs encapsulated in either RGD or RDG hydrogels halted activated T-cell proliferation in a similar fashion indicating no effect of adhesive ligand. Furthermore, upon probing the hMSCs for immunomodulatory markers, similar levels of IDO and PD-L1 were found between hMSCs encapsulated in RGD or RDG hydrogels. Together, this data supports the notion that the presence of adhesive ligand has no effect on the immunomodulatory properties of hMSCs.

B.2 Hydrogel encapsulated hMSCs inhibit T-cell proliferation in a dose-dependent manner independently of the presence of an adhesive peptide on hydrogels

In addition to understanding how integrin-specificity affects bone regeneration, we were also interested in understanding how the adhesive property of a material affects the immunomodulatory property of hMSCs. To do this, we chose to focus on the ability of

hMSCs to inhibit activated T-cell proliferation. For the first experiment, we encapsulated different numbers of hMSCs within hydrogels functionalized with either the adhesive RGD ligand or the non-adhesive RDG ligand. The hMSC-encapsulated hydrogels were kept in culture for 3 days after which, they were placed in co-culture with purified and activated human CD4+ T-cells. The hMSCs were allowed to interact with the T-cells for 4 days after which the T-cells were collected and assessed for proliferation via EdU incorporation (Fig. 28). The ratio of hMSCs : T-cells had a significant effect on the proliferation of T-cells with higher numbers of hMSCs significantly decreasing T-cell proliferation (Fig. 28B). No differences however were seen in between hMSCs encapsulated in either adhesive or non-adhesive ligands at the same ratio of hMSC : T-cells even though, at the time of co-culture, the morphology of the cells in either adhesive or non-adhesive hydrogels were strikingly different (Fig. 28A). This finding shows that while hMSCs have a significant effect on T-cell proliferation, the presence of an adhesive ligand has no effect.

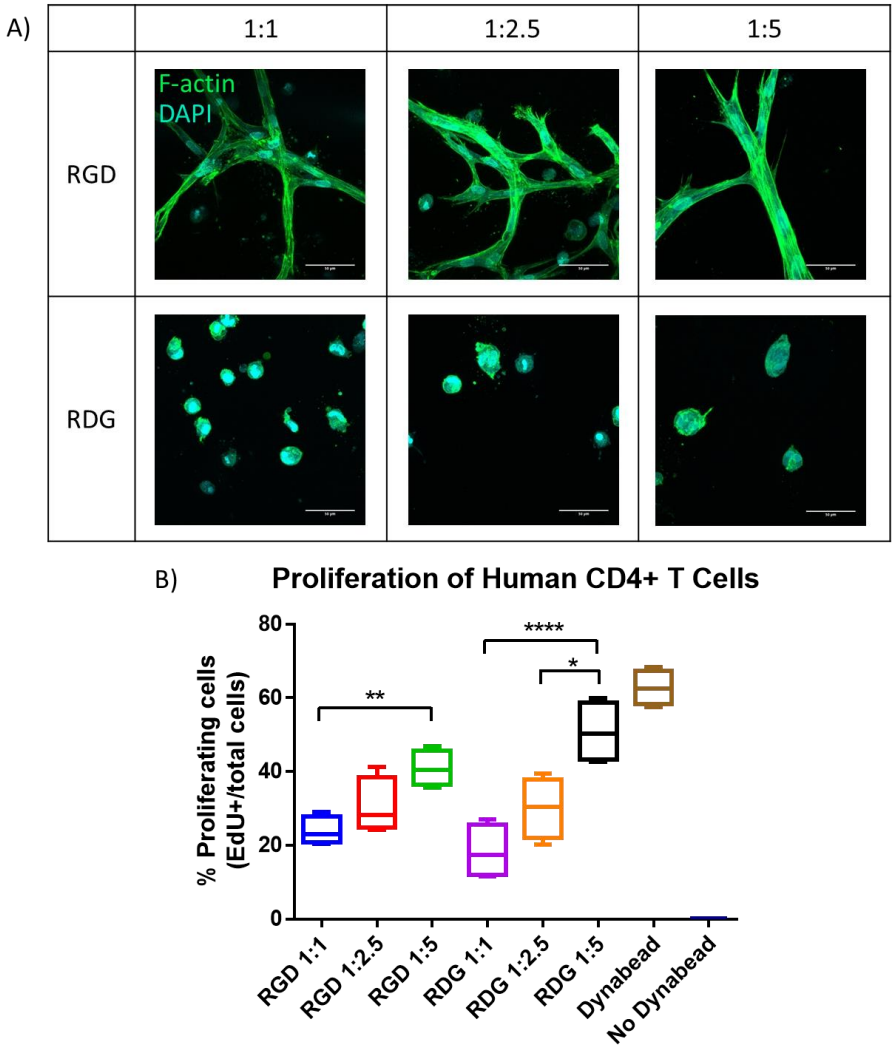

Figure B1: hMSC-based inhibition of T-cell proliferation is dose-dependent but independent of adhesive ligand. (A) Representative images of hMSCs within either RGD- or RDG-functionalized hydrogels at the time of initiation of T-cell co-culture. (B) Quantification of T-cell EdU indicating T-cell proliferation. N=3-4 separate wells with >100 T-cells analyzed per well. Error bars ± SEM. One-way ANOVA * $p<0.05$, ** $p<0.01$, **** $p<0.0001$

B.3 HMSC-based inhibition on T-cell proliferation is dependent on the presence of IFN-γ in the co-culture but remains independent of adhesive ligand.

We wanted to further investigate the cause of hMSC-based inhibition of T-cell proliferation. Previous literature and results shown previously indicates that hMSCs need to be licensed by IFN-γ in order to exhibit immunomodulatory capabilities. Furthermore, we hypothesized that we did not previously see an effect of adhesive ligand on T-cell proliferation due to IFN-γ exhibiting a saturating effect. We thus conducted an experiment where fixed number of hMSCs were encapsulated within either RGD- or RGD-functionalized hydrogels, cultured for 3 days and then placed in co-culture with purified and activated CD4+ T-cells. Additionally, IFN-γ neutralizing antibody was added to the cultures to a final concentration of 100, 10 or 1 μg/mL (The ND50 for the antibody is ~30 μg/mL). After 4 days, T-cells were collected and proliferation assessed via EdU incorporation (Fig. 29). IFN-γ neutralizing antibody at a concentration of 100 μg/mL resulted in a significant increase in T-cell proliferation in conditions in which hMSCs were encapsulated in either RGD- or RDG-functionalized hydrogels compared to conditions of IFN-γ neutralizing antibody at concentrations of 10, and 1 μg/mL. Importantly, for each dose of IFN-γ neutralizing antibody, there were no differences in T-cell proliferation for hMSCs encapsulated in either RGD- or RDG-functionalized hydrogels.

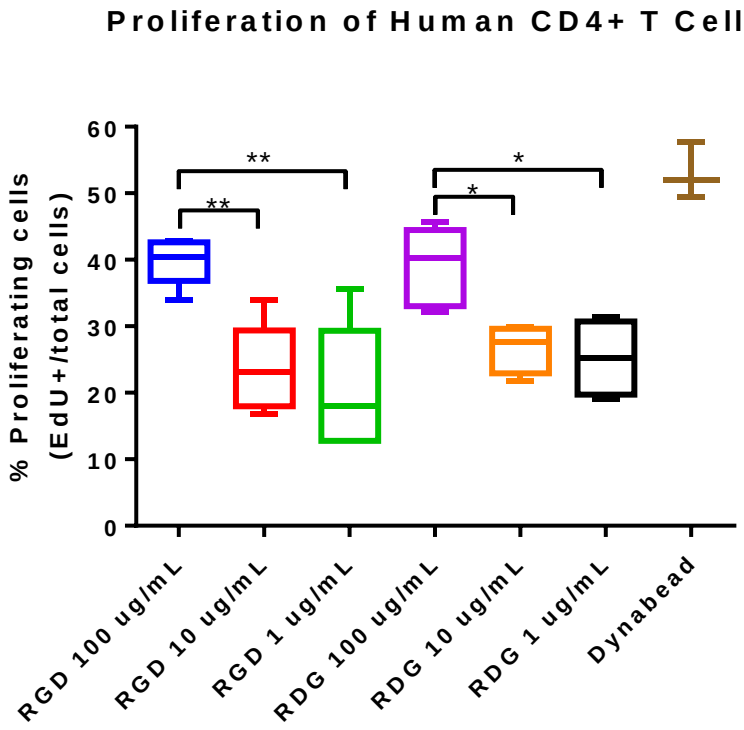

Figure B2: hMSC-based inhibition of T-cell proliferation is significantly affected by IFN-γ but independent of adhesive ligand. HMSCs encapsulated in either RGD- or RDG-hydrogels were incubated with activated T-cells for 4 days in the presence of differing concentrations of IFN-γ neutralizing antibody. (A) Quantification of T-cell proliferation as assessed by EdU. N=3-5 separate wells with >100 T-cells analyzed per well. Error bars ± SEM. One-way ANOVA * $p<0.05$, ** $p<0.01$

B.4 IDO and PD-L1 expression in hMSCs encapsulated in adhesive or non-adhesive hydrogels is dependent on the presence of T-cells but independent of the adhesive property of the hydrogel

Noting that hMSCs in either RGD- or RDG-functionalized hydrogels with differing concentrations of IFN-γ neutralizing antibody still showed no effect of adhesive or non-adhesive ligand on T-cell proliferation, we wanted to remove the step of measuring T-cell activity to focus on whether any effect of adhesive ligand can be there. The rationale of this being that if a difference is imparted on the encapsulated hMSCs, it is possible that because we are measuring T-cell activity, the measurement is too far from the effect that it is not accurately measured. Thus, to directly measure the activity of the hMSCs, we chose to stain for expression markers IDO and PD-L1 as these two proteins have been implicated in the immunomodulatory ability of hMSCs both in previous literature. In addition to the testing whether the adhesive property of the hydrogel affected hMSC IDO and PD-L1 expression, we also wanted to test whether PEG weight percent had an effect. hMSCs were thus encapsulated in either RGD or RDG-functionalized and in either 6% or 12% PEG weight percent hydrogels and then either co-cultured with purified and activated CD4+ T-cells or cultured without T-cells. After 4 days, hydrogels were degraded, hMSCs extracted and stained for IDO and PD-L1 followed by assessment by flow cytometric analysis (Fig. 30). IDO and PD-L1 were significantly upregulated in hMSCs encapsulated within hydrogels at equal PEG weight percent and co-cultured with T-cells compared to those not cultured with T-cells. Additionally, IDO and PD-L1 were significantly upregulated in

hMSCs encapsulated in 6% PEG weight percent hydrogels in co-culture with T-cells compared to hMSCs encapsulated in 12% PEG weight percent hydrogels in co-culture with T-cells. Importantly, among equal PEG weight percent and T-cell condition, there were no significant differences between hMSCs in adhesive hydrogels or non-adhesive hydrogels. This further supports the conclusion that hMSC-based immunomodulation is not based on the presence of adhesive ligand.

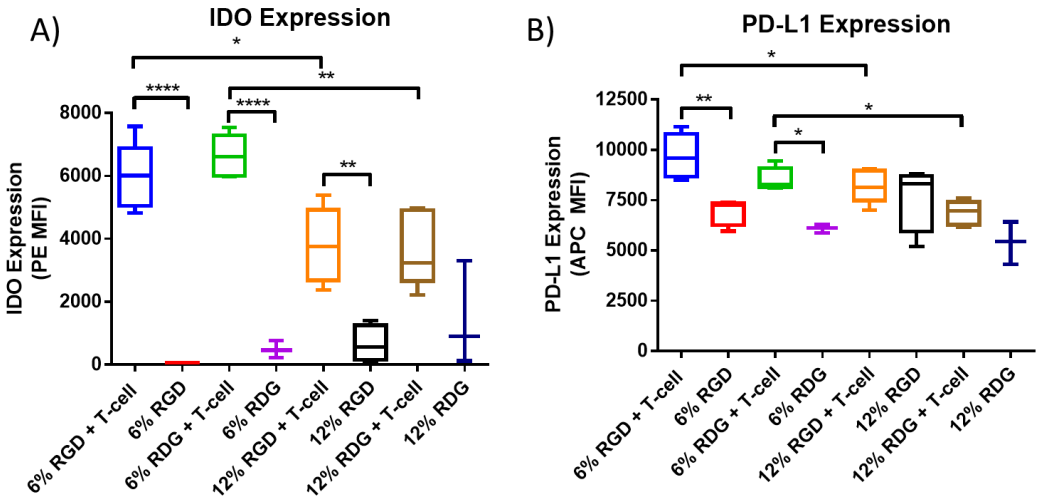

Figure B3: IDO and PD-L1 expression on hMSCs is dependent on T-cell co-culture and PEG weight percent but not hydrogel adhesive property. HMSCs were encapsulated in either 6% or 12% PEG weight percent hydrogels with either RGD- or RDG-functionalized onto the hydrogel. Hydrogels were then either incubated with activated T-cells or with no T-cells. After 4 days, hydrogels were degraded and hMSCs stained for IDO and PD-L1 followed by flow cytometric analysis. Quantification of median fluorescence intensity for

(A) IDO and (B) PD-L1. N=3-4 separate hydrogels with 5000 hMSCs analyzed per hydrogel. Error bars ± SEM One-way ANOVA * *p<0.05, ** p<0.01, **** p<0.0001*

APPENDIX C: CYS-IFN-Γ HYDROGELS FOR USE IN COLONIC WOUNDS

C.1 HMSCs encapsulated within tethered IFN-γ hydrogels exhibit significantly more healing than IFN-γ hydrogels without hMSCs in a colonic wound model

An initial pilot study was performed to ascertain the feasibility of the implanting hMSC-laden hydrogels in mouse colonic wounds. This study also determined whether cys-IFN-γ hydrogels without hMSCs would have an effect compared to cys-IFN-γ hydrogels with encapsulated hMSCs. This animal experiment was performed with the approval of the University of Michigan Animal Care and Use Committee within the guidelines of the Guide for the Care and Use of Laboratory Animals and in accordance with the US Department of Agriculture (USDA) Animal and Plant Health Inspection Service (APHIS) regulations and the National Institutes of Health (NIH) Office of Laboratory Animal Welfare (OLAW) regulations governing the use of vertebrate animals. Colonic wounds were induced in a method similar to previously published protocols [289]. Briefly, male (8 weeks old) C57-Black6 mice (Jackson Laboratory) were anaesthetized by intraperitoneal injection of a ketamine (100 mg/kg)/xylazine (10mg/kg) solution. A high-resolution miniaturized colonoscope system equipped with biopsy forceps (Coloview Veterinary Endoscope, Karl Stortz) was used to biopsy-injure the colonic mucosa at 5 sites along the dorsal artery. Wound size averaged approximately 1 mm^2. 50 µL hydrogel injections were performed 1 day following wounding with the aid of a custom-made device comprising a 29-gauge needle connected to a small tube. Endoscopic procedures were viewed with high-resolution (1,024 x 768 pixels) live video on a flat-panel color monitor. Each wound region

was digitally photographed at day 1 and day 5 and resulting wound images for which the wound area was calculated by a blinded observer using ImageJ.

Results from day 5 quantification of colonic wound closure show a significant increase in the wound closure for mice treated with cys-IFN-γ hydrogels with encapsulated hMSCs compared to those treated with cys-IFN-γ hydrogels without hMSCs and control animals that were injected with saline (Fig. C1).

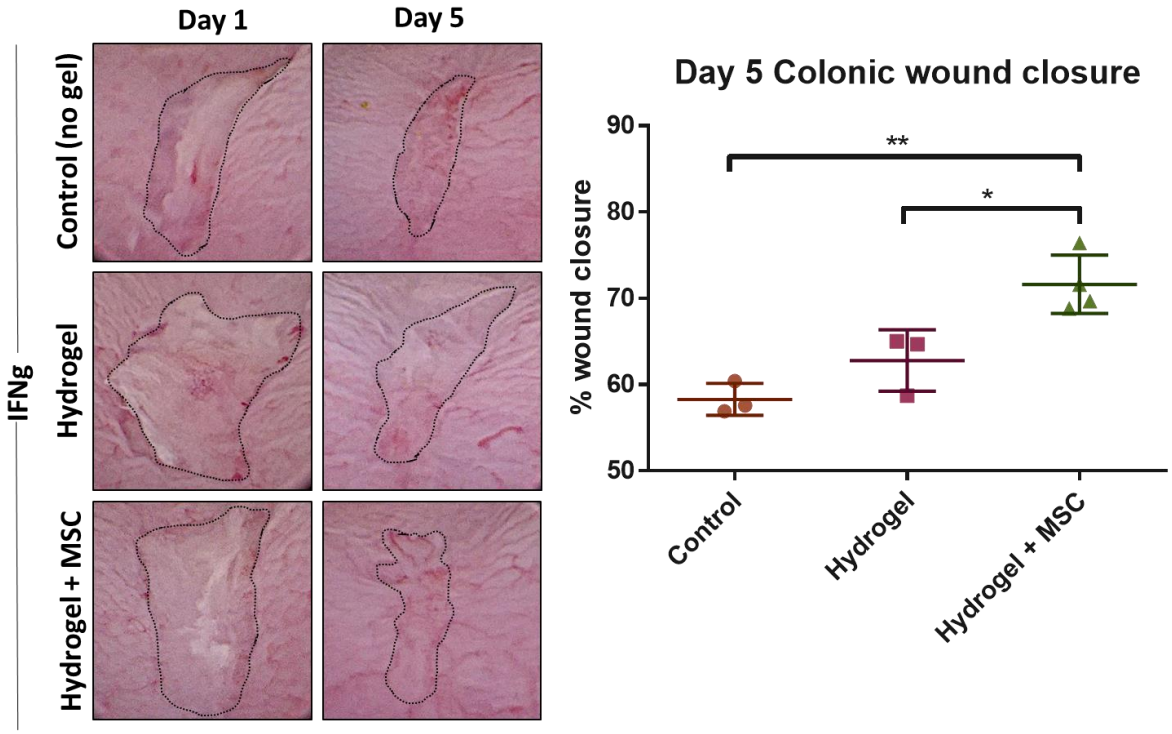

Figure C1: Representative images and quantification of colonic wound closure at 5 days post injury. Dashed lines indicate wound area. Error bars ± SEM. Nested ANOVA analysis

with N=3 wounds per mouse and each point indicating the average of one mouse. N=3-4 mice. * $p<0.05$, ** $p<0.01$.

APPENDIX D: PUBLICATIONS

A minimally invasive, translational method to deliver hydrogels to the heart through the pericardial space. **JACC: Basic to Translational Science**

JACC: BASIC TO TRANSLATIONAL SCIENCE
VOL. 2, NO. 5, 2017

ISSN 2452-302X
http://dx.doi.org/10.1016/j.jacbts.2017.06.003

NOVEL TRANSLATIONAL METHODS

A Minimally Invasive, Translational Method to Deliver Hydrogels to the Heart Through the Pericardial Space

Jose R. Garcia, MS,[a] Peter F. Campbell, MD,[b] Gautam Kumar, MBBS,[c,d] Jonathan J. Langberg, MD,[c] Liliana Cesar, DVM,[e] Lanfang Wang, MS,[c] Andrés J. García, PhD,[a] Rebecca D. Levit, MD[c]

VISUAL ABSTRACT

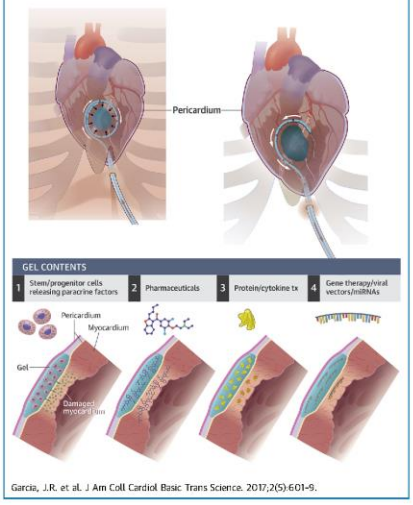

Garcia, J.R. et al. J Am Coll Cardiol Basic Trans Science. 2017;2(5):601-9.

HIGHLIGHTS

- The pericardial space is an unexploited anatomic location for hydrogel delivery.
- Hydrogels can be delivered to the pericardial space in a localized, minimally invasive manner, without detectable hemodynamic effects.
- Pericardial hydrogel delivery is a new strategy to direct therapeutics to the heart with reduced systemic delivery and off-target effects.

From the [a]Woodruff School of Mechanical Engineering, Petit Institute for Bioengineering and Bioscience, Georgia Institute of Technology, Atlanta, Georgia; [b]Innovatiê LifeSciences, Santa Clara, California; [c]Division of Cardiology, Department of Medicine, Emory University School of Medicine, Atlanta, Georgia; [d]Division of Cardiology, Atlanta VA Medical Center, Atlanta, Georgia; and [e]T3 Labs-Translational, Testing and Training Laboratories, Inc., Atlanta, Georgia. Dr. Campbell and Dr. Levit are listed as inventors on a patent application filed by Emory University on technology related to the delivery device. Dr. Levit is a principal in a startup company, CorAmi LLC, which seeks to commercialize this technology but as of yet has no investment, revenue, or intellectual property. Funded by Coulter Translational Research Partnership, Georgia Research Alliance. All authors have reported that they have no relationships relevant to the contents of this paper to disclose.
All authors attest they are in compliance with human studies committees and animal welfare regulations of the authors' institutions and Food and Drug Administration guidelines, including patient consent where appropriate. For more information, visit the *JACC: Basic to Translational Science* author instructions page.

Manuscript received April 5, 2017; revised manuscript received May 21, 2017, accepted June 1, 2017.

JACC: BASIC TO TRANSLATIONAL SCIENCE VOL. 2, NO. 5, 2017
OCTOBER 2017:601–9

ABBREVIATIONS AND ACRONYMS

CVD = cardiovascular disease

miRNA = micro-ribonucleic acid

PEG = polyethylene glycol

SUMMARY

Biomaterials are a new treatment strategy for cardiovascular diseases but are difficult to deliver to the heart in a safe, precise, and translatable way. We developed a method to deliver hydrogels to the epicardium through the pericardial space. Our device creates a temporary compartment for hydrogel delivery and gelation using anatomic structures. The method minimizes risk to patients from embolization, thrombotic occlusion, and arrhythmia. In pigs there were no clinically relevant acute or subacute adverse effects from pericardial hydrogel delivery, making this a translatable strategy to deliver biomaterials to the heart. (J Am Coll Cardiol Basic Trans Science 2017;2:601–9)

Despite pharmacological and technologic advances, cardiovascular diseases (CVD) remain the leading cause of morbidity and mortality in the United States, costing $215.6 billion per year (1). More patients are surviving, but with heart failure, arrhythmias, and poor quality of life. Micro-ribonucleic acid (miRNA), gene therapy, stem cells, cytokines, and other biologics are new treatments that have shown promise in preclinical and early phase clinical trials (2–4). Many of these therapies require focused delivery of the therapeutic to the heart, or even localization to particular anatomic areas, such as the peri-infarction region. Dilution of these therapeutics by systemic administration increases cost and risks off-target effects. For example, poor retention of stem cells in the heart is thought to limit efficacy in clinical trials (5–7). The proangiogenic cytokine vascular endothelial growth factor encourages neoangiogenesis and cardiac regeneration (8) but can also accelerate tumor metastasis (9). Efficient, targeted, and temporally appropriate delivery of therapeutics to the heart are keys to their successful translation into clinical use.

SEE PAGE 610

Early phase clinical trials are underway using hydrogels as therapeutic agents for cardiac repair (10–12). Both solid patches and injectable gel materials are under investigation and may have benefits for different applications. Cardiac patches and solid materials have been tested as structural support for the heart in a clinical trial (13) and therapeutic delivery platforms in numerous preclinical studies (14). Their widespread use is limited by the need for surgical placement. Injectable materials with liquid or gel phases, such as decellularized matrix, alginate, and engineered hydrogels, can provide scaffolds, tactile signals, and structural support for cardiac regeneration and repair (10,11,15,16). Biomaterial gels are particularly suited to deliver stem cells to the heart and retain viable cells at the site of delivery (12,17). Other materials are in preclinical trial for delivery and sustained release of miRNAs, cytokines, and other therapeutics (4,18,19). Whereas biocompatible materials may be beneficial for the treatment of CVD, there are no dedicated delivery methods that are safe and minimally invasive.

There are challenges inherent to delivering biomaterials to the heart. Open heart surgery, although feasible, is less desirable from a cost and patient perspective. Catheter delivery using commercially available single-lumen coronary catheters or Noga XP Cardiac Navigation System (Biosense Webster, Diegem, Belgium) cannot keep material components separate as they travel to the heart and thus cannot control the timing of material interaction and gelation. Premature gelation causes clogging within catheter lumen. Delayed gelation can lead to embolization, stroke, and failure to deliver material to targeted area. Another challenge with biomaterial delivery to the heart is the potential for inducing arrhythmias if the electrical conductivity of the material creates a substrate for a re-entrant circuits as it interdigitates between cardiomyocytes. Therefore the development of material-specific strategies is necessary for the safe, precise, and practical delivery of biomaterial to the heart.

The pericardium is a novel site for therapeutic delivery that has been shown in animal studies to act as a reservoir for drug delivery to the heart (20–22). The advent of epicardial ablations and external left atrial appendage ligation has demonstrated the feasibility of accessing a “dry” pericardial space for therapeutic purposes (23–25). Herein we describe a minimally invasive device to deliver biomaterials to the heart by using the pericardial space as a novel anatomic site for biomaterial delivery. Our device uses the existing anatomic structures to form a temporary compartment for gel delivery. Features of the device eliminate the risk of premature gelation and embolization and allow

precise placement of biomaterial over the area of interest. Pericardial hydrogel delivery with our device circumvents many of the obstacles to vascular or intracardiac delivery, facilitating rapid translation of biomaterial gels into clinical use.

METHODS

DEVICE DESIGN. We built a device to deliver biomaterial hydrogels to the heart through the pericardial space in a large animal model (pig). The hydrogel delivery device is constructed from varying durometers of polyether block amid (PEBAX) (Temecula Custom Extrusions, Temecula, California) biocompatible polymeric resin, using custom multilumen tooling, extrusion, and fusing processes. Two internal lumens for biomaterials keep components separated throughout the length of the device. The core is comprised of a super-elastic shape-memory nickel titanium alloy (nitinol) that facilitates fence deployment and retraction. Suction and gel ports were cut in the desired location using precision skiving. The sheath is comprised of a laminated composite shaft with an imbedded coil. Key locations of the device and sheath (distal tip, fence apparatus) are fitted with radiopaque markers to enable visualization with fluoroscopy. The device is constructed in a cleanroom and sterilized using ethylene oxide before survival procedures.

HYDROGEL GEL DESIGN AND DELIVERY. Polyethylene glycol (PEG) hydrogels were based on 4-arm PEG macromer (20 kDa, Laysan Bio, Arab, Alabama) with maleimides at each terminus cross-linked with dithiothreitol. This platform provides structurally defined hydrogels with stoichiometric incorporation of ligands and improved cross-linking efficiency (18). Hydrogel components (macromer, cross-linker) were delivered into the pericardial space in cadaver and live pigs (n = 9) using the delivery device. The hydrogel components and cross-linker were delivered through separate lumens into the fenced area in the pericardial space for in situ mixing and cross-linking. Hydrogel components were adjusted to yield a 5-ml, 4.0% wt/vol PEG hydrogel. For nonsurvival studies, gel was labeled with radiopaque contrast agent iohexol (Omnipaque, GE Healthcare, Princeton, New Jersey) and in others trypan blue (Sigma, St. Louis, Missouri).

LARGE ANIMAL MODEL. Farm pigs (n = 9; 45 to 55 kg) were obtained from a commercial supplier and raised on swine feed. On the procedure day, animals were sedated with intramuscular telazol (4.4 mg/kg) and xylazine (0.5 mg/kg) and maintained on inhaled isoflurane (2% to 4%). Animals were intubated, ventilated, and continuously monitored. We accessed the pericardial space through a fluoroscopically guided percutaneous subxiphoid approach using 12-cm 21-gauge micropuncture needle. Intrapericardial location was confirmed by contrast injection and wire confinement to the outer cardiac silhouette. Arterial and venous pressures were monitored using a Swan-Ganz and pigtail catheter, respectively, connected to a MacLab Hemodynamic Recording System (GE Healthcare).

A flexible 10-F catheter sheath was placed into the pericardial space. The hydrogel delivery device was positioned over the desired anatomic area of the heart and temporarily secured in place by negative suction. PEG macromere and dithiothreitol (cross-linker) were delivered through two distinct lumens and combined within the fenced region. After allowing 5 min for gelation, the fence was retracted from around the hydrogel. Invasive hemodynamics were measured before pericardial instrumentation, immediately after hydrogel delivery device removal, and at time of sacrifice 4 to 6 weeks later. Animals received intrapericardial methylprednisolone, 1 mg/kg, and oral colchicine, 0.6 mg, by mouth twice daily.

STATISTICAL ANALYSIS. Statistical analysis of hemodynamic data from different time points was compared using repeated measures one-way analysis of variance using PRISM version 6 (GraphPad, San Diego, California). A priori power analysis was performed using G*Power version 3.0.10 (Dusseldorf, Germany) with the assumption of α 0.05, power 0.6, and an effect size calculated to 1.0.

RESULTS

HYDROGEL DELIVERY DEVICE DESIGN AND CONSTRUCTION. The feasibility and safety of pericardial access in the absence of pericardial effusion (i.e., dry tap) have been shown by other devices, such as the Lariat device (Sentre Heart, Redwood City, California) (23,24). In this study, we engineered a system consisting of a hydrogel biomaterial delivery device and sheath to access the pericardial space using standard micropuncture technique (**Figure 1**). Device features include a shape memory core, a deployable and retractable fence that creates the lateral wall of the temporary hydrogel compartment, two separated lumens for gel components, a suction mechanism to temporarily secure the device in place, electrical sensors, and an atraumatic tip (**Figure 1**).

As the delivery device is advanced out of the sheath, it forms a circular fence that physically isolates a 5-cm diameter area of epicardium (Supplemental Video 1). The device forms a lateral border, or fence, while the epicardium acts as a floor, and pericardium acts as a roof for the temporary gel compartment. Gentle suction further seals the

FIGURE 1 Hydrogel Delivery Device Creates a Temporary Compartment for Biomaterial Gel Delivery Within the Pericardial Space

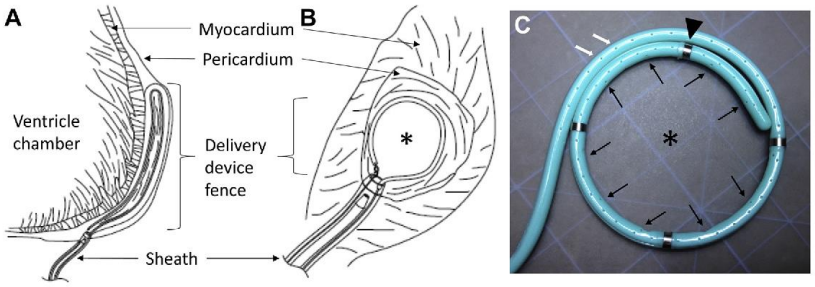

Schematic representation of lateral **(A)** and frontal view **(B)** of the device placed over the cardiac epicardium within the pericardial space. The device forms a lateral wall for the gel compartment, whereas the pericardium and epicardium act as a natural roof and floor, respectively **(A and B)**. Once in position, the device is secured in place by gentle suction ports **(C, white arrows)** to the epicardium as floor, and the pericardium as ceiling. Gel components are delivered through separate lumens and combined only after exiting the device **(B and C, asterisk)** through ports arrayed around fence **(C, black arrows)**. Electrical sensors **(C, arrowhead)** allow precise placement over areas of electrical abnormalities, such as infarcts. See Supplemental Video 1.

compartment and secures the device in place on the moving heart (Supplemental Video 1, **Figure 1**). Radiopaque markers allow precise placement over desired anatomic area using biplane fluoroscopy. Inside the device hydrogel components are kept within separate internal lumens until delivery through ports arrayed around the circular fenced area (**Figure 1C**). After gelation, the shape memory core allows retraction of the delivery device without disruption of hydrogel architecture (Supplemental Video 1).

VISUALIZATION OF HYDROGEL DELIVERY. Four-arm PEG maleimide macromer was cross-linked with dithiothreitol to form hydrogels (18). This hydrogel system is a flexible platform for therapeutic delivery of stem cells, growth factors, and pancreatic islets in various preclinical models (16,17,26). Bench studies showed that gelation occurred within 1 min after combining both components at physiological pH. We tested the delivery device in live pigs (n = 9). One animal was excluded from analysis because of infection unrelated to gel delivery. The delivery procedure was minimally invasive and conducted using standard cardiac catheterization laboratory equipment (Supplemental Figure 1). There were no acute complications with pericardial access, device placement in the pericardial space, or hydrogel deployment. All animals had successful hydrogel placement and solidification. No sustained arrhythmias occurred and there were only occasional premature ventricular contractions during the pericardial access procedure. Retraction of the device respected the hydrogel boundary and did not disrupt the hydrogel by visual inspection (Supplemental Video 1). Pericardial access and delivery procedure took approximately 35 min.

We visualized gelation within the temporary compartment created by the delivery device directly and using fluoroscopy with radiopaque gel (**Figures 2A and 2B**). Sixty minutes after gel delivery, heart was excised and a well-circumscribed trypan blue gel was present under the pericardium and localized to the inferoposterior wall (**Figure 2C**). There were no instances of premature gelation within the device in 12 live and cadaver studies. After 4 weeks hearts were excised and examined for gel. On 2 hearts areas of possible gel were observed but could not be confirmed with PEG-directed antibody.

HEMODYNAMIC ASSESSMENT OF EPICARDIAL HYDROGEL DELIVERY. Complications of pericardial access procedures can include tamponade or constriction causing hypotension, tachycardia, and elevated diastolic filling pressures (27). We measured acute and chronic changes in cardiac hemodynamics (4 to 6 weeks) after gel placement. There were no detectable changes in heart rate, blood pressure, right atrial pressure, wedge pressure, or left ventricular end diastolic pressure (**Figure 3**, Supplemental Table 1). Other hemodynamic features of pericardial construction, such as ventricular discordance, were not detected (**Figure 3C**). There was no periprocedural mortality. One animal was excluded from analysis because of infection unrelated to pericardial procedure but showed no hemodynamic abnormality.

FIGURE 2 Successful Hydrogel Delivery to the Pericardial Space Using the Hydrogel Delivery Device Visualized Directly and by Fluoroscopy

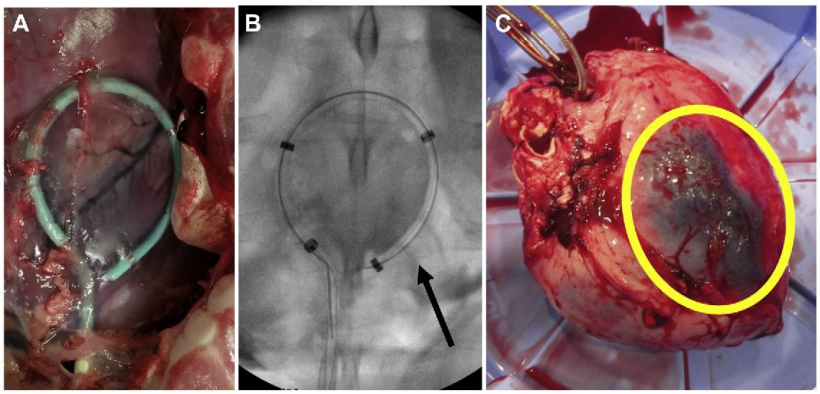

(A) The delivery device was successfully placed over the left anterior descending artery in a porcine cadaver. Sternum was removed to allow direct visualization. **(B)** Contrast-labeled hydrogel delivery by the device **(arrow)** was visualized in situ by fluoroscopy. **(C)** In a live animal, trypan blue–labeled gel was delivered with the device to the posterior wall and gelled within the temporary compartment created by the device, epicardium, and pericardium. Sixty minutes after device removal, the gel remained localized over delivery location.

INFLAMMATORY EFFECTS OF PERICARDIAL PROCEDURE AND GEL DELIVERY. Pericarditis is a well-known consequence of pericardial procedures and we evaluated animals for signs of systemic or local inflammation (23–25). We measured white blood cell count, differential, creatinine, and liver function tests, which remained normal in all animals (Supplemental Table 2). Total white blood cell count decreased in 6 of 8 animals (mean decrease by $2.1 \times 10^9 \pm 2.1$ cells/l) (Supplemental Table 2). Neutrophil and lymphocyte counts were also stable (Supplemental Table 2).

FIGURE 3 Invasive Hemodynamics Were Unchanged After Pericardial Gel Placement

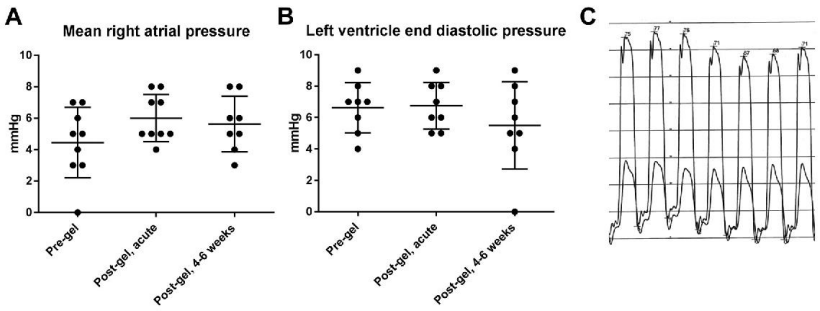

The right atrium is the lowest pressure cardiac chamber with the thinnest wall and most susceptible to compression from increased pericardial pressure. **(A and B)** Right atrial pressure and left ventricle end-diastolic pressure did not change in pigs in the immediate post-procedure period or after 4 to 6 weeks ($n = 8$; error bars ± SD). **(C)** Simultaneous left and right ventricle pressure showed no accentuated respiratory variation and no ventricular interdependence (paper speed 25 mm/s, representative image).

FIGURE 4 Histological Appearance of Pericardium and Myocardium 4 Weeks After Pericardial Instrumentation and Gel Delivery Suggest Mild Inflammatory Response

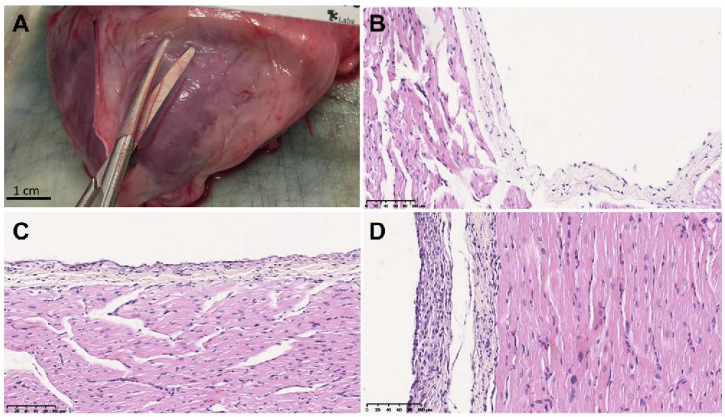

(A) On gross histologic examination, pericardium had normal thin and translucent appearance 4 weeks after hydrogel deliver. After formalin fixation and staining with hematoxylin and eosin (original magnification 10x), pericardium overlying the left atrium **(B)** and right ventricle **(C)** showed normal histologic appearance. **(D)** In some animals a small 1-cm^2 area of thickening and increased cellularity was seen at the site of pericardial puncture involving the visceral pericardium.

On gross examination, pericardium was thin and translucent 4 to 6 weeks after hydrogel delivery (Figure 4A). Cardiac samples from each chamber were preserved in formalin and stained with hematoxylin and eosin (Figures 4B to 4D). Histologic evaluation showed mostly normal pericardial thickness and cellularity (Figures 4B and 4C). In some animals, in a localized area close to the site of pericardial access near the left ventricular apex, pericardial thickening was observed (Figure 4C). Mononuclear cellular infiltration of the parietal pericardium in this area suggests an inflammatory response or fibroblast proliferation at the sight of pericardial puncture. No abnormalities were seen in the myocardial architecture.

DISCUSSION

Biocompatible materials are an emerging category of therapeutics to treat CVD. They come in a variety of physical forms (solid, gels) and can be designed to act alone or as carriers for other therapeutics, such as stem cells, miRNAs, and cytokines. The hydrogel used in this study has been shown to improve cardiac function by increasing retention of transplanted mesenchymal stem cells in the heart in small animal studies (17). Although this material does not directly incorporate into the myocardium, other materials nearing or in phase 1 clinical trials work by other mechanisms of action (10–12,15,19). To date, these materials are delivered by techniques or procedures designed for other purposes, such as intracoronary catheters, Noga XP Cardiac Navigation System (Biosense Webster), and open heart surgery. Biomaterial delivery using these techniques may increase the risk of complications, such as arrhythmia, coronary thrombosis, and embolic events, and device failure, such as catheter occlusion. Applying materials to the heart at the time of open heart surgery is feasible but expensive and invasive. There is an unmet need for safe and precise minimally invasive delivery methods for patients not undergoing surgical procedures.

Biomaterial delivery to the pericardial space has several potential advantages over traditional intracoronary, intramyocardial, and intravenous delivery. First, the pericardium is not a vascular space, eliminating the risk of embolization, stroke, and infarction. Second, therapeutics delivered to this space remain focused and concentrated onto the heart by the pericardium, limiting off-target delivery (21,22). Third, pericardial delivery allows a more liberal gelation time because gel components are not subjected to immediate vascular washout. Fourth, biomaterials may degrade slower in the pericardial

space because of lower mechanical forces and reduced access of the immune system. Finally, arrhythmias may be less likely compared with intramyocardial delivery because the electrical conduction and coordination between cardiomyocytes is not disrupted by the material.

With these considerations in mind, we have demonstrated the feasibility and safety of our epicardial hydrogel delivery device using an example of a clinically translatable hydrogel. The delivery device created a temporary compartment within the pericardial space for biomaterial gel delivery that can be positioned using standard cardiac catheterization laboratory fluoroscopy. This allows localization of gel over an anatomic area of interest, such as an infarction. The compartment also allows for complete separation of gel components within the device. The compartment is stable over many minutes securing the timeframe needed for materials to gel. We had no device malfunction because of premature gelation or clogging. Our simple but effective suction mechanism used existing anatomic structures to stabilize the device in vivo while the heart is moving, and to seal the compartment for gelation. Thus this device can be used with other hydrogels not compatible with vascular delivery because of their extended gelation times, or thrombotic or embolic risk.

We have shown a lack of significant hemodynamic and inflammatory effects of pericardial gel delivery. Triggering inflammation in the pericardium is of especially great concern because this area is prone to refractory symptoms and chronic pathologic consequences. Inflammation of the pericardium can cause hemodynamically significant pericardial effusions or thickening and fibrosis of the pericardium leading to cardiac constriction. We undertook careful histologic and hemodynamic studies to assess for these changes. In our study invasive measurements of intracardiac pressures showed stable filling pressures over 4 to 6 weeks. This suggests that pericardial biomaterial delivery will not have negative hemodynamic effects. Histology did show some inflammation localized to the parietal pericardium overlying the pericardial puncture site, whereas the white blood cell count and differential remained stable (Supplemental Table 2). The increased cellularity was localized to a 1-cm^2 area that was the site of pericardial puncture and was likely the result of the puncture injury and healing. Other areas of the pericardium and the myocardium appeared normal.

STUDY LIMITATIONS. For other pericardial procedures, such as the Lariat device, prophylactic anti-inflammatory medications, such as colchicine, are commonly used. Although reported incidence of pericarditis is low, most patients are prophylactically treated with anti-inflammatory agents, specifically colchicine (28). In one study of the Lariat device, the reported incidence of pericarditis was 5% but 54% of patients were treated with colchicine (23,28). In the current study, we chose to treat our animals with colchicine based on a preliminary study that showed significant pericardial inflammation when anti-inflammatory agents were not used. Colchicine was selected over systemic steroids because of its efficacy at treating pleuritis and lack of significant side effects compared with steroids or other nonsteroidal anti-inflammatory agents. Future studies are needed to confirm the long-term safety of pericardial biomaterials.

There are other concerns specific to accessing and working within the pericardial space. Our technique is unable to form the delivery compartment in patients without a pericardium (post-surgical or congenitally absent). Large pericardial effusions could potentially be drained before biomaterial delivery, but the safety and device functionality would need to be investigated. The risks of this technique in the acute myocardial infarction period may be elevated because of ischemia-reperfusion-induced inflammation of the pericardium and myocardium. Despite these potential concerns, the safety of pericardial access has been demonstrated by the development of epicardial ablations, the Lariat device, and other procedures. Interventionalists and electrophysiologists have gained experience in this technique (23–25). Alternatives to percutaneous routs of pericardial access, such as right atrial exit, are under clinical investigation and may be safer in some patients (29). We had no difficulties with percutaneous pericardial access and no instances of myocardial puncture or coronary artery damage.

Many biomaterials close to translation for clinical use have a liquid or gel phase and could be delivered using our device. However there are some biomaterials in development, such as cell sheets and patches, which do not and would not be amenable to our delivery by our method. Our device is also not capable of delivering ultra violet light as required for gelation for some biomaterials, but could be modified to do so. Lastly, most materials have only been tested by intramyocardial or intracoronary injection, through which they are instilled into the myocardium. They may not be as effective if delivered to the epicardium. Although it is unlikely a single technique could accommodate all biomaterials for cardiac

application, we believe our technique and device are applicable to many biomaterials. We also wish to advocate for early consideration of the technique for material delivery to facilitate rapid and safe translation of biomaterials into clinical use.

CONCLUSIONS

We have developed a novel method for delivering biomaterial gels to the heart through the pericardial space. Our platform can be used with many types of gels and is a new treatment strategy for CVD that may be particularly useful for emerging therapeutics, such as cytokines, miRNAs, and stem cells. Our minimally invasive epicardial hydrogel delivery technique takes advantage of the proximity of the pericardial space to the heart, and its relatively protected status. Minimally invasive, precise, and safe delivery techniques help facilitate translation of biomaterials into clinical use for CVD.

ADDRESS FOR CORRESPONDENCE: Dr. Rebecca D. Levit, Division of Cardiology, Department of Medicine, Emory University School of Medicine, 101 Woodruff Circle, Woodruff Memorial Building, Room 319, Atlanta, Georgia 30322. E-mail: rlevit@emory.edu.

PERSPECTIVES

COMPETENCY IN MEDICAL KNOWLEDGE: Many new technologies, such as stem cells, nucleic acid–based therapies (microRNA, viruses), and biocompatible materials, are under investigation as new treatments for cardiac disease. However, these therapeutics may not be safely delivered to the heart by traditional means. Intracoronary or intramyocardial administration resulted in poor retention of viable stem cells in the heart. Intravascular delivery of biomaterials could cause thrombosis or embolic events.

TRANSLATIONAL OUTLOOK: The technique described here uses the pericardial space as a novel site for therapeutic administration. The technique can be adapted to many types of biomaterials with embedded therapeutics and can serve to focus and localize them over anatomic areas of interest, such as the peri-infarct zone. Early consideration of the mode of administration may improve safety, efficacy, and the speed of translation of new therapeutics into clinical use.

REFERENCES

1. Mozaffarian D, Benjamin EJ, Go AS, et al. Heart disease and stroke statistics—2015 update: a report from the American Heart Association. Circulation 2015;131:e29–322.

2. Kamps JA, Krenning G. Micromanaging cardiac regeneration: targeted delivery of microRNAs for cardiac repair and regeneration. World J Cardiol 2016;8:163–79.

3. Nagai T, Komuro I. Gene and cytokine therapy for heart failure: molecular mechanisms in the improvement of cardiac function. Am J Physiol Heart Circ Physiol 2012;303:H501–12.

4. Peng B, Chen Y, Leong KW. MicroRNA delivery for regenerative medicine. Adv Drug Deliv Rev 2015;88:108–22.

5. Goussetis E, Manginas A, Koutelou M, et al. Intracoronary infusion of CD133+ and CD133 CD34+ selected autologous bone marrow progenitor cells in patients with chronic ischemic cardiomyopathy: cell isolation, adherence to the infarcted area, and body distribution. Stem Cells 2006;24:2279–83.

6. Teng CJ, Luo J, Chiu RCJ, Shum-Tim D. Massive mechanical loss of microspheres with direct intramyocardial injection in the beating heart: implications for cellular cardiomyoplasty. J Thorac Cardiovasc Surg 2006;132:628–32.

7. Tossios P, Krausgrill B, Schmidt M, et al. Role of balloon occlusion for mononuclear bone marrow cell deposition after intracoronary injection in pigs with reperfused myocardial infarction. Eur Heart J 2008;29:1911–21.

8. Taimeh Z, Loughran J, Birks EJ, Bolli R. Vascular endothelial growth factor in heart failure. Nat Rev Cardiol 2013;10:519–30.

9. Saharinen P, Eklund L, Pulkki K, Bono P, Alitalo K. VEGF and angiopoietin signaling in tumor angiogenesis and metastasis. Trends Mol Med 2011;17:347–62.

10. Mann DL, Lee RJ, Coats AJ, et al. One-year follow-up results from AUGMENT-HF: a multicentre randomized controlled clinical trial of the efficacy of left ventricular augmentation with Algisyl in the treatment of heart failure. Eur J Heart Fail 2015;18:314–25.

11. Frey N, Linke A, Suselbeck T, et al. Intracoronary delivery of injectable bioabsorbable scaffold (IK-5001) to treat left ventricular remodeling after ST-elevation myocardial infarction: a first-in-man study. Circ Cardiovasc Interv 2014;7:806–12.

12. Menasche P, Vanneaux V, Hagege A, et al. Human embryonic stem cell-derived cardiac progenitors for severe heart failure treatment: first clinical case report. Eur Heart J 2015;36:2011–7.

13. Mann DL, Kubo SH, Sabbah HN, et al. Beneficial effects of the CorCap cardiac support device: five-year results from the Acorn Trial. J Thorac Cardiovasc Surg 2011;143:1036–42.

14. Wang Q, Yang H, Bai A, et al. Functional engineered human cardiac patches prepared from nature's platform improve heart function after acute myocardial infarction. Biomaterials 2016;105:52–65.

15. Seif-Naraghi SB, Singelyn JM, Salvatore MA, et al. Safety and efficacy of an injectable extracellular matrix hydrogel for treating myocardial infarction. Sci Transl Med 2013;5:173ra25.

16. Phelps EA, Landázuri N, Thulé PM, Taylor WR, García AJ. Bioartificial matrices for therapeutic vascularization. Proc Natl Acad Sci 2010;107:3323–8.

17. Levit RD, Landazuri N, Phelps EA, et al. Cellular encapsulation enhances cardiac repair. J Am Heart Assoc 2013;2:e000367.

18. Phelps EA, Enemchukwu NO, Fiore VF, et al. Maleimide cross-linked bioactive PEG hydrogel exhibits improved reaction kinetics and cross-linking for cell encapsulation and in situ delivery. Adv Mater 2012;24:64–70.

19. Cohen JE, Purcell BP, MacArthur JW, et al. A Bioengineered hydrogel system enables targeted and sustained intramyocardial delivery of Neuregulin, activating the cardiomyocyte cell cycle and enhancing ventricular function in a murine model of ischemic cardiomyopathy. Circ Heart Fail 2014;7:619–26.

20. Tio RA, Grandjean JG, Suurmeijer AJH, van Gilst WH, van Veldhuisen DJ, van Boven AJ.

Thoracoscopic monitoring for pericardial application of local drug or gene therapy. Int J Cardiol 2002;82:117–21.

21. Xiao YF, Sigg DC, Ujhelyi MR, Wilhelm JJ, Richardson ES, Iaizzo PA. Pericardial delivery of omega-3 fatty acid: a novel approach to reducing myocardial infarct sizes and arrhythmias. Am J Physiol Heart Circ Physiol 2008;294:H2212–8.

22. Moreno R, Waxman S, Rowe K, Verrier RL. Intrapericardial beta-adrenergic blockade with esmolol exerts a potent antitachycardic effect without depressing contractility. J Cardiovasc Pharmacol 2000;36:722–7.

23. Lakkireddy D, Afzal MR, Lee RJ, et al. Short and long-term outcomes of percutaneous left atrial appendage suture ligation: results from a US multicenter evaluation. Heart Rhythm 2016;13:1030–6.

24. Chatterjee S, Herrmann HC, Wilensky RL, et al. Safety and procedural success of left atrial appendage exclusion with the Lariat device: a systematic review of published reports and analytic review of the FDA MAUDE Database. JAMA Intern Med 2015;175:1104–9.

25. Patel MB, Rasekh A, Shuraih M, et al. Safety and effectiveness of compassionate use of LARIAT(R) device for epicardial ligation of anatomically complex left atrial appendages. J Interv Card Electrophysiol 2015;42:11–9.

26. Phelps EA, Headen DM, Taylor WR, Thule PM, Garcia AJ. Vasculogenic bio-synthetic hydrogel for enhancement of pancreatic islet engraftment and function in type 1 diabetes. Biomaterials 2013;34:4602–11.

27. Sorajja P. Invasive hemodynamics of constrictive pericarditis, restrictive cardiomyopathy, and cardiac tamponade. Cardiol Clin 2011;29:191–9.

28. Gunda S, Reddy M, Nath J, et al. Impact of periprocedural colchicine on postprocedural management in patients undergoing a left atrial appendage ligation using LARIAT. J Cardiovasc Electrophysiol 2016;27:60–4.

29. Greenbaum AB, Rogers T, Paone G, et al. Intentional right atrial exit and carbon dioxide insufflation to facilitate subxiphoid needle entry into the empty pericardial space: first human experience. J Am Coll Cardiol EP 2015;1:434–41.

KEY WORDS biomaterials, device, hydrogel, pericardial delivery

APPENDIX For a supplemental figure, tables, and video, please see the online version of this article.

Cellular Mechanotransduction: Sensing Rigidity **Nature Materials: News and Views**

CELLULAR MECHANOTRANSDUCTION

Sensing rigidity

Cells use differences in the binding rates between the extracellular matrix and integrin adhesion receptors to sense matrix rigidity.

José R. García and Andrés J. García

The ability of cells to sense the rigidity of the extracellular matrix (ECM) affects the regulation of cellular activities in development, wound healing and even malignant transformation[1,2]. For instance, mesenchymal stem cells that adhere to stiff substrates commit to an osteogenic fate, whereas when those same stem cells adhere to softer substrates, the cells express a neurogenic phenotype[3]. The stiffness of a cell's underlying substrate also regulates proliferation, cell motility and cell spreading. For the underlying substrate to have such an effect on cells, two conditions must be met: cells must be able to somehow probe the mechanical properties of the substrate, and then be able to respond by translating the substrate's mechanical cues into biochemical signals that regulate gene and protein targets. Although a multitude of studies have documented the diverse signalling pathways (including transcription factors) involved in these mechanotransduction events[4–6], the molecular mechanisms responsible for sensing matrix stiffness remain poorly understood. Writing in *Nature Materials*, Pere Roca-Cusachs, Xavier Trepat and colleagues show that myoepithelial cells that adhere to the ECM protein fibronectin sense and adapt to ECM rigidity through the bond dynamics of integrin adhesion receptors[7].

Integrins are transmembrane adhesion receptors that anchor cells to the ECM and transduce 'outside-in' or 'inside-out' biochemical signals[8]. For outside-in signalling, integrins transmit information about a cell's adhesive state through a cascade of biochemical reactions that in turn regulates subsequent cellular responses such as motility and differentiation. In contrast, inside-out signalling involves intracellular reactions that result in changes in the integrin affinity for its extracellular ligand[9]. Interestingly, recent evidence suggests that integrins can undergo changes in affinity that depend on the stiffness of the culture substrate[10]. Because of their mechanotransductive properties, integrins have thus long been thought to be responsible for sensing (and responding to) the rigidity of the cell's microenvironment.

Roca-Cusachs and co-authors provide a simple model of how integrin binding kinetics regulate rigidity sensing. The authors investigated the interplay of two fibronectin-binding integrin receptors, $\alpha_5\beta_1$ and $\alpha_v\beta_6$, on cells cultured on fibronectin-coated gels of varying stiffness. Two different immortalized cell lines were used: myoepithelial cells expressing $\alpha_5\beta_1$, and myoepithelial cells expressing $\alpha_5\beta_1$ and overexpressing $\alpha_v\beta_6$. These two integrin types play important roles in mediating adhesive responses in physiological and pathological states (such as cancer). When cultured on the fibronectin-coated gel substrates, the cells adhered to the substrate, spread, and exerted traction forces whose magnitude depended on the substrate's

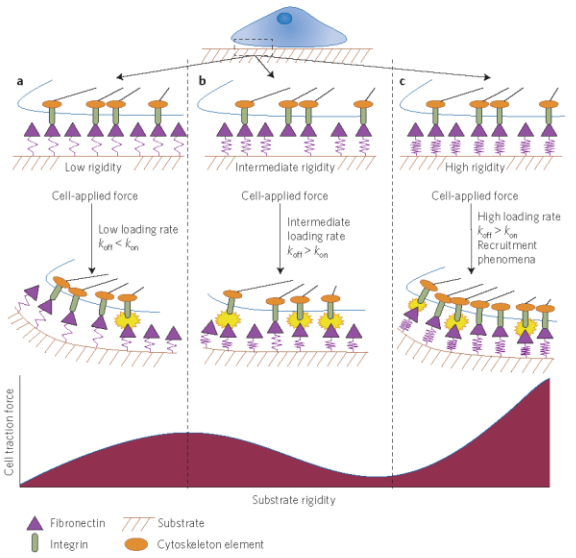

Figure 1 | Cells sense matrix rigidity through integrin binding dynamics. **a**, On soft substrates, the underlying ECM deforms easily, which causes the force-loading rate on the integrin–fibronectin bond to be relatively low. In this case, the unbinding of the integrin–fibronectin bond is controlled by the intrinsic unbinding rate (k_{off}) rather than by bond 'ripping off' (denoted by yellow stars) resulting from excess loading. **b**, On substrates with intermediate rigidities, the matrix creates a higher rate of force loading on the integrin–fibronectin bond. This causes a fraction of the integrins to tear away from fibronectin. **c**, On high-rigidity substrates, the high force-loading rate exceeds the threshold value for integrin recruitment, where integrins cluster at the site of force application. This reinforcement mechanism compensates for the increased unbinding, hence providing enhanced traction force. Therefore, cellular-traction forces reach a local minimum at intermediate substrate rigidities (bottom).

rigidity (specifically, the elastic modulus). Control cells with constitutive $\alpha_5\beta_1$-integrin expression responded in a biphasic fashion: with low traction forces at low and high substrate stiffness, and a peak in traction force at intermediate stiffness values (~1 kPa) corresponding to those of healthy breast tissue. Instead, cells overexpressing the $\alpha_v\beta_6$ integrin increased their traction force with increasing substrate stiffness, yet blocking the $\alpha_v\beta_6$ integrin–fibronectin interaction restored the biphasic behaviour. Furthermore, the authors found that the binding dynamics of the two integrin types were different: $\alpha_v\beta_6$ exhibited higher binding (k_{on}) and unbinding (k_{off}) rates, and had a higher affinity to fibronectin, than $\alpha_5\beta_1$.

On the basis of these experimental findings, Roca-Cusachs and co-workers explain the cells' rigidity-sensing mechanism with a model that integrates integrin-bond kinetics, substrate stiffness and the rate of bond loading (essentially, how fast the cells pull on the substrate). Because the integrin–fibronectin bond rates depend on force[11], the rigidity of the substrate affects how fast the traction force generated by the cell loads the integrin–fibronectin bonds, and therefore how long the bonds last (Fig. 1). At low rigidities (soft substrates), the matrix deforms as the cell pulls on it, causing the rate of force loading of the integrin–fibronectin bond to be so low that the bonds detach stochastically because of their intrinsic unbinding rate (k_{off}). In this regime, $k_{off} < k_{on}$, yet increased traction forces can be achieved by increasing the speed at which the cell pulls on the substrate. Above a threshold stiffness value, the matrix effectively resists the cell-generated force, resulting in increased bond loading and force-enhanced dissociation. In this regime, $k_{off} > k_{on}$, and thus bonds break before new bonds are formed, which results in decreased adhesive forces. At even higher substrate stiffness, the rate of bond loading is high enough that before the bonds can break, a force threshold is exceeded that brings about a reinforcement mechanism by which additional integrins are recruited at the cell/ECM interface to increase force transmission. Such clustering of integrins could arise from force-induced conformational changes in cytoskeletal proteins interacting with integrins to expose binding sites, or from the mechanostabilization of integrin clusters by cytoskeletal proteins such as vinculin[12,13].

Roca-Cusachs and collaborators' model predicts a biphasic traction-force response with substrate stiffness for a single integrin type, and a monotonic force response for two competing integrins, in full agreement with the experimental results for both the control and the $\alpha_v\beta_6$ integrin-overexpressing cells. Therefore, rigidity sensing and adaptation emerge naturally from integrin–ECM matrix bond dynamics. Cells can tune their traction-force responses to matrix stiffness by regulating the expression of different integrin types to target optimal responses for healthy tissues or pathological conditions. This observation is exciting, yet raises multiple questions. Is this model applicable to other integrin types and cell types? With over 20 distinct integrin receptors and many cells expressing numerous integrin types, the details of this sensing mechanism become more complex, particularly given the range of matrix-stiffness values present in healthy and pathological tissues. Given the central role of the ECM as a reservoir of growth and differentiation factors, it will be important to explore the interplay of mechanical factors and growth-factor signalling in modulating integrin–ECM interactions. Additional investigations of how mechanical stimuli are specifically translated and integrated into biochemical signals, and how these signals are fed back into the contractile and adhesive machinery, are certainly warranted. Finally, it will be important to exploit these mechanosensitive responses in therapeutic strategies to treat tissue dysfunction and pathologies. For instance, can therapeutics be targeted to specific integrins to prevent cells from sensing the abnormal ECM stiffness and responding in an undesired manner? The insights into rigidity sensing and adaptation provided by Roca-Cusachs and colleagues will surely spur new lines of investigation on the interplay of substrate mechanics and cell signalling. ❐

José R. García and Andrés J. García are at the Woodruff School of Mechanical Engineering and Petit Institute for Bioengineering and Bioscience, Georgia Institute of Technology, Atlanta, Georgia 30332, USA.
e-mail: andres.garcia@me.gatech.edu

References
1. Wozniak, M. A. & Chen, C. S. *Nature Rev. Mol. Cell Biol.* **10,** 34–43 (2009).
2. Kumar, S. & Weaver, V. M. *Cancer Metastasis Rev.* **28,** 113–127 (2009).
3. Engler, A. J., Sen, S., Sweeney, H. L. & Discher, D. E. *Cell* **126,** 677–689 (2006).
4. Schwartz, M. A. *Cold Spring Harb. Perspect. Biol.* **2,** a005066 (2010).
5. Dupont, S. *et al. Nature* **474,** 179–183 (2011).
6. Vogel, V. & Sheetz, M. P. *Curr. Opin. Cell. Biol.* **21,** 38–46 (2009).
7. Elosegui-Artola, A. *et al. Nature Mater.* **13,** 631–637 (2014).
8. Hynes, R. O. *Cell* **110,** 673–687 (2002).
9. Lad, Y., Harburger, D. S. & Calderwood, D. A. *Methods Enzymol.* **426,** 69–84 (2007).
10. Du, J. *et al. Proc. Natl Acad. Sci. USA* **108,** 9466–9471 (2011).
11. Kong, F., García, A. J., Mould, A. P., Humphries, M. J. & Zhu, C. *J. Cell Biol.* **185,** 1275–1284 (2009).
12. Del Rio, A. *et al. Science* **323,** 638–641 (2009).
13. Dumbauld, D. W. *et al. Proc. Natl Acad. Sci. USA* **110,** 9788–9793 (2013).

STEM CELL MECHANICS

Auxetic nuclei

The nuclei of naive mouse embryonic stem cells that are transitioning towards differentiation expand when the cells are stretched and contract when they are compressed. What drives this auxetic phenotype is, however, unclear.

Ning Wang

The characterization of both metastable and fully committed embryonic stem cells (ESCs) — pluripotent cells that are able to differentiate into almost all cell types in the body — is highly elusive. Because metastable cells can return to their undifferentiated state or become fully committed to differentiation, these physiological ESC states are crucial to the understanding and control of differentiation and de-differentiation — a process where differentiated cells are reprogrammed back into undifferentiated pluripotent cells — and hence to tissue-engineering and regenerative-medicine applications. Writing in *Nature Materials*, Kevin Chalut and colleagues report the discovery of an unexpected biophysical phenotype of the nuclei of mouse ESCs in the metastable transition state: contrary to the behaviour of most known materials, the nucleus of the cell expands when stretched[1].

To characterize the different physiological states of ESCs when

Light-triggered in vivo activation of adhesive peptides regulates cell adhesion, inflammation and vascularization of biomaterials. **Nature Materials**

ARTICLES
PUBLISHED ONLINE: 15 DECEMBER 2014 | DOI: 10.1038/NMAT4157
nature materials

Light-triggered *in vivo* activation of adhesive peptides regulates cell adhesion, inflammation and vascularization of biomaterials

Ted T. Lee[1,2], José R. García[1,2], Julieta I. Paez[3], Ankur Singh[1,2,4], Edward A. Phelps[1,2], Simone Weis[3], Zahid Shafiq[3], Asha Shekaran[1,2], Aránzazu del Campo[3] and Andrés J. García[1,2]*

Materials engineered to elicit targeted cellular responses in regenerative medicine must display bioligands with precise spatial and temporal control. Although materials with temporally regulated presentation of bioadhesive ligands using external triggers, such as light and electric fields, have recently been realized for cells in culture, the impact of *in vivo* temporal ligand presentation on cell–material responses is unknown. Here, we present a general strategy to temporally and spatially control the *in vivo* presentation of bioligands using cell-adhesive peptides with a protecting group that can be easily removed via transdermal light exposure to render the peptide fully active. We demonstrate that non-invasive, transdermal time-regulated activation of cell-adhesive RGD peptide on implanted biomaterials regulates *in vivo* cell adhesion, inflammation, fibrous encapsulation, and vascularization of the material. This work shows that triggered *in vivo* presentation of bioligands can be harnessed to direct tissue reparative responses associated with implanted biomaterials.

Cell adhesion to the extracellular matrix (ECM) provides mechanical support and biochemical signals regulating diverse cell behaviours critical to tissue morphogenesis, homeostasis and repair[1,2]. Far from static, the adhesion process comprises dynamic interactions over multiple time and length scales, spanning nanoscale integrin receptor–ECM ligand binding (seconds), clustering of integrins with cytoskeletal elements into sub-micrometre/micrometre-scale focal adhesions (minutes–hours), activation of signalling pathways and transcriptional programs (hours–days), and meso/macroscale ECM remodelling and tissue organization (days–weeks)[3,4]. Cell–ECM adhesion is tightly regulated, and misregulated interactions often result in pathological conditions such as developmental defects, wound healing deficiencies and tumorigenesis[2,5]. In an analogous fashion, the engineering of materials to elicit desired cellular responses in regenerative medicine will require precise control over spatiotemporal bioligand presentation[6–10]. Despite progress in the fabrication of biomaterials with exquisite spatial control of bioligand display[11–13], materials with temporally regulated presentation of bioadhesive ligands using external triggers (for example, temperature, light, electric field) under *in vitro* culture conditions have only recently been realized[14–21]. A standing question in the biomaterials field is whether temporal presentation of bioligands on implanted materials can be exploited to modulate *in vivo* cell behaviours to elicit targeted reparative responses. As biological responses to implanted materials comprise temporal cascades, control over *in vivo* material properties such as presentation of bioactive ligands represents a powerful and new approach to engineer host responses to implanted materials. In the work presented here, we establish a general strategy to temporally and spatially control the *in vivo* presentation of bioligands using a synthetic cell-adhesive RGD (Arg-Gly-Asp) peptide with a protecting group ('cage') on its integrin-receptor-binding site that can be easily removed with light at prescribed wavelengths to render the RGD peptide fully active. Furthermore, we demonstrate that non-invasive, transdermal activation of the cell-adhesive RGD peptide on biomaterials at particular time points after implantation regulates *in vivo* cell adhesion, inflammation and vascularization of the material.

Light-triggered activation of caged RGD peptide

We engineered light-triggerable cell-adhesive materials using the cyclic RGD peptide cyclo(Asp-D-Phe-Lys-Arg-Gly) modified with a 3-(4,5-dimethoxy-2-nitrophenyl)-2-butyl ester (DMNPB) photolabile caging group on the carboxylic side group of the aspartic acid residue[14]. On exposure to light ($\lambda \sim 350–365$ nm), the caging group is released resulting in the presentation of the active cyclic RGD peptide (Fig. 1a). We first examined presentation of cell-adhesive peptides on the surface of poly(ethylene glycol) di-acrylate (PEGDA) hydrogels, a widely used biomaterial with excellent non-fouling and cell-adhesion-resistant properties. For tethering onto hydrogels, adhesive peptides were first acrylated using a commercial reagent. Matrix-assisted laser desorption/ionization mass spectrometry demonstrated acrylation of the caged RGD peptide as demonstrated by the predicted shift in mass/charge ratio (Supplementary Fig. 1). Hydrogels presenting adhesive peptides were generated by covalently incorporating acrylated peptides (2% w/v) onto the surface of bulk PEGDA hydrogels using free-radical polymerization.

To test the ability to trigger cell adhesion to these materials *in vitro*, peptide-modified and unfunctionalized PEGDA hydrogels were either exposed to ultraviolet (UV) light ($\lambda = 351$ nm, 20 mW cm^{-2}) for 10 min or not exposed. Fibroblasts were then cultured on these hydrogels for 24 h, and adherent cell numbers and spreading were evaluated by image analysis. Very few cells

[1]Woodruff School of Mechanical Engineering, Georgia Institute of Technology, Atlanta, Georgia 30332, USA. [2]Petit Institute for Bioengineering and Bioscience, Georgia Institute of Technology, Atlanta, Georgia 30332, USA. [3]Max-Planck-Institut für Polymerforschung, Mainz 55128, Germany. [4]Sibley School of Mechanical and Aerospace Engineering, Cornell University, Ithaca, New York 14853, USA. *e-mail: andres.garcia@me.gatech.edu

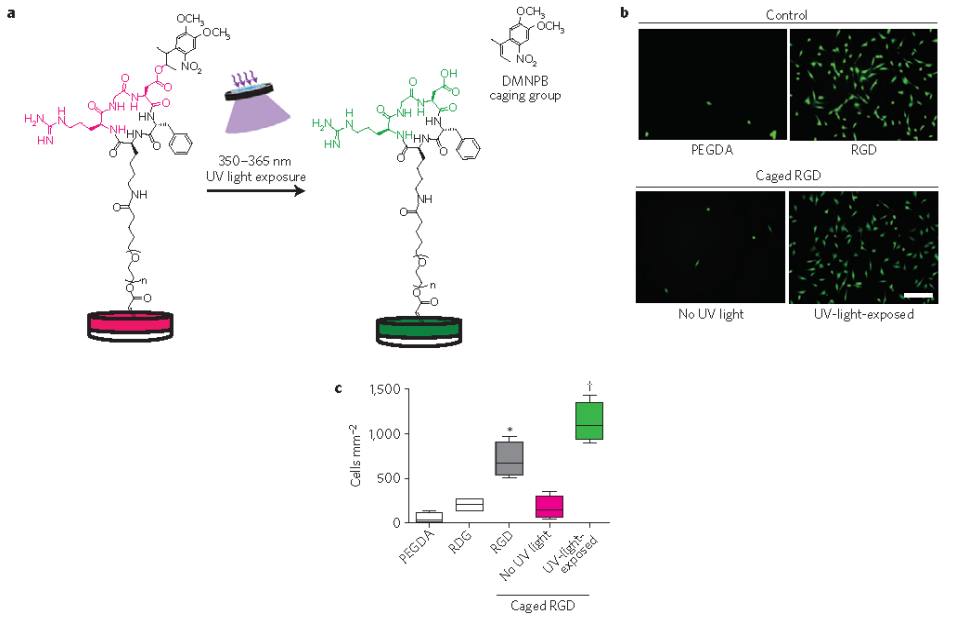

Figure 1 | Light-triggered activation of cell adhesion activity of caged RGD peptide on hydrogels. **a**, Schematic representation of caged RGD peptide-functionalized PEGDA hydrogels. Light exposure at 350–365 nm cleaves the UV-light-labile caging group to present the active cyclic RGD peptide. Magenta/green denotes caged/active RGD peptide. **b**, Photographs of fluorescently labelled cells cultured on unmodified PEGDA and peptide-modified hydrogels that were either exposed to UV light or not exposed (scale bar, 300 μm). Hydrogels presenting control RGD peptide and UV-light-exposed caged RGD peptide supported high levels of adherent cells. Unmodified PEGDA gels and hydrogels presenting RDG scrambled peptide and non-exposed caged RGD peptide supported very low numbers of adherent cells with rounded morphology. **c**, Adherent cell density on hydrogels, box–whisker plot (minimum, 25th percentile, median, 75th percentile, and maximum) for 4 samples per group. Kruskal–Wallis $p < 0.0026$. UV-light-exposed gels presenting caged RGD supported fourfold higher adherent cell densities than hydrogels functionalized with caged RGD peptide that were not exposed to UV light ($^{\dagger}p < 0.01$), surfaces presenting scrambled RDG peptide, and bare PEGDA hydrogels ($p < 0.01$). Cell density was higher on control RGD compared with RDG peptide ($^{*}p < 0.05$). No differences in cell adhesion density were observed between UV-light-exposed caged RGD peptide-presenting gels and hydrogels presenting control RGD peptide ($p = 0.08$).

adhered to unmodified PEGDA, confirming the cell-adhesion-resistant background provided by this material (Fig. 1b). Hydrogels presenting caged RGD peptide that were not exposed to light also supported very low numbers of adherent cells, and the few cells that adhered were round, similar to the levels of cell adhesion to unmodified PEGDA (Fig. 1b). In contrast, hydrogels presenting caged RGD peptide that were UV-light-exposed to remove the caging group supported high numbers of well spread, adherent cells, similar to those on hydrogels presenting control cyclic RGD peptide (Fig. 1b). As expected, no differences in cell adhesion were observed between UV-light-exposed and non-exposed gels that presented control RGD peptide or unmodified PEGDA. Quantification of the number of adherent cells over multiple fields demonstrated equivalent low levels of cell adhesion between non-UV-light-exposed caged RGD peptide-presenting gels and unmodified PEGDA ($p = 0.5$, Fig. 1c). UV-light-exposed gels presenting caged RGD peptide supported fourfold higher adherent cell densities ($p < 0.01$). No differences in cell density ($p = 0.08$) or spreading ($892 \pm 83\,\mu m^2$ versus $871 \pm 91\,\mu m^2$ (mean $\pm$ s.d.), $p = 0.73$) were observed between UV-light-exposed caged RGD-presenting gels and hydrogels presenting control RGD peptide, demonstrating that the uncaged RGD peptide exhibits full adhesive activity. Finally, low levels of adhesion were observed on hydrogels presenting a scrambled RGD peptide (RDG), showing that cell adhesion in this system is specific to the presence of the RGD sequence.

Transdermal activation of caged bioligands

We selected light as the trigger for the display of bioactive molecules because this stimulus offers unparalleled spatiotemporal control and the potential to use transdermal light exposure to remove the caging group *in vivo* in a non-invasive fashion. For *in vivo* studies in mice, we used ultraviolet-A light ($\lambda = 351$ nm, $20\,mW\,cm^{-2}$) for short exposures (10 min) to minimize photodamage. This longer wavelength produces less damage than ultraviolet-B and ultraviolet-C light and has been used for transdermal photopolymerization[22]. Preliminary experiments demonstrated no skin photodamage or adverse effects at the doses used.

We measured UV light attenuation through murine skin in our experimental set-up using a photometer. UV light attenuation increased with the thickness of the skin sample and follows an exponential decay as predicted by Beer's law (Supplementary Fig. 2). For the skin from the murine dorsum where the biomaterial samples were implanted, we estimate 90% attenuation of the UV light.

We next analysed the stability and uncaging efficiency of the caged RGD peptide-functionalized gels following subcutaneous implantation in mice and transdermal UV light exposure. For these

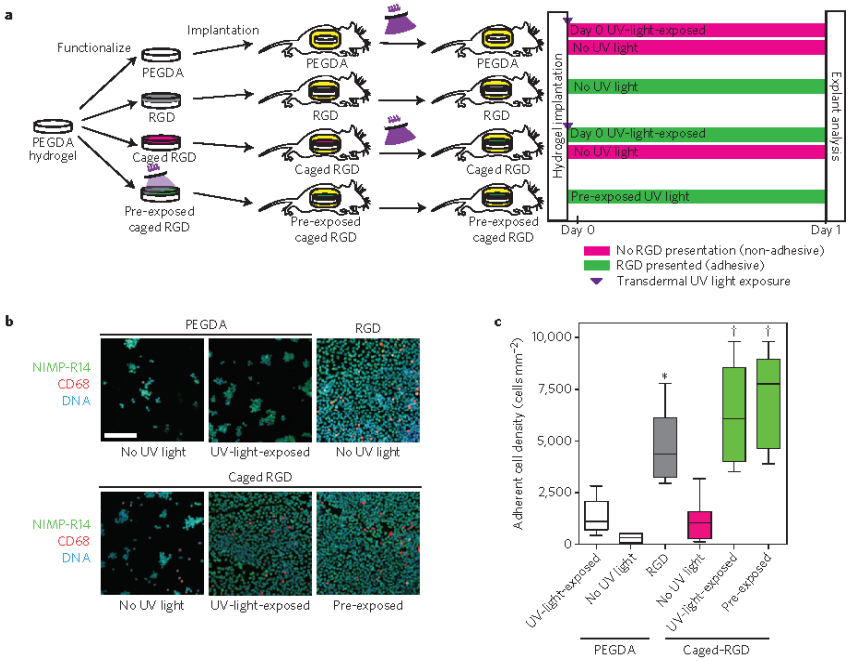

Figure 2 | Transdermal activation of *in vivo* inflammatory cell adhesion. a, Schematic representation of the time line for *in vivo* activation of cell adhesion using transdermal UV light exposure. **b**, Photographs of explanted hydrogels stained for adherent inflammatory cells (green, NIMP-R14 (neutrophil); magenta, CD68 (macrophage); blue, DAPI (DNA); scale bar, 80 μm). Unfunctionalized PEGDA hydrogels exhibited minimal cell adhesion regardless of UV light exposure, whereas hydrogels presenting control RGD peptide supported uniformly high numbers of adherent cells. Hydrogels presenting caged RGD peptide that were not UV-light-exposed exhibited background levels of cell adhesion. In contrast, caged RGD-functionalized gels that were exposed to UV light transdermally exhibited high numbers of adherent cells that were uniformly distributed over the biomaterial surface. **c**, Adherent cell density, box–whisker plot (minimum, 25th percentile, median, 75th percentile, and maximum) for 6–8 mice per group, demonstrating light-based triggering of inflammatory cell adhesion to caged RGD-presenting implants. ANOVA $p < 0.0001$, $^{*}p < 0.05$ versus UV-light-exposed PEGDA, $^{\dagger}p < 0.001$ versus no-UV-light caged RGD.

studies, we used an acrylate derivative of bis-(5-carboxymethoxy-2-nitrobenzyl)ether (CMNB)-caged fluorescein as an analogue for the caged RGD peptide (Supplementary Fig. 3). This caged fluorescein has low fluorescence when the caging group is present but exhibits high fluorescence when the caging group is removed. PEGDA gels presenting UV-light-exposed or non-exposed caged fluorescein and unfunctionalized gels were implanted into mice, and at prescribed times the area of the skin corresponding to where the implant was located was either exposed to UV light or left untreated (Supplementary Fig. 4). After euthanization at 7 or 14 days, the implants were recovered and the fluorescence intensity, corresponding to the extent of uncaging, was quantified. Hydrogels presenting caged fluorescein that were not exposed to UV light exhibited minimal fluorescence after 7 and 14 days of implantation (Supplementary Fig. 4), equivalent to background fluorescence levels associated with unmodified PEGDA gels. Hydrogels that were UV-light-exposed transdermally immediately after implantation exhibited tenfold higher fluorescence levels compared with implants presenting caged fluorescein that were not UV-light-exposed to UV light ($p < 0.0001$, Supplementary Fig. 4), demonstrating that transdermal UV light exposure removes the caging group to trigger *in vivo* presentation of the caged molecule. Importantly, there are no differences in the fluorescence signal among hydrogels presenting caged fluorescein exposed to UV light before implantation (pre-exposed) and hydrogels presenting caged fluorescein exposed to UV light transdermally immediately after implantation (day 0) or at 14 days post-implantation (day 14; Supplementary Fig. 4). These results demonstrate that both caged and uncaged compounds remain stable *in vivo* and that transdermal uncaging efficiency is high and independent of implantation time.

Transdermal activation of cell adhesion

Having established the ability to trigger transdermal uncaging of the bioligand, we assessed whether transdermal activation of caged RGD peptide-tethered hydrogels regulates *in vivo* cell adhesion (Fig. 2). Unmodified PEGDA gels and hydrogels presenting control or caged RGD were implanted subcutaneously in mice. Immediately after wound closure, implants were either exposed to UV light transdermally or not exposed. Twenty-four hours after implantation, hydrogels were carefully explanted and adherent cells were stained for DNA, neutrophil (NIMP-R14) and macrophage (CD68) markers using fluorescent antibodies and analysed by microscopy (Fig. 2b,c). Few cells adhered to unexposed or UV-light-exposed unfunctionalized PEGDA hydrogels, showing that UV light exposure does not alter cell adhesion to these non-fouling materials. Equivalent low cell numbers were observed on hydrogels presenting caged RGD

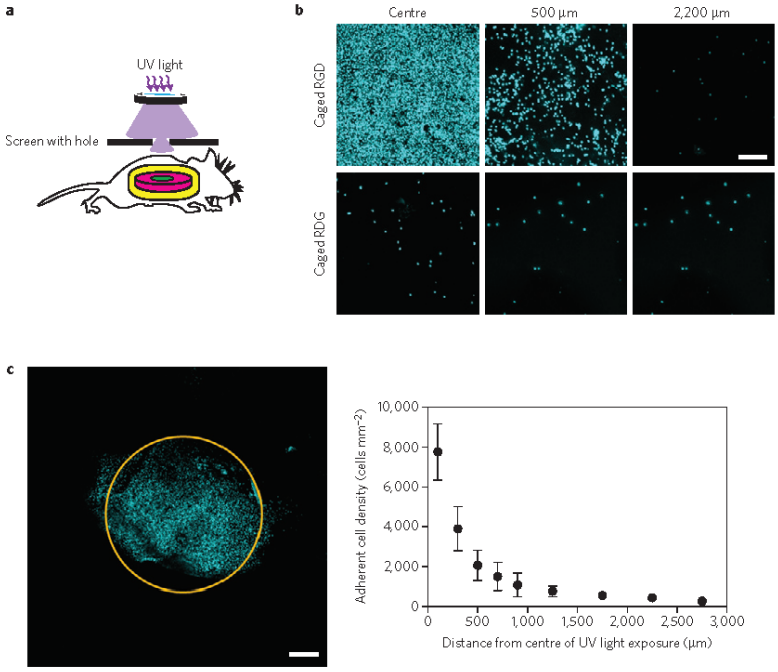

Figure 3 | Light-triggered spatial patterning of *in vivo* cell adhesion. a, Schematic representation of patterning experiment using transdermal UV light exposure through a mask. **b**, Photographs of explanted hydrogels stained for adherent cell nuclei for caged RGD and RDG presenting hydrogels at different distances from the centre of irradiation (DAPI, colour-coded cyan, scale bar, 40 μm). **c**, Left: Composite image of photographs of adherent cell nuclei (cyan). Yellow circle designates exposure spot (scale bar, 200 μm). Right: Adherent cell density versus distance away from irradiation point. Data represent mean ± standard error for hydrogels explanted for 5 mice per group.

peptide that were not UV-light-exposed, showing that the caged RGD peptide retains low cell-adhesive activity *in vivo*. In contrast, hydrogels presenting caged RGD peptide that were transdermally exposed to UV light exhibited high numbers of adherent cells that were uniformly distributed over the biomaterial surface ($p < 0.001$), equivalent to cell numbers and distribution on control RGD or caged RGD peptide that was UV-light-exposed before implantation. Immunostaining of adherent cells showed that most of the recruited cells were neutrophils (NIMP-R14+) with macrophages (CD68+) comprising the rest of the adherent cells, consistent with the expected inflammatory cell profile at this acute time point[23]. Taken together, these results demonstrate transdermal activation of caged RGD peptide to trigger *in vivo* acute cell adhesion to biomaterials.

We also examined transdermal activation of cell adhesion to a different class of PEG hydrogel. PEG-maleimide hydrogels offer significant advantages over PEGDA hydrogels such as well-defined hydrogel structure, stoichiometric incorporation of adhesive peptides, and flexibility in using protease-degradable crosslinks that allow for robust cell spreading and migration within the gel[24]. For this follow-up study, we synthesized a cysteine-containing caged RGD peptide for reacting with maleimides in 4-arm PEG-maleimide macromers (Supplementary Fig. 5a,b). Importantly, we also generated a caged RDG scrambled peptide to serve as a stringent non-adhesive control peptide for the caged RGD peptide. Peptide-functionalized hydrogels were implanted subcutaneously and exposed to UV light transdermally immediately after wound closure. Twenty-four hours later, the hydrogels were explanted and the number of cells adherent to the material was quantified by image analysis. Consistent with our observations for the PEGDA gels, PEG-maleimide gels presenting caged RGD peptide that were not UV-light-exposed had background levels of adherent cells, equivalent to hydrogels presenting control RDG peptides (Supplementary Fig. 5c). Hydrogels that had been exposed to transdermal UV light had approximately threefold higher cell numbers than non-UV-light-exposed controls (Supplementary Fig. 5c, $p < 0.0001$). No differences in cell numbers were detected among hydrogels presenting caged RGD peptide that were exposed to UV light transdermally or exposed to UV light before implantation and hydrogels presenting control cyclic RGD peptide. Importantly, hydrogels presenting the caged scrambled RDG peptide exhibited low numbers of adherent cells regardless of whether they received UV light exposure or not. These results demonstrate control of *in vivo* cell adhesion to biomaterials using UV-light-based activation of RGD peptides.

In vivo spatial patterning of adhesive ligands

A major advantage of the use of light as an external trigger is the ability to spatially pattern light exposure to control the spatial activation of caged bioligands. To demonstrate this application, we implanted PEG hydrogels presenting either caged RGD or caged RDG peptides subcutaneously and exposed them to UV light transdermally through a mask containing a 0.9 mm hole centred

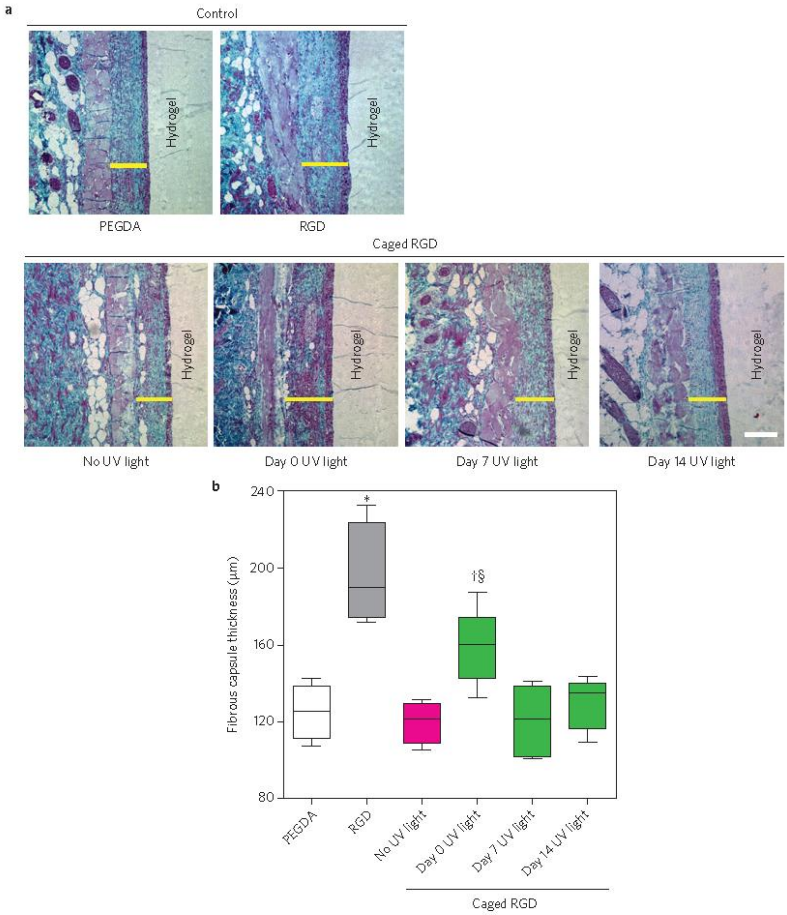

Figure 4 | Time-regulated *in vivo* activation of RGD peptide modulates fibrous encapsulation of implanted biomaterials. Unfunctionalized PEGDA hydrogels and gels presenting either control RGD or caged RGD peptides were implanted subcutaneously and at prescribed time points were exposed to UV light transdermally. Biomaterials and associated tissue were explanted at 28 days. **a**, Photographs of plastic-embedded sections stained by Mason's trichrome of fibrous capsule formation around implanted hydrogels at 28 days (scale bar, 100 μm). Yellow bars denote fibrous capsule. **b**, Fibrous capsule thickness around implanted hydrogels; box-whisker plot (minimum, 25th percentile, median, 75th percentile, and maximum) for 4–6 mice per group. ANOVA $p < 0.0001$, $^{*}p < 0.001$ versus PEGDA, $^{\dagger}p < 0.01$ versus no-UV-light caged RGD, $^{\S}p < 0.05$ versus day 0 UV-light caged RGD.

over the area where the hydrogel was implanted (Fig. 3a). The next day, hydrogels were explanted and stained for cell nuclei (DNA). For hydrogels presenting caged RGD peptides, high cell numbers were observed directly at the site of UV light exposure and cell numbers decreased to background levels away from the irradiation spot (Fig. 3b). For hydrogels presenting caged RDG peptide, adherent cell numbers were low and independent of position. Figure 3c presents a composite image of photographs of adherent cells at different positions along the hydrogel surface showing high numbers of adherent cells localized to the exposure spot (yellow circle) and low levels of adherent cells outside the exposure point. Quantification of cell numbers at different spatial positions on the hydrogel shows monotonic decreases in cell density with distance away from the irradiation spot (Fig. 3c). These results demonstrate spatial control over *in vivo* RGD presentation and cell patterning using transdermal illumination.

RGD peptide activation modulates fibrous encapsulation

We next examined whether time-regulated presentation of RGD peptide modulates chronic inflammatory responses to biomaterials. We used PEGDA hydrogels because these gels are non-degradable and elicit a uniform collagenous fibrous capsule allowing direct comparisons among different exposure conditions. Unmodified PEGDA hydrogels and gels presenting control RGD or caged RGD peptide were implanted subcutaneously in mice. At 0, 7 or 14 days post-implantation, implants were exposed to UV

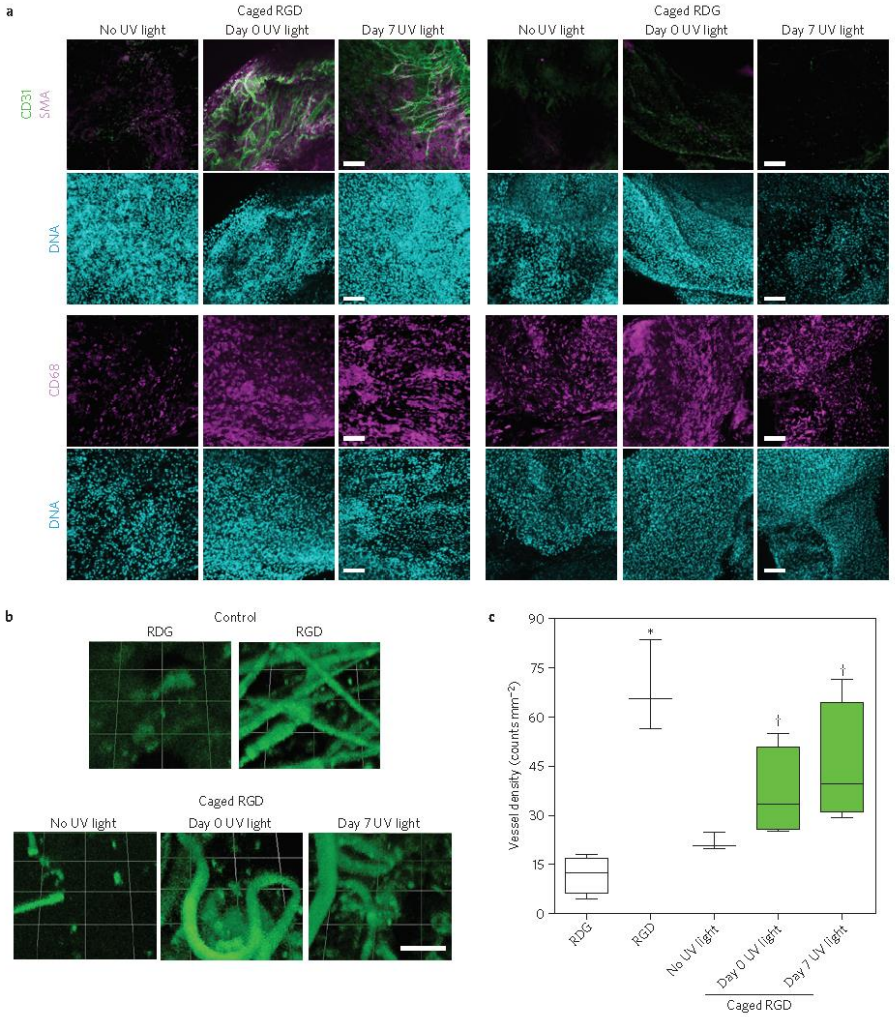

Figure 5 | Light-based activation of cell-adhesive peptide promotes vascularization of implanted biomaterials. a, Immunostaining images for hydrogels presenting caged RGD or caged RDG peptide for different UV light exposure conditions explanted at 14 days. Top: Green, CD31 (endothelial cell); magenta, αSMA (smooth muscle cell); blue, DAPI (DNA); scale bars, 100 μm. Bottom: Magenta, CD68 (macrophage); blue, DAPI (DNA); scale bars, 100 μm. **b**, Fluorescent images of blood vessel ingrowth (green) into PEG-maleimide hydrogels implanted subcutaneously for 14 days (scale bar, 100 μm). PEG-maleimide hydrogels presenting peptides were implanted subcutaneously and exposed to UV light transdermally at selected time points. Mice were perfused with DyLight488-conjugated tomato lectin at euthanization to label functional blood vessels. Hydrogels presenting caged RGD peptides that were exposed to UV light transdermally at day 0 and day 7 exhibited robust blood vessel growth, similar to gels presenting control RGD. Hydrogels functionalized with scrambled RDG peptide or caged RGD peptide that was not exposed to UV light exhibited minimal blood vessel infiltration. **c**, Blood vessel density; box-whisker plot (minimum, 25th percentile, median, 75th percentile, and maximum) for 4 mice per group for caged RGD conditions, 3 mice per group for control peptides. Kruskal–Wallis $p < 0.01$, $^{*}p < 0.01$ versus RDG, $^{\dagger}p < 0.05$ versus no-UV-light caged RGD.

light transdermally. After euthanization at day 28, implants and associated tissues were carefully explanted, embedded in plastic and processed for Masson's trichrome staining. Figure 4a presents sections of the biomaterial–tissue interface showing the collagenous fibrous capsule characteristic of chronic inflammation in response to biomaterials[23,25]. The fibrous capsule thickness (yellow bar) was quantified as a measure of chronic inflammation (Fig. 4b). Unmodified PEGDA gels elicited thin capsules, whereas hydrogels

presenting control RGD peptide produced fibrous capsules that were 60% thicker than capsules for unmodified PEGDA ($p < 0.001$). This result shows that static presentation of RGD adhesive peptides on biomaterials promotes chronic inflammation and fibrous encapsulation. In addition, no differences in fibrous capsule thickness were observed between UV-light-exposed and non-UV-light-exposed subjects for these control implant groups (Supplementary Fig. 6), demonstrating that transdermal UV light exposure does not alter chronic inflammatory responses to these materials. Hydrogels presenting caged RGD peptide that were not exposed to UV light had thin fibrous capsules, equivalent to those for unmodified gels (Fig. 4a,b). In contrast, hydrogels presenting caged RGD peptide that were irradiated immediately after implantation (day 0) exhibited fibrous capsules that were 50% thicker than capsules for gels with caged RGD peptide that were not exposed to UV light ($p < 0.01$). The fibrous capsule thickness for caged RGD peptide-tethered gels exposed at day 0 was equivalent to the capsule thickness for gels with control static RGD peptide ($p = 0.12$). Hydrogels presenting caged RGD peptide transdermally exposed to UV light at either 7 or 14 days post-implantation exhibited fibrous capsules that were 50% thinner than those for hydrogels presenting caged RGD peptide that were irradiated immediately after implantation ($p < 0.05$), and the capsule thickness was not different from that for unmodified hydrogels or gels presenting caged RGD peptides that were not exposed to UV light ($p = 0.2$). These results demonstrate that delayed presentation of adhesive ligands on implanted biomaterials significantly reduces chronic inflammation and fibrosis.

In vivo RGD activation triggers vascularization of hydrogels

Having demonstrated that time-dependent *in vivo* activation of RGD peptide presentation modulates cell adhesion and inflammation at the tissue–biomaterial interface, we next examined whether light-based activation of adhesive peptides could trigger three-dimensional (3D) cell invasion and vascularization of implanted biomaterials. We used PEG-maleimide hydrogels with precise incorporation of adhesive peptides and protease-degradable crosslinks that allow for robust cell spreading and migration within the gel[24]. We first examined *in vitro* cell invasion into these biomaterials by polymerizing peptide-functionalized hydrogels around a cell pellet and evaluating cell sprouting into the gel (Supplementary Fig. 7). Fibroblast sprouting into the gel was completely dependent on the presentation of adhesive RGD peptide as shown by significant cell invasion into the gel for control RGD peptide and no cell outgrowth for scrambled RDG control peptide ($p < 0.0001$). UV light exposure of hydrogels presenting caged RGD peptide resulted in significant fibroblast sprouting ($p < 0.05$), whereas no cell outgrowth was observed in gels that were not exposed to UV light, demonstrating light-triggered cell invasion into these biomaterials.

We have shown that PEG-maleimide hydrogels with adhesive peptides and protease-degradable crosslinks are suitable vehicles for controlled delivery of VEGF that direct *in vivo* vascularization[26]. In this system, VEGF is released on protease-dependent degradation of the hydrogel. To demonstrate that VEGF is retained within the hydrogel over time, we performed an *ex vivo* VEGF release experiment. Fluorescently labelled VEGF was incorporated within PEG hydrogels and incubated in buffer without or with collagenase to degrade the hydrogel. At defined time points, VEGF released into the surrounding media was measured to quantify VEGF release. More than 60% of the incorporated VEGF remains within the hydrogel over 7 days in culture (Supplementary Fig. 8). However, in the presence of collagenase, the gel degrades releasing the incorporated VEGF. These results demonstrate that VEGF is retained with the hydrogel network and released in response to collagenase-mediated degradation.

To examine triggerable control over *in vivo* vascularization, PEG-maleimide hydrogels presenting caged RGD or RDG peptides, protease-degradable crosslinks and VEGF vasculogenic protein were polymerized directly into subcutaneous pockets in mice. At 0 or 7 days post-implantation, implants were exposed to UV light transdermally. Following euthanization at day 14, hydrogels were explanted, stained for different cell markers, and analysed by confocal microscopy to examine cell infiltration and vascularization within the hydrogel. As shown by cell nuclei staining, all implanted hydrogels exhibited high cell numbers within the implant with no gross differences for cell infiltration among hydrogel type (RGD, RDG) or UV light exposure condition (Fig. 5a). This observation is in agreement with previous reports[26–28]. Staining for inflammatory cell markers revealed that most cells were macrophages and no staining for neutrophils was evident, which is the expected inflammatory cell profile at this time point[23,25]. Importantly, hydrogels presenting caged RGD peptide that had been UV-light-exposed transdermally at day 0 or day 7 contained many tubular structures that stained positive for the endothelial cell marker CD31 and smooth muscle cell marker αSMA (Fig. 5a and Supplementary Fig. 9), indicating vascularization of these hydrogels. In contrast, hydrogels presenting caged RGD peptide that had not been exposed to UV light exhibited diffuse staining for CD31 and αSMA, and no tubular structures resembling blood vessels were observed (Fig. 5a and Supplementary Fig. 9). Likewise, hydrogels presenting caged scrambled RDG peptide showed diffuse CD31 and αSMA staining and no evidence of blood vessels for any UV light exposure condition. These results demonstrate that UV-light-triggered activation of RGD peptides promotes vascularization of these hydrogels.

To examine whether hydrogels presenting caged RGD peptide supported formation of functional blood vessels, VEGF-containing hydrogels were polymerized *in situ* subcutaneously and exposed to UV light transdermally at day 0 or 7 post-implantation. At day 14, DyLight488-conjugated tomato lectin was infused intravenously to label functional vasculature, and implants were recovered and imaged by confocal microscopy as whole-mount preparations. Image projections from 3D reconstructions and vessel counts clearly show functional vessels within hydrogels presenting control RGD peptide and sparse vessels for gels presenting scrambled RDG peptide (Fig. 5b,c). This result shows that adhesive RGD peptide is required for the *in vivo* formation of functional blood vessels within implanted hydrogels, consistent with our previous reports[26,27]. Gels presenting caged RGD peptides that were not exposed to UV light had few blood vessels, with equivalent low vessel counts to gels presenting scrambled peptides. In contrast, hydrogels presenting caged RGD peptides that were UV-light-exposed transdermally exhibited robust functional blood vessel formation and had 3 times more vessels than non-UV-light-exposed gels ($p < 0.05$). There are no significant differences in blood vessel density between hydrogels presenting caged RGD peptides that were exposed to UV light at day 0 or day 7 ($p = 0.1$) or between these groups and the control RGD peptide ($p = 0.06$). Taken together, the immunostaining and lectin perfusion results demonstrate that *in vivo* triggering of cell-adhesive RGD peptides regulates vascularization of VEGF-containing hydrogels.

The present study establishes a general strategy to spatially and temporally control the *in vivo* presentation of bioligands using bioactive peptides with a protecting group that can be easily removed using transdermal light exposure to render the peptide fully active. This strategy is fundamentally different from other work using light for *in vivo* drug delivery and self-assembly applications that relies on energy-driven physical changes in the material[29–31]. We demonstrate that non-invasive, transdermal activation of the cell-adhesive RGD peptide on implanted biomaterials regulates *in vivo* cell adhesion and spatial patterning, inflammation, fibrous encapsulation, and vascularization of the material. This work shows that

triggered *in vivo* presentation of bioligands can be harnessed to direct tissue reparative responses associated with implanted biomaterials. As shown in this study, light-regulated ligand activation can be exploited to promote desired healing responses (for example, cell adhesion, vascularization) while avoiding deleterious biological consequences (for example, inflammation, fibrous encapsulation). We targeted the cell-adhesive RGD peptide because of its critical importance in binding to several integrin receptors associated with host responses to biomaterials. Delayed activation of RGD presentation reduced the thickness of the fibrous capsule around the implanted biomaterial. A possible explanation for this reduced chronic inflammatory response is altered adhesion and signalling by neutrophils and macrophages recruited to the biomaterial surface. Blocking of RGD peptide binding to $\alpha_M\beta_2$ (Mac-1) integrin among others on macrophages results in reduced pro-inflammatory cytokine secretion in cultured cells and thinner fibrous capsules around polymeric implants[32]. The RGD peptide also binds the $\alpha_V\beta_3$ integrin, which plays a central role in endothelial cell function and vascularization[33].

The present research focused on a UV-light-labile cage. This light trigger is limited for *in vivo* applications in terms of spatial resolution and depth of penetration because of the significant attenuation and scattering due to the optical properties of biological tissue and target biomaterials. However, we expect that photosensitive groups with near-infrared response regimes would provide for enhanced tissue penetration and reduced scattering. Owing to the high degree of spatiotemporal control afforded by light and the availability of various photosensitive groups, we anticipate that this strategy will find widespread adoption in biomedical applications requiring precise spatiotemporal bioligand presentation. Exemplary applications include directed host–material integration and vascularization, antigen recognition and tolerance induction for immunoengineering, targeting of nano/microparticles to local sites in cancer and inflammatory disorders, and generation of stem cell niches with dynamic bioligand presentation.

Methods

RGD peptides and hydrogels. Synthetic protocols are included in the Supplementary Information. Synthesis of the caged RGD peptide has been described previously[14]. Caged RDG peptide and fluorescein and cysteine-containing peptides were synthesized using similar methods described in Supplementary Information. Acrylated caged RGD peptide was generated by reacting a 1.1:1 molar ratio of acryl–PEG–SVA (Laysan Bio) with the primary amine of the caged RGD peptide for 4 h in $NaHCO_3$ buffer (pH = 8.2). PEGylated control RGD and scrambled RDG peptides (Peptides International) were generated in the same fashion. Acrylated peptides were dialysed and lyophilized for storage at −20 °C. Peptide acrylation was confirmed by matrix-assisted laser desorption/ionization mass spectrometry.

PEGDA hydrogels were prepared using a mixture of 10% PEGDA (relative molecular mass 3,400 (M_r 3.4K), Laysan Bio) and 0.05% Irgacure 2959 (BASF) in phosphate-buffered saline. These precursors were crosslinked in a sterilized silicon mould mounted to a glass coverslip sealed by a Sigmacote-coated microscope slide. Hydrogels were crosslinked using an UV light table (λ = 351 nm, 10 mW cm^{-2}) for 15 min. Bulk gels were functionalized with a thin top gel (25 µl) consisting of 8% PEGDA and 2% acrylated peptide and crosslinked using free-radical polymerization using TEMED and ammonium persulphate. This chemical polymerization resulted in a 50-µm-thick functionalized gel that was mechanically integrated onto the bulk hydrogel.

For PEG-maleimide gels, 4-arm PEG-maleimide macromers (M_r20K, Laysan Bio) were functionalized with cysteine-containing RGD or RDG peptides and crosslinked with a protease-degradable peptide (GCRDVPMSMRGGDRCG) as previously described[24]. The final peptide density in these gels was 2.0 mM. Hydrogels were prepared as discs (8 mm diameter, 2 mm thick) or polymerized directly *in situ* (75 µl).

Hydrogels were prepared using sterile filtered components under sterile conditions. Precursor solutions and hydrogels were tested using *Limulus* amoebocyte lysate assay and found to be endotoxin-free, with values well below the 20 EU per device as specified by ISO10993 standards.

UV light exposure system. A custom-built UV light exposure system consisting of an X-Cite 120 Arc Lamp (Exfo), collimator, band-pass filter, VS14/25 shutter and VMM-T1 Shutter Driver Controller (Uniblitz) was used for all *in vitro* and *in vivo* experiments.

***In vitro* cell adhesion and outgrowth.** NIH3T3 fibroblasts (20,000 cm^{-2}) were cultured overnight on peptide-functionalized or unmodified PEGDA hydrogels. Cells were labelled with the Live/Dead assay (Invitrogen) and fluorescence images were acquired in a Nikon TE-300 microscope with a ×20 objective and Spot RT digital camera. Cell densities were quantified using in-house macros in ImageJ.

IMR-90 fibroblasts were detached, pelleted and pipetted into polymerizing PEG-maleimide gels to encapsulate the cell pellet within gel. After 30 min, cell medium was added. Cell outgrowth sprout length was analysed at 24 h post-encapsulation using ImageJ.

Implantation of hydrogels and transdermal UV light exposure. Sterile, endotoxin-free hydrogels (8 mm diameter, 1 mm thick), were implanted subcutaneously (2 implants per mouse) following IACUC-approved procedures in 6–10-week-old male Balb/c mice (Jackson Laboratories). The custom-built UV light exposure system was used for transdermal irradiation. At prescribed time points, mice were anaesthetized and the skin in the vicinity of the implant was treated with depilatory cream to remove hair and exposed to UV light (λ = 351 nm, 20 mW cm^{-2}) for 10 min.

To measure UV light attenuation through skin, the dermal layer of the ventral and dorsal sides of Balb/c mice euthanized following IACUC-approved methods was removed and cut into 2 cm × 2 cm squares and kept in ice-cold PBS. Dermal layer thickness was then measured in triplicate using a digital calliper (Storm Equipment). The percentage of UV light attenuation was measured in triplicate for each piece of derma using a UVX radiometer (UVP). For Beer's law analysis, data for UV light attenuation as a function of skin thickness were fitted with a single exponential curve using GraphPad Prism 6.0.

For *in vivo* uncaging efficiency studies, CMNB-caged fluorescein was acrylated with acryl–PEG–SVA using a 1:1.1 ratio and DMF/DIPEA coupling conditions (Supplementary Information). Caged fluorescein-functionalized PEGDA hydrogels were generated in the same manner as described for RGD peptide-presenting hydrogels. Pre-exposed and unexposed caged fluorescein-presenting gels and control bare hydrogels were implanted subcutaneously in mice, and exposed to UV light transdermally at defined time points. Following euthanization, implants were recovered and fluorescence imaged using a Nikon TE-300 microscope and quantified using ImageJ.

For transdermal patterning studies, an exposure mask consisting of a large sheet of aluminium foil with a central 0.9 mm hole created with a 20-gauge needle was prepared. Anaesthetized mice were exposed to UV light for 10 min through the mask gently pressed onto the skin with the hole aligned over the centre of the implanted hydrogel. At day 1, mice were euthanized and implants were extracted and washed in cold PBS followed by fixation in 4% paraformaldehyde for 30 min. Cells were stained with DAPI and explants were imaged using a Nikon Eclipse Ti microscope connected to a Nikon C2+ confocal module. Cell adhesion and patterning were quantified using ImageJ.

For histological analyses of fibrous encapsulation, explants were fixed in formalin and embedded using the Immunobed Kit (Polysciences). Tissue sections (2 µm thick) were stained by Mason's trichrome stain, imaged and collagenous capsule thickness was analysed in ImageJ.

Vascularization. RGD or RDG peptide-functionalized PEG-maleimide macromers were mixed with recombinant human VEGF-165 (R&D, 10 µg ml^{-1} final concentration) and crosslinking peptides, and the resulting mixture (75 µl) was directly polymerized within subcutaneous pockets in the backs of mice. At day 14, mice were euthanized and the hydrogels explanted, washed with ice-cold PBS, and fixed in 10% formalin overnight. Whole-mounted implants were cut in half, blocked with 3% bovine serum albumin, and stained for either CD31 and α-smooth muscle actin or CD68 and NIMP-R14 (Abcam). The secondary antibodies used were either conjugated to AlexaFluor488 or AlexaFluor555 (Invitrogen). Explants were then stained with DAPI and imaged using a Nikon Eclipse Ti microscope connected to a Nikon C2+ confocal module. 2D images over the sample thickness were acquired to generate 3D reconstructions using a Nikon C2+ laser scanning confocal head on a Nikon Eclipse-Ti microscope and Elements software to image cells and structures within the hydrogel.

To label functional blood vessels, DyLight488-conjugated tomato lectin (1 mg ml^{-1}) was injected through the tail vein and allowed to circulate for 20 min. Mice were then perfused with 0.4% papaverine in saline through the left ventricle and bled through the inferior vena cava. The circulatory system was then perfused with 50 ml of 1% papaverine-containing saline for 5 min. Hydrogels were explanted, fixed in formalin and whole mounted on microscope slides. 2D images over the sample thickness were acquired to generate 3D reconstructions using a Nikon C2+ laser scanning confocal head on a Nikon Eclipse-Ti microscope and Elements software to image vessels within the hydrogel.

Statistical analyses. Statistical analyses were performed using GraphPad Prism 6.0. For normally distributed data with equal variances, one-way ANOVA with Tukey's multiple comparison test was used. For data that did not satisfy the requirements for ANOVA, non-parametric Kruskal–Wallis tests with Bonferroni–Dunn's multiple comparison tests were used. A p value < 0.05 was considered significant. Nonlinear regression analyses were also performed in GraphPad Prism 6.0.

Received 24 November 2013; accepted 31 October 2014; published online 15 December 2014

References

1. Hynes, R. O. The extracellular matrix: Not just pretty fibrils. *Science* **326,** 1216–1219 (2009).
2. Hynes, R. O. Integrins: Bidirectional, allosteric signaling machines. *Cell* **110,** 673–687 (2002).
3. Wolfenson, H., Lavelin, I. & Geiger, B. Dynamic regulation of the structure and functions of integrin adhesions. *Dev. Cell* **24,** 447–458 (2013).
4. Schiller, H. B. & Fassler, R. Mechanosensitivity and compositional dynamics of cell-matrix adhesions. *EMBO Rep.* **14,** 509–519 (2013).
5. Kumar, S. & Weaver, V. M. Mechanics, malignancy, and metastasis: The force journey of a tumor cell. *Cancer Metast. Rev.* **28,** 113–127 (2009).
6. Ranga, A. & Lutolf, M. P. High-throughput approaches for the analysis of extrinsic regulators of stem cell fate. *Curr. Opin. Cell Biol.* **24,** 236–244 (2012).
7. Fisher, O. Z., Khademhosseini, A., Langer, R. & Peppas, N. A. Bioinspired materials for controlling stem cell fate. *Acc. Chem. Res.* **43,** 419–428 (2010).
8. Pashuck, E. T. & Stevens, M. M. Designing regenerative biomaterial therapies for the clinic. *Sci. Transl. Med.* **4,** 160sr164 (2012).
9. Rice, J. J. *et al.* Engineering the regenerative microenvironment with biomaterials. *Adv. Healthc. Mater.* **2,** 57–71 (2013).
10. Vogel, V. & Sheetz, M. Local force and geometry sensing regulate cell functions. *Nature Rev. Mol. Cell Biol.* **7,** 265–275 (2006).
11. DeForest, C. A., Polizzotti, B. D. & Anseth, K. S. Sequential click reactions for synthesizing and patterning three-dimensional cell microenvironments. *Nature Mater.* **8,** 659–664 (2009).
12. Lohmuller, T. *et al.* Nanopatterning by block copolymer micelle nanolithography and bioinspired applications. *Biointerphases* **6,** 1–12 (2011).
13. Stephanopoulos, N., Ortony, J. H. & Stupp, S. I. Self-assembly for the synthesis of functional biomaterials. *Acta Mater.* **61,** 912–930 (2013).
14. Petersen, S. *et al.* Phototriggering of cell adhesion by caged cyclic RGD peptides. *Angew. Chem. Int. Ed.* **47,** 3192–3195 (2008).
15. Yeo, W. S., Yousaf, M. N. & Mrksich, M. Dynamic interfaces between cells and surfaces: Electroactive substrates that sequentially release and attach cells. *J. Am. Chem. Soc.* **125,** 14994–14995 (2003).
16. Ohmuro-Matsuyama, Y. & Tatsu, Y. Photocontrolled cell adhesion on a surface functionalized with a caged arginine-glycine-aspartate peptide. *Angew. Chem. Int. Ed.* **47,** 7527–7529 (2008).
17. Liu, D. B., Xie, Y. Y., Shao, H. W. & Jiang, X. Y. Using azobenzene-embedded self-assembled monolayers to photochemically control cell adhesion reversibly. *Angew. Chem. Int. Ed.* **48,** 4406–4408 (2009).
18. Wirkner, M. *et al.* Triggered cell release from materials using bioadhesive photocleavable linkers. *Adv. Mater.* **23,** 3907–3910 (2011).
19. Boekhoven, J., Rubert Perez, C. M., Sur, S., Worthy, A. & Stupp, S. I. Dynamic display of bioactivity through host-guest chemistry. *Angew. Chem. Int. Ed.* **52,** 12077–12080 (2013).
20. Kloxin, A. M., Kasko, A. M., Salinas, C. N. & Anseth, K. S. Photodegradable hydrogels for dynamic tuning of physical and chemical properties. *Science* **324,** 59–63 (2009).
21. Mosiewicz, K. A. *et al.* *In situ* cell manipulation through enzymatic hydrogel photopatterning. *Nature Mater.* **12,** 1072–1078 (2013).
22. Elisseeff, J. *et al.* Transdermal photopolymerization for minimally invasive implantation. *Proc. Natl Acad. Sci. USA* **96,** 3104–3107 (1999).
23. Anderson, J. M., Rodriguez, A. & Chang, D. T. Foreign body reaction to biomaterials. *Semin. Immunol.* **20,** 86–100 (2008).
24. Phelps, E. A. *et al.* Maleimide cross-linked bioactive PEG hydrogel exhibits improved reaction kinetics and cross-linking for cell encapsulation and *in situ* delivery. *Adv. Mater.* **24,** 64–70 (2012).
25. Franz, S., Rammelt, S., Scharnweber, D. & Simon, J. C. Immune responses to implants—A review of the implications for the design of immunomodulatory biomaterials. *Biomaterials* **32,** 6692–6709 (2011).
26. Phelps, E. A., Headen, D. M., Taylor, W. R., Thule, P. M. & Garcia, A. J. Vasculogenic bio-synthetic hydrogel for enhancement of pancreatic islet engraftment and function in type 1 diabetes. *Biomaterials* **34,** 4602–4611 (2013).
27. Phelps, E. A., Landazuri, N., Thule, P. M., Taylor, W. R. & Garcia, A. J. Bioartificial matrices for therapeutic vascularization. *Proc. Natl Acad. Sci. USA* **107,** 3323–3328 (2010).
28. Lynn, A. D., Blakney, A. K., Kyriakides, T. R. & Bryant, S. J. Temporal progression of the host response to implanted poly(ethylene glycol)-based hydrogels. *J. Biomed. Mater. Res. A* **96,** 621–631 (2011).
29. Dreaden, E. C., Alkilany, A. M., Huang, X., Murphy, C. J. & El-Sayed, M. A. The golden age: Gold nanoparticles for biomedicine. *Chem. Soc. Rev.* **41,** 2740–2779 (2012).
30. Timko, B. P. *et al.* Near-infrared-actuated devices for remotely controlled drug delivery. *Proc. Natl Acad. Sci. USA* **111,** 1349–1354 (2014).
31. Xia, Y. *et al.* Gold nanocages: From synthesis to theranostic applications. *Acc. Chem. Res.* **44,** 914–924 (2011).
32. Zaveri, T. D., Lewis, J. S., Dolgova, N. V., Clare-Salzler, M. J. & Keselowsky, B. G. Integrin-directed modulation of macrophage responses to biomaterials. *Biomaterials* **35,** 3504–3515 (2014).
33. Brooks, P. C., Clark, R. A. & Cheresh, D. A. Requirement of vascular integrin alpha v beta 3 for angiogenesis. *Science* **264,** 569–571 (1994).

Acknowledgements

This work was supported by the Materials World Network Program grants DFG AOBJ 569628 (AdC) and NSF DMR-0909002 (A.J.G.) and the National Institutes of Health (NIH) grants R01-AR062368 and R01-AR062920 (A.J.G.). T.T.L. and J.R.G. were supported by the Cell and Tissue Engineering NIH Biotechnology Training Grant (T32 GM-008433).

Author contributions

T.T.L. and J.R.G. conducted all experiments, collected data and performed data analysis. J.I.P., S.W. and Z.S. synthesized and characterized caged compounds. A.S. performed the *in vivo* uncaging efficiency study, and A.S. and E.A.P. assisted with hydrogel development and implantation procedures. A.J.G. and A.d.C. developed the concept, and together with T.T.L. contributed to the planning and design of the project. T.T.L., A.d.C. and A.J.G. wrote the manuscript and all authors discussed the results and commented on the manuscript.

Additional information

Supplementary information is available in the online version of the paper. Reprints and permissions information is available online at www.nature.com/reprints. Correspondence and requests for materials should be addressed to A.J.G.

Competing financial interests

The authors declare no competing financial interests.

Bone regeneration using an alpha 2 beta 1 integrin-specific hydrogel as a BMP-2 delivery vehicle. **Biomaterials**

Biomaterials 35 (2014) 5453–5461

Contents lists available at ScienceDirect

Biomaterials

journal homepage: www.elsevier.com/locate/biomaterials

Bone regeneration using an alpha 2 beta 1 integrin-specific hydrogel as a BMP-2 delivery vehicle

Asha Shekaran [a,b,1], José R. García [b,c], Amy Y. Clark [b,c], Taylor E. Kavanaugh [a], Angela S. Lin [b,c], Robert E. Guldberg [b,c], Andrés J. García [b,c,*]

[a] Department of Biomedical Engineering, Georgia Institute of Technology and Emory University, 313 Ferst Drive, Atlanta, GA 30332, USA
[b] Petit Institute for Bioengineering and Biosciences, Georgia Institute of Technology, 315 Ferst Drive, Atlanta, GA 30332, USA
[c] School of Mechanical Engineering, Georgia Institute of Technology, 801 Ferst Drive, Atlanta, GA 30332, USA

ARTICLE INFO

Article history:
Received 23 January 2014
Accepted 21 March 2014
Available online 13 April 2014

Keywords:
Integrin-specific
Hydrogel
Polyethylene glycol
Bone healing
BMP-2
Protein delivery

ABSTRACT

Non-healing bone defects present tremendous socioeconomic costs. Although successful in some clinical settings, bone morphogenetic protein (BMP) therapies require supraphysiological dose delivery for bone repair, raising treatment costs and risks of complications. We engineered a protease-degradable poly(ethylene glycol) (PEG) synthetic hydrogel functionalized with a triple helical, α2β1 integrin-specific peptide (GFOGER) as a BMP-2 delivery vehicle. GFOGER-functionalized hydrogels lacking BMP-2 directed human stem cell differentiation and produced significant enhancements in bone repair within a critical-sized bone defect compared to RGD hydrogels or empty defects. GFOGER functionalization was crucial to the BMP-2-dependent healing response. Importantly, these engineered hydrogels outperformed the current clinical carrier in repairing non-healing bone defects at low BMP-2 doses. GFOGER hydrogels provided sustained *in vivo* release of encapsulated BMP-2, increased osteoprogenitor localization in the defect site, enhanced bone formation and induced defect bridging and mechanically robust healing at low BMP-2 doses which stimulated almost no bone regeneration when delivered from collagen sponges. These findings demonstrate that GFOGER hydrogels promote bone regeneration in challenging defects with low delivered BMP-2 doses and represent an effective delivery vehicle for protein therapeutics with translational potential.

1. Introduction

Over 1 million bone grafting, bone excision and fracture repair surgeries are performed annually in the US at a cost of approximately $5 billion [1–4]. While autografts are the gold-standard therapy for non-healing bone defects, these grafts are limited by low availability as well as donor site pain and inflammation [5]. More recently, bone morphogenetic protein (BMP) therapies have emerged as promising alternatives to autografts and allografts. While BMP therapy has been successful in stimulating bone repair, the BMP doses used clinically are orders of magnitude higher [6] than physiological concentrations of BMP, resulting in high costs of treatment and complications such as ectopic bone formation, nerve injuries and inflammation [5,7–10]. Therefore, there is an unmet clinical need for improved BMP delivery vehicles which promote bone healing at low delivered BMP doses to enable safe, cost-effective and efficacious BMP treatments.

Hydrogels, water-swollen cross-linked polymer networks, offer tremendous advantages as vehicles for protein delivery due to their high cytocompatibility, low inflammatory profile, tailorable mechanics and biofunctionality, and injectable delivery method [11–13]. In particular, poly(ethylene glycol) (PEG) hydrogels are attractive because they resist non-specific protein adsorption, providing a 'clean-slate' background onto which desired biofunctionalities may be incorporated [14]. In addition, PEGs are widely used in FDA-approved therapeutic products as covalent modifiers of proteins and lipids [15], indicating a history of safety in patients. This has led to increasing research interest in delivering protein therapeutics such as BMP-2 and BMP-7 from synthetic and natural hydrogels to improve bone healing [16–19].

* Corresponding author. Petit Institute for Bioengineering and Biosciences, Georgia Institute of Technology, 315 Ferst Drive, Atlanta, GA 30332, USA.
E-mail address: andres.garcia@me.gatech.edu (A.J. García).
[1] Current address: Bioprocessing Technology Institute, 20 Biopolis Way, #06-01 Centros, Singapore 138668.

http://dx.doi.org/10.1016/j.biomaterials.2014.03.055
0142-9612/

We have recently established PEG hydrogels cross-linked via maleimide groups as an alternative cross-linking chemistry to address limitations associated with other widely used PEG hydrogel polymerization chemistries such as free-radical polymerization [20]. The maleimide reactive group is extensively used in peptide bioconjugate chemistry because of its fast reaction kinetics and high specificity for thiols at physiological pH. Maleimide-based cross-linking of PEG hydrogels has significant advantages over other cross-linking chemistries, namely well-defined hydrogel structure, stoichiometric incorporation of bioligands, increased cytocompatibility, improved cross-linking efficiency, and reaction time scales appropriate for *in situ* gelation for *in vivo* applications [20]. Additionally, the base macromer exhibits minimal toxicity and inflammation *in vivo* and is rapidly excreted via the urine [21] – important considerations in establishing the safety and translational potential of these hydrogels.

A critical consideration in the design of protein delivery systems for regenerative medicine is the incorporation of extracellular matrix (ECM)-mimetic adhesive ligands. Many orthopedic biomaterials utilize ECM-inspired peptides which promote integrin–ECM interactions to direct desired host cell responses [16,22,23] as these interactions regulate cell survival, proliferation, migration and differentiation [24–26]. In particular, the interaction of α2β1 integrin with collagen I is a crucial signal for osteoblastic differentiation and mineralization [27–32]. The hexapeptide sequence Gly–Phe–Hyp–Gly–Glu–Arg (GFOGER), residues 502–507 of the α1(I) chain of type I collagen, serves as the major recognition site for α2β1 integrin binding [33–35]. Our group has previously engineered a synthetic collagen I-mimetic GFOGER-containing peptide, GGYGGGP(GPP)$_5$GFOGER(GPP)$_5$GPC, which recapitulates the triple helical structure of native collagen (Fig. S1) and binds α2β1 integrin with high affinity and specificity [36]. GFOGER peptide coatings on plastic, titanium and poly(caprolactone) support equivalent levels of α2β1 integrin-mediated cell adhesion as native collagen I [36], promote osteoblastic differentiation *in vitro* [22,37], improve fixation of metal implants to rat cortices [22], and enhance bone healing in rat femur defects [38]. In contrast to the collagen I-mimetic GFOGER peptide, the widely used bioadhesive RGD peptides bind primarily to the αvβ3 integrin and do not have intrinsic osteogenic properties [39–41].

We hypothesized that presentation of the pro-osteogenic α2β1 integrin-specific GFOGER peptide to host cells combined with sustained release of low doses of BMP-2 would direct endogenous stem cell differentiation *in vivo* and promote bone healing. Therefore, we synthesized matrix metalloproteinase (MMP)-degradable PEG-maleimide hydrogels functionalized with GFOGER and incorporating recombinant human BMP-2. In order to test this hypothesis, we implanted protease-degradable GFOGER-modified PEG hydrogel BMP-2 carriers within critical-sized, non-healing murine radial bone defects in order to evaluate their effects on bone regeneration.

2. Materials and methods

2.1. GFOGER-modified PEG hydrogel synthesis

GFOGER peptide, GGYGGGP(GPP)$_5$GFOGER(GPP)$_5$GPC (Activotec), four-arm, maleimide-end functionalized (>95%) PEG macromer (PEG-MAL, 20 kDa, Laysan Bio), GRGDSPC (RGD adhesive peptide), and GCRDVPMSMRGGDRCG (VPM) cross-linker peptide (AAPTEC), and rhBMP-2 (R&D Biosystems) were used. PEG-MAL hydrogels (4% wt/v) were synthesized by reacting PEG-MAL with adhesive peptides (RGD or GFOGER) followed by mixing in BMP-2 and VPM cross-linker at a volume ratio of 2:1:1:1 at the required concentrations to obtain the desired final concentrations of the adhesive peptide (0.5–2.0 mM) and BMP-2 (0.03, 0.06 or 0.3 μg per 1.5 μL hydrogel implant). The concentration of VPM used for the synthesis of each hydrogel was calculated to match the number of cysteine residues on the peptide cross-linker with the number of free (unreacted) maleimide groups remaining in the adhesive peptide-functionalized PEG-maleimide solution. The mixture of peptide-functionalized PEG-maleimide, BMP-2 and VPM cross-linker was incubated at 37 °C for 2–6 h to allow for cross-linking before adding PBS to the hydrogels. For *in vitro* studies, thin gel discs were fabricated by covering polymerizing gel solutions with sterile Sigmacote-treated coverslips. For *in vivo* studies, hydrogel (1.5 μL) was cast within 4-mm long polyimide tube sleeves with laser machined 200 μm diameter holes to improve nutrient transport and cell invasion into the defect. All hydrogels used for *in vivo* studies contained 4% (wt/v) PEG-maleimide and 2.0 mM adhesive peptide. Collagen sponges were cut with a 1 mm diameter biopsy sponge and placed within the polyimide sleeves, injected with a BMP-2 solution at an equivalent dose as was loaded in the GFOGER hydrogels and incubated for 10 min at room temperature to allow for adsorption to the collagen sponge prior to implantation.

2.2. In vitro assays

hMSCs (Lonza) were cultured in MSCGM (Lonza) and seeded (10,000 cells/cm^2) on hydrogel surfaces. Cells were cultured for up to 21 days in osteogenic media (Lonza). After 3 days of culture in osteogenic media, cells were incubated in 2 μM calcein and 4 μM ethidium homodimer for 30 min for Live/Dead staining and imaged on a Zeiss fluorescence microscope. At 14 days hMSCs were lysed and assayed for alkaline phosphatase activity (ALP) by incubating with MUP substrate. hMSCs were scraped in PBS, transferred to cold 50 mM Tris–HCl and sonicated to lyse the cells. The total protein content for each lysate sample was determined using a BCA assay kit (Thermo Scientific). Samples were diluted to the same total protein content before assaying for ALP. Samples and ALP standards were loaded into a 96-well plate, then incubated with MUP substrate at 37 °C for 1 h and read at 360 nm excitation/465 nm emission. Mineral deposition at 21 days post-induction was assayed by Alizarin Red staining and extraction. Cells were fixed in 10% formalin, rinsed in water and incubated in 2% Alizarin Red solution for 20 min. After 4 washes in water, the stained cells were scraped in 10% acetic acid and heated to 85 °C for 10 min. The supernatant was collected after centrifugation, neutralized with 10% ammonium hydroxide and read at 405 nm.

2.3. Radial defect surgery

All animal experiments were performed with the approval of the Georgia Tech Animal Care and Use Committee with veterinary supervision and within the guidelines of the Guide for the Care and Use of Laboratory Animals. B6129SF2/J wild-type male mice (8–10 week old, Jackson Laboratories) were anesthetized under isoflurane, and fur was removed from the right forelimb. The forelimb was then swabbed with chlorohexidine and alcohol and a 1.5-cm incision was made in the skin. Muscle tissue overlying the ulna and radius were blunt dissected, and 2.5 mm defects were made in the right radius using a custom-machined bone cutter, while leaving the ulna intact. Hydrogel or collagen sponge placed within polyimide sleeves were implanted into the defect by fitting the sleeve over the radius at the proximal and distal ends of the defect, so that the hydrogel or collagen sponge filled the defect space. The incision was then closed with vicryl suture and wound clips. Mice were provided with a single dose of slow-release buprenorphine for pain relief and were monitored post-surgery for signs of distress, normal eating habits and movement.

2.4. BMP-2, GFOGER in vivo retention

GFOGER and BMP-2 were labeled with Vivotag 680 and Vivotag 800 IR dyes, respectively. Labeled GFOGER and BMP-2 were incorporated into PEG hydrogels and implanted into mice as described earlier. GFOGER peptide and BMP-2 retention within the defect site ($n = 6$) was analyzed by scanning mouse forelimbs (FMT 4000) on the 680 or 790 laser channels (Perkin Elmer, 1 mm source density, 65 source points per scan). The signal was quantified by placing 3D regions of interest markers around the forelimb, using a 0.0 nM IR dye threshold and normalizing to the day 0 value.

2.5. Faxitron/μCT imaging and mechanical testing

Radial defects were imaged with the MX-20 Radiography System (Faxitron, 23 kV energy setting, 15 s scan time). For μCT scanning, a 3.2 mm length of the radius centered around the 2.5 mm radial defects was scanned in anesthetized, live subjects using a VivaCT system (Scanco Medical, 145 μA intensity, 55 kVp energy, 200 ms integration time, and 15 μm resolution). Bone formation was evaluated by contouring 2D slices to include only the radius and applying a Gaussian filter (sigma = 1, support = 1, threshold = 540 mg HA/ccm). 3D μCT reconstructions display the full 3.2 mm length of radius scanned. However, in order to ensure that only new bone formation was measured, quantification of bone volume and mineral density within the defect was performed by evaluating only the middle 2.0 mm of defect.

Torsion to failure testing was performed on 8-week radial defects ($n = 5–9$) as described [42] with modifications. The radii and ulnae were excised post-euthanasia, wrapped in PBS-soaked gauze and stored at −20 °C. On the day of testing, the bones were thawed and potted in woods–metal within potting blocks. After the ulna was cut, the potting blocks were tested using a Bose Electroforce ELF 3200 system. The radius was torqued to failure at a rate of 3° per second and the torque was measured using a 0.07 N m torque sensor (Transducer Techniques) (Fig. S3).

2.6. Histology and stem cell recruitment

For histology, bones were fixed in 10% neutral-buffered saline, decalcified and embedded in Immunobed or MMA. Sections (2 μm thick) were deplasticized and stained with Safranin-O/Fast Green. To quantify osteoprogenitor cell recruitment, radii were excised 7 days post-surgery. Cells were harvested by a 45 min collagenase I incubation of tissue and stained with anti-CD45 (FITC) and anti-CD 90 (APC) antibodies (Biolegend) and analyzed by flow cytometry (Accuri C6 cytometer, FlowJo software) to determine the proportion CD45 /CD90^{+} cells in the defect.

2.7. Statistical analyses

Error bars graphs represent SEM. Statistical comparisons between multiple groups were made by one-way ANOVA with post-hoc Tukey tests for parametric data, by Kruskal Wallis test with Dunn's post-hoc test for non-parametric data (bridging scores), and by *t*-test for comparisons of two groups in Graphpad. A p value of <0.05 was considered significant.

3. Results

3.1. Synthesis of GFOGER/BMP-2 hydrogels

We synthesized MMP-degradable, GFOGER-functionalized hydrogels with encapsulated BMP-2 in a facile two-step reaction (Fig. 1). The terminal maleimide groups on the 4-armed PEG macromer (Fig. 1A and B) underwent a Michael addition reaction with free sulfhydryl groups on the cysteine residues of the GFOGER peptide, resulting in a GFOGER-tethered PEG-maleimide precursor (Fig. 1B). The subsequent reaction of the GFOGER-functionalized PEG-maleimide macromer with a bi-cysteine cross-linking peptide (VPM) [43,44], containing an MMP cleavage site, resulted in the formation of an insoluble cross-linked PEG hydrogel network (Fig. 1B). In this modular system, BMP-2 can be incorporated into the hydrogel by physical entrapment during network cross-linking. In the presence of cell-secreted proteases, the VPM cross-linker is cleaved, disrupting the PEG network and releasing the entrapped BMP-2 (Fig. 1B). We chose a peptide cross-linker which undergoes rapid degradation in response to MMP in order to tailor the *in vivo* degradation rate of the PEG hydrogels to obtain a half-life of 1–2 weeks. To determine the efficiency at which GFOGER ligand was covalently tethered to PEG-maleimide, we measured the free sulfhydryl groups in reaction mixtures of GFOGER and PEG-maleimide at varying maleimide:GFOGER molar ratios. At a molar ratio higher than 5, ~100% of added GFOGER was tethered to PEG-maleimide (Fig. S2), providing precise control of GFOGER density within the hydrogel.

3.2. In vitro cell activities on engineered hydrogels

We first evaluated the potential of GFOGER-functionalized PEG hydrogels to direct osteoblastic differentiation in human mesenchymal stem cells (hMSCs). GFOGER-functionalized hydrogels were compared to hydrogels modified with RGD peptides as RGD is the most commonly used adhesive peptide in the biomaterials field. We tested the levels of *in vitro* osteoblastic differentiation of hMSCs cultured on hydrogel surfaces. GFOGER- and RGD-functionalized hydrogels supported dose-dependent levels of hMSC adhesion and spreading (Fig. 2A), while significantly fewer cells adhered to PEG-only (no ligand) gels or scrambled RDG peptide-modified gels and these cells remained rounded (Fig. 2A). hMSCs exhibited high viability on both GFOGER- and RGD-tethered hydrogels at 3 days in culture (Fig. 2B). Despite comparable levels of adhesion and viability on GFOGER- and RGD-functionalized gels, hMSCs on GFOGER-functionalized hydrogels exhibited 94% and 40% increases in alkaline phosphatase activity and Alizarin Red staining, respectively, compared to RGD-presenting gels (Fig. 2C).

3.3. Repair of non-healing bone defects

We evaluated the potential of GFOGER-functionalized hydrogels to promote bone repair in a murine non-healing radial bone defect model [45]. If left untreated, this critical-sized defect does not heal over the experimental period and provides a stringent bone repair model analogous to non-healing, long bone defects in humans. To improve the ease of handling, we pre-cast hydrogels within polyimide tube sleeves. The sleeve walls were laser machined with holes to improve nutrient transport and cell migration across the sleeve walls as including perforations within a mesh sleeve surrounding a BMP-containing hydrogel has been shown to improve healing outcomes [46]. We implanted hydrogel constructs into 2.5 mm-long unilateral murine radial critical-sized defects (Fig. 2D) and evaluated bone healing by radiography and micro-computed tomography (μCT) at 4 and 8 weeks post-surgery. Defects treated with GFOGER-functionalized hydrogels exhibited significantly improved bone healing compared to those treated with no

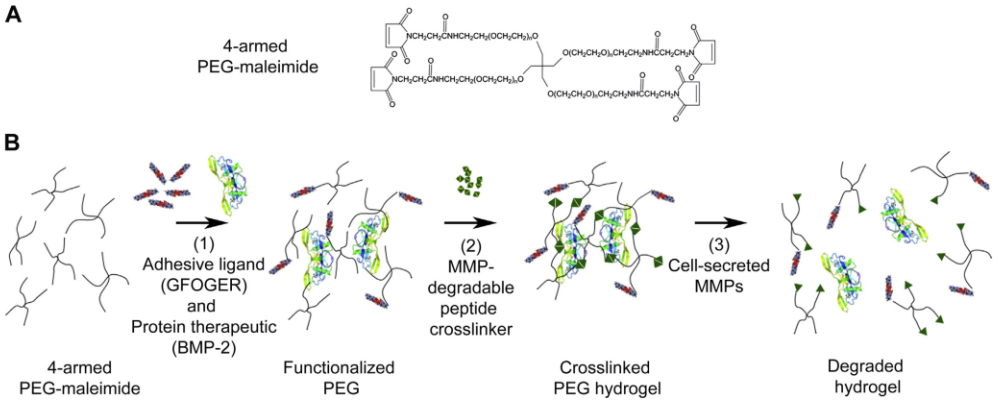

Fig. 1. Protease-degradable integrin-specific GFOGER-modified PEG hydrogels are synthesized with precise control of GFOGER density. (A) Chemical structure of branched 4-armed PEG-maleimide. (B) Synthesis of GFOGER- and BMP-2-functionalized hydrogels.

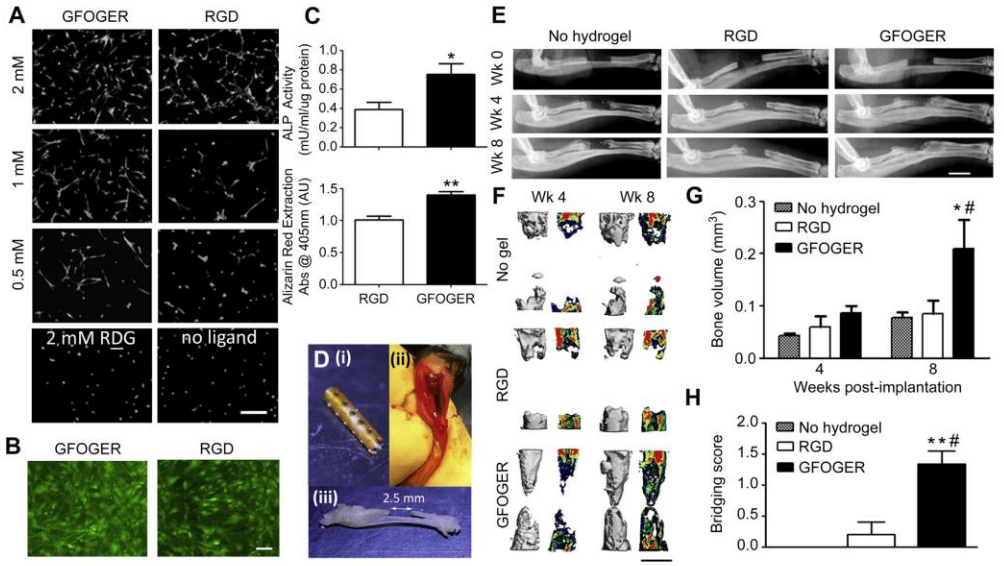

Fig. 2. GFOGER-functionalized hydrogels promote differentiation and bone healing. (A) Calcein-stained hMSCs on GFOGER- and RGD-tethered gels at varying densities of ligand and non-adhesive controls 1 day after seeding, scale bar 50 μm, $n = 3$. (B) Live/dead stained hMSCs on 2.0 mM GFOGER- and 2.0 mM RGD-presenting hydrogels 3 days after osteogenic induction, scale bar 20 μm, $n = 3$. (C) ALP activity at 14 days, $n = 4$ (top) and Alizarin Red stain for mineralization of hMSCs at 21 days, $n = 4$ (bottom). Hydrogels were pre-cast in a polyimide sleeve with 200 μm diameter holes along tube walls. (D) Pictures indicate (i) a polyimide tube sleeve, (ii) radial defect with hydrogel-sleeve implant, hydrogel stained blue, and (iii) excised radius and ulna with 2.5 mm radial defect (iii). (E) Radiographic images of radial defects treated with hydrogel, scale bar 2 mm. (F) 3D μCT reconstructions (left) and mineral density mappings on sagittal sections of the defects (right), scale bar 1 mm, $n = 5$–6. (G) μCT measures of bone volume within defects, $n = 5$–6. (H) Bridging scores for defects receiving implants containing no hydrogel, or hydrogels functionalized with RGD or GFOGER, $n = 5$–6, 0: < half bridged, 1: >half bridged, and 2: completely bridged − 8 weeks post-surgery. $^{*}p < 0.05$, $^{**}p < 0.01$ compared to RGD, #$p < 0.05$, ##$p < 0.01$ compared to No hydrogel.

hydrogel (defects received an empty polyimide sleeve implant) and RGD-modified gel implants (Fig. 2E–H). Bone volume at 8 weeks for defects treated with GFOGER-functionalized gel was 140% and 150% higher than no hydrogel and RGD-presenting gel-treated defects, respectively (Fig 2F,G). There was no difference in bone volume between RGD-modified gels and empty defects. Furthermore, while minimal bone formation and no defect bridging was observed in all subjects treated with RGD-functionalized gel and empty defect controls, several defects treated with GFOGER-functionalized hydrogels were close to full bridging after 8 weeks (Fig. 2E–F). We scored the degree to which defects were bridged 8 weeks after implantation according to the following criteria: 0 – defect is less than half bridged, 1 – defect is more than half bridged, and 2 – defect is fully bridged. Bridging scores for GFOGER-functionalized hydrogels were higher than RGD-presenting gels and empty defects (Fig 2H). These results demonstrate that α2β1 integrin-specific GFOGER-functionalized hydrogels promote hMSC osteogenic differentiation and enhance bone repair compared to conventional RGD-tethered gels or treatment with no hydrogel.

3.4. Dose response of BMP-2 in hydrogels in bone repair

Because GFOGER-modified PEG hydrogels supported great enhancements in bone healing, we explored whether combining GFOGER gels with low doses of BMP-2 could yield further improvements in bone healing and bridge critical-sized segmental defects. Five groups were tested: implants containing no hydrogel (empty sleeve) as a negative control and GFOGER-functionalized hydrogels lacking BMP-2 (0 μg) or incorporating increasing BMP-2 doses (0.03, 0.06 and 0.3 μg, referred to as low, medium and high doses respectively). There was minimal bone healing in defects treated with no hydrogel and high levels of bone formation and almost complete bridging with treatment with GFOGER-functionalized hydrogels without BMP-2 (Fig. 3A–D). For the medium and high BMP-2 doses, defect bridging was observed by week 4 (Fig. 3B(i)), and for all BMP-2 doses, bone volumes were increased compared to no hydrogel implants, and bridging occurred by week 8 (Fig. 3A–C). Even within defects treated with the low BMP-2 dose, bone volume was 200% higher than defects which received no hydrogel (Fig. 3C). Treatment with all GFOGER-functionalized hydrogels including those lacking BMP-2 resulted in increased bridging scores compared to the no hydrogel treatment (Fig. 3D). Histological analysis revealed that PEG hydrogels were completely degraded by week 8, facilitating cell invasion into the defects (Fig. 3E). In addition, non-woven bone containing marrow compartments was formed in defects treated with GFOGER-functionalized hydrogels but not in the no hydrogel group (Fig. 3E). Importantly, low dose BMP-2 treatment within GFOGER-functionalized hydrogels induced bone defect bridging after 8 weeks without any structural change to the adjacent ulna (Fig. 3B(ii)). In mice receiving implants with the medium and high BMP-2 doses, radial defect bridging also occurred, but was accompanied by unintended alterations to the ulna (Fig. 3B(ii)). Treatment with medium dose BMP-2 resulted in expansion of the ulna around the radius, while for the high dose BMP-2 group, the ulna completely encircled the radius and fused with the radius

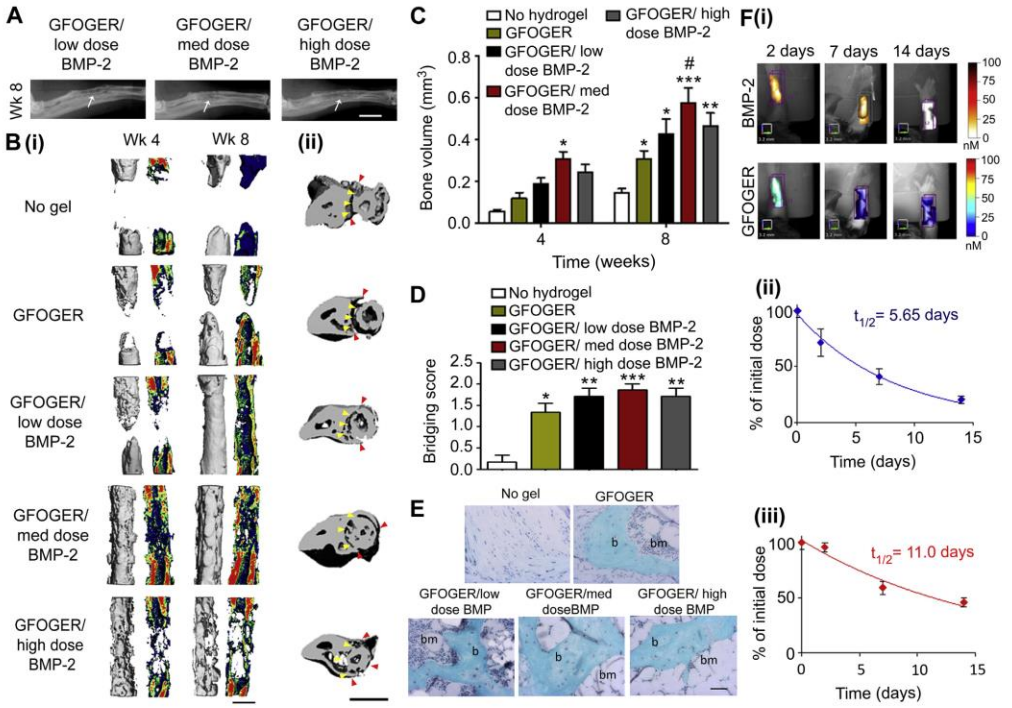

Fig. 3. GFOGER-functionalized PEG hydrogels with low dose BMP-2 bridge radial segmental defects without altering ulnar structure. (A) Radiographic images, white arrows indicate space between ulna and radius which is not present in the high BMP-2 dose image, scale bar 2 mm. (B) 3D μCT reconstructions of (i) radius in sagittal view (left) with mineral density mapping (right), and (ii) radius and ulna in transverse view. Yellow arrowheads indicate boundary between the ulna and radius prior to implantation, red arrowheads indicate the position of the ulna closest to the radius at 8 weeks, scale bar 1 mm. (C) μCT measures of bone formation, $n = 6–7$. (D) Scoring of defect bridging at 8 weeks, $n = 6–7$. (E) Sections stained with Safranin-O/Fast Green at the center of defect, scale bar 50 μm; b – bone, bm – bone marrow. (F) (i) Representative FMT images and FMT quantification of % implanted dose retained in radial defect space over time *in vivo* for (ii) high dose BMP-2 labeled with Vivotag 800 and (iii) GFOGER peptide labeled with Vivotag 680, $n = 6$. $^{*}p < 0.05$, $^{**}p < 0.01$, $^{***}p < 0.001$ compared to defect receiving no hydrogel implant, $^{\#}p < 0.05$ compared to GFOGER hydrogel. (For interpretation of the references to color in this figure legend, the reader is referred to the web version of this article.)

(Fig. 3B(ii)). These results highlight the adverse effects of excessive BMP-2 delivery, recapitulating off-target clinical results in humans [47], and underscore the importance of precise control of the dose and release mechanism of BMP-2.

Because BMP-2 release kinetics as well as scaffold degradation and cell invasion are important factors which contribute to tissue healing in response to implantable biomaterials, we examined the retention times of near infrared (IR) dye-labeled GFOGER peptide and BMP-2 in PEG hydrogels within the radial defect site using fluorescence molecular tomography (FMT). BMP-2 was localized within the defect site over a prolonged period of time (Fig. 3F). The half-life for BMP-2 was 5.65 days and more than 20% of the initial BMP-2 dose remained 14 days after surgery, indicating sustained release of BMP-2 from GFOGER hydrogels *in vivo* (Fig. 3F(ii)). The half-life of GFOGER peptide within the defect site was considerably longer than BMP-2 at 11.0 days and is an indication of the retention time of the bulk PEG polymer to which the peptide was tethered (Fig. 3D (iii)). This result confirms our targeted *in vivo* hydrogel degradation rate of 1–2 week half-life using the MMP-cleavable VPM cross-linker. Because GFOGER-functionalized hydrogels incorporating low dose BMP-2 supported localized bone formation and bridging within the radial defect without inducing any off-target alterations to bone volume or structure in the ulna, we used GFOGER gels with low BMP-2 dose (GFOGER/low BMP-2) delivery in subsequent analyses.

3.5. Contributions of GFOGER and BMP-2 to bone healing

A major advantage of the PEG-maleimide hydrogel platform is the ability to independently control its modular components to examine their relative contributions to tissue repair. We therefore systematically tested combinations of implants containing GFOGER peptide, low BMP-2 dose, or the combination of both. Four groups were tested (Fig. 4A): GFOGER/low BMP-2 (PEG/GFOGER/BMP-2), GFOGER/no BMP-2 (PEG/GFOGER), no ligand/low dose BMP-2 (PEG/BMP-2), and no ligand/no BMP-2 (PEG). GFOGER/low BMP-2 hydrogels supported robust healing and defect bridging within 8 weeks, while GFOGER/no BMP-2 gels induced significant bone formation and almost complete bridging (Fig. 4B–D, Fig. S2). GFOGER/low BMP-2 gels displayed enhancements in bone volume, defect bridging and maximum torque compared to groups lacking GFOGER (Fig. 4B–E). BMP-containing implants that lacked GFOGER

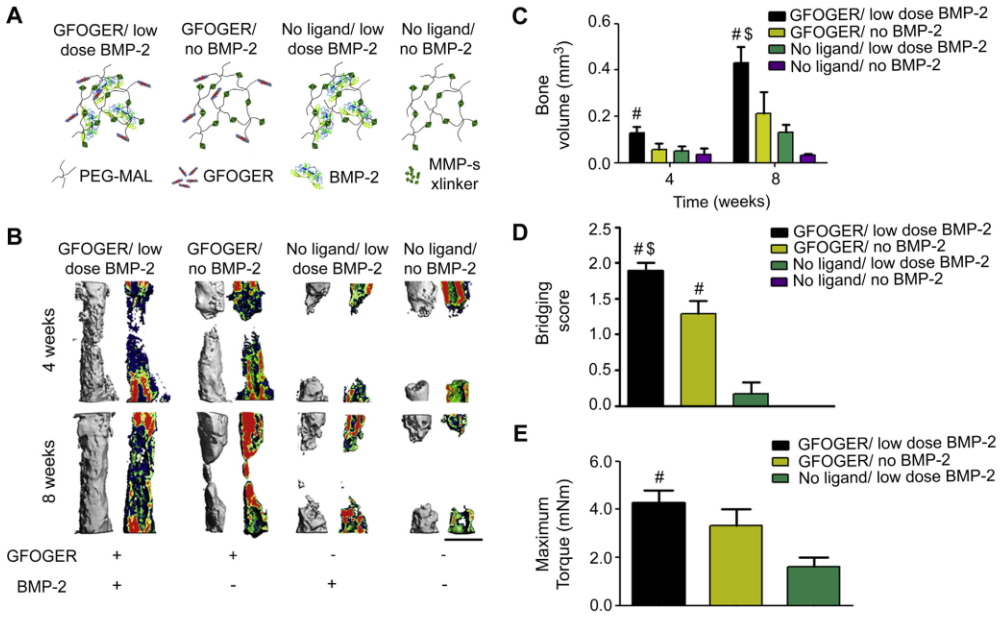

Fig. 4. GFOGER ligand is crucial to and BMP-2 improves bone healing in response to engineered hydrogel. (A) Cartoon of hydrogel formulations tested in this study, MMP x-linker – MMP-sensitive cross-linker. (B) 3D μCT reconstructions (left) and mineral density mappings on sagittal sections of the same defects (right), scale bar 1 mm. (C) μCT measures of bone formation at 4 and 8 weeks post-surgery. (D) Bridging scores for defects 8 weeks post-surgery. (E) Maximum torque values for radial samples 8 weeks after surgery. $^{\#}p < 0.05$ compared to No ligand/no BMP-2 gels, $^{\$}p < 0.05$ compared to No ligand/low dose BMP-2 gels. $n = 5$ for No ligand/no BMP-2 and $n = 6$–7 for other groups.

(no ligand/low dose BMP-2) gels supported no defect bridging and exhibited ~70% lower bone volume than GFOGER/low dose BMP-2 gels and 30% less bone volume than GFOGER/no BMP-2 gels (Fig 4C), indicating that the GFOGER peptide is critical to the bone repair activity of the engineered hydrogel. Taken together, these results demonstrate that GFOGER is critical to bone repair and BMP-2 further enhances the osteoreparative properties of these hydrogels.

3.6. Bone repair and osteoprogenitor recruitment compared to the standard carrier

In current clinical practice, BMP-2 is delivered by injecting a BMP-2 solution into collagen foams prior to implantation. Therefore, in order to compare our engineered biomaterial to the clinical standard, we examined the role of the delivery vehicle on bone formation in response to 0.03 μg BMP-2 dose, the lowest dose tested in the dose response study. Two groups were compared: GFOGER hydrogels and collagen sponges loaded with 0.03 μg BMP-2. μCT evaluation of bone volume within defects revealed that GFOGER/BMP-2 hydrogel implants improved bone healing compared to collagen sponge/BMP-2 implants by 200% and >300% at 4 and 8 weeks, respectively (Fig. 5A and B). Defects treated with GFOGER/BMP-2 hydrogels bridged consistently, whereas collagen sponge/BMP-2 treated defects exhibited minimal bone healing (Fig. 5A and B) with no bridging (Fig. 5C). Importantly, GFOGER/BMP-2 treated defects were mechanically robust and showed a 100% increase in maximum torque at 8 weeks compared to defects treated with collagen sponge/BMP-2 (Fig. 5D). Notably, the maximum torque levels for the defects treated with GFOGER/BMP-2 were equivalent to the maximum torque of intact radii (3.2 ± 0.3 mN m), demonstrating that the quality of the repair tissue is similar to native bone. Histological analysis at 8 weeks showed fibrous tissue with almost no bone tissue formation for collagen sponge/BMP-2, whereas defects treated with GFOGER/BMP-2 hydrogels exhibited abundant bone formation as well as establishment of bone marrow in the center of the defect (Fig. 5E). Both the collagen sponge and PEG hydrogel were fully degraded by 8 weeks after implantation (Fig. 5E).

Because BMP-2 release kinetics greatly impact bone healing, we compared the release rates of BMP-2 from GFOGER gels and collagen sponges in the bone defect using Vivotag 800-labeled BMP-2. GFOGER-functionalized hydrogels exhibited 30% higher levels of BMP-2 retained within the radial defect space at 1 day and 90% higher levels at 5 days post-implantation compared to the collagen sponge (Fig. 5F) by fluorescence molecular tomography. Because BMP-2 is known to have chemotactic effects on mesenchymal stem cells and osteoprogenitor cells [48], we evaluated the recruitment of $CD45^{-}/CD90^{+}$ osteoprogenitor stem cells to the defect site following the implantation of GFOGER/BMP-2 hydrogels or collagen sponge/BMP-2 (Fig. 5G). At 7 days post-implantation, there was a 300% increase in $CD45^{-}/CD90^{+}$ cells in defects treated with GFOGER/BMP-2 gels compared to collagen/BMP-2 (Fig. 5G). These results demonstrate that GFOGER-functionalized PEG hydrogels delivering BMP-2 outperform the current clinical standard delivery vehicle in terms of bone repair and provide sustained release of BMP-2 and enhanced osteoprogenitor stem cell recruitment.

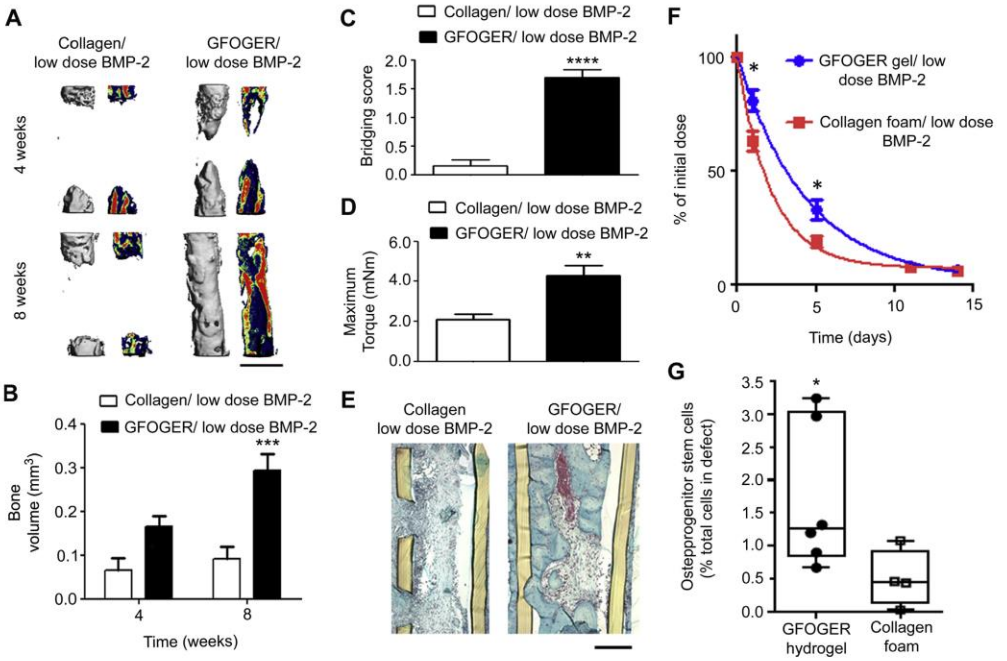

Fig. 5. BMP-2 delivery from GFOGER-functionalized gels improves bone regeneration compared to collagen foams. (A) 3D μCT reconstructions of radii (left) and mineral density sagittal sections (right), scale bar 1 mm. (B) μCT measures of bone volume in radial defects. (C) Bridging score at 8 weeks post-implantation $n = 13$. (D) Maximum torque values for 8 week radial samples subjected to torsion mechanical testing to failure $n = 5–9$. (E) Sections of 8 week radial samples stained with Safranin-O/Fast Green, scale bar 200 μm. (F) Retention of infrared dye-labeled BMP-2 at implanted defect site *in vivo* $n = 6$. (G) Quantification of $CD45^-/CD90^+$ osteoprogenitor cells present in defect 7 days post-implantation, $n = 4–6$. $^*p < 0.05$, $^{***}p < 0.001$ and $^{****}p < 0.0001$ compared to Collagen foam/low dose BMP-2.

4. Discussion

Bone grafts are widely used in clinical practice for spinal, foot and ankle fusions, revision arthroplasties, and treating large, non-healing bone defects. Because the gold-standard autograft treatments cause donor pain and are in limited supply [5] and processed allografts exhibit limited bioactivity or risks of infection [2,5,49,50], protein therapeutics are becoming extensively used in the clinic. However, BMP treatments present cost limitations [7] and clinical safety concerns [5,8–10], primarily because suboptimal growth factor carriers require BMP to be delivered at supraphysiological doses. Therefore, there is a strong motivation to engineer protein therapeutic delivery systems which offer greater safety and cost-effectiveness by reducing the therapeutic dose of growth factors required for healing of critical-sized bone defects.

Here, we engineered a hydrogel carrier functionalized with a collagen-mimetic, triple helical, integrin-specific peptide (GFOGER) which significantly enhanced bone healing compared to collagen sponges, the current clinical BMP-2 carrier. GFOGER-modified gels incorporating low doses of BMP-2 promoted osteoprogenitor cell recruitment to the defect site and produced robust repair and bridging of segmental bone defects within 8 weeks. Importantly, the repair tissue had equivalent mechanical strength to native bone. Furthermore, this result was achieved with GFOGER gels loaded with a low dose of BMP-2 which supported almost no bone formation within clinical standard collagen foam vehicles. These results show that GFOGER gels produce superior healing outcomes compared to current carriers for protein therapeutics. Follow-up studies with large animal models are required to fully establish the translational potential of these delivery vehicles.

The improved healing induced by the GFOGER-tethered PEG gels compared to collagen foams can be attributed to a combination of factors. First, in contrast to collagen foams [51], GFOGER-functionalized materials enhance bone formation without cell or protein co-delivery due to the intrinsic osteogenic bioactivity of the $\alpha2\beta1$ integrin-specific GFOGER peptide. Simple presentation of GFOGER within the hydrogel significantly enhanced bone formation, outperforming other adhesive peptides such as RGD. Second, GFOGER gels provided sustained release of encapsulated BMP-2 compared to the clinical collagen sponge carrier. This improvement in BMP-2 release kinetics from GFOGER gels is due to effective entrapment of BMP-2 within the tightly cross-linked hydrogel network and MMP-dependent gel degradation. In contrast, collagen foams have large micron-scale pores and release BMP-2 through protein desorption from scaffold surfaces, diffusion of BMP-2 from solution trapped in the pores, and collagenase-mediated degradation of the foams. Third, GFOGER-functionalized hydrogels support rapid MMP-mediated hydrogel degradation and cell invasion that allows for replacement of the carrier with repair tissue. Indeed, we demonstrated a 3-fold enhancement in

the recruitment of osteoprogenitor cells for GFOGER gels compared to collagen sponges.

The α2β1 integrin-specific PEG hydrogel BMP-2 carrier described in this study has potential for clinical translation because it demonstrates superior bone healing compared to the commonly used adhesive RGD peptide and collagen sponges and is a purely synthetic, well tolerated, and tunable system. GFOGER gels supported 150% more bone formation than RGD gels. Notably, the well-defined, synthetic nature of the GFOGER-functionalized PEG hydrogel carrier makes it amenable to scale-up in production and well-regulated quality control. Furthermore, the modularity of the PEG-maleimide hydrogels allows key properties such as degradation rate as well as the density or combinations of adhesive ligands and therapeutic proteins to be tuned to optimize or adapt the material for other applications.

5. Conclusion

This study highlights the bone regeneration potential of a synthetic PEG-maleimide hydrogel functionalized with the α2β1 integrin-specific GFOGER peptide as a BMP-2 carrier. GFOGER-functionalized hydrogels displayed intrinsic osteogenic activity, provided sustained release of BMP-2, underwent rapid degradation *in vivo*, bridged critical-sized bone defects at low BMP-2 doses, and exhibited improved bone repair compared to the collagen foams which are the clinical standard carriers. These findings underscore the effectiveness of targeting pro-osteogenic integrins to enhance bone regeneration and establish the GFOGER-modified PEG-maleimide hydrogel as an effective BMP-2 delivery vehicle with significant translational potential.

Author contributions

A.S. and A.J.G. designed all experiments. A.S., T.E.K., J.R.G. and A.Y.C. performed research and performed data analysis. A.S.L. and R.E.G. provided critical input on μCT and mechanical testing. A.S. and A.J.G. wrote the paper and all co-authors edited the manuscript.

Acknowledgments

We thank Ningtao Cheng for his assistance with mechanical testing and Aby Thyparambil and Robert Latour at Clemson University for CD analysis. The facilities at Clemson University were supported by NIH Grants 5P20RR021949 and 8P20GM103444. This work was funded by the National Institutes of Health (_100000002), USA (R01 AR062920, R01 AR062368). A.S. was supported by the Singaporean Agency for Science, Technology and Research (_501100001348).

Appendix A. Supplementary data

Supplementary data related to this article can be found at http://dx.doi.org/10.1016/j.biomaterials.2014.03.055.

References

[1] Bucholz RW. Nonallograft osteoconductive bone graft substitutes. Clin Orthop Relat Res 2002;395:44–52.
[2] Finkemeier CG. Bone-grafting and bone-graft substitutes. J Bone Joint Surg Am 2002;84-A(3):454–64.
[3] Giannoudis PV, Dinopoulos H, Tsiridis E. Bone substitutes: an update. Injury 2005;36(Suppl. 3):S20–7.
[4] Kretlow JD, Mikos AG. Review: mineralization of synthetic polymer scaffolds for bone tissue engineering. Tissue Eng 2007;13(5):927–38.
[5] De Long Jr WG, Einhorn TA, Koval K, McKee M, Smith W, Sanders R, et al. Bone grafts and bone graft substitutes in orthopaedic trauma surgery. A critical analysis. J Bone Joint Surg Am 2007;89(3):649–58.
[6] Schmidmaier G, Schwabe P, Strobel C, Wildemann B. Carrier systems and application of growth factors in orthopaedics. Injury 2008;39(Suppl. 2):S37–43.
[7] Desai BM. Osteobiologics. Am J Orthop (Belle Mead NJ) 2007;36(4 Suppl.):8–11.
[8] Carragee EJ, Hurwitz EL, Weiner BK. A critical review of recombinant human bone morphogenetic protein-2 trials in spinal surgery: emerging safety concerns and lessons learned. Spine J 2011;11(6):471–91.
[9] Yoon ST, Boden SD. Osteoinductive molecules in orthopaedics: basic science and preclinical studies. Clin Orthop Relat Res 2002;395:33–43.
[10] Bishop GB, Einhorn TA. Current and future clinical applications of bone morphogenetic proteins in orthopaedic trauma surgery. Int Orthop 2007;31(6):721–7.
[11] Mikos AG, Herring SW, Ochareon P, Elisseeff J, Lu HH, Kandel R, et al. Engineering complex tissues. Tissue Eng 2006;12(12):3307–39.
[12] Salinas CN, Anseth KS. Mesenchymal stem cells for craniofacial tissue regeneration: designing hydrogel delivery vehicles. J Dent Res 2009;88(8):681–92.
[13] Lutolf MP, Hubbell JA. Synthetic biomaterials as instructive extracellular microenvironments for morphogenesis in tissue engineering. Nat Biotechnol 2005;23(1):47–55.
[14] Ratner BD, Hoffman AS. Non-fouling surfaces. In: Buddy DR, Allan SH, Frederick JS, Jack EL, editors. Biomaterials science: an introduction to materials in medicine. Academic Press; 2013. pp. 241–7.
[15] Bailon P, Won CY. PEG-modified biopharmaceuticals. Expert Opin Drug Deliv 2009;6(1):1–16.
[16] Lutolf MP, Weber FE, Schmoekel HG, Schense JC, Kohler T, Muller R, et al. Repair of bone defects using synthetic mimetics of collagenous extracellular matrices. Nat Biotechnol 2003;21(5):513–8.
[17] Mariner PD, Wudel JM, Miller DE, Genova EE, Streubel SO, Anseth KS. Synthetic hydrogel scaffold is an effective vehicle for delivery of INFUSE (rhBMP2) to critical-sized calvaria bone defects in rats. J Orthop Res 2013;31(3):401–6.
[18] Reichert JC, Cipitria A, Epari DR, Saifzadeh S, Krishnakanth P, Berner A, et al. A tissue engineering solution for segmental defect regeneration in load-bearing long bones. Sci Transl Med 2012;4(141):141ra93.
[19] Boerckel JD, Kolambkar YM, Dupont KM, Uhrig BA, Phelps EA, Stevens HY, et al. Effects of protein dose and delivery system on BMP-mediated bone regeneration. Biomaterials 2011;32(22):5241–51.
[20] Phelps EA, Enemchukwu NO, Fiore VF, Sy JC, Murthy N, Sulchek TA, et al. Maleimide cross-linked bioactive PEG hydrogel exhibits improved reaction kinetics and cross-linking for cell encapsulation and in situ delivery. Adv Mater 2012;24(1):64–70. 2.
[21] Phelps EA, Headen DM, Taylor WR, Thule PM, Garcia AJ. Vasculogenic bio-synthetic hydrogel for enhancement of pancreatic islet engraftment and function in type 1 diabetes. Biomaterials 2013;34(19):4602–11.
[22] Reyes CD, Petrie TA, Burns KL, Schwartz Z, Garcia AJ. Biomolecular surface coating to enhance orthopaedic tissue healing and integration. Biomaterials 2007;28(21):3228–35.
[23] Martino MM, Tortelli F, Mochizuki M, Traub S, Ben-David D, Kuhn GA, et al. Engineering the growth factor microenvironment with fibronectin domains to promote wound and bone tissue healing. Sci Transl Med 2011;3(100):100ra89.
[24] Bourdoulous S, Orend G, MacKenna DA, Pasqualini R, Ruoslahti E. Fibronectin matrix regulates activation of RHO and CDC42 GTPases and cell cycle progression. J Cell Biol 1998;143(1):267–76.
[25] Chen CS, Mrksich M, Huang S, Whitesides GM, Ingber DE. Geometric control of cell life and death. Science 1997;276(5317):1425–8.
[26] Giancotti FG, Ruoslahti E. Integrin signaling. Science 1999;285(5430):1028–32.
[27] Mizuno M, Fujisawa R, Kuboki Y. Type I collagen-induced osteoblastic differentiation of bone-marrow cells mediated by collagen-alpha 2 beta 1 integrin interaction. J Cell Physiol 2000;184(2):207–13.
[28] Jikko A, Harris SE, Chen D, Mendrick DL, Damsky CH. Collagen integrin receptors regulate early osteoblast differentiation induced by BMP-2. J Bone Min Res 1999;14(7):1075–83.
[29] Mizuno M, Kuboki Y. Osteoblast-related gene expression of bone marrow cells during the osteoblastic differentiation induced by type I collagen. J Biochem 2001;129(1):133–8.
[30] Suzawa M, Tamura Y, Fukumoto S, Miyazono K, Fujita T, Kato S, et al. Stimulation of Smad1 transcriptional activity by Ras-extracellular signal-regulated kinase pathway: a possible mechanism for collagen-dependent osteoblastic differentiation. J Bone Min Res 2002;17(2):240–8.
[31] Takeuchi Y, Suzawa M, Kikuchi T, Nishida E, Fujita T, Matsumoto T. Differentiation and transforming growth factor-beta receptor down-regulation by collagen-alpha2beta1 integrin interaction is mediated by focal adhesion kinase and its downstream signals in murine osteoblastic cells. J Biol Chem 1997;272(46):29309–16.
[32] Xiao G, Wang D, Benson MD, Karsenty G, Franceschi RT. Role of the alpha2-integrin in osteoblast-specific gene expression and activation of the Osf2 transcription factor. J Biol Chem 1998;273(49):32988–94.
[33] Morton LF, Peachey AR, Zijenah LS, Goodall AH, Humphries MJ, Barnes MJ. Conformation-dependent platelet adhesion to collagen involving integrin alpha 2 beta 1-mediated and other mechanisms: multiple alpha 2 beta 1-recognition sites in collagen type I. Biochem J 1994;299(Pt 3):791–7.

[34] Knight CG, Morton LF, Peachey AR, Tuckwell DS, Farndale RW, Barnes MJ. The collagen-binding A-domains of integrins alpha(1)beta(1) and alpha(2)beta(1) recognize the same specific amino acid sequence, GFOGER, in native (triple-helical) collagens. J Biol Chem 2000;275(1):35–40.
[35] Knight CG, Morton LF, Onley DJ, Peachey AR, Messent AJ, Smethurst PA, et al. Identification in collagen type I of an integrin alpha2 beta1-binding site containing an essential GER sequence. J Biol Chem 1998;273(50):33287–94.
[36] Reyes CD, Garcia AJ. Engineering integrin-specific surfaces with a triple-helical collagen-mimetic peptide. J Biomed Mater Res A 2003;65(4):511–23.
[37] Reyes CD, Garcia AJ. Alpha2beta1 integrin-specific collagen-mimetic surfaces supporting osteoblastic differentiation. J Biomed Mater Res A 2004;69(4):591–600.
[38] Wojtowicz AM, Shekaran A, Oest ME, Dupont KM, Templeman KL, Hutmacher DW, et al. Coating of biomaterial scaffolds with the collagen-mimetic peptide GFOGER for bone defect repair. Biomaterials 2010;31(9):2574–82.
[39] Miljkovic ND, Cooper GM, Hott SL, Disalle BF, Gawalt ES, Smith DM, et al. Calcium aluminate, RGD-modified calcium aluminate, and beta-tricalcium phosphate implants in a calvarial defect. J Craniofac Surg 2009;20(5):1538–43.
[40] Hennessy KM, Clem WC, Phipps MC, Sawyer AA, Shaikh FM, Bellis SL. The effect of RGD peptides on osseointegration of hydroxyapatite biomaterials. Biomaterials 2008;29(21):3075–83.
[41] Jager M, Boge C, Janissen R, Rohrbeck D, Hulsen T, Lensing-Hohn S, et al. Osteoblastic potency of bone marrow cells cultivated on functionalized biometals with cyclic RGD-peptide. J Biomed Mater Res A 2013;101(10):2905–14.
[42] Duvall CL, Taylor WR, Weiss D, Wojtowicz AM, Guldberg RE. Impaired angiogenesis, early callus formation, and late stage remodeling in fracture healing of osteopontin-deficient mice. J Bone Min Res 2007;22(2):286–97.
[43] Patterson J, Hubbell JA. SPARC-derived protease substrates to enhance the plasmin sensitivity of molecularly engineered PEG hydrogels. Biomaterials 2011;32(5):1301–10.
[44] Patterson J, Hubbell JA. Enhanced proteolytic degradation of molecularly engineered PEG hydrogels in response to MMP-1 and MMP-2. Biomaterials 2010;31(30):7836–45.
[45] Kimelman-Bleich N, Pelled G, Zilberman Y, Kallai I, Mizrahi O, Tawackoli W, et al. Targeted gene-and-host progenitor cell therapy for nonunion bone fracture repair. Mol Ther 2011;19(1):53–9.
[46] Kolambkar YM, Boerckel JD, Dupont KM, Bajin M, Huebsch N, Mooney DJ, et al. Spatiotemporal delivery of bone morphogenetic protein enhances functional repair of segmental bone defects. Bone 2011;49(3):485–92.
[47] Lehman Jr RA, Kang DG. Symptomatic ectopic intracanal ossification after transforaminal lumbar interbody fusion with rhBMP-2. Spine J 2012;12(6):530–1.
[48] Fiedler J, Roderer G, Gunther KP, Brenner RE. BMP-2, BMP-4, and PDGF-bb stimulate chemotactic migration of primary human mesenchymal progenitor cells. J Cell Biochem 2002;87(3):305–12.
[49] Sorger JI, Hornicek FJ, Zavatta M, Menzner JP, Gebhardt MC, Tomford WW, et al. Allograft fractures revisited. Clin Orthop Relat Res 2001;382:66–74.
[50] Mankin HJ, Hornicek FJ, Raskin KA. Infection in massive bone allografts. Clin Orthop Relat Res 2005;432:210–6.
[51] Azad V, Breitbart E, Al-Zube L, Yeh S, O'Connor JP, Lin SS. rhBMP-2 enhances the bone healing response in a diabetic rat segmental defect model. J Orthop Trauma 2009;23(4):267–76.

Synthetic matrices reveal contributions of ECM biophysical and biochemical properties to epithelial morphogenesis **Journal of Cell Biology**

JCB: Tools

Synthetic matrices reveal contributions of ECM biophysical and biochemical properties to epithelial morphogenesis

Nduka O. Enemchukwu,[1,2] Ricardo Cruz-Acuña,[2,3] Tom Bongiorno,[1,2] Christopher T. Johnson,[2,3] José R. García,[1,2] Todd Sulchek,[1,2] and Andrés J. García[1,2]

[1]Woodruff School of Mechanical Engineering, [2]Petit Institute for Bioengineering and Bioscience, and [3]Coulter Department of Biomedical Engineering, Georgia Institute of Technology, Atlanta, GA 30332

Epithelial cells cultured within collagen and laminin gels proliferate to form hollow and polarized spherical structures, recapitulating the formation of a rudimentary epithelial organ. However, the contributions of extracellular matrix (ECM) biochemical and biophysical properties to morphogenesis are poorly understood because of uncontrolled presentation of multiple adhesive ligands, limited control over mechanical properties, and lot-to-lot compositional variability in these natural ECMs. We engineered synthetic ECM-mimetic hydrogels with independent control over adhesive ligand density, mechanical properties, and proteolytic degradation to study the impact of ECM properties on epithelial morphogenesis. Normal cyst growth, polarization, and lumen formation were restricted to a narrow range of ECM elasticity, whereas abnormal morphogenesis was observed at lower and higher elastic moduli. Adhesive ligand density dramatically regulated apicobasal polarity and lumenogenesis independently of cell proliferation. Finally, a threshold level of ECM protease degradability was required for apicobasal polarity and lumen formation. This synthetic ECM technology provides new insights into how cells transduce ECM properties into complex morphogenetic behaviors.

Introduction

Cell–ECM adhesion transduces mechanical and biochemical signals that regulate epithelial morphogenesis (Klinowska et al., 1999; Lubarsky and Krasnow, 2003; Wozniak et al., 2003; Paszek et al., 2005; Yu et al., 2005; Nelson et al., 2006; Bryant and Mostov, 2008; Zhang et al., 2009, 2011). Bissell, Mostov, and others have pioneered the use of 3D collagen and laminin (i.e., Matrigel) gels in organotypic cultures that recreate the epithelial morphogenetic developmental program (O'Brien et al., 2002; Mroue and Bissell, 2013). In these natural matrices, epithelial cells, such as MDCK cells, proliferate from single cells to form multicellular, hollow spherical monolayer structures (cysts) within 10 d that bear the hallmarks of epithelial polarity, recapitulating the morphogenetic program for the formation of a rudimentary epithelial organ (McAteer et al., 1986). These 3D cultures have revealed that interactions between integrin adhesion receptors and secreted laminin and the density of ECM, which impacts the gel mechanical properties, regulate the establishment of cell polarity and morphogenesis as well as tumorigenesis (Barcellos-Hoff et al., 1989; O'Brien et al., 2001; Wozniak et al., 2003; Levental et al., 2009; Provenzano et al., 2009). Nevertheless, these natural matrices are inherently limited by the inability to decouple mechanical properties from matrix and ligand density and lot-to-lot compositional and structural variability (Yu et al., 2005; Hughes et al., 2010). Additionally, tumor-derived matrices such as Matrigel have limited clinical translational potential in regenerative medicine applications. In the work presented here, we describe a modular, synthetic ECM-mimetic hydrogel platform with controlled presentation of cell-adhesive ligands, tunable mechanical properties, and protease-dependent degradation to direct epithelial morphogenesis. Whereas previous work has established synthetic polymer hydrogels as engineered ECMs to investigate single cell behaviors (Lutolf et al., 2003; Kloxin et al., 2009; Huebsch et al., 2010; Khetan et al., 2013) and multicellular assemblies of cancer cell lines with a focus on tumorigenesis (Gill et al., 2012; Weiss et al., 2012; Beck et al., 2013; Raza et al., 2013), we analyze the contributions of ECM mechanical and biochemical properties to the coordinated multicellular epithelial morphogenesis developmental program. Understanding how cells transduce ECM properties into complex morphogenetic behaviors is paramount to developmental biology, pathogenesis, and materials-based regenerative medicine. Finally,

Correspondence to Andrés J. García: andres.garcia@me.gatech.edu

Abbreviations used in this paper: EdU, 5-ethynyl-2′-deoxyuridine; EMEM, Eagle's minimal essential media; MMP, matrix metalloproteinase; PEG, polyethylene glycol; PEG-4MAL, 4-arm PEG-maleimide; TEA, triethanolamine.

Supplemental material can be found at:
http://doi.org/10.1083/jcb.201506055

The Rockefeller University Press $30.00
J. Cell Biol.
www.jcb.org/cgi/doi/10.1083/jcb.201506055

this platform technology is straightforward to implement and uses commercially available reagents, allowing for facile and broad adoption by the community.

Results

Synthetic PEG hydrogels as ECM mimics with tunable biophysical and biochemical properties

To overcome the inability to tune the mechanical, structural, and biochemical characteristics and lot-to-lot compositional variability of natural ECMs, we engineered synthetic ECM-mimetic hydrogels with independent control over the presentation of cell-adhesive ligand type/density, mechanical and structural properties, and protease-dependent degradation to study the impact of ECM biophysical and biochemical properties on epithelial morphogenesis. These polyethylene glycol (PEG) hydrogels are based on a four-arm PEG macromer with maleimide groups at each terminus (PEG-4MAL; Fig. 1 A). The PEG-4MAL platform outperforms other synthetic chemistries in generating structurally defined hydrogels with stoichiometric incorporation of ligands and improved cross-linking efficiency (Phelps et al., 2012), providing an ideal material platform for the systematic and rigorous evaluation of the effects of ECM biochemical and biophysical properties on cell functions. Furthermore, these hydrogels exhibit superior in vitro and in vivo biocompatibility for several cell types including mesenchymal stem cells, skeletal myoblasts, and pancreatic islets (Phelps et al., 2012, 2013; Salimath et al., 2012). In a rapid reaction with quantitative yields, thiol-containing ligands such as cysteine-containing peptides can be conjugated to the PEG-4MAL macromer via reaction with the maleimide group to yield a functionalized macromer (Fig. 1 A). In this fashion, PEG-4MAL macromers presenting GRGDSPC (RGD) peptide that binds to integrin adhesion receptors were prepared (Fig. 1 A). RGD peptides were tethered onto the PEG-4MAL macromer with high yield (Fig. 1 B), demonstrating precise control over adhesive ligand density. Cysteine-flanked, protease-degradable peptide was then reacted with RGD-functionalized PEG-4MAL macromers in the presence of cells to cross-link macromers into a hydrogel network encapsulating the cells (Fig. 1 A). Importantly, in this synthetic platform, macromer size, polymer density, adhesive ligand type and density, and cross-linker type and density can be independently controlled to tune hydrogel structure (mesh size), mechanical properties, ECM ligand presentation, and protease-dependent degradation. For example, for a given macromer size (e.g., 20 kD PEG-4MAL), hydrogel elastic modulus increases, whereas equilibrium swelling (which is related to hydrogel structure) decreases as a function of polymer density as a tighter network is formed (Fig. 1 C), in excellent agreement with Flory-Rehner theory (Flory and Rehner, 1943; Canal and Peppas, 1989).

A major limitation for natural matrices such as collagen gels and Matrigel is that changes in protein concentration to vary mechanical properties invariably alter adhesive site local density and organization through changes to fiber structure and density. In contrast, for this modular synthetic system, mechanics, degradation, and adhesive ligand presentation can be independently tuned (Fig. 1 D). Because the PEG-4MAL macromers are symmetric and, when cross-linked into a hydrogel, form a regular mesh structure that is fully swollen, the adhesive peptide is uniformly distributed throughout the hydrogel network within the "statistical mean" of the mesh size. For the 20-kD macromer hydrogel system described here, the mesh size is 30–40 nm. Because of the small size of the PEG macromer arms and the swollen state of the gel, the mobility of the adhesive peptide is very limited. FRAP experiments with fluorescently labeled RGD peptide within hydrogels showed negligible fluorescence recovery, indicating very limited mobility of the adhesive peptide and uniform distribution throughout the hydrogel (Fig. S1 A). We also examined whether the spatial distribution of RGD peptide changes at the cell–hydrogel interface because of cell contractility. Using hydrogels presenting labeled RGD peptide and confocal microscopy, we monitored signal intensity at the cell–hydrogel interface as a function of time for cell cysts (Fig. S1 B). We observed no differences in signal intensity over time for either Y-27632–treated (10 µM) or control cysts, indicating no changes in local ligand density (i.e., clustering) with cell contractility. Taken together, these results demonstrate uniform spatial presentation of the adhesive peptide in a length scale relevant to the cell. Using this modular and well-controlled hydrogel platform, we analyzed the effects of ECM biochemical and biophysical properties on epithelial morphogenesis.

Normal epithelial morphogenesis requires an optimal range of ECM elasticity

We first investigated the influence of hydrogel polymer density, which is analogous to ECM concentration, on epithelial morphogenesis. Single MDCK cells were embedded in PEG-4MAL hydrogels formulated over a range of polymer densities (3.5%–5.0%, wt/vol). This range of polymer densities results in hydrogels with varying mechanical properties (0.85–8.0 kPa elastic modulus) and swelling behavior (Fig. 1 C). All these hydrogels were engineered to present the same density of RGD peptide (2,000 µM) and cross-linked by a fast-degrading, collagen-derived peptide (GPQ-W). This RGD density was chosen based on pilot experiments demonstrating cell attachment and robust spreading on top of such gels (unpublished data). Type I collagen gels (2.0 mg/ml) were used as a reference, because this natural ECM supports epithelial morphogenesis. Single cells embedded in hydrogels formulated at 3.5%, 4.0%, and 4.5% PEG-4MAL remained rounded and maintained high viability at 24 h and, after 48 h, formed multicellular clusters (Fig. 2, A and B; and Fig. S2 A). Formation of these cell clusters did not result from individual cells migrating toward each other, and 5-ethynyl-2′-deoxyuridine (EdU) incorporation confirmed that clusters arose from robust cell proliferation (Fig. 2, A and C). In contrast, cells encapsulated in 5.0% and higher-density PEG-4MAL gels had high viability at 24 h but remained as single and rounded cells at 48 h, with dramatically diminished viability and a complete abrogation of proliferation and formation of multicellular clusters (Fig. 2, A and C). These results demonstrate polymer density–dependent effects on epithelial cell survival and proliferation within PEG-4MAL hydrogels with a nonpermissive barrier at polymer densities of 5.0% and higher.

Columnar epithelia are characterized by polarized distribution of membrane complexes and morphological features between an apical domain facing a lumen/free space and a continuous basolateral domain interfacing with ECM and neighboring cells. This apicobasal polarity is critical for transport, secretion, and barrier functions in several organ systems (Roignot et al., 2013). Furthermore, in morphogenesis of 3D epithelial tissues such as ducts and sacs, establishment of a central

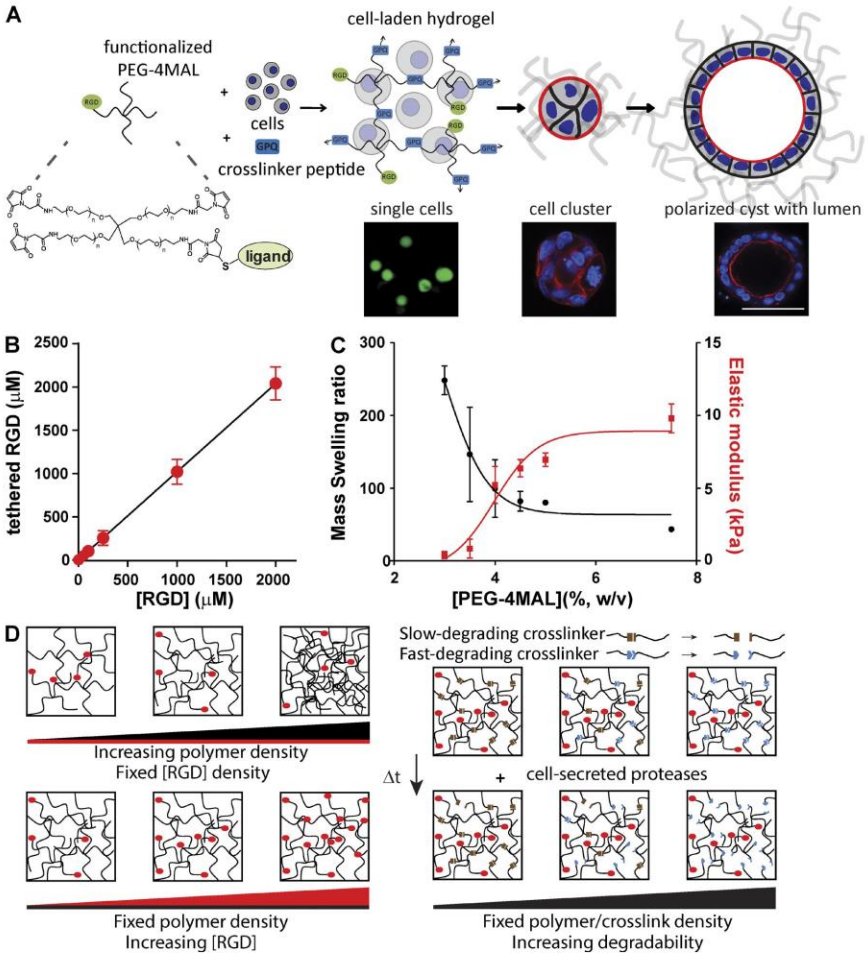

Figure 1. **Synthetic ECMs with tunable biophysical and biochemical properties.** (A) Schematic of cell-encapsulating hydrogel. Adhesive ligand-functionalized 4-arm PEG (PEG-4MAL) is reacted with a thiol-flanked protease-degradable peptide in the presence of cells to form a hydrogel network. Hydrogels support epithelial morphogenesis program. Bar, 50 µm. (B) Tethered RGD density (mean ± SEM) in hydrogel as a function of input RGD concentration. Linear regression: $y = 1.02x + 0.55$, $P < 0.0001$. (C) Relationship between polymer density (wt%) and hydrogel equilibrium mass swelling ratio (Q_m; left axis, mean ± SEM) and elastic modulus (right axis, mean ± SEM). (D) Cartoon illustrating independent control of polymer density, adhesive ligand density, and cross-link density/network degradation rate in PEG-4MAL hydrogels.

lumen is a critical phase in sculpting tissue architecture (Bryant and Mostov, 2008). For cell proliferation–permissive hydrogel polymer densities, hollowing of the multicellular clusters was visible after 4 d in culture (Fig. S2, A and B). Cleaved caspase-3 labeling indicated the presence of apoptotic cells in developing cysts (Fig. 3, A and B), demonstrating a mode of lumen clearance in permissive hydrogels similar to that observed in collagen gels (Martín-Belmonte et al., 2008). Moreover, MDCK cells in permissive PEG-4MAL hydrogels formed differentiated epithelial cysts after 10 d in culture consisting of spherical (50- to 100-µm diameter, Fig. 3 C) cellular assemblies with lumens and apicobasal polarity (Fig. 2 D). These well-defined spherical cell structures exhibited canonical markers of apicobasal polarity, including podocalyxin/gp135, actin, ZO-1, GM130, and β-catenin (O'Brien et al., 2006; Fig. S3 A). Cysts in different hydrogel formulations were analyzed for apicobasal polarity and lumen formation using a scoring system (Fig. S3 B). Remarkably, hydrogel polymer density modulated apicobasal

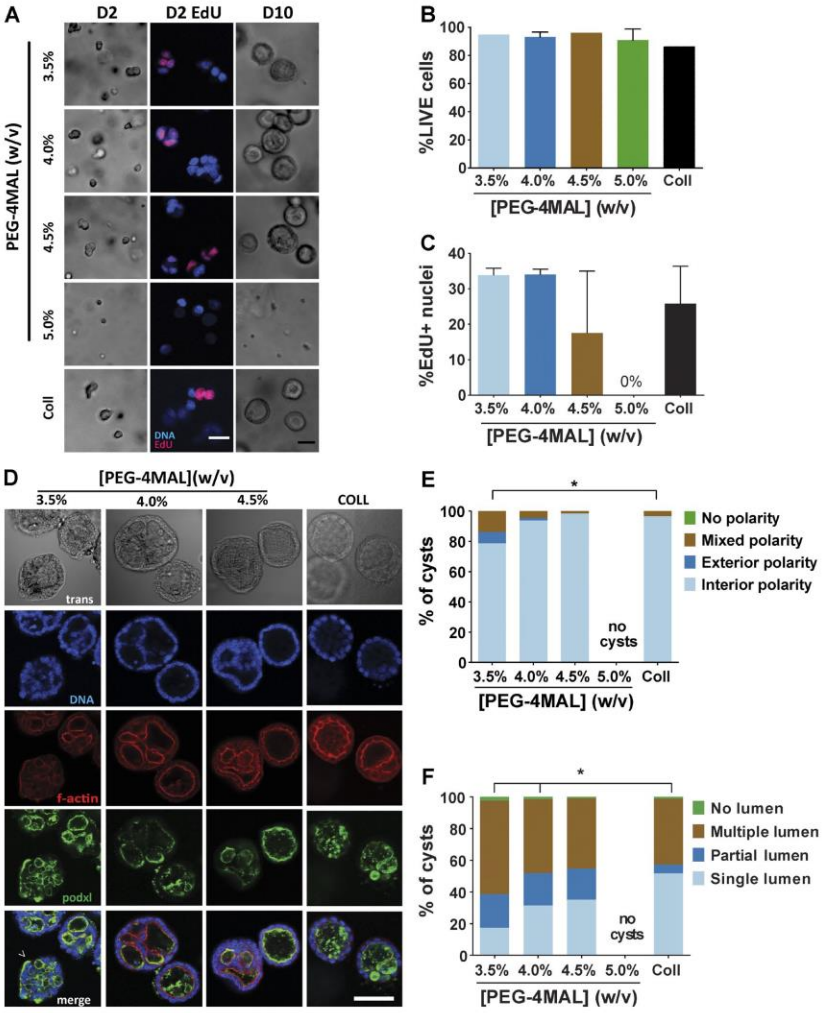

Figure 2. **PEG-4MAL polymer density regulates epithelial morphogenesis.** (A) Transmitted light and fluorescence microscopy images of single MDCK cells cultured in PEG-4MAL hydrogels of different polymer weight percentages over 10 d. At day 2, newly synthesized DNA was labeled by EdU incorporation. Bar, 50 µm. (B) Cell viability (mean ± range in two independent experiments) assessed by calcein-AM (live) and TOTO-3 iodide (dead) labeling at day 1 (>500 cells counted per condition). (C) Proliferation (mean ± range in two independent experiments) as determined by EdU labeling (>590 nuclei counted per condition). (D) Transmitted light and fluorescence microscopy images for MDCK cultures at day 10 and labeled for apical polarity marker gp135/podocalyxin (podxl) and filamentous actin. No cysts were detected in 5.0% PEG-4MAL gels. Bar, 50 µm. (E) Distribution of apical polarity phenotypes at day 10 (>90 cysts analyzed per condition). χ^2 test with Bonferroni's correction; *, $P < 0.014$, 3.5% versus collagen. (F) Distribution of lumen phenotypes at day 10 (>90 cysts scored per condition). χ^2 test with Bonferroni's correction; *, $P < 3 \times 10^{-6}$, 3.5% versus collage; $P < 0.02$, 4.0% versus collagen.

polarity (Fig. 2 E) and lumen formation (Fig. 2 F). Epithelial cysts grown in 4.0% and 4.5% PEG-4MAL gels exhibited normal, internal apical polarity and partial or fully formed single lumens. The frequencies of internal apical polarity and single lumen formation in 4.0% and 4.5% PEG-4MAL gels were equivalent to those for cysts formed in collagen gels (Fig. 2 D–F). In contrast, epithelial cysts grown in 3.5% PEG-4MAL gels exhibited aberrant polarity, with >20% of the cysts

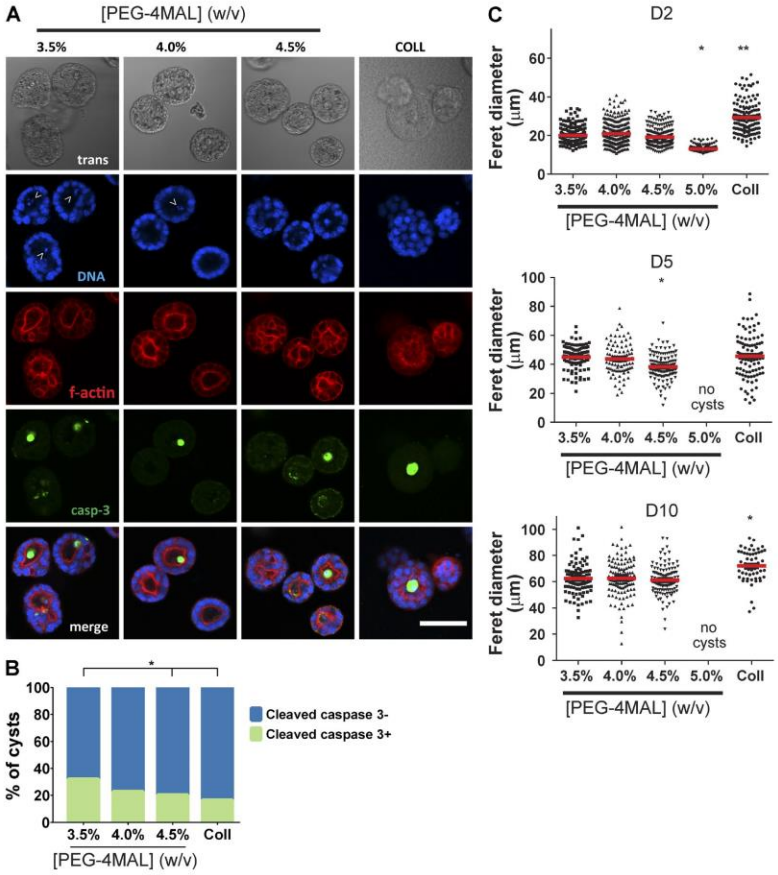

Figure 3. **Lumen formation for epithelial cysts within PEG-4MAL hydrogels involves cell apoptosis.** (A) Transmitted light and fluorescence microscopy images of MDCK cells cultured within PEG-4MAL hydrogels. Samples were stained for filamentous actin and caspase-3. (B) Distribution of cysts staining positive for caspase-3 (>103 cysts analyzed per condition). χ^2 test with Bonferroni's correction *, $P < 0.005$, 3.5% versus 4.5% and collagen. (C) Epithelial cyst size (median shown as red line) as a function of PEG-4MAL hydrogel polymer density (>62 cysts analyzed per condition). χ^2 test with Bonferroni's correction. Day 2: *, $P < 0.05$, 5.0% versus all other polymer densities; **, $P < 0.01$, 5.0% versus collagen. Day 5: *, $P < 0.05$, 4.5% versus collagen. Day 10: *, $P < 0.05$, collagen versus PEG-4MAL groups.

exhibiting mixed or exclusively external (or inverted) polarity (Fig. 2, D and E). Furthermore, only 17% of cysts grown in 3.5% PEG-4MAL exhibited a well-defined single lumen versus 31% and 35% for 4.0% and 4.5% PEG-4MAL gels, respectively (Fig. 2, D and F). Although polymer density regulated polarization and lumen formation, there were no differences in cyst diameter among these permissive hydrogel formulations (Fig. 3 C). No epithelial cysts formed in PEG-4MAL hydrogels with polymer densities of 5.0% and higher.

Normal cyst development, polarization and lumen formation were restricted to a narrow range of hydrogel polymer density, whereas abnormal epithelial morphogenesis and complete abrogation of this developmental program were observed at lower and higher polymer densities, respectively. Because polymer density strongly dictates the mechanical properties of the hydrogel (Fig. 1 C), these results suggest that normal epithelial morphogenesis requires an optimal range of ECM elasticity (E, ~4 kPa). This conclusion is consistent with previous studies reporting changes in epithelial morphogenesis with collagen concentration (Wozniak et al., 2003; Paszek et al., 2005). However, polymer density (as well as collagen concentration) also controls hydrogel structure, as evidenced by changes in swelling behavior (Fig. 1 C), which impacts other important hydrogel properties such as permeability that can influence cell behaviors (Ghajar et al., 2008). To assess whether the polymer density–dependent effects on epithelial morphogenesis were

caused by changes in hydrogel elasticity, we compared cyst polarization and lumen formation in RGD-functionalized hydrogels generated from different macromer sizes (20 vs. 40 kD) but different polymer densities (4.0% vs. 8.0%) engineered to have equivalent mean cross-link densities. Measurements for diffusion of labeled protein (α-bungarotoxin, 8 kD) through these hydrogels demonstrated differences in permeability caused by the differences in macromer arm length (Fig. S4 A). Nevertheless, as expected for gels with equivalent mean cross-link densities, these two gel formulations had equivalent mechanical properties (Fig. S4 B). MDCK cell cyst development proceeded normally in both hydrogel formulations, and there were no differences in polarization or lumen formation between these two formulations (Fig. S4, C and D). This result demonstrates that the effects of polymer density on epithelial morphogenesis are related to hydrogel mechanical properties. Taken together, these results show that normal epithelial morphogenesis requires an optimal range of ECM elasticity.

Adhesive ligand density regulates polarization and lumen formation independently of cell proliferation

We next examined the effects of RGD adhesive ligand density on epithelial morphogenesis within synthetic ECM hydrogels. A constant total density (2,000 µM) of a mixture of cell-adhesive RGD peptide and scrambled inactive RDG peptide was used to vary RGD density (0–2,000 µM) while maintaining identical structures among hydrogel formulations of 4.0% polymer density and constant GPQ-W cross-linking peptide density. Cell proliferation and assembly into multicellular structures was insensitive to RGD peptide density (Fig. 4, A and B). However, epithelial cyst polarity and lumen phenotypes showed a dramatic dependence on RGD density (Fig. 4 C). Hydrogels presenting low (≤100 µM) RGD densities supported the formation of very few cysts with internal apical polarity (<14%), in striking contrast to hydrogels presenting high (≥250 µM) RGD density in which >60% of cysts had internal apical polarity (Fig. 4, C and D). A similarly dramatic shift in the distribution of lumen phenotypes occurred at 250 µM RGD density. Nearly all (>90%) cysts in hydrogels presenting high densities of RGD peptide contained lumens, whereas the majority of cysts in low-density RGD gels lacked lumens (Fig. 4, C and E). The extent of cyst polarization and lumen formation was not different between PEG-4MAL hydrogels presenting 2,000 µM RGD peptide and collagen gels. These results show that although RGD peptide is not required for initial proliferation and generation of cell aggregates, differentiation of polarized cysts with lumens requires a threshold density of RGD in the matrix.

To explore the role of integrins in the RGD density–dependent effects on cyst phenotype within the synthetic hydrogel system, we cultured MDCK cells in PEG-4MAL hydrogels presenting 2,000 µM RGD peptide in the presence of LM609, an antibody that blocks binding of the αVβ3 integrin to RGD peptides, or AIIB2, an antibody that blocks the function of the β1 integrin that binds and assembles secreted laminin during cyst morphogenesis (Yu et al., 2005). Nearly all (>98%) cysts that developed in the presence AIIB2 or control isotype antibodies had normal, interior apical polarity (Fig. 4, F–H). In contrast, only 80% of epithelial cysts grown in the presence of LM609 exhibited interior apical polarity. Similarly, ∼18% of cysts grown with AIIB2 or control antibodies exhibited a well-developed single lumen, whereas none of the cysts grown in the presence of LM609 had well-formed, single lumens. These results demonstrate that the RGD-dependent effects on epithelial morphogenesis within PEG-4MAL are mediated by the αVβ3 integrin. Although statistically significant, the cyst phenotype shifts observed in RGD-presenting PEG-4MAL hydrogels in the presence of LM609 were considerably less than those seen in the absence of RGD. We attribute this discrepancy to the presence of other integrin heterodimers that bind RGD and provide significant signaling in the presence of LM609 (Teräväinen et al., 2013). The absence of a cyst phenotype shift in the presence of AIIB2 suggests that β1 integrin function is dispensable for polarized cyst morphogenesis in the RGD-functionalized synthetic hydrogel.

To demonstrate the versatility of the synthetic platform to study different adhesive ligands, we performed additional experiments for apicobasal polarization and lumen formation with other cysteine-terminated cell-adhesive peptides: laminin α1 chain–derived AG73 peptide (CGGRKRLQVQLSIRT; Hoffman et al., 1998), EF1zz peptide (CGGATLQLQEGRLHFXFD LGKGR, X: Nle; Suzuki et al., 2003), and collagen IV–derived peptide (CGGGEFYFDLRLKGDKY; Miles et al., 1994). This study showed peptide-specific differences in epithelial morphogenesis for MDCK cells (Fig. S5, A and B). We note that synthetic hydrogels presenting full-length proteins such as laminin and collagen can be prepared by blending the matrix protein with the PEG components during cross-linking, and these hydrogels also support lumen formation and polarization (Fig. S5 C). However, this approach has limitations, as these full-length proteins are considerable larger than the PEG macromer and will disrupt the local structure and cross-linking of the hydrogel, potentially resulting in ill-defined local mechanical and biochemical properties. At high concentrations of protein, these effects may be large enough such that performing dose-dependent studies as shown here for RGD peptide will be difficult.

A threshold level of ECM protease degradability is required for apicobasal polarity and lumen formation without alterations in cyst size

Epithelial morphogenesis requires local, cell-mediated matrix degradation to create space for expansion of cellular aggregates or extension of cellular processes (Weaver et al., 2014). We used two different experimental approaches to examine the effects of cross-link degradation on epithelial cyst development in PEG-4MAL hydrogels. First, we directly tuned the degradability of the hydrogel matrix by titrating a slower-degrading variant peptide (GPQ-A; Patterson and Hubbell, 2010) of the GPQ-W cross-linker in hydrogel formulations (4% polymer density, 2,000 µM RGD) that typically support high proliferation and formation of cell aggregates. Whereas 5% and 10% substitution of GPQ-A had no effect on cyst morphogenesis, GPQ-A content of 20% increased the incidence of abnormal polarity and altered lumen phenotypes (Fig. 5, A–C). GPQ-A content of >20% resulted in complete abrogation of cell proliferation and multicellular cyst precursor formation (Fig. 5 A). This result is consistent with the observation that cells did not proliferate or form cysts in PEG-4MAL gels of ≥5.0% polymer density with GPQ-W (Fig. 2).

We also incubated MDCK cells embedded in 4.0% PEG-4MAL hydrogels functionalized with RGD (2,000 µM) and cross-linked with GPQ-W in the broad-range matrix metalloproteinase (MMP) inhibitors GM6001 and MMPII. Interestingly,

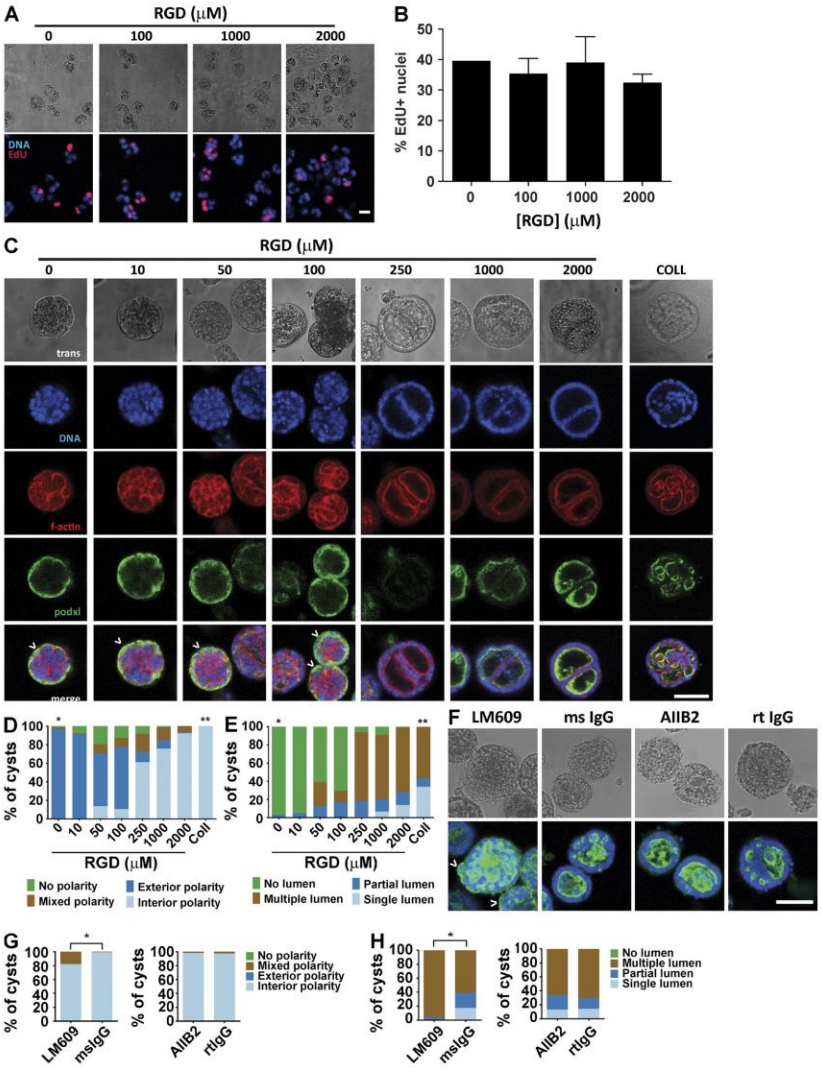

Figure 4. **Adhesive ligand density in PEG-4MAL hydrogel modulates cyst phenotype and apical polarity.** (A) Transmitted light and fluorescence microscopy images for MDCK cells cultured for 2 d in 4.0% PEG-4MAL hydrogels incorporating different amounts of RGD. Newly synthesized DNA was labeled by EdU. Bar, 20 μm. (B) Cell proliferation (mean ± SEM) at day 2 as assessed by EdU incorporation (>374 nuclei counted per condition). (C) Transmitted light and fluorescence microscopy images for MDCK cells cultured in 4.0% PEG-4MAL for 10 d and labeled for apical polarity marker gp135/podocalyxin (podxl). Inverted apical polarity indicated by ^. Bar, 50 μm. F-actin, filamentous actin. (D) Distribution of apical polarity phenotypes at day 10 (>78 cysts counted per condition). χ^2 test with Bonferroni's correction; *, $P < 0.0001$, 0 μM RGD versus every other condition except 10 μM RGD; **, $P < 0.0001$, collagen versus every other condition except 2,000 μM RGD. (E) Distribution of lumen phenotypes at day 10 (>78 cysts counted per condition). χ^2 test with Bonferroni's correction; *, $P < 0.0001$, 0 μM RGD versus every other condition except 10 μM RGD; **, $P < 0.0001$, collagen versus every other group. (F) MDCK cultured for 10 d in 4.0% PEG-4MAL gels with 2,000 μM RGD in the presence of function-blocking antibodies against integrin αVβ3 (LM609) or integrin β1 (AIIB2) or isotype control antibodies (mouse [ms] or rat [rt] IgG). Cysts were labeled with antibodies against gp135/podocalyxin (podxl). Bar, 50 μm. (G) Distribution of lumen phenotypes in F at day 10 (>100 cysts counted per condition). χ^2 test; *, $P < 0.0001$, mouse IgG versus LM609. (H) Distribution of apical polarity phenotypes in F at day 10 (>100 cysts counted per condition). χ^2 test; *, $P < 0.0001$, mouse IgG versus LM609.

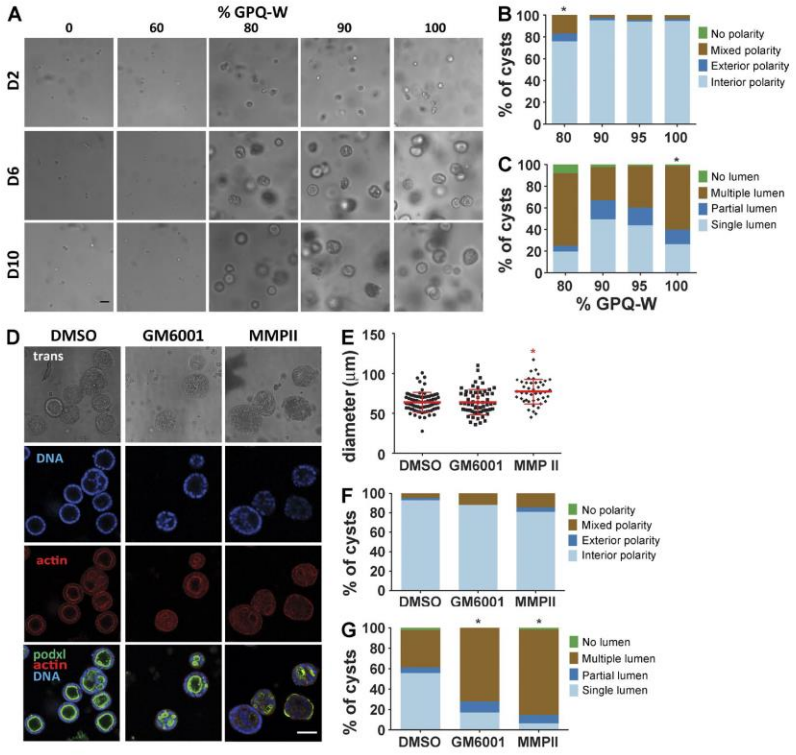

Figure 5. **Hydrogel cross-link degradation rate regulates cyst growth, lumen formation, and polarity.** (A) Transmitted light microscope images of MDCK cells cultures for 10 d in 4.0% PEG-4MAL hydrogels with 2,000 µM RGD cross-linked with either fast-degrading (GPQ-W) or slow-degrading (GPQ-A) cross-linking peptides titrated from 0% GPQ-W (100% GPQ-A) to 100% GPQ-W (0% GPQ-A). Bar, 50 µm. (B) Distribution of apical polarity phenotypes at day 10 (>135 cysts counted per condition). χ^2 test with Bonferroni's correction; *, $P < 0.0001$, 80% GPQ-W versus 100% GPQ-W. (C) Distribution of lumen phenotypes at day 10 (>135 cysts counted per condition). χ^2 test with Bonferroni's correction; *, $P < 0.005$, 100% GPQ-W versus all other conditions. (D) MDCK cells cultured for 10 d in PEG-4MAL hydrogels with 2,000 µM RGD and incubated with MMP inhibitors MMPII or GM6001 or control. Cysts were labeled with rhodamine phalloidin (filamentous actin), Hoechst 3342 (DNA), and an antibody against apical polarity marker gp135/podocalyxin (podxl; green). Bar, 50 µm. (E) Cyst size at day 10 (>44 cysts counted per condition). χ^2 test with Bonferroni's correction; *, $P < 0.05$, MMPII versus all other conditions. (F) Distribution of apical polarity phenotypes at day 10 (>108 cysts counted per condition). (G) Distribution of lumen phenotypes at day 10 (>108 cysts counted per condition). χ^2 test with Bonferroni's correction; *, $P < 0.0001$, GM6001 versus DMSO and MMPII versus DMSO.

these MMP inhibitors had modest effects on cyst size at day 10 (Fig. 5, D and E). However, both MMP inhibitors reduced the proportion of cysts with internal apical polarity and well-defined single lumen compared with the vehicle-only (DMSO) control (Fig. 5, D, F, and G). These alterations in cyst polarization and lumen formation mirror the effects of incorporating 20% of the slower-degrading GPQ-A cross-linking peptide in the permissive hydrogel formulation (Fig. 5 B). Taken together, these results show that MMP-dependent degradation of the PEG-4MAL hydrogel network is essential for normal epithelial morphogenesis within these synthetic ECM.

Synthetic ECM platform is applicable to study other epithelial cell models

We performed additional experiments with Caco-2 colon epithelial cells to demonstrate that the synthetic ECM platform can be used to study epithelial morphogenesis with other cell systems. This study demonstrated that specific hydrogel formulations supported multicellular cyst assembly, lumen formation, and polarization with this epithelial cell line (Fig. 6). Interestingly, for Caco-2 cells, RGD adhesive peptide was required for multicellular cyst formation, as scrambled RDG-presenting gels supported poorly organized cell clusters with fewer cells. In addition, the range of permissive formulations for cyst formation occurred at higher polymer densities (6.0–8.0%) for Caco-2 cells compared with MDCK cells. Even though the hydrogel of 8.0% polymer density supported lumen formation and polarization, the resulting cysts were smaller than those developed in the formulation with 6.0% polymer density. These results show differences on the effects of ECM biochemical and biophysical cues on the morphogenetic program for different epithelial cell lines.

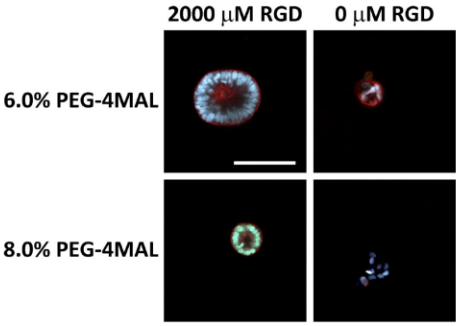

Figure 6. **Hydrogel polymer density and RGD adhesive ligand regulate epithelial morphogenesis in Caco-2 cells.** Fluorescence microscopy images of Caco-2 cells grown within PEG-4MAL hydrogels for 10 d. Bar, 100 µm. Cysts were labeled with rhodamine phalloidin (filamentous actin) and Hoechst 3342 (DNA). Cyst formation, lumen formation, and polarization required RGD adhesive peptide. Hydrogel polymer density influences the size of the resulting epithelial cyst.

Discussion

This study establishes a modular synthetic ECM-mimetic hydrogel platform with controlled presentation of cell-adhesive ligands, tunable mechanical properties, and protease-dependent degradation that can be precisely engineered to study the contributions of ECM biophysical and biochemical properties on the epithelial morphogenetic program. Systematic changes in hydrogel formulation to independently tune hydrogel polymer density, elasticity, adhesive ligand density, and protease-dependent degradation revealed that each of these properties has profound effects on specific stages of this coordinated morphogenetic process, including proliferation, multicellular cyst development, polarization, and lumen formation. Importantly, these effects occur via mechanisms that parallel development in natural matrices. Because of their inherent complexity, these new insights into the contributions of ECM biochemical and mechanical properties to the regulation of epithelial morphogenesis are simply not tractable using natural collagen and laminin ECMs. Remarkably, a spectrum of developmental outcomes including cell apoptosis, normal cyst development comprising a spherical polarized cell monolayer enclosing a single lumen, and abnormal cellular assemblies consisting of solid spheres with no lumen or structures with inverted polarity and multiple lumens reminiscent of pathological states could be engineered within the same synthetic hydrogel platform.

We identified synthetic hydrogel formulations that supported the epithelial morphogenesis program to the same extent as type I collagen matrices. Interestingly, the collagen gels used as a reference in the experiments presented here have a fibrillar architecture with micrometer-sized pores, whereas the PEG-4MAL gels have an amorphous structure with a nanoscale mesh size. Our results suggest that the epithelial morphogenesis program is insensitive to these differences in matrix architecture. However, because of the complex nature of the collagen gels, it is difficult to determine whether other important parameters (e.g., adhesive ligand density) regulating epithelial morphogenesis are equivalent between the optimal synthetic analog and the natural ECM.

Our results for the effects of ECM properties on the normal epithelial morphogenetic program are fundamentally different from those reported for cancer cells in synthetic gels, most likely reflecting central differences between developmental morphogenesis and tumorigenesis. For instance, MDCK cell proliferation and assembly into multicellular structures was insensitive to RGD peptide density, whereas cyst polarity and lumen phenotypes showed a dramatic dependence on RGD density. Additionally, the literature has major inconsistencies regarding the effects of polymer density (equated in these papers to stiffness) on the organization of cancer cells into aggregates of varying size (Gill et al., 2012; Beck et al., 2013; Raza et al., 2013). We observe different responses for normal epithelial cells. Multicellular cysts formed at polymer densities below a threshold that supported cell proliferation; above this threshold, no cell aggregates were formed owing to inhibited proliferation and apoptosis. Moreover, for permissive formulations, we report polymer density-dependent differences in the establishment of apicobasal polarity and the formation of cysts with no lumen, a single lumen, and multiple lumens, which are hallmarks of normal epithelial morphogenesis and formation of a rudimentary epithelial organ. Yet all these cysts had equivalent size. Raza et al. reported that hydrogels that were not protease-degradable did not support formation of larger cell aggregates (Raza et al., 2013). This result is the expected consequence of a tight hydrogel network encapsulating the cells. In the present study, we show this effect for a hydrogel with 100% nondegradable cross-links. However, we also find that intermediate levels of protease-degradability regulate apicobasal polarity and lumen phenotypes without alterations in cyst size, demonstrating that protease-degradability of the ECM regulates these critical epithelial characteristics independently of simply constraining cells from forming cell aggregates.

We expect that this biomaterial platform will find widespread adoption in developmental cell and tumor biology fields to study ECM-regulated morphogenetic processes. Furthermore, this technology enables the engineering of instructive epithelial synthetic niches for cell expansion and controlled differentiation as well as delivery vehicles for regenerative medicine applications that overcome the limitations of natural matrices such as lot-to-lot variability and regulatory and translational constraints.

Materials and methods

Antibodies and labeling reagents

Primary antibodies used were mouse anti-gp135/podocalyxin (clone 3F21D8; provided by G. Ojakian, SUNY Downstate Medical Center, Brooklyn, NY), rabbit anti-laminin (Sigma-Aldrich), mouse anti-αvβ3 integrin (LM609; EMD Millipore), rat anti–β1 integrin (AIIB2; Developmental Studies Hybridoma Bank), mouse anti-GM130 (BD Transduction Laboratories), mouse anti-ZO-1 (Life Technologies), and rabbit anti–β-catenin (H-102; Santa Cruz Biotechnology). The following secondary antibodies were used: goat anti–mouse IgG Alexa Fluor 488, goat anti–rat IgG Alexa Fluor 555, goat anti–rabbit IgG Alexa Fluor 488 (Life Technologies), and donkey anti–rabbit IgG Dylight649 (Thermo Fisher Scientific). Nuclei were stained with Hoechst 33342, and filamentous actin was stained with rhodamine phalloidin (Life Technologies).

Cell culture and hydrogel formation

MDCK strain II epithelial cells (Sigma-Aldrich) were maintained in Eagle's minimal essential media (EMEM; ATCC) supplemented with fetal bovine serum (Life Technologies) at 10% (vol/vol), penicillin (100 IU/ml) and streptomycin (100 µg/ml), and fungizone.

To prepare PEG hydrogels, PEG-4MAL (MW 22,000; Laysan Bio) was dissolved in a triethanolamine (TEA) buffer (4 mM in DPBS, pH 7.4). Adhesive and cross-linking peptides were custom-synthesized by AAPPTec. Adhesive peptide (GRGDSPC) or nonadhesive peptide (GRDGSPC) or combination was dissolved in TEA to generate functionalized PEG-4MAL precursor. Bis-cysteine cross-linking peptide GCRDGPQG↓IWGQDRCG (GPQ-W; ↓ denotes enzymatic cleavage site) or GCRDGPQG↓IAGQDRCG (GPQ-A) was dissolved in TEA at 1:1 maleimide/cysteine ratio after accounting for maleimide groups reacted with adhesive peptide. MDCK cells were resuspended at 5× final cell density in ice-cold serum-free EMEM and kept on ice. To form gels, adhesive peptide-functionalized PEG-4MAL macromer, cells, and cross-linking peptides were polymerized under serum-free conditions for 20 min before addition of complete medium. For studies with integrin-blocking antibodies, cells were preincubated (30 min, gentle rocking, at 22°C) in 0.1% bovine serum albumin in serum-free EMEM containing antibodies. For collagen gels, type I collagen from bovine tendon (3 mg/ml; Sigma-Aldrich) was mixed with cell suspension in serum-free media to achieve a 2.0 mg/ml type I collagen gels cast onto polyester permeable supports (0.4-µm pore; Corning) in a 24-well plate.

Hydrogel characterization

Hydrogel elastic modulus measurements were obtained by atomic force microscopy as described previously (Phelps et al., 2012) with cantilever spring constants of 10 mN/m, indentation speed of ∼2.0 µm/s, and force trigger set point of 1.25 nN. Using an MFP-3D-BIO atomic force microscope (Asylum Research), samples were probed under fluid conditions (ultrapure H_2O) using a pyramidal-tipped silicon nitride cantilever (Bruker). The force–indentation curve was obtained for each measurement and then analyzed with a Hertzian model for a pyramidal tip (Wavemetrics; IgorPro software routines), from which the Young's modulus values were calculated. The sample Poisson's ratio was assumed as 0.33, and a power law of 2.0 for the sample indentation distance was used to model tip geometry. Hydrogel mass swelling ratio and ligand tethering were measured as described previously (Phelps et al., 2012). The storage and loss moduli of hydrogels were assessed by dynamic oscillatory strain and frequency sweeps performed on a MCR 302 stress-controlled rheometer (Anton Paar) with a 9-mm diameter, 2° cone, and plate geometry. Oscillatory frequency sweeps were used to examine the storage and loss moduli (ω = 0.5–100 rad s^{-1}) at a strain of 1%. For permeability experiments, hydrogels were incubated in FITC-labeled α-bungarotoxin (500 µg/ml), and signal intensity at the center of the gel sample was measured over time via confocal microscopy. Intensity profiles were fit to Fick's second law to obtain diffusion coefficients (Koutsopoulos et al., 2009). For ligand mobility studies, a Ti-E inverted microscope (Nikon) with Perfect Focus System and C2-Plus Confocal System with a Plan Fluor 40× (NA 0.75) objective was used for FRAP. Hydrogels were prepared with Alexa Fluor 594–labeled RGD peptide and allowed to equilibrate. Initial fluorescence intensity was measured using low laser power followed by photobleaching of a 0.20-mm-diameter circle within the hydrogel at 38 mW with 561-nm laser for 10 s. The recovery of fluorescence was monitored for up to 5.8 h. Image series were imported into MATLAB, where background subtraction and correction for incidental bleaching during image acquisition were applied to data extracted from the bleached region. For analysis of cell-dependent RGD peptide clustering, MDCK cells were cultured within hydrogels presenting a mixture of Alexa Fluor 594–labeled and control RGD peptide for 8 d. Fluorescence signal intensity was measured for 35 min at different radial positions from the cell–hydrogel interface in the presence or absence of 10 µM Y-27632.

RGD labeling

RGD peptide was labeled using Alexa Fluor 594 NHS-ester dye (Life Technologies). To quantify labeling efficiency, size-exclusion chromatography was performed using a HiPrep Sephacryl S-100 HR gel filtration column on an AKTA Pure 25 chromatography system (GE Healthcare). DPBS supplemented with 0.15 M NaCl was used as the elution buffer to separate conjugated from unconjugated dye at a volumetric rate of 0.5 ml/min. Onboard absorbance readings of the eluted sample at 280/594 nm yielded a set of curves with peaks that corresponded to labeled and unlabeled peptide. Quantification of the area under the peaks was determined, and the ratio of the areas was used as the labeling efficiency.

Viability and proliferation assays

PEG-4MAL gels were incubated in 0.5% collagenase I (Worthington Biochemical), 2 µM calcein-AM (live), and 1 µM TOTO-3 iodide (dead; Life Technologies) in serum-free EMEM media until hydrogel was completely dissolved and cells settled at bottom of well. For collagen gels, gel was incubated in 2 µM calcein-AM and 1 µM TOTO-3 for 30 min and placed in chambered coverglass for imaging. Proliferation was assayed using the Click-iT EdU Imaging Kit (Life Technologies). Samples were imaged with Nikon Plan Fluor 10× (NA 0.30) or Plan Fluor 20× (NA 0.45) objectives in a Nikon Eclipse TE2000 inverted microscope and C1 Confocal System (EZ-C1 acquisition software) or Ti-E inverted microscope with Perfect Focus System and C2-Plus Confocal System (NIS Elements acquisition software). Cells were counted with ImageJ macros.

Immunofluorescence labeling of cysts

Gels were washed extensively in DPBS and fixed in 4% formaldehyde in DPBS for 15 min. Gels were incubated for 30 min in blocking buffer (1% bovine serum albumin, 1% goat serum, 0.1% fish skin gelatin, 0.5% Triton X-100, and 0.05% sodium azide in PBS). Samples were incubated in primary antibodies diluted in blocking buffer on an orbital shaker at 4°C overnight. Secondary antibodies and nuclear stain were diluted in blocking buffer and incubated on an orbital shaker at 4°C overnight. After immunostaining, cysts were recovered by collagenase digestion and mounted in 2% low-melt agarose. Fluorescent images for cyst scoring were captured with Nikon Plan Fluor 20× (NA 0.45) or Plan Apo 60× (NA 1.40) objectives in a Nikon Eclipse TE2000 inverted microscope and C1 Confocal System (EZ-C1 acquisition software) or Ti-E inverted microscope with Perfect Focus System and C2-Plus Confocal System (NIS Elements acquisition software). Cyst size was measured from fluorescent images of cyst cross sections using ImageJ FIJI package. The following scoring system was used for polarity: (1) interior apical polarity: a cyst cross section in which the interior of one or more lumens is lined with gp135 staining and the exterior of cyst lacks gp135 staining; (2) exterior apical polarity: a cyst cross section in which the interior of one or more lumens lacks gp135 staining and the exterior of cyst is lined with gp135 staining; (3) mixed apical polarity: a cyst cross section in which the interior of one or more lumens and the exterior of cysts show staining for gp135; and (4) no apical polarity: a cyst cross section with no staining for gp135. The following scoring system was used for lumen phenotypes: (1) single lumen: a cyst cross section having a single hollow space and outlined by a monolayer of cells; (2) partial lumen: a cyst cross section having a single hollow space bounded by multiple layers or groups of cells; (3) multiple lumens: a cyst cross section having multiple hollow spaces; and (4) no lumen: a cyst cross section having no hollow spaces. Fig. S3 presents exemplary cysts for each scoring category.

Statistical analyses

Results are presented either as mean ± SEM or percentages of population. Statistical analyses were performed using GraphPad Prism 6.0. For normally distributed data with equal variances, one-way analysis of variance with Tukey's multiple comparison test was used. For categorical data such as polarity and lumen phenotypes, χ^2 test with Bonferroni's test for multiple comparisons was used. A p-value <0.05 was considered significant.

Online supplemental material

Fig. S1 shows adhesive ligand mobility within PEG hydrogels. Fig. S2 shows epithelial cyst polarization and lumen formation. Fig. S3 shows that epithelial cysts within PEG-4MAL hydrogels exhibit canonical markers of apicobasal polarity and lumen phenotypes. Fig. S4 shows biophysical characterization and epithelial cyst phenotypes for PEG-4MAL hydrogel formulations generated with different macromer sizes. Fig. S5 shows epithelial cyst phenotypes for PEG-4MAL hydrogels presenting different adhesive peptides. Online supplemental material is available at http://www.jcb.org/cgi/content/full/jcb.201506055/DC1. Additional data are available in the JCB DataViewer at http://dx.doi.org/10.1083/jcb.201506055.dv.

Acknowledgments

We thank George Ojakian for the gp135/podocalyxin antibody as well as Asma Nusrat, Thomas Barker, and David Collard for helpful discussions.

This work was supported by National Institutes of Health grants R01-EB004496, R01-AR062368, and R01-AR062920. N.O. Enemchukwu was supported by the GEM graduate fellowship, Ford Foundation fellowship, NASA Harriet G. Jenkins predoctoral fellowship, and United Negro College Fund/Merck dissertation fellowship. T. Bongiorno and J.R. García are supported by the Cell and Tissue Engineering National Institutes of Health Biotechnology training grant (T32-GM008433). R. Cruz-Acuña is supported by a National Science Foundation graduate fellowship.

The authors declare no competing financial interests.

Submitted: 10 June 2015
Accepted: 2 December 2015

References

Barcellos-Hoff, M.H., J. Aggeler, T.G. Ram, and M.J. Bissell. 1989. Functional differentiation and alveolar morphogenesis of primary mammary cultures on reconstituted basement membrane. *Development.* 105:223–235.

Beck, J.N., A. Singh, A.R. Rothenberg, J.H. Elisseeff, and A.J. Ewald. 2013. The independent roles of mechanical, structural and adhesion characteristics of 3D hydrogels on the regulation of cancer invasion and dissemination. *Biomaterials.* 34:9486–9495. http://dx.doi.org/10.1016/j.biomaterials.2013.08.077

Bryant, D.M., and K.E. Mostov. 2008. From cells to organs: building polarized tissue. *Nat. Rev. Mol. Cell Biol.* 9:887–901. http://dx.doi.org/10.1038/nrm2523

Canal, T., and N.A. Peppas. 1989. Correlation between mesh size and equilibrium degree of swelling of polymeric networks. *J. Biomed. Mater. Res.* 23:1183–1193. http://dx.doi.org/10.1002/jbm.820231007

Flory, P.J., and J. Rehner. 1943. Statistical mechanics of cross-linked polymer networks II. Swelling. *J. Chem. Phys.* 11:1183–1193.

Ghajar, C.M., X. Chen, J.W. Harris, V. Suresh, C.C. Hughes, N.L. Jeon, A.J. Putnam, and S.C. George. 2008. The effect of matrix density on the regulation of 3-D capillary morphogenesis. *Biophys. J.* 94:1930–1941. http://dx.doi.org/10.1529/biophysj.107.120774

Gill, B.J., D.L. Gibbons, L.C. Roudsari, J.E. Saik, Z.H. Rizvi, J.D. Roybal, J.M. Kurie, and J.L. West. 2012. A synthetic matrix with independently tunable biochemistry and mechanical properties to study epithelial morphogenesis and EMT in a lung adenocarcinoma model. *Cancer Res.* 72:6013–6023. http://dx.doi.org/10.1158/0008-5472.CAN-12-0895

Hoffman, M.P., M. Nomizu, E. Roque, S. Lee, D.W. Jung, Y. Yamada, and H.K. Kleinman. 1998. Laminin-1 and laminin-2 G-domain synthetic peptides bind syndecan-1 and are involved in acinar formation of a human submandibular gland cell line. *J. Biol. Chem.* 273:28633–28641. http://dx.doi.org/10.1074/jbc.273.44.28633

Huebsch, N., P.R. Arany, A.S. Mao, D. Shvartsman, O.A. Ali, S.A. Bencherif, J. Rivera-Feliciano, and D.J. Mooney. 2010. Harnessing traction-mediated manipulation of the cell/matrix interface to control stem-cell fate. *Nat. Mater.* 9:518–526. http://dx.doi.org/10.1038/nmat2732

Hughes, C.S., L.M. Postovit, and G.A. Lajoie. 2010. Matrigel: a complex protein mixture required for optimal growth of cell culture. *Proteomics.* 10:1886–1890. http://dx.doi.org/10.1002/pmic.200900758

Khetan, S., M. Guvendiren, W.R. Legant, D.M. Cohen, C.S. Chen, and J.A. Burdick. 2013. Degradation-mediated cellular traction directs stem cell fate in covalently crosslinked three-dimensional hydrogels. *Nat. Mater.* 12:458–465. http://dx.doi.org/10.1038/nmat3586

Klinowska, T.C., J.V. Soriano, G.M. Edwards, J.M. Oliver, A.J. Valentijn, R. Montesano, and C.H. Streuli. 1999. Laminin and beta1 integrins are crucial for normal mammary gland development in the mouse. *Dev. Biol.* 215:13–32. http://dx.doi.org/10.1006/dbio.1999.9435

Kloxin, A.M., A.M. Kasko, C.N. Salinas, and K.S. Anseth. 2009. Photodegradable hydrogels for dynamic tuning of physical and chemical properties. *Science.* 324:59–63. http://dx.doi.org/10.1126/science.1169494

Koutsopoulos, S., L.D. Unsworth, Y. Nagai, and S. Zhang. 2009. Controlled release of functional proteins through designer self-assembling peptide nanofiber hydrogel scaffold. *Proc. Natl. Acad. Sci. USA.* 106:4623–4628. http://dx.doi.org/10.1073/pnas.0807506106

Levental, K.R., H. Yu, L. Kass, J.N. Lakins, M. Egeblad, J.T. Erler, S.F. Fong, K. Csiszar, A. Giaccia, W. Weninger, et al. 2009. Matrix crosslinking forces tumor progression by enhancing integrin signaling. *Cell.* 139:891–906. http://dx.doi.org/10.1016/j.cell.2009.10.027

Lubarsky, B., and M.A. Krasnow. 2003. Tube morphogenesis: making and shaping biological tubes. *Cell.* 112:19–28. http://dx.doi.org/10.1016/S0092-8674(02)01283-7

Lutolf, M.P., G.P. Raeber, A.H. Zisch, N. Tirelli, and J.A. Hubbell. 2003. Cell-responsive synthetic hydrogels. *Adv. Mater.* 15:888–892. http://dx.doi.org/10.1002/adma.200304621

Martín-Belmonte, F., W. Yu, A.E. Rodríguez-Fraticelli, A.J. Ewald, Z. Werb, M.A. Alonso, and K. Mostov. 2008. Cell-polarity dynamics controls the mechanism of lumen formation in epithelial morphogenesis. *Curr. Biol.* 18:507–513. http://dx.doi.org/10.1016/j.cub.2008.02.076

McAteer, J.A., A.P. Evan, E.E. Vance, and K.D. Gardner. 1986. MDCK cysts: An in vitro model of epithelial cyst formation and growth. *Methods Cell Sci.* 10:245–248.

Miles, A.J., A.P. Skubitz, L.T. Furcht, and G.B. Fields. 1994. Promotion of cell adhesion by single-stranded and triple-helical peptide models of basement membrane collagen alpha 1(IV)531-543. Evidence for conformationally dependent and conformationally independent type IV collagen cell adhesion sites. *J. Biol. Chem.* 269:30939–30945.

Mroue, R., and M.J. Bissell. 2013. Three-dimensional cultures of mouse mammary epithelial cells. *Methods Mol. Biol.* 945:221–250. http://dx.doi.org/10.1007/978-1-62703-125-7_14

Nelson, C.M., M.M. Vanduijn, J.L. Inman, D.A. Fletcher, and M.J. Bissell. 2006. Tissue geometry determines sites of mammary branching morphogenesis in organotypic cultures. *Science.* 314:298–300. http://dx.doi.org/10.1126/science.1131000

O'Brien, L.E., T.S. Jou, A.L. Pollack, Q. Zhang, S.H. Hansen, P. Yurchenco, and K.E. Mostov. 2001. Rac1 orientates epithelial apical polarity through effects on basolateral laminin assembly. *Nat. Cell Biol.* 3:831–838. http://dx.doi.org/10.1038/ncb0901-831

O'Brien, L.E., M.M. Zegers, and K.E. Mostov. 2002. Opinion: Building epithelial architecture: insights from three-dimensional culture models. *Nat. Rev. Mol. Cell Biol.* 3:531–537. http://dx.doi.org/10.1038/nrm859

O'Brien, L.E., W. Yu, K. Tang, T.S. Jou, M.M. Zegers, and K.E. Mostov. 2006. Morphological and biochemical analysis of Rac1 in three-dimensional epithelial cell cultures. *Methods Enzymol.* 406:676–691. http://dx.doi.org/10.1016/S0076-6879(06)06053-8

Paszek, M.J., N. Zahir, K.R. Johnson, J.N. Lakins, G.I. Rozenberg, A. Gefen, C.A. Reinhart-King, S.S. Margulies, M. Dembo, D. Boettiger, et al. 2005. Tensional homeostasis and the malignant phenotype. *Cancer Cell.* 8:241–254. http://dx.doi.org/10.1016/j.ccr.2005.08.010

Patterson, J., and J.A. Hubbell. 2010. Enhanced proteolytic degradation of molecularly engineered PEG hydrogels in response to MMP-1 and MMP-2. *Biomaterials.* 31:7836–7845. http://dx.doi.org/10.1016/j.biomaterials.2010.06.061

Phelps, E.A., N.O. Enemchukwu, V.F. Fiore, J.C. Sy, N. Murthy, T.A. Sulchek, T.H. Barker, and A.J. García. 2012. Maleimide cross-linked bioactive PEG hydrogel exhibits improved reaction kinetics and cross-linking for cell encapsulation and in situ delivery. *Adv. Mater.* 24:64–70: 2. http://dx.doi.org/10.1002/adma.201103574

Phelps, E.A., D.M. Headen, W.R. Taylor, P.M. Thulé, and A.J. García. 2013. Vasculogenic bio-synthetic hydrogel for enhancement of pancreatic islet engraftment and function in type 1 diabetes. *Biomaterials.* 34:4602–4611. http://dx.doi.org/10.1016/j.biomaterials.2013.03.012

Provenzano, P.P., D.R. Inman, K.W. Eliceiri, and P.J. Keely. 2009. Matrix density-induced mechanoregulation of breast cell phenotype, signaling and gene expression through a FAK-ERK linkage. *Oncogene.* 28:4326–4343. http://dx.doi.org/10.1038/onc.2009.299

Raza, A., C.S. Ki, and C.C. Lin. 2013. The influence of matrix properties on growth and morphogenesis of human pancreatic ductal epithelial cells in 3D. *Biomaterials.* 34:5117–5127. http://dx.doi.org/10.1016/j.biomaterials.2013.03.086

Roignot, J., X. Peng, and K. Mostov. 2013. Polarity in mammalian epithelial morphogenesis. *Cold Spring Harb. Perspect. Biol.* 5:a013789. http://dx.doi.org/10.1101/cshperspect.a013789

Salimath, A.S., E.A. Phelps, A.V. Boopathy, P.L. Che, M. Brown, A.J. García, and M.E. Davis. 2012. Dual delivery of hepatocyte and vascular endothelial growth factors via a protease-degradable hydrogel improves cardiac function in rats. *PLoS One.* 7:e50980. http://dx.doi.org/10.1371/journal.pone.0050980

Suzuki, N., H. Nakatsuka, M. Mochizuki, N. Nishi, Y. Kadoya, A. Utani, S. Oishi, N. Fujii, H.K. Kleinman, and M. Nomizu. 2003. Biological activities of homologous loop regions in the laminin alpha chain G domains. *J. Biol. Chem.* 278:45697–45705. http://dx.doi.org/10.1074/jbc.M304667200

Teräväinen, T.P., S.M. Myllymäki, J. Friedrichs, N. Strohmeyer, J.V. Moyano, C. Wu, K.S. Matlin, D.J. Muller, and A. Manninen. 2013. αV-integrins are required for mechanotransduction in MDCK epithelial cells. *PLoS One.* 8:e71485. http://dx.doi.org/10.1371/journal.pone.0071485

Weaver, S.A., B. Wolters, N. Ito, A.M. Woskowicz, K. Kaneko, Y. Shitomi, M. Seiki, and Y. Itoh. 2014. Basal localization of MT1-MMP is essential for epithelial cell morphogenesis in 3D collagen matrix. *J. Cell Sci.* 127:1203–1213. http://dx.doi.org/10.1242/jcs.135236

Weiss, M.S., B.P. Bernabé, A. Shikanov, D.A. Bluver, M.D. Mui, S. Shin, L.J. Broadbelt, and L.D. Shea. 2012. The impact of adhesion peptides within hydrogels on the phenotype and signaling of normal and cancerous mammary epithelial cells. *Biomaterials.* 33:3548–3559. http://dx.doi.org/10.1016/j.biomaterials.2012.01.055

Wozniak, M.A., R. Desai, P.A. Solski, C.J. Der, and P.J. Keely. 2003. ROCK-generated contractility regulates breast epithelial cell differentiation in response to the physical properties of a three-dimensional collagen matrix. *J. Cell Biol.* 163:583–595. http://dx.doi.org/10.1083/jcb.200305010

Yu, W., A. Datta, P. Leroy, L.E. O'Brien, G. Mak, T.S. Jou, K.S. Matlin, K.E. Mostov, and M.M. Zegers. 2005. Beta1-integrin orients epithelial polarity via Rac1 and laminin. *Mol. Biol. Cell.* 16:433–445. http://dx.doi.org/10.1091/mbc.E04-05-0435

Zhang, H., F. Landmann, H. Zahreddine, D. Rodriguez, M. Koch, and M. Labouesse. 2011. A tension-induced mechanotransduction pathway promotes epithelial morphogenesis. *Nature.* 471:99–103. http://dx.doi.org/10.1038/nature09765

Zhang, X., G. Mernaugh, D.H. Yang, L. Gewin, M.B. Srichai, R.C. Harris, J.M. Iturregui, R.D. Nelson, D.E. Kohan, D. Abrahamson, et al. 2009. beta1 integrin is necessary for ureteric bud branching morphogenesis and maintenance of collecting duct structural integrity. *Development.* 136:3357–3366. http://dx.doi.org/10.1242/dev.036269

Tuning cell adhesive properties via layer-by-layer assembly of chitosan and alginate **Acta Biomaterialia**

Acta Biomaterialia 51 (2017) 279–293

Contents lists available at ScienceDirect

Acta Biomaterialia

journal homepage: www.elsevier.com/locate/actabiomat

Tuning cell adhesive properties via layer-by-layer assembly of chitosan and alginate

Joana M. Silva [a,b], José R. García [c,d], Rui L. Reis [a,b], Andrés J. García [c,d], João F. Mano [a,b,*]

[a] 3B's Research Group – Biomaterials, Biodegradables and Biomimetics, University of Minho, Headquarters of the European Institute of Excellence of Tissue Engineering and Regenerative Medicine, Avepark – Parque de Ciência e Tecnologia, Zona Industrial da Gandra, 4805-017 Barco GMR, Portugal
[b] ICVS/3B's – PT Government Associate Laboratory, 4710-243 Braga/Guimarães, Portugal
[c] Petit Institute for Bioengineering and Bioscience, Georgia Institute of Technology, Atlanta, GA 30332, USA
[d] Woodruff School of Mechanical Engineering, Georgia Institute of Technology, Atlanta, GA 30332, USA

ARTICLE INFO

Article history:
Received 10 October 2016
Received in revised form 19 January 2017
Accepted 20 January 2017
Available online 23 January 2017

Keywords:
Surface chemistry
Cross-linking
Cell adhesion
Fibronectin
Tissue engineering

ABSTRACT

Understanding the mechanisms controlling cell-multilayer film interactions is crucial to the successful engineering of these coatings for biotechnological and biomedical applications. Herein, we present a strategy to tune the cell adhesive properties of multilayers based on marine polysaccharides with and without cross-linking and/or coating with extracellular matrix proteins. Chemical cross-linking of multilayers improved mechanical properties of the coatings but also elicited changes in surface chemistry that alter the adhesion of human umbilical vein endothelial cells. We evaluated a strategy to decouple the mechanical and chemical properties of these films, enabling the transition from cell-adhesive to cell-resistant multilayers. Addition of chitosan/alginate multilayers on top of cross-linked films decreased endothelial cell adhesion, spreading, and proliferation to similar levels as uncross-linked films. Our findings highlight the key role of surface chemistry in cell-multilayer film interactions, and these engineered nanocoatings represent a tunable model of cell adhesive and non-adhesive multilayered films.

Statement of Significance

Multilayered films based on marine-derived polysaccharides were obtained by layer-by-layer (LbL). Biological tests with human umbilical vein endothelial cells (HUVECs) showed the potential of these films to tailor cell adhesion, spreading and proliferation. These multilayered films promise to be versatile and tunable model of cell adhesive and non-adhesive films.

1. Introduction

Layer-by-layer (LbL) assembly can produce hierarchical films with fine and precise control over the film properties [1–7]. Since its discovery, LbL assembly has been shown to be a simple, versatile and elegant bottom-up approach for template-assisted assembly of materials [4,8–10]. This method is based on the sequential adsorption of multivalent molecules on virtually any type of substrate via electrostatic, non-electrostatic, or a combination of thereof [2,11–13]. The overall properties of the film can be controlled simply by adjusting processing parameters: nature of polyelectrolytes, functional groups, molecular weight, charge density, concentration of the adsorption species, adsorption and rising time, pH, ionic strength, and humidity [14–19].

By using LbL assembly, an unprecedented variety of different components (i.e. hundreds of different materials) can be used. The nature and intrinsic properties of the building blocks dictate the bulk properties of the film [2,4,20]. Natural origin polymer-based multilayers have received particular attention due to their ability to impart unique properties to the polyelectrolyte multilayers (PEMs), such as cytocompatibility, biodegradability, presence of cell recognition sites, and natural similarity to the biological tissues [21–26]. Herein, two polysaccharides were used as polyelectrolytes: chitosan (CHI) and alginate (ALG). Multilayers based on these polysaccharides are stable over a pH range of 3–9, but exhibit high hydration levels and low mechanical strength, which impair cell adhesion [27–29]. Post-assembly modifications can be used to tune these properties, namely adsorption or immobilization of

* Corresponding author at: Department of Chemistry, CICECO – Aveiro Institute of Materials, University of Aveiro, 3810-193 Aveiro, Portugal.
E-mail address: jmano@ua.pt (J.F. Mano).

http://dx.doi.org/10.1016/j.actbio.2017.01.058
1742-7061/

extracellular matrix (ECM) proteins such as laminin (LM) and fibronectin (FN) as well as chemical cross-linking of the films.

Multilayers with poor cell adhesion ability are ideal candidates for an adsorption or chemical attachment of an ECM layer. The kinetics of protein adsorption is governed by electrostatic interactions and other secondary interactions such as hydrophobic interactions and hydrogen bonding [30]. The advantages of covalent immobilization over the adsorption strategy are that the biomolecules immobilized are not easily removed by physical force (e.g., rinsing) and are robust enough to withstand the possible harsh conditions of *in vivo* exposure [31]. Using this approach, it is also possible to avoid the diffusion of biomolecules along the multilayers, allowing a spatial control over its distribution [30].

Modulation of mechanical properties is a common approach used to tailor the bulk properties of multilayered films. Different approaches can be used to tune mechanical properties including the incorporation of nanocolloids [32], assembly pH [33], or by using covalent cross-linkers such as glutaraldehyde, [34,35] 1-ethyl-3-(3-dimethylaminopropyl)-carbodiimide (EDC) in combination with sulfo- N-hydroxysulfo-succinimide (EDC/s-NHS) [36–38] and genipin [29,39]. Genipin is a naturally derived chemical from the gardenia fruit that has been extensively investigated due to its ability to cross-link amine-containing polymers [40,41] in diverse systems, including multilayered films [39,42]. Using genipin as cross-linker, a wide range of films of increased stiffness can be obtained by simply varying the reaction time or the concentration of the cross-linker [43,44]. Genipin cross-linker, however, is reported to have effects on the wettability and roughness of the film. Thus, upon cross-linking of multilayers with genipin, it is challenging to decouple the mechanical and chemical properties of the films. In a previous study, Discher and co-workers achieved the decoupling of both parameters using polyacrylamide gels grafted with increased densities of collagen [45]. In the present work, we performed a systematic study of the cell adhesive properties of CHI/ALG multilayers upon cross-linking and ECM protein adsorption or immobilization (Scheme 1). Although the production and characterization of such multilayered films have been reported, to the best of our knowledge, this is the first time that such films have been used to decouple the effects of mechanical and chemical cues on cell adhesion.

2. Materials and methods

2.1. Production of multilayered films

The multilayers were processed using CHI of medium molecular weight (M_w 150–300 kDa, 90% degree of deacetylation, Heppe Medical Chitosan, Germany) and low viscosity ALG (538 kDa, ~250 cP, ref.71238, Sigma Aldrich, USA). PEMs were constructed by alternately immersing the tissue culture-grade polystyrene substrate (96 well plate, TCPS, Corning, USA) into a polyethylenimine solution (PEI, 0.5 mg mL^{-1}, 0.15 M sodium acetate buffer, pH 5.5) for 10 min, with an intermediate rinsing step of 10 min. TCPS coated with PEI presents a positive charge, providing support for the multilayer assembly. The substrates were then immersed in an ALG solution (1 mg mL^{-1}, 0.1 M sodium acetate buffer/0.15 M NaCl, pH 5.5) for 6 min. After rinsing with 0.1 M sodium acetate buffer/0.15 M NaCl (4 min), the same procedure was followed for CHI deposition (1 mg mL^{-1}, 0.1 M sodium acetate buffer/0.15 M NaCl 0.15 M, pH 5.5). Multilayers were generated by repeating the ALG/CHI deposition for five cycles. After buildup, the multilayers were cross-linked with genipin (Wako chemical, USA). Briefly, genipin solutions (0.125–5.0 mg mL^{-1}) were prepared by dissolving the adequate amount of lyophilized genipin into dimethyl sulfoxide (DMSO, Sigma Aldrich USA)/sodium acetate buffer (0.15 M NaCl, pH 5.5) mixture (1:4, v/v). The cross-linked films were then

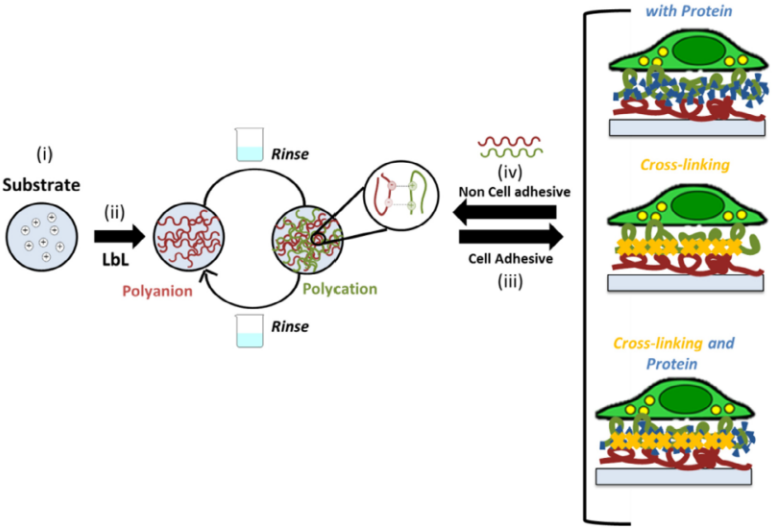

Scheme 1. Schematic representation of layer-by-layer (LbL) adsorption of polyelectrolytes based on electrostatic interactions. (i) The substrate (polystyrene well plates) was first modified with polyethylenimine (PEI) and extensive washed. (ii) The positive charged substrate was coated with polysaccharides that shared marine origin (ALG and CHI) using LbL assembly. Between the polyelectrolyte depositions a washing step was performed. (iii) The adhesive properties of ALG/CHI multilayers can be tuned by the addition of ECM proteins, chemical cross-linking or a combination of thereof. (iv) Upon the addition of ALG/CHI on the top of the cell adhesive ALG/CHI multilayers the films became non-adhesive.

rinsed in sodium acetate buffer (0.15 M NaCl, pH 5.5) for 1 h, followed by extensively washing in ultrapure water. Upon studying the behavior of films at different concentrations of cross-linker, the concentration of 3.5 mg mL^{-1} was selected, which corresponds to a cross-linking degree of ≈60.5%. After cross-linking the films, another bilayer was added on top of the film.

2.2. Protein immobilization

Human plasma FN (10 μg mL^{-1}, PBS, pH 7.4, Life Technologies, USA) and murine LM-1 (50 μg mL^{-1}, PBS, pH 7.4, Life Technologies, USA) were adsorbed or immobilized on unmodified or cross-linked films with or without an additional bilayer of ALG/CHI post-ECM coating. The procedure used for protein immobilization was based on pilot studies. Briefly, EDC (2.0 mM) and sulfo-NHS (5.0 mM) were used to pre-activate the proteins by reaction with their carboxyl groups. This step was performed for 20 min at room temperature (RT). The protein solution was then added to the multilayered films. After 4 h of incubation, the multilayered films were extensively washed in PBS. TCPS were used as control surfaces.

2.3. Quartz crystal microbalance with dissipation monitoring

The buildup of PEMs was followed *in situ* by quartz crystal microbalance (QCM-Dissipation, Q-Sense, Sweden) using gold-coated sensors excited at the several overtones (25, 35, 45, 55 MHz). The conditions used for the assembly were optimized in previous works [43,46]. The crystals were cleaned in an ultrasound bath at 30 °C using successive acetone, ethanol and isopropanol washes. Exposure of freshly prepared polyelectrolyte solutions (1 mg mL^{-1}) was performed at a constant flow rate of 100 μL min^{-1}. An initial layer of PEI (0.5 mg mL^{-1}, sodium acetate buffer 0.15 M, pH 5.5) was adsorbed for 10 min, followed by a washing step of 10 min. Afterwards, ALG solution was flowed for 6 min to allow ALG adsorption until equilibrium at the crystal surface was reached. After rinsing with 0.1 M sodium acetate buffer/0.15 M NaCl (4 min), the same procedure was followed for CHI deposition. These steps were repeated to generate 5 bilayers. The frequency and dissipation were monitored in real time. The thickness of the film was estimated using the *Voigt* model and the Q-Tools Software (Q-Sense) [47]. For the model, solvent viscosity was fixed at 0.001 Pa s (water) and the film density at 1050 kg m^{-3} (often assumed to return the lowest calculation error) [48–50]. The solvent density was varied by trial and error until the total error, χ^2, was minimized.

2.4. Scanning Electronic Microscopy (SEM)

The morphology of the different multilayered films formulations was observed by Scanning Electronic Microscopy (SEM), using a Jeol JSM-6010LV microscope operated at an accelerating voltage of 15 kV. All samples were sputtered with a conductive gold layer, using a sputter coater 108A (Cressington, UK). Three samples were evaluated for each condition.

2.5. Atomic force microscopy (AFM) Imaging

The multilayered films were imaged using a dimension Icon microscope controlled by NanoScope 9.1 (Bruker, France), operating in peak force tapping (ScanAsyst) mode with quantitative nanomechanical analysis, following established protocols [51,52]. AFM silicon nitride cantilevers (ScanAsyst-Air, Bruker) with a spring constant of 0.5 N/m, a frequency of 70 kHz, and a radius of the tip of 5 nm were used. The peak-force set-point was adjusted to 3.0 μN and the Poisson's ratio was assumed to be equal to 0.3 for the entire 512 × 512 pixels (2 × 2 μm^2) scan of the sample. The line scan rate was 0.4 Hz. The root mean squared roughness (R_{RMS}), average height value (H_{av}), and average elastic modulus (E_{av}) were calculated for each formulation in the wet state. Image analysis was performed using Gwyddion and Nanoscope Analysis 1.5. At least three measurements were performed in different specimens.

2.6. Water contact angle (WCA)

The wettability of the multilayered films was characterized by WCA measurements. Static WCA measurements were performed using the sessile drop method on an OCA15+ goniometer (DataPhysics, Germany) at RT. Milli-Q water (6 μL) was dropped onto the PEMs and pictures were taken after water drop stabilization.

2.7. Determination of Cross-linking degree

The cross-linking of CHI/ALG multilayers was evaluated using the Trypan blue method, using a published protocol. [27,43] Briefly, the test was performed by immersing uncross-linked and cross-linked multilayers in 0.4% Trypan blue (Invitrogen, USA) diluted 50-fold in sodium acetate buffer overnight at 37 °C. The supernatant absorbance was measured at 580 nm in a microplate reader (Sinergy HT, Bio-Tek, USA). The cross-linking degree was calculated as follows:

$$CL(\%) = \frac{(NH_3^+ \text{non-Xlinked solution}) - (NH_3^+ \text{ Xlinked solution})}{(NH_3^+ \text{non-Xlinked solution})}$$

where NH_3^+ non-Xlinked and NH_3^+ Xlinked solution are the free charge amines in uncross-linked and in cross-linked multilayers, respectively.

2.8. Protein adsorption resistance

The resistance to protein adsorption of modified of the multilayered films with and without cross-linking were evaluated using AlexaFluor488-labeled donkey anti-mouse IgG (Invitrogen, USA). Multilayers with and without cross-linking were incubated in IgG-AF488 for 60 min followed by extensive washing in PBS solution. Samples were immediately observed in a fluorescence microscope (TE300, Nikon, USA). To quantify the differences between ALG/CHI with and without cross-linking as well as the effect of multilayer numbers on the top of the film, a more sensitive protein assay was performed using alkaline phosphatase-conjugated donkey anti-mouse IgG (Jackson Immunoresearch, USA). All multilayers formulations were incubated with 1 μg mL^{-1} of this protein for 30 min, followed by extensive washing in PBS (Gibco, USA) containing 0.05% (v/v) Trinton-X-100 (Sigma, USA). Samples were then immersed in 4-methylumbelliferyl phosphate (25 mg mL^{-1}) in diethanolamine buffer for 15 min. Supernatant was collected and the fluorescence was measured on a microplate reader (HTS Plus, Perkin Elmer, USA), using an excitation of 360 nm and emission of 465 nm.

2.9. Cell adhesion to PEMs

Cell culture studies were performed with human umbilical vein endothelial cells (HUVECs, Lonza, USA) during passages 2–6. Cells were cultured in endothelial basal medium (EBM-2; Lonza, Switzerland), supplemented with Endothelial Growth Medium (EGM-2 SingleQuots, Lonza, USA) containing 2% fetal bovine serum (FBS), 5 ng mL^{-1} epidermal growth, 10 ng mL^{-1} basic fibroblast growth factor, 20 ng mL^{-1} insulin-like growth factor, 0.5 ng mL^{-1} vascular endothelial growth factor, 1 μg mL^{-1} ascorbic acid,

22.5 μg mL^{-1} heparin, 0.2 μg mL^{-1} hydrocortisone, penicillin (200 U/ml), 200 μg mL^{-1} streptomycin, and 0.25 μg mL^{-1} amphotericin B. All substrates (i.e., 96 well plates coated with PEMs and control (TCPS)) were sterilized by exposure to ultraviolet light for 40 min. Cells were seeded at 9000 cells/cm^2 and cultured for 1 day in EBM-2 supplemented with EGM-2 at 37 °C in a humidified 5% CO_2 atmosphere. 4,6-diaminidino-2-phenylindole-dilactate (DAPI, Sigma-Aldrich, USA) and Alexa Fluor 488-conjugated phalloidin (Invitrogen, USA) were used to label nuclei and actin cytoskeleton. Briefly at each time point, culture medium was removed and the samples fixed in 4% (v/v) paraformaldehyde (Electron Microscopy Science, USA) for 1 h, and replaced by PBS. Cells were permeabilized with 0.2% Triton X-100 (Sigma, USA) in PBS for 5 min. Samples were incubated in 30 mg mL^{-1} bovine albumin serum (BSA, Sigma, USA) for 30 min to block non-specific binding. Following PBS washing, DAPI (300 nM) and phalloidin (33 nM) staining was performed for 40 min at RT and protected from light. After extensive washing, samples were visualized in an inverted fluorescence microscope (TE300, Nikon, USA). The images obtained were analyzed using Image J software to determine cell area and density. In addition, cellular tests on native and cross-linked films with or without ALG/CHI multilayers on the top of PEMs were also performed in medium with or without serum.

Cell proliferation was measured using a Click-iT EdU Imaging Kit (Invitrogen, C10340, USA). After 3 h of incubation, half of the medium was removed and 10 mM EdU solution was added to the samples. After 24 h, the samples were washed with PBS, followed by cell fixation with 4% paraformaldehyde for 40 min. After permeabilization, samples were washed with 3% BSA twice and ClickiT reaction cocktail was added, followed by 30 min of incubation and by a washing step. For nucleus staining, Hoechst 33342 solution (30 mM, Fisher Scientific, USA) was added for 30 min, followed by extensive washing with PBS. The samples were visualized using an inverted fluorescence microscope (TE300, Nikon, USA). The images obtained were analyzed using Image J software to determine the percentage of EdU-positive nuclei as a measure of proliferation.

2.10. Statistical analyses

The experiments were carried out in triplicate unless otherwise specified. The results were presented as mean ± standard error of mean (SEM). Statistical analysis was performed by one-way ANOVA followed by Tukey pair-wise tests using Graph Pad Prism 5.0 for Windows.

3. Results and discussion

3.1. LbL assembly of ALG/CHI multilayers

The assembly of 5 bilayers of ALG/CHI multilayered films was monitored *in situ* by QCM-D. Fig. 1A shows the buildup of 5 bilayers of ALG/CHI, in terms of variations on normalized resonance frequency ($\Delta f_7/7$) and dissipation (ΔD_7) of the seventh overtone (35 MHz). Before the deposition of marine polysaccharides, PEI was flushed into the system, which confers a positive charge, as well as, an homogeneous deposition of PEMs [53]. As expected, the normalized frequency decreases upon each flushing of polyelectrolyte solution, reflecting the increase of mass over the gold sensor (including water), and the deposition of polymer on the surface of the crystal. On the other hand, the ΔD_7 mirrors the behavior of Δf_7, and a decrease is observed revealing that the film is not rigid and exhibits the typical viscoelastic behavior, which is characteristic of macromolecular systems. In addition, such variation indicates a shift toward a film with a higher viscous component and a great ability to adsorb water [37,48]. During the washing steps,

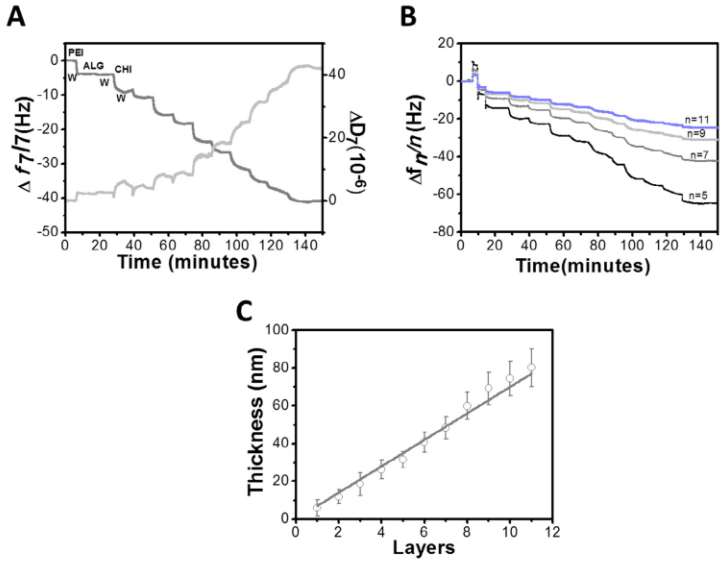

Fig. 1. Monitoring the buildup of five bilayers of ALG/CHI on gold modified initially modified with PEI: (A) Normalized resonance frequency ($\Delta f_7/7$) and dissipation shift (ΔD_7) obtained at 35 MHz; (B) Normalized resonance frequency shift for four overtones (n = 5,7,9,11); (C) Cumulative thickness evolution of polymeric film as a function of the number of deposited layers. Linear fitting matches well with the cumulative thickness variation ($r^2 = 0.99$).

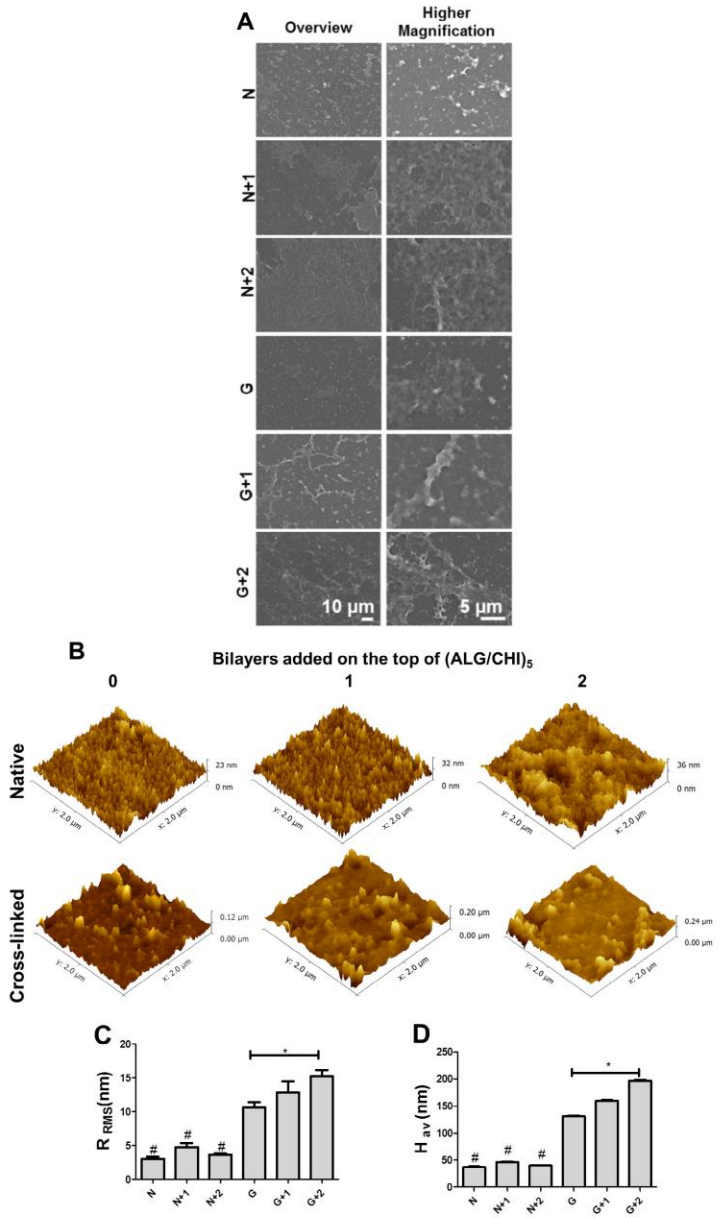

Fig. 2. (A) SEM micrographs of $(ALG/CHI)_5$ multilayers without (N) or with cross-linking (G), as well as with additional bilayers (1 or 2) on the top of the films. (B) AFM images ($2 \times 2\ \mu m^2$) of $(ALG/CHI)_5$ multilayered films without and with cross-linking upon the addition of bilayers on the top. (C) Root mean squared roughness (R_{RMS}) and (D) Average height value (H_{av}) for the different formulations. Statistical analysis was performed, and data was considered statistically different for p values <0.05 (*). (#) denotes significant differences when compared to all the native films.

the change of both $\Delta f_7/7$ and ΔD_7 are relatively small, indicating a strong association of the layers on the surface of the quartz crystal, and a weak desorption. The ladder trace of $\Delta f_7/7$ decrease and the trace of ΔD_7 increase, indicating the alternative adsorption of ALG or CHI molecules onto the substrate. The decrease in $\Delta f_n/n$ for the other overtones is different, which indicates that the adsorbed layer does not obey the Sauerbey law, as it was previously reported for these multilayers (Fig. 2B) [34]. Thus, the thickness of the film was estimated modeling the frequency and dissipation data, using the Voigt model instead of the Sauerbrey model [47]. For viscoelastic materials, the adsorbed mass does not fully couple to the oscillation of the crystal and dampens the oscillation, making the use of the *Voigt* model more appropriate [34,47]. The film thickness increased linearly with the deposited layers, as previously reported [27,34,44,54]. A thickness of ~80 nm was estimated for the final 5 bilayers. The thickness of the film is related to the water-uptake of each polyelectrolyte, the charge matching between the polyelectrolyte pairs and the affinity of polyelectrolytes for each other [32].

3.2. Physicochemical characterization

The surface properties of the multilayers such as morphology, topography and wettability influence protein adsorption and cell behavior. As previously reported, using ALG and CHI as polyelectrolytes lead to robust and compliant multilayers [34,44,46]. In the present work, the multilayered films were cross-linked with genipin (G, 3.5 mg mL^{-1}, cross-linking degree ≈65%) to improve their stability at all pH values, biodegradability, hydration, and mechanical strength. The morphology of different multilayer formulations was evaluated by SEM (Fig. 2A and S1). The results reveal a similar surface topography among different formulations and an increase in film's homogeneity as the number of bilayers increases. In order to have a better understanding of films topography at a smaller scale, AFM analysis was also performed. All formulations exhibit a rough surface, represented by polymer aggregates, usually called "islets" (Fig. 2B–D). It is also important to point out that one should be aware that the surface may not be fully coated, as suggested in previous works of Richert and coworkers [55]. Upon chemical cross-linking, the mean squared roughness (R_{RMS}) and average height value (H_{av}) increase due to the formation of a semi-interpenetrating network where ALG chains remain entrapped the cross-linked CHI chains [44]. It should also be pointed out that upon addition of multilayers on the top of the cross-linked films the roughness slightly increases.

The cross-linking of multilayers with genipin gives rise to semi-interpenetrating networks, since genipin only interacts with polyelectrolyte containing free amine groups (i.e. the amine groups that are not involved in the electrostatic interactions) (Fig. 3A).

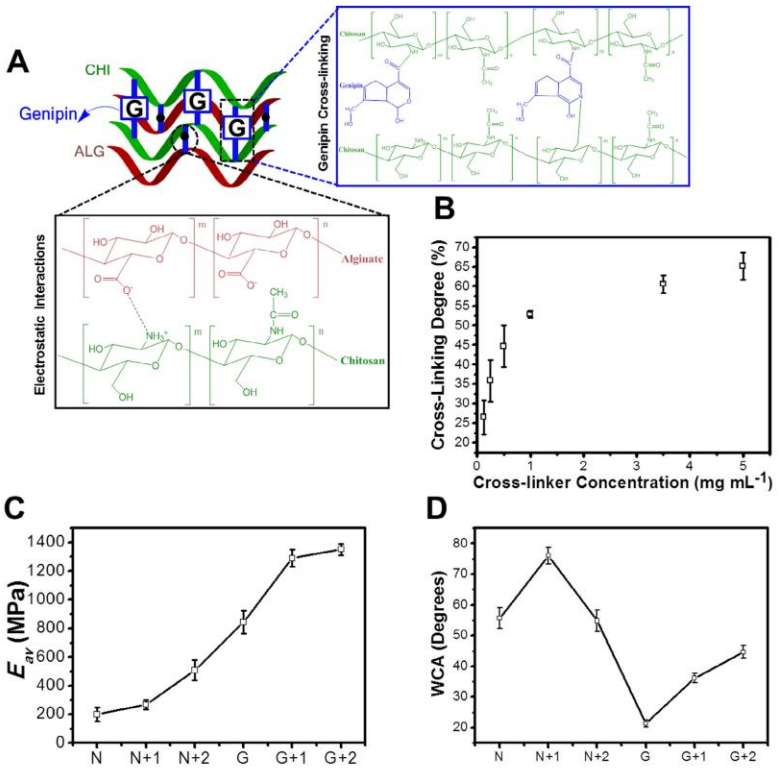

Fig. 3. (A) Schematic representation showing the multilayered rearrangements within the film, namely its electrostatic interactions and genipin cross-linking. (B) Cross-linking degree of ALG/CHI at different genipin concentrations; (C) Elastic modulus (E_{av}) upon cross-linking and/or deposition of bilayers on the top of the films using AFM indentation (D) Water contact angle (WCA) upon cross-linking and/or deposition of bilayers on the top of the films.

Using genipin, both color and fluorescence are generated upon its efficient reaction with primary amine groups and oxygen-radical induced polymerization [28,56]. The Trypan blue assay was performed to determine the cross-linking degree of the CHI within the multilayers [57]. The cross-linking degree could be varied from 0% to 65% by simple adjustment of the cross-linker concentration.

AFM experiments were also performed to assess the mechanical properties of the multilayered films (Fig. 3C). The elastic modulus (E_{av}) increases from 199.2 ± 46.5 MPa to 842.2 ± 79.5 MPa upon cross-linking. The results confirm an increase in stiffness upon increasing the cross-linker concentration which corroborated the results obtained in Trypan blue assay (Fig. S2A). In addition, the results confirm an increase in stiffness upon cross-linking and/or by adding bilayers on the top of the film which can be explained by an increase on film's homogeneity and thickness, which corroborated the AFM and QCM-D results.

In contrast to EDC/s-NHS-based cross-linking, genipin reaction is not a "zero length" reaction, since additional monomers and further dimerization are introduced within the film, altering the chemistry of the surface. It has been reported that genipin acts through nucleophilic attack of CHI amine groups, establishing a secondary amide linkage [28,56]. Subsequent steps involve radical-induced polymerization that creates genipin heterocyclic derivatives, which are richer in hydrophilic groups such as amine, amides and hydroxyl groups [28,56]. The wetting behavior of the multilayered films was evaluated by water contact angle (WCA) measurements. Fig. 3D shows that WCA decreases upon cross-linking, decreasing gradually with increases in the cross-linker concentration (Fig. S2B). This finding is consistent with earlier studies where a consistent decrease of WCA was found with increasing cross-linker concentrations [28,39]. This decrease has been previously explained by the denser polyelectrolyte connections and increase of cross-linker conjugates within the films [44]. In addition, upon the adsorption of another bilayer on the top of uncross-linked or cross-linked films, the WCA increases due to changes on the surface chemistry. Upon deposition of ALG/CHI bilayers on the top of the cross-linked films (G+1/G+2) the chemistry of the surface is changed, masking the hydrophilic character of the cross-linker derivatives.

3.3. Protein adsorption resistance

The resistance to IgG adsorption of these multilayers was evaluated by measuring the adsorption of labeled IgG onto these monolayers (Fig. 4A). Upon cross-linking with genipin, adsorption of IgG-AF488 substantially decreased. In order to quantify the effects of cross-linking on protein adsorption, an assay based on donkey anti-mouse IgG antibody conjugated to alkaline phosphatase was performed (Fig. 4B). In this assay the same trend was observed, and a decrease on substrate reaction occurs

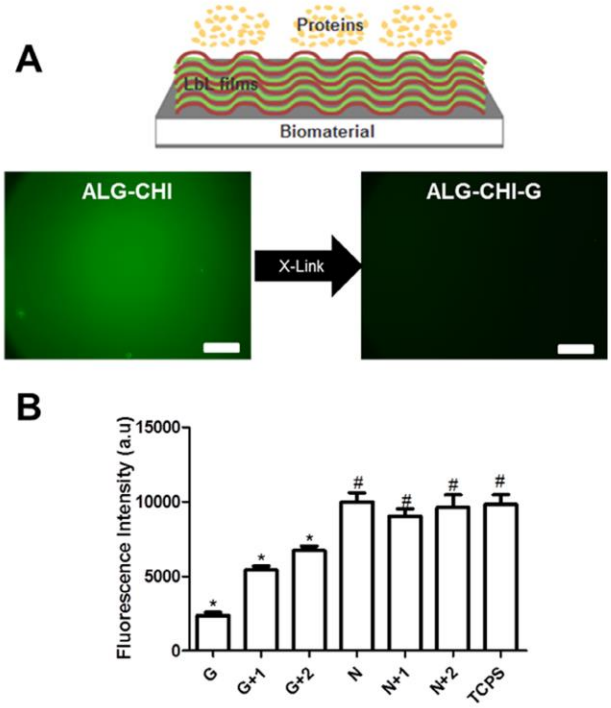

Fig. 4. Non-fouling properties of ALG/CHI films. (A) Donkey anti-mouse IgG AF488 fluorescence assay in multilayers with (G) and without cross-linking (N). The scale bar is 250 μm. The inset image is a schematic representation of non-fouling PEMs. (B) Enzymatic assay for IgG adsorption onto PEMs. Statistical analysis was performed, and data was considered statistically different for p values <0.05. (*) denotes significant differences when compared to all PEMs formulations. (#) denotes significant differences relative to cross-linked multilayers.

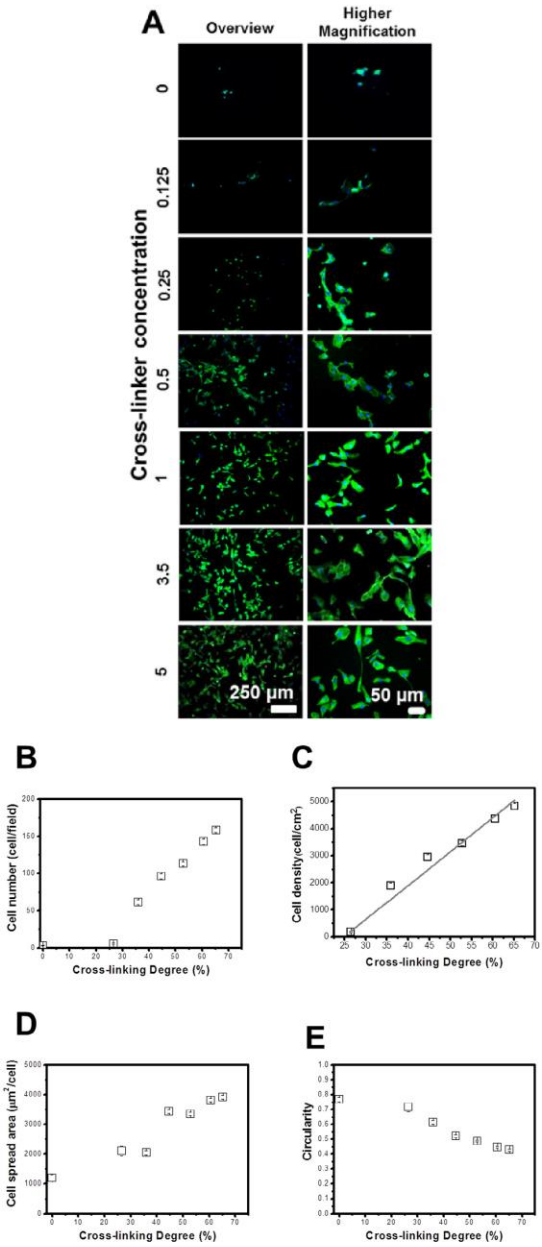

Fig. 5. (A) DAPI-phalloidin fluorescence assay at 1 day of HUVECs culture in multilayers with different cross-linking degrees. Cells nuclei were stained blue by DAPI and F-actin filaments in green by phalloidin. (B) Cell number per field, (C) Cell density and (D) Cell spread area, and (E) Cell circularity as a function of cross-linking degree. Linear fitting matches well with the cell density variation as a function of cross-linking degree ($r^2 = 0.98$).

following chemical cross-linking. However, this behavior is reversed with the addition of another bilayer of ALG and CHI on the top of cross-linked films prior to exposure to IgG. The addition of another bilayer effectively acts as a physical barrier for the underlying cross-linked films, leading to 2-fold increase in the fluorescence intensity when compared to the cross-linked films. These results were further confirmed by WCA, where a decrease in the hydrophilicity of cross-linked multilayers is observed upon the addition of a multilayer on top of cross-linked films (Fig. 3D). To establish the general protein adsorption resistant properties of these films however, additional proteins must be evaluated.

3.4. Cell adhesion to ALG/CHI films

Multilayers based on polysaccharides are resistant to cell adhesion due to high hydration and low stiffness [27–29]. However, these multilayers can also be used to control cellular behavior upon tailoring the mechanical properties (matrix stiffness, elasticity and viscosity), which influence how cells spread, migrate, proliferate, differentiate, and organize key intracellular structures [44,58]. Herein, using different genipin concentrations ranging from 0 to 5 mg mL^{-1}, an increase in cell number and spread area and a decrease in cell circularity occur with increases in cross-linker concentration (Fig. 5). In addition, cell density increases linearly with cross-linking degree ($r^2 = 0.98$) (Fig. 5C), and the cell morphology, number, area, and proliferation are in the same range as values for cells adhering to TCPS (Fig. S3). Similar behavior is observed for cell density, spread area and circularity plotted as a function of E_{av} (Fig. 6). However, cell density was not linearly increasing with E_{av}, because certain cross-linker concentrations led to an increase of cross-linking degree and to minor differences on E_{av}. These results corroborated previous reports, where CHI/ALG multilayers upon cross-linking with genipin presented a decrease in water-uptake ability, decrease in the viscous component of the film, increase in stiffness and enhancements in cell adherence, spreading and proliferation [43,59]. Similar behavior has also been reported for other multilayers [36,60,61], and for a large variety of cells, including endothelial cells, which prefer stiffer substrate (i.e., less gel-like substrates) for attachment and spreading [53].

We also tailored the cell adhesive properties of the multilayers by the adsorption or immobilization of ECM proteins (e.g. FN and LM). Using this approach, cell number and spread area increase, whereas the circularity decreases, with adsorption or immobilization of these ECM components (Fig. 7). Similar results have been reported for multilayered films containing FN [62,63] or LM [64,65]. High cell adhesive and proliferation activities were observed for FN compared to LM. These differences may arise from the higher molecular weight of LM compared to FN which may affect its conformation and orientation upon adsorption or immobilization onto the multilayers. In addition, larger proteins bind more strongly and can even repel pre-adsorbed proteins during post-adsorption spreading [66].

Our data demonstrate that both cross-linking and ECM immobilization modulate cell adhesion. We next combined films cross-linked with two different genipin concentrations (3.5 and 5 mg mL^{-1}) with ECM proteins by adsorption or immobilization. This analysis reveals a modest impact of protein adsorption or immobilization on cell behavior when compared with the uncross-linked film (Figs. S4 and S5). Similar results have been reported for poly(L-lysine)/poly(L-glutamic acid) (PLL/PGA) multilayers upon cross-linking and grafting with arginine-glycine-aspartic acid (RGD) [67]. Covalent cross-linking enhances

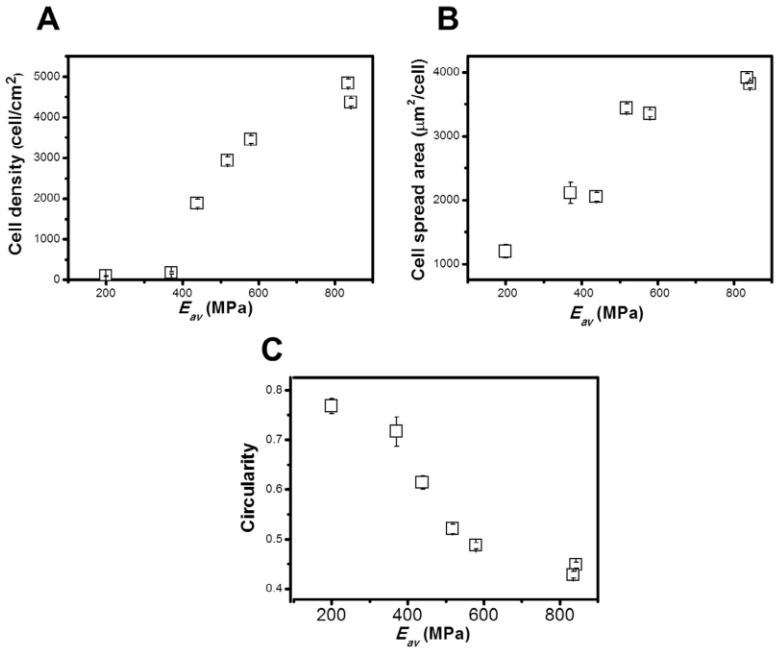

Fig. 6. HUVECs seeded on multilayers with different Elastic modulus (E_{av}). (A) Cell density and (B) Cell spread area and (C) Cell circularity as a function of E_{av}.

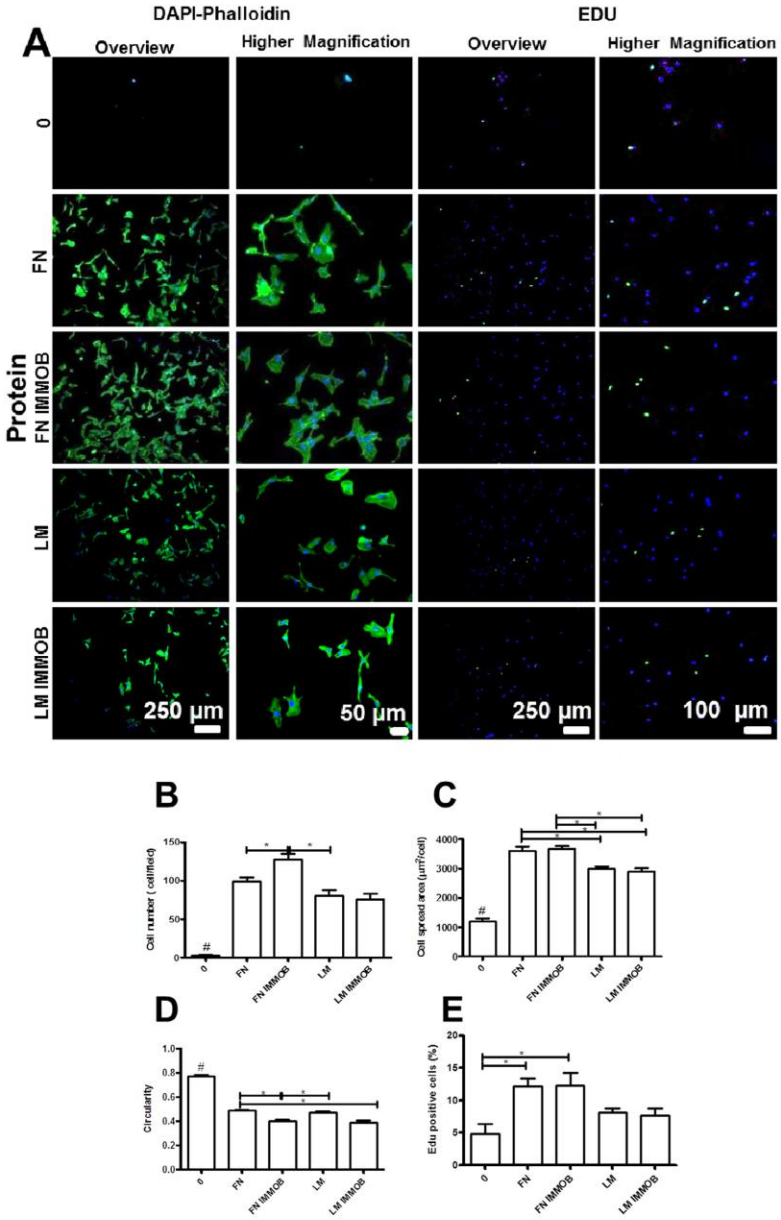

Fig. 7. (A) DAPI/phalloidin staining and representative images of EDU assay for HUVECs adhered on native films with and without adsorbed or immobilized proteins (IMMOB). Quantification of (B) Cell number per field, (C) Cell spread area, and (D) Cell circularity. (E) Percentage of proliferating cells measured by the EDU assay. Statistical analysis was performed, and data was considered statistically different for p values <0.05 (*). (#) denotes significant differences when compared to all PEMs formulations.

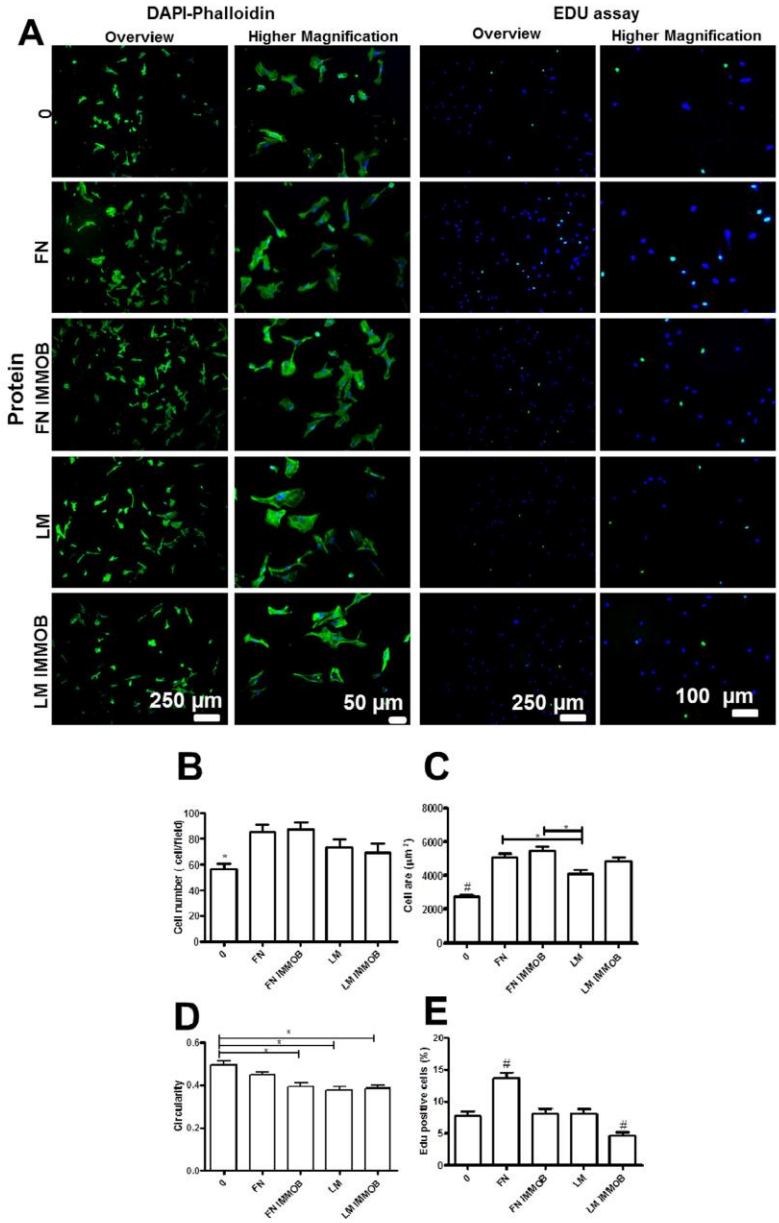

Fig. 8. (A) DAPI/phalloidin staining and representative images of EDU assay for HUVECs adhered on cross-linked films with a bilayer of ALG/CHI on the top in the presence or absence of adsorbed or immobilized proteins (IMMOB). Quantification of (B) Cell number per field, (C) Cell spread area, and (D) Cell circularity. (E) Percentage of proliferating cells measured by the EDU assay. Statistical analysis was performed, and data was considered statistically different for p values <0.05 (*). (#) denotes significant differences when compared to all PEMs formulations.

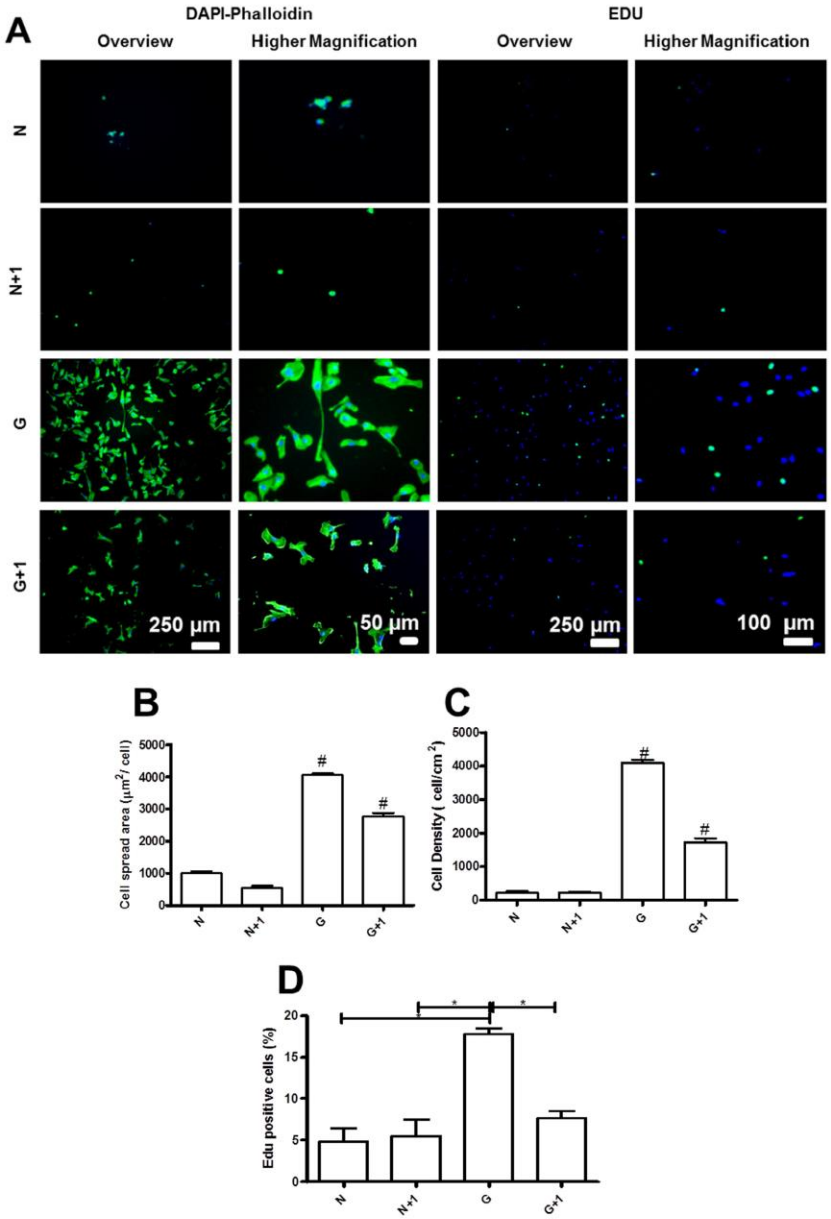

Fig. 9. (A) DAPI/phalloidin staining and representative images of EDU assay for HUVECs adhered on native films (N) and cross-linked films (G) with an additional bilayer on the top of the film and in the presence or absence of adsorbed or immobilized proteins. Quantification of (B) Cell number per field, (C) Cell spread area, and (D) Cell circularity. (E) Percentage of proliferating cells measured by the EDU assay. Statistical analysis was performed, and data was considered statistically different for p values <0.05 (*). (#) denotes significant differences when compared to all PEMs formulations.

endothelial cell adhesion and allows high cellular coverage without the pre-adsorption or immobilization of ECM proteins. However, the cell adhesion was hindered upon deposition of additional bilayers of polyelectrolytes on the top of cross-linked films (3.5 mg mL^{-1}, cross-linking degree ≈60.5%) (Fig. 8). Finally, EdU labeling demonstrates a decrease in endothelial cell proliferation upon addition of ALG/CHI bilayers on top of cross-linked films. However, upon adsorption or immobilization of ECM proteins, cell proliferation was enhanced. The positive effect of ECM proteins on HUVECs proliferation has been reported for PEMs [31,63,68].

As the number of bilayers on the top of cross-linked films increase, the resistance to cell adhesion was more pronounced (Fig. S6). However, upon adsorption or immobilization of ECM proteins, the cell adhesive and proliferation properties of PEMs were recovered. We performed a similar study with uncross-linked films, and additional layers were deposited on the top of the film, which further decreased the cell spread area and cell density (Fig. 9 and S7). Notably, Richert et al. demonstrated that the number of layers influence cellular responses, because it led to an increase of thickness and higher hydration rates [69–71]. EdU labeling indicated a decrease in cell proliferation upon the adsorption of bilayers on the top of cross-linked films and no differences for native films. These results highlight the key role of surface chemistry on cell proliferation.

To evaluate the contribution of the adsorption of serum proteins on cell adhesion on multilayered films, adhesion experiments were performed in serum-free media (Fig. 10 and S8). For cross-linked films, endothelial cells adhered and spread on the surface

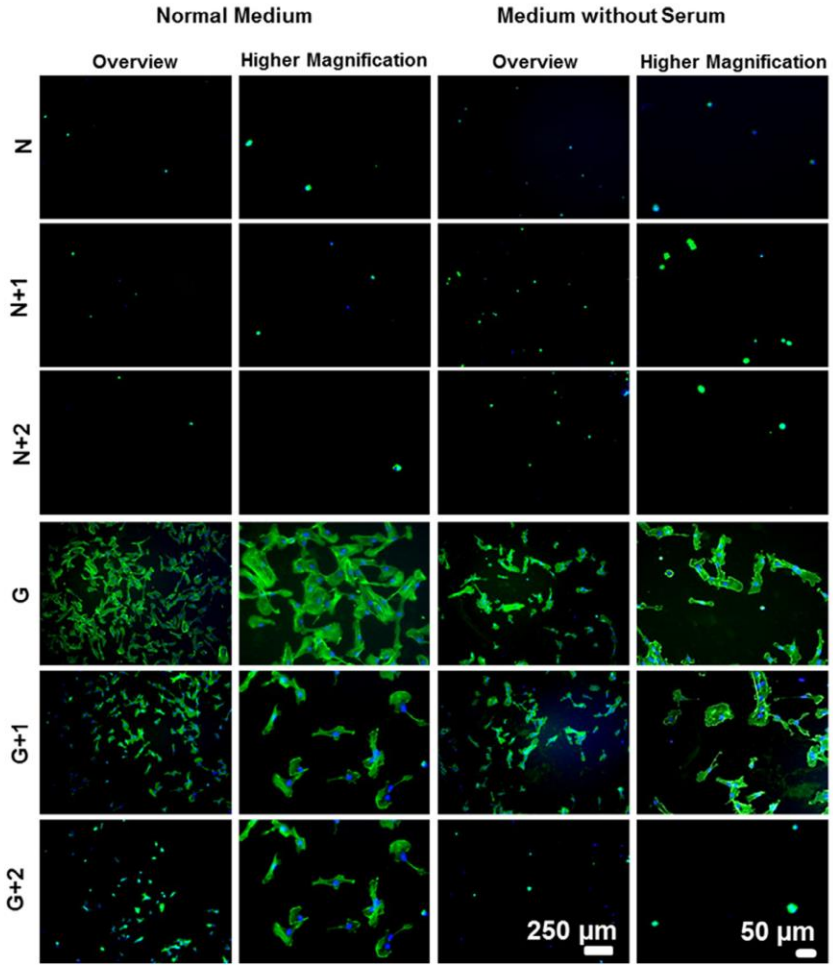

Fig. 10. Adhesion of HUVECS on native (N) and cross-linked films (G) with or without additional bilayers on the top when resuspended in normal medium or medium without serum. Cells nuclei were stained blue by DAPI and F-actin filaments in green by phalloidin.

even in serum-free media conditions, indicating that the adhesion was not primarily mediated by the proteins present in serum but by the mechanical and chemical cues on the substrate and/or proteins secreted by the cells. For native films the same behavior was observed, validating results where cell adhesion and proliferation were achieved upon chemical cross-linking or ECM proteins adsorption/immobilization.

4. Conclusion

We present a strategy to tune the cell adhesive properties of multilayers based on ALG and CHI with and without cross-linking and/or coating with ECM proteins. Chemical cross-linking of multilayers improved mechanical properties of the coatings but also elicited changes in surface chemistry that alter the adhesion of human umbilical vein endothelial cells. Addition of CHI/ALG multilayers on top of cross-linked films decreased endothelial cell adhesion, spreading, and proliferation to similar levels as uncross-linked films. Our findings highlight the key role of surface chemistry in cell-multilayer film interactions, and these engineered nanocoatings represent a tunable model of cell adhesive and non-adhesive multilayered films.

Acknowledgements

The authors acknowledge the financial support by the Luso-American Foundation and the USA National Institutes of Health (R01 AR062920). Joana M. Silva would also like to acknowledge the Portuguese Foundation for Science and Technology (FCT) for her PhD grant.

Appendix A. Supplementary data

Supplementary data associated with this article can be found, in the online version, at http://dx.doi.org/10.1016/j.actbio.2017.01.058.

References

[1] K. Ariga, J.P. Hill, Q. Ji, Layer-by-layer assembly as a versatile bottom-up nanofabrication technique for exploratory research and realistic application, Phys. Chem. Chem. Phys. 9 (2007) 2319–2340.
[2] T. Boudou, T. Crouzier, K. Ren, G. Blin, C. Picart, Multiple functionalities of polyelectrolyte multilayer films: new biomedical applications, Adv. Mater. 22 (2010) 441–467.
[3] M.M. De Villiers, D.P. Otto, S.J. Strydom, Y.M. Lvov, Introduction to nanocoatings produced by layer-by-layer (LbL) self-assembly, Adv. Drug Deliv. Rev. 63 (2011) 701–715.
[4] G. Decher, Layer-by-Layer Assembly (Putting Molecules to Work). Multilayer Thin Films, second ed., Wiley, Weinheim, 2012, pp. 1–21.
[5] C.J. Detzel, A.L. Larkin, P. Rajagopalan, Polyelectrolyte multilayers in tissue engineering, Tissue Eng. Part B Rev. 17 (2011) 101–113.
[6] P.T. Hammond, Engineering materials layer-by-layer: challenges and opportunities in multilayer assembly, AIChE J. 57 (2011) 2928–2940.
[7] Z. Tang, Y. Wang, P. Podsiadlo, N.A. Kotov, Biomedical applications of layer-by-layer assembly: from biomimetics to tissue engineering, Adv. Mater. 18 (2006) 3203–3224.
[8] Y. Lvov, G. Decher, H. Moehwald, Assembly, structural characterization, and thermal behavior of layer-by-layer deposited ultrathin films of poly (vinyl sulfate) and poly (allylamine), Langmuir 9 (1993) 481–486.
[9] R. Iler, Multilayers of colloidal particles, J. Colloid Interface Sci. 21 (1966) 569–594.
[10] F. Lim, A.M. Sun, Microencapsulated islets as bioartificial endocrine pancreas, Science 210 (1980) 908–910.
[11] P.T. Hammond, Form and function in multilayer assembly: new applications at the nanoscale, Adv. Mater. 16 (2004) 1271–1293.
[12] P.T. Hammond, Building biomedical materials layer-by-layer, Mater. Today 15 (2012) 196–206.
[13] J. Borges, J.F. Mano, Molecular interactions driving the layer-by-layer assembly of multilayers, Chem. Rev. 114 (2014) 8883–8942.
[14] N. Aggarwal, N. Altgärde, S. Svedhem, G. Michanetzis, Y. Missirlis, T. Groth, Tuning cell adhesion and growth on biomimetic polyelectrolyte multilayers by variation of pH during layer-by-layer assembly, Macromol. Biosci. 13 (2013) 1327–1338.
[15] D.S. Salloum, S.G. Olenych, T.C. Keller, J.B. Schlenoff, Vascular smooth muscle cells on polyelectrolyte multilayers: hydrophobicity-directed adhesion and growth, Biomacromolecules 6 (2005) 161–167.
[16] R.A. Ghostine, M.Z. Markarian, J.B. Schlenoff, Asymmetric growth in polyelectrolyte multilayers, J. Am. Chem. Soc. 135 (2013) 7636–7646.
[17] A. Vidyasagar, C. Sung, K. Losensky, J.L. Lutkenhaus, PH-dependent thermal transitions in hydrated layer-by-layer assemblies containing weak polyelectrolytes, Macromolecules 45 (2012) 9169–9176.
[18] S.E. Burke, C.J. Barrett, Swelling behavior of hyaluronic acid/polyallylamine hydrochloride multilayer films, Biomacromolecules 6 (2005) 1419–1428.
[19] Y. Jang, J. Seo, B. Akgun, S. Satija, K. Char, Molecular weight dependence on the disintegration of spin-assisted weak polyelectrolyte multilayer films, Macromolecules 46 (2013) 4580–4588.
[20] P.T. Hammond, Recent explorations in electrostatic multilayer thin film assembly, Curr. Opin. Colloid Interface Sci. 4 (1999) 430–442.
[21] P.B. Malafaya, G.A. Silva, R.L. Reis, Natural–origin polymers as carriers and scaffolds for biomolecules and cell delivery in tissue engineering applications, Adv. Drug Deliv. Rev. 59 (2007) 207–233.
[22] M. Cascone, N. Barbani, P. Giusti, C. Cristallini, G. Ciardelli, L. Lazzeri, Bioartificial polymeric materials based on polysaccharides, J. Biomater. Sci. Polym. Ed. 12 (2001) 267–281.
[23] J.F. Mano, G.A. Silva, H.S. Azevedo, P.B. Malafaya, R.A. Sousa, S.S. Silva, L.F. Boesel, J.M. Oliveira, T.C. Santos, A.P. Marques, N.M. Neves, R.L. Reis, Natural origin biodegradable systems in tissue engineering and regenerative medicine: present status and some moving trends, J. R. Soc. Interface 4 (2007) 999–1030.
[24] S.H. Brown, P.E. Pummill, Recombinant production of hyaluronic acid, Curr. Pharm. Biotechnol. 9 (2008) 239–241.
[25] O. Etienne, A. Schneider, C. Taddei, L. Richert, P. Schaaf, J.-C. Voegel, C. Egles, C. Picart, Degradability of polysaccharides multilayer films in the oral environment: an in vitro and in vivo study, Biomacromolecules 6 (2005) 726–733.
[26] C. Picart, A. Schneider, O. Etienne, J. Mutterer, P. Schaaf, C. Egles, N. Jessel, J.-C. Voegel, Controlled degradability of polysaccharide multilayer films in vitro and in vivo, Adv. Funct. Mater. 15 (2005) 1771–1780.
[27] J.M. Silva, S.G. Caridade, R.R. Costa, N.M. Alves, T. Groth, C. Picart, R.L. Reis, J.F. Mano, PH responsiveness of multilayered films and membranes made of polysaccharides, Langmuir 31 (2015) 11318–11328.
[28] L. Gao, H. Gan, Z. Meng, R. Gu, Z. Wu, L. Zhang, X. Zhu, W. Sun, J. Li, Y. Zheng, G. Dou, Effects of genipin cross-linking of chitosan hydrogels on cellular adhesion and viability, Colloids Surf., B 117 (2014) 398–405.
[29] F. Gaudière, S. Morin-Grognet, L. Bidault, P. Lembré, E. Pauthe, J.-P. Vannier, H. Atmani, G. Ladam, B.A. Labat, Genipin-cross-linked layer-by-layer assemblies: biocompatible microenvironments to direct bone cell fate, Biomacromolecules 15 (2014) 1602–1611.
[30] J.M. Silva, R.L. Reis, J.F. Mano, Biomimetic extracellular environment based on natural origin polyelectrolyte multilayers, Small 12 (2016) 4308–4342.
[31] G. Li, P. Yang, Y. Liao, N. Huang, Tailoring of the titanium surface by immobilization of heparin/fibronectin complexes for improving blood compatibility and endothelialization: an in vitro study, Biomacromolecules 12 (2011) 1155–1168.
[32] V. Gribova, R. Auzely-Velty, C. Picart, Polyelectrolyte multilayer assemblies on materials surfaces: from cell adhesion to tissue engineering, Chem. Mater. 24 (2011) 854–869.
[33] S. Boddohi, C.E. Killingsworth, M.J. Kipper, Polyelectrolyte multilayer assembly as a function of pH and ionic strength using the polysaccharides chitosan and heparin, Biomacromolecules 9 (2008) 2021–2028.
[34] N.M. Alves, C. Picart, J.F. Mano, Self assembling and crosslinking of polyelectrolyte multilayer films of chitosan and alginate studied by QCM and IR spectroscopy, Macromol. Biosci. 9 (2009) 776–785.
[35] A.L. Larkin, R.M. Davis, P. Rajagopalan, Biocompatible, detachable, and free-standing polyelectrolyte multilayer films, Biomacromolecules 11 (2010) 2788–2796.
[36] L. Richert, F. Boulmedais, P. Lavalle, J. Mutterer, E. Ferreux, G. Decher, P. Schaaf, J.-C. Voegel, C. Picart, Improvement of stability and cell adhesion properties of polyelectrolyte multilayer films by chemical cross-linking, Biomacromolecules 5 (2004) 284–294.
[37] C. Picart, P. Lavalle, P. Hubert, F. Cuisinier, G. Decher, P. Schaaf, J.-C. Voegel, Buildup mechanism for poly (L-lysine)/hyaluronic acid films onto a solid surface, Langmuir 17 (2001) 7414–7424.
[38] K. Ren, T. Crouzier, C. Roy, C. Picart, Polyelectrolyte multilayer films of controlled stiffness modulate myoblast cells differentiation, Adv. Funct. Mater. 18 (2008) 1378.
[39] A.L. Hillberg, C.A. Holmes, M. Tabrizian, Effect of genipin cross-linking on the cellular adhesion properties of layer-by-layer assembled polyelectrolyte films, Biomaterials 30 (2009) 4463–4470.
[40] L. Cui, J. Jia, Y. Guo, Y. Liu, P. Zhu, Preparation and characterization of IPN hydrogels composed of chitosan and gelatin cross-linked by genipin, Carbohydr. Polym. 99 (2014) 31–38.
[41] M. Mekhail, K. Jahan, M. Tabrizian, Genipin-crosslinked chitosan/poly-l-lysine gels promote fibroblast adhesion and proliferation, Carbohydr. Polym. 108 (2014) 91–98.
[42] C. Chaubaroux, E. Vrana, C. Debry, P. Schaaf, B. Senger, J.-C. Voegel, Y. Haikel, C. Ringwald, J. Hemmerlé, P. Lavalle, F. Boulmedais, Collagen-based fibrillar multilayer films cross-linked by a natural agent, Biomacromolecules 13 (2012) 2128–2135.

[43] J.M. Silva, A.R.C. Duarte, S.G. Caridade, C. Picart, R.L. Reis, J.F. Mano, Tailored freestanding multilayered membranes based on chitosan and alginate, Biomacromolecules 15 (2014) 3817–3826.
[44] J.M. Silva, S.G. Caridade, N.M. Oliveira, R.L. Reis, J.F. Mano, Chitosan–alginate multilayered films with gradients of physicochemical cues, J. Mater. Chem. B 3 (2015) 4555–4568.
[45] A. Engler, L. Bacakova, C. Newman, A. Hategan, M. Griffin, D. Discher, Substrate compliance versus ligand density in cell on gel responses, Biophys. J. 86 (2004) 617–628.
[46] S.G. Caridade, C. Monge, F. Gilde, T. Boudou, J.F. Mano, C. Picart, Free-standing polyelectrolyte membranes made of chitosan and alginate, Biomacromolecules 14 (2013) 1653–1660.
[47] M.V. Voinova, M. Rodahl, M. Jonson, B. Kasemo, Viscoelastic acoustic response of layered polymer films at fluid-solid interfaces: continuum mechanics approach, Phys. Scr. 59 (1999) 391–396.
[48] R.R. Costa, C.A. Custódio, F.J. Arias, J.C. Rodríguez-Cabello, J.F. Mano, Layer-by-layer assembly of chitosan and recombinant biopolymers into biomimetic coatings with multiple stimuli-responsive properties, Small 7 (2011) 2640–2649.
[49] A.K. Dutta, G. Belfort, Adsorbed gels versus brushes: viscoelastic differences, Langmuir 23 (2007) 3088–3094.
[50] N. Weber, A. Pesnell, D. Bolikal, J. Zeltinger, J. Kohn, Viscoelastic properties of fibrinogen adsorbed to the surface of biomaterials used in blood-contacting medical devices, Langmuir 23 (2007) 3298–3304.
[51] D. Alsteens, V. Dupres, S. Yunus, J.-P. Latgé, J. Heinisch Jr., Y.F. Dufrêne, High-resolution imaging of chemical and biological sites on living cells using peak force tapping atomic force microscopy, Langmuir 28 (2012) 16738–16744.
[52] P. Trtik, J. Kaufmann, U. Volz, On the use of peak-force tapping atomic force microscopy for quantification of the local elastic modulus in hardened cement paste, Cem. Concr. Res. 42 (2012) 215–221.
[53] C. Boura, P. Menu, E. Payan, C. Picart, J. Voegel, S. Muller, J. Stoltz, Endothelial cells grown on thin polyelectrolyte mutlilayered films: an evaluation of a new versatile surface modification, Biomaterials 24 (2003) 3521–3530.
[54] G.V. Martins, E.G. Merino, J.F. Mano, N.M. Alves, Crosslink effect and albumin adsorption onto chitosan/alginate multilayered systems: an in situ QCM-D Study, Macromol. Biosci. 10 (2010) 1444–1455.
[55] L. Richert, P. Lavalle, E. Payan, X.Z. Shu, G.D. Prestwich, J.-F. Stoltz, P. Schaaf, J.-C. Voegel, C. Picart, Layer by layer buildup of polysaccharide films: physical chemistry and cellular adhesion aspects, Langmuir 20 (2004) 448–458.
[56] H. Chen, W. Ouyang, B. Lawuyi, C. Martoni, S. Prakash, Reaction of chitosan with genipin and its fluorogenic attributes for potential microcapsule membrane characterization, J. Biomed. Mater. Res., Part A 75A (2005) 917–927.
[57] W.-C. Shen, D. Yang, H.J.P. Ryser, Colorimetric determination of microgram quantities of polylysine by trypan blue precipitation, Anal. Biochem. 142 (1984) 521–524.
[58] F. Rehfeldt, A.J. Engler, A. Eckhardt, F. Ahmed, D.E. Discher, Cell responses to the mechanochemical microenvironment—implications for regenerative medicine and drug delivery, Adv. Drug Deliv. Rev. 59 (2007) 1329–1339.
[59] J.M. Silva, A.R.C. Duarte, C.A. Custódio, P. Sher, A.I. Neto, A. Pinho, J. Fonseca, R. L. Reis, J.F. Mano, Nanostructured hollow tubes based on chitosan and alginate multilayers, Adv. Healthcare Mater. 3 (2014) 433–440.
[60] L. Richert, A. Schneider, D. Vautier, C. Vodouhe, N. Jessel, E. Payan, P. Schaaf, J.-C. Voegel, C. Picart, Imaging cell interactions with native and crosslinked polyelectrolyte multilayers, Cell. Biochem. Biophys. 44 (2006) 273–285.
[61] A. Schneider, G. Francius, R. Obeid, P. Schwinté, J. Hemmerlé, B. Frisch, P. Schaaf, J.-C. Voegel, B. Senger, C. Picart, Polyelectrolyte multilayers with a tunable Young's modulus: influence of film stiffness on cell adhesion, Langmuir 22 (2006) 1193–1200.
[62] C.R. Wittmer, J.A. Phelps, C.M. Lepus, W.M. Saltzman, M.J. Harding, P.R. Van Tassel, Multilayer nanofilms as substrates for hepatocellular applications, Biomaterials 29 (2008) 4082–4090.
[63] S.G. Olenych, M.D. Moussallem, D.S. Salloum, J.B. Schlenoff, T.C. Keller, Fibronectin and cell attachment to cell and protein resistant polyelectrolyte surfaces, Biomacromolecules 6 (2005) 3252–3258.
[64] N. Giamblanco, E. Martines, G. Marletta, Laminin adsorption on nanostructures: switching the molecular orientation by local curvature changes, Langmuir 29 (2013) 8335–8342.
[65] L. He, S. Tang, M.P. Prabhakaran, S. Liao, L. Tian, Y. Zhang, W. Xue, S. Ramakrishna, Surface modification of PLLA nano-scaffolds with laminin multilayer by LbL assembly for enhancing neurite outgrowth, Macromol. Biosci. 13 (2013) 1601–1609.
[66] J. Borges, J.M. Campiña, A.F. Silva, Probing the contribution of different intermolecular forces to the adsorption of spheroproteins onto hydrophilic surfaces, J. Phys. Chem. B 117 (2013) 16565–16576.
[67] V. Gribova, C. Gauthier-Rouvière, C. Albigès-Rizo, R. Auzely-Velty, C. Picart, Effect of RGD functionalization and stiffness modulation of polyelectrolyte multilayer films on muscle cell differentiation, Acta Biomater. 9 (2013) 6468–6480.
[68] C.R. Wittmer, J.A. Phelps, W.M. Saltzman, P.R. Van Tassel, Fibronectin terminated multilayer films: protein adsorption and cell attachment studies, Biomaterials 28 (2007) 851–860.
[69] P. Tryoen-Tóth, D. Vautier, Y. Haikel, J.C. Voegel, P. Schaaf, J. Chluba, J. Ogier, Viability, adhesion, and bone phenotype of osteoblast-like cells on polyelectrolyte multilayer films, J. Biomed. Mater. Res. 60 (2002) 657–667.
[70] A. Schneider, L. Richert, G. Francius, J.-C. Voegel, C. Picart, Elasticity, biodegradability and cell adhesive properties of chitosan/hyaluronan multilayer films, Biomed. Mater. 2 (2007) S45.
[71] S.T. Dubas, J.B. Schlenoff, Polyelectrolyte multilayers containing a weak polyacid: construction and deconstruction, Macromolecules 34 (2001) 3736–3740.

Contributions of the integrin β1 tail to cell adhesive forces **Experimental Cell Research**

EXPERIMENTAL CELL RESEARCH 332 (2015) 212–222

Available online at www.sciencedirect.com

ScienceDirect

journal homepage: www.elsevier.com/locate/yexcr

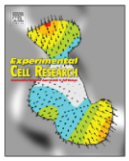

Research Article

Contributions of the integrin β1 tail to cell adhesive forces

*Imen Elloumi-Hannachi, José R. García, Asha Shekeran, Andrés J. García**

Woodruff School of Mechanical Engineering and Petit Institute for Bioengineering and Bioscience, Georgia Institute of Technology, Atlanta, GA 30332, USA

ARTICLE INFORMATION

Article Chronology:
Received 13 October 2014
Received in revised form
14 November 2014
Accepted 15 November 2014
Available online 25 November 2014

Keywords:
Cell adhesion
Fibronectin
Cell spreading

ABSTRACT

Integrin receptors connect the extracellular matrix to the cell cytoskeleton to provide essential forces and signals. To examine the contributions of the β1 integrin cytoplasmic tail to adhesive forces, we generated cell lines expressing wild-type and tail mutant β1 integrins in β1-null fibroblasts. Deletion of β1 significantly reduced cell spreading, focal adhesion assembly, and adhesive forces, and expression of human β1 (hβ1) integrin in these cells restored adhesive functions. Cells expressing a truncated tail mutant had impaired spreading, fewer and smaller focal adhesions, reduced integrin binding to fibronectin, and lower adhesion strength and traction forces compared to hβ1-expressing cells. All these metrics were equivalent to those for β1-null cells, demonstrating that the β1 tail is essential to these adhesive functions. Expression of the constitutively-active D759A hβ1 mutant restored many of these adhesive functions in β1-null cells, although with important differences when compared to wild-type β1. Even though there were no differences in integrin-fibronectin binding and adhesion strength between hβ1- and hβ1-D759A-expressing cells, hβ1-D759A-expressing cells assembled more but smaller adhesions than hβ1-expressing cells. Importantly, hβ1-D759A-expressing cells generated lower traction forces compared to hβ1-expressing cells. These differences between hβ1- and hβ1-D759A-expressing cells suggest that regulation of integrin activation is important for fine-tuning cell spreading, focal adhesion assembly, and traction force generation.

Introduction

Cell adhesion to extracellular matrices (ECMs) is central to tissue organization, maintenance, repair and pathogenesis by providing forces and signals that direct cell survival, migration, cell cycle progression, and differentiation [1–3]. Heterodimeric (αβ) integrin transmembrane receptors constitute the principal mechanism of cell-ECM adhesion [1]. The β1 integrin subfamily binds to fibronectin (FN), collagens, and laminins, and genetic deletion of the β1 subunit results in early embryonic lethality [4,5]. Both α and β integrin subunits form the extracellular domain that conveys ECM ligand binding and specificity, whereas binding sites in the β integrin tail mediate interactions with numerous cytoskeletal components and regulate adhesive functions [6–8]. For example, two conserved NPxY motifs bind talin, kindlin, and other cytoskeletal adapters required for integrin activation and localization to focal adhesion (FA) complexes [9–14].

Early work demonstrated that binding sites in the integrin β1 tail mediate interactions with structural cytoskeletal components that regulate diverse adhesive functions. The β1 tail is required for

*Corresponding author. Fax: +1 404 385 1326.
E-mail address: andres.garcia@me.gatech.edu (A.J. García).

http://dx.doi.org/10.1016/j.yexcr.2014.11.008
0014-4827/

integrin localization to FAs [15]. COOH-terminal truncation of β1 eliminating the distal NPxY motif disrupted its ability to mediate cell spreading, and a more proximal truncation (5 amino acids) also disrupted talin binding [16]. A truncation of only five amino acids from the COOH-terminal end of the β1 cytoplasmic domain abrogated the ability of the integrin to activate tyrosine phosphorylation [17]. Using site directed mutagenesis, Horwitz et al. identified three clusters of amino acids, including the two NPxY motifs, within the β1 subunit tail that regulate integrin localization to FAs [18]. These regions are well-conserved among different β subunits and across species [1]. In addition, D759 in the membrane proximal β1 tail forms a salt bridge with a conserved arginine in the α subunit to stabilize a default inactive conformation of the receptor [19], and mutation of this residue (D759A) results in high affinity, ligand binding integrin [9]. More recent work has established a critical role for the NPxY motifs in diverse cellular functions in development and tumorigenesis [9,12,20–22]. Interestingly, mutations of tyrosines to alanine in NPxY resulted in developmental defects, whereas mutation of these amino acids to phenylalanine (to prevent phosphorylation) or the D759A mutation had no deleterious effects. These studies establish important roles for β1 tail residues in integrin activation, FA assembly and cellular functions. However, it is not clear the extent to which the β1 tail contributes to adhesive force generation. In this study, we analyzed the contributions of the integrin β1 tail to adhesive forces. Stable cell lines expressing wild-type and mutant human β1 integrins in β1-null fibroblasts were generated. We demonstrate that the β1 tail differentially regulates adhesion strength and traction forces.

Materials and methods

Antibodies and reagents

PE-Cy7-conjugated anti-mouse β1 (25-0291-82) was obtained from eBioscience. FITC-labeled anti-integrin β3 (ab36437) and rat anti-mouse αv (ab64639) antibodies, as well as isotype controls (rat IgM (ab35774), rat IgG (ab18446, ab37368), goat IgG (ab37377) and hamster IgG (ab32662)) were purchased from Abcam. APC-conjugated anti-human β1 (559883), anti-mouse integrin α1 (555000), anti-mouse integrin α2 (557017), and anti-mouse integrin α4 (553314) were purchased from BD Pharmingen, and polyclonal anti-mouse integrin α3 (FAB2787P) was purchased from R&D systems. Anti-mouse integrin α5 (sc-19668) was purchased from Santa Cruz Biotechnology. Isotype control APC-conjugated mouse IgG (554681) and PE/Cy7 Armenian hamster IgG (#25-4888-81) were purchased from BD Pharmingen and eBioscience, respectively. Blocking antibodies against mouse β1 (555002), mouse β3 (553343) and isotype controls (553958, 553968) were from BD Pharmingen, whereas the blocking antibody against human β1 (MAB2253Z) was purchased from Millipore. For immunostaining, antibodies against β1 (MAB1952, Chemicon), vinculin (hVIN-1, Sigma), phosphoY397 FAK (ab39976, Abcam), vimentin (ab45939, Abcam), and cytokeratin (ab9026, Abcam) were used. AlexaFluor488-conjugated antibodies against mouse, rat and rabbit IgG were obtained from Invitrogen, and PE-conjugated goat anti-Armenian hamster IgG (sc-3733) was from Santa Cruz Biotechnology. AlexaFluor555-conjugated phalloidin (A34055) and the Live/Dead kit (L3224) from Invitrogen. Magnetic anti-Cy7 microbeads (130-091-652) were from Miltenyi Biotec. All other reagents were from Sigma.

Integrin hβ1 plasmids and retrovirus production

The human β1 integrin sequence (plasmid 16042, Addgene) was cloned into a gateway pENTR/DEST plasmid (Invitrogen) using primers (forward primer 5′-CAACATGAATTTACAACCAATTTTCT-3′, reverse primer 5′-TCATTTTCCCTCATACTTCGGATT-3′). The hβ1 sequence was ligated to a retroviral pMSCV-puro gateway vector using a Gateway LR Clonase II reaction. Mutations were produced using the QuikChange II Site Directed Mutagenesis kit (Promega). All plasmids were sequenced and verified.

Retrovirus was produced by transient transfection of helper virus-free Phoenix amphotropic producer cells [23] with wild-type or mutant hβ1 DNA plasmids. Phoenix cells were transfected using a Nucleofector II (Amaxa). For each sample, 10^6 cells were resuspended in 100 μL of nucleofector solution MEF 2 with 2 μg of DNA plasmid and transfected using program Q-01. Retroviral supernatants were collected and stored at −80 °C.

Dermal fibroblast isolation

All protocols were approved by the Institutional Animal Care and Use Committee in adherence to federal guidelines for animal care. β1-floxed (B6;129-Itgb1tm1Efu/J, itgβ1fl/fl) and control B6129SF2/J mice were obtained from Jackson Laboratories. Mice (7–10 weeks old mice) were euthanized, the dorsa were shaved and cleaned with ethanol, and full-thickness skin tissue was harvested. Skin sections were incubated in 0.25% trypsin for 20 min at 37 °C in order to strip off the skin at dermal-epidermal junction. The epidermis was mechanically separated from the dermis and cut into small pieces. Strips of dermis were washed, diced and incubated for 15 min at 37 °C in 0.3% collagenase (type I, Worthington). The resulting cell suspension was filtered through 100 μm cell strainers, and cells were washed with ice-cold DMEM, 20% fetal bovine serum (FBS), and 1% penicillin/streptomycin (P/S). After centrifugation at 1300 rpm for 10 min, cells were re-suspended in high glucose DMEM with 10% FBS and 1% P/S. Cells were counted and plated at a density of 4000 cells/cm^2 and passaged using standard methods.

β1-null and hβ1-expressing cell lines

β1-floxed cells were transduced with Ad5CMV-Cre-GFP virus (Vector Development Lab) at a MOI 400 and after a week of culture, β1-null cells were purified by negative selection using a Miltenyi Biotec sorting kit and anti-Cy7 microbeads. To generate cells expressing human β1 integrins, β1-null cells were transduced with retrovirus encoding for hβ1 variants as described previously [23]. Cells were plated on tissue culture polystyrene at 2×10^4 cells/cm^2 24 h prior to retroviral transduction. Cells were transduced with 0.2 mL/cm^2 of retroviral supernatant supplemented with 4 μg/mL hexadimethrine bromide and 10% fetal bovine serum, and centrifuged at 1200g for 30 min in Beckman model GS-6R centrifuge with a swinging bucket rotor. Retroviral supernatant was replaced with growth media (DMEM, 10% FBS, 1% P/S). Five days after transduction, cells were switched to puromycin (2.5 μg/cm^2)-supplemented growth media and maintained under selective pressure during culture and expansion.

Cell plating on micropatterned FN substrates

Micropatterned substrates were generated by microcontact printing of self-assembled monolayers of alkanethiols on gold [24] using a PDMS stamp (Sylgard 184/186 elastomer kit). Arrays of methyl-terminated alkanethiol ($HS–(CH_2)_{11}–CH_3$; Sigma) islands (10 μm diameter circles, 75 μm center to center spacing) were stamped onto gold-coated glass coverslips. The remaining exposed areas were functionalized with tri(ethylene glycol)-terminated alkanethiol ($HS–(CH_2)_{11}–(CH_2CH_2O)_3–OH$; ProChimia Surfaces) to generate a cell adhesive-resistant background. Patterned substrates were coated with human plasma FN (25 μg/mL), blocked with 1% heat-denatured bovine serum albumin, incubated in PBS (Ca^{2+}/Mg^{2+}). Cells were seeded at 40,000 cells/cm^2 in serum-containing media.

For antibody blocking studies, cells were resuspended in appropriate blocking antibody or isotype control for 30 min with gentle rocking. Cells were seeded on FN-coated micropatterned substrates for 15 min prior to washing three times with PBS. Adherent cells were counted using ImageJ.

Cell adhesion strength

Cell adhesion to FN-coated islands was measured using a hydrodynamic spinning disk system [24,25]. Cells were cultured overnight on coverslips with FN-coated islands in serum-containing media. Micropatterned substrates with adherent cells were then spun in PBS supplemented with 2 mM dextrose for 5 min at constant speed. The applied shear stress (τ) is given by the formula $\tau = 0.8r(\rho\mu\omega^3)^{1/2}$, where r is the radial position and ρ, μ and ω are the fluid density, viscosity and rotational speed respectively. After spinning, cells were fixed in 3.7% formaldehyde, permeabilized in 1% Triton X-100, stained with ethidium homodimer-1. Adherent cells were counted at specific radial positions using a 10X objective lens in a Nikon TE300 microscope equipped with a Ludl motorized stage, Spot-RT camera and Image-Pro analysis system. A total of 61 fields (80–100 cells per field before spinning) were analyzed and cell counts were normalized to the number of cell counts at the center of the disk. The fraction of adherent cells (f) as a function of shear stress τ (force/area) was then fitted to a sigmoid curve $f = 1/(1+\exp b[\tau - \tau_{50}])$, where τ_{50} is the shear stress for 50% detachment and b is the inflection slope, using in-house macros in MATLAB. τ_{50} represents the mean adhesion strength for the cell population. More than 8 samples were analyzed for each condition.

Integrin binding and focal adhesion assembly

Integrin binding was quantified via a cross-linking/extraction procedure [26,27]. Cells were cultured overnight on coverslips with FN-coated islands in serum-containing media. After rinsing cultures three times with PBS, DTSSP (1.0 mM in cold PBS+2 mM dextrose) was incubated for 30 min to cross-link integrins bound to FN. The cross-linking reaction was quenched by addition of Tris (50 mM in PBS) for 15 min. Uncross-linked cellular components were then extracted in 0.1% SDS containing 10 μg/mL leupeptin, 10 μg/mL aprotinin and 350 μg/mL PMSF. Cross-linked integrins to their bound ligands were visualized by immunostaining with β1 integrin-specific antibodies and analyzed using ImageJ. More than 20 cells were analyzed for each condition.

For staining of FAs, cells cultured overnight on FN-coated surfaces were rinsed and permeabilized in cytoskeleton-stabilizing buffer (0.5% Triton X-100, 10 mM PIPES buffer, 50 mM NaCl, 150 mM sucrose, 3 mM $MgCl_2$, 1 mM PMSF, 1 μg/mL leupeptin, 1 μg/mL aprotinin, and 1 μg/mL pepstatin) for 10 min, fixed in 3.7% formaldehyde for 5 min, blocked in 5% goat serum, and incubated with primary antibodies against FA components followed by AlexaFluor-labeled secondary antibodies. Images were captured using a Nikon Eclipse E400 equipped with a 60X APO (1.4 NA) TIRF objective and Spot RT Camera. FAs were quantified using ImageJ and custom image analysis macros.

Traction force

Microfabricated postarray deflection device (mPAD) silicon masters were prepared as previously described [28]. Elastomeric micropost arrays were then fabricated using PDMS replica molding. Briefly, PDMS prepolymer was cast on top of mPAD silicon masters, cured at 110 °C for 1 h, peeled off and oxidized with oxygen plasma (Plasma-Preen II-862, Terra Universal). Immediately following oxidization, molds were then silanized with (tridecafluoro-1,1,2,2-tetrahydrooctyl)-1-trichlorosilane vapor overnight under vacuum. Following silanization, PDMS prepolymer was cast over the template and stamped onto 1.5 thickness 25-mm diameter coverslips, degassed under vacuum and cured at 110 °C for 24 h. Collapsed posts were recovered by sonicating in ethanol for 5 min followed by supercritical drying in liquid CO_2 using a critical point dryer (Samdri-PVT-3D, Tousimis).

Flat PDMS stamps were generated by casting PDMS prepolymer on silanized silicon wafers and curing for 1 h. Stamps were coated in 50 μg/mL FN for 1 h. These stamps were then washed in distilled water and dried with N_2 gas. FN-coated stamps were placed in contact with plasma-treated mPAD substrates for 5 min to allow FN transfer to the mPAD device posts. mPAD substrates were labeled with 2.5 μg/mL of Δ^9-DiI (Invitrogen) in distilled water for 1 h. Substrates were then transferred to a solution of 0.1% Pluronics F127 for 30 min to prevent non-specific protein absorption. Cells were seeded in growth medium and allowed to attach and spread overnight.

Following overnight incubation, mPAD substrates were transferred to a coverslip holder and placed in a stage top incubator maintained at 37 °C, 90% humidity and 5% CO_2 (Live Cell, Pathology Devices). Confocal images were taken with a Nikon C2 module connected to a Nikon Eclipse Ti inverted microscope with a high magnification objective (60X Apochromat TIRF, NA 1.49, Nikon). Bottoms and tops of posts were imaged using a 561-nm laser and deflections between the two regions of the posts were measured. Resulting forces for each post, F, were calculated using the Euler–Bernoulli beam theory, $F = \frac{\delta(3\pi ED^4)}{64L^3}$, where E, D, L and δ are the Young's modulus, post-diameter, post-height and post-deflection respectively. More than 25 cells were analyzed for each condition.

Statistical analyses

Statistical analyses were performed using GraphPad Prism 6.0. For normally distributed data with equal variances, one-way ANOVA with Tukey's multiple comparison test was used and results are displayed as mean ± standard error of the mean. For data that did not satisfy the requirements for ANOVA, non-parametric Kruskal–Wallis tests with Dunn's multiple comparison tests were used and

results are displayed using box-whisker plots. A p-value <0.05 was considered significant. Non-linear regression analyses were also performed in GraphPad Prism 6.0.

Results

Engineered cells provide a suitable system to analyze the function of target integrins in the absence of endogenous integrins

We generated stable cell lines expressing wild-type and mutant human β1 integrins in β1-null fibroblasts. A major advantage of this system is the lack of endogenous, wild-type murine β1 (mβ1) integrins that could confound interpretation of the data. Dermal fibroblasts from β1-floxed mice (carrying the murine *ItgB1* gene flanked by loxP sites [29]) were isolated by enzymatic digestion. Immunostaining for vimentin and cytokeratin confirmed a high purity population of fibroblasts without appreciable keratinocyte contamination (Fig. S1). These cells (flox) were transduced with adenovirus encoding for Cre-GFP to delete the *ItgB1* gene. After a week in culture, β1-null cells were purified by negative selection using magnetic beads coated with antibodies against mβ1. Flow cytometry analyses showed that >98% of the cells lacked mβ1 integrin expression (Fig. 1A). In addition, expression of murine α1, α2, and α5 subunits was also reduced whereas expression of αv integrin remained unchanged (Fig. S2).

β1-null cells were then transduced with retrovirus encoding for human β1A (hβ1) integrin and puromycin resistance. A stable polyclonal population of hβ1-expressing cells was established following culture in the presence of puromycin. Flow cytometry analyses showed high levels of hβ1 integrin expression in the absence of mβ1 (Fig. 1A). Expression levels for hβ1 integrin were comparable to expression levels of mβ1 in floxed cells and control cells (WT) isolated from wild-type mice. Furthermore, expression of hβ1 resulted in expression of α1 and α5 integrin subunits (Fig. S2), suggesting expression of integrin heterodimers. The expressed hβ1 is functional as adhesion to FN was completely blocked by antibodies against hβ1 ($p<0.01$), whereas antibodies against mβ1 had no effect (Fig. 1B). Integrin β3 provided residual adhesion to FN in these cells as anti-β3 antibodies reduced adhesion by 20% but this was not statistically significant. Importantly, the strong dependence of adhesion on β1 integrin for hβ1-expressing cells is consistent with results for control WT and floxed cells. As expected, adhesion of β1-null cells to FN was completely blocked by antibodies against integrin β3 ($p<0.01$), whereas antibodies against mβ1 had no effect (Fig. 1B).

hβ1-expressing cells spread on FN to the same extent as control floxed cells, whereas the average spread area of β1-null cells was approximately 25% lower ($p<0.01$) (Fig. 1C). hβ1-expressing cells assembled robust vinculin-containing FAs and actin stress fibers and phosphorylated FAK localized to FAs (Fig. 1D), similar to results for floxed cells. These results demonstrate that the expressed hβ1 integrin is functional and these engineered cells recapitulate many of the adhesive characteristics of control floxed and WT cells that express endogenous mβ1.

As a final validation, we measured the adhesion strength to FN of these stable lines using our spinning disk device that applies hydrodynamic detachment forces. The adhesion strength is the force required to detach cells from the FN-coated surface and provides a sensitive measure of adhesive function [24]. Because cell spreading alters adhesion strength, cells were cultured on micropatterned FN islands to control cell shape and adhesive area. For the spinning disk assay, a coverslip containing adherent cells is exposed to a gradient of hydrodynamic forces with detachment forces increasing linearly with distance from the center of the coverslip. After spinning, cells are counted at radial positions of known applied force. Fig. 2A presents typical detachment profiles showing sigmoidal decreases in the number of adherent cells with increasing shear stress. The rightward shift in the adhesion profile for the floxed cells compared to the β1-null cells indicates higher adhesive forces. The shear stress for 50% detachment, which represents the mean adhesion strength, was measured for the cell lines (Fig. 2B). Deletion of β1 integrin resulted in a 50% decrease in adhesion strength to FN compared with floxed and WT cells ($p<0.001$). The residual adhesion in β1-null cells is attributed to β3-dependent adhesion (Fig. 1). Importantly, expression of hβ1 in null cells rescued the deficits in adhesion strength and restored adhesion strength to the levels of floxed and WT cells. Taken together, these results demonstrate that deletion of β1 integrin significantly reduces cell spreading and adhesion strength to FN and expression of hβ1 integrin in these cells restores adhesive functions, including adhesion strength, to the levels of control cells.

The β1 tail regulates cell spreading, morphology and FA assembly

We developed stable lines for β1-null cells expressing integrin mutants following the strategy outlined above (Fig. 3A). A cell line expressing a truncation mutant at position 760 (hβ1-tr) was generated. This mutant severely reduces integrin recruitment and FA assembly [30]. We note that a stable cell line expressing the truncation mutant at position 754 previously described [31] could not be established as these cells did not grow. We also generated a stable cell line expressing the D759A mutant (hβ1-D759A); this mutant results in constitutively active β1 integrin [9,19]. Flow cytometry analysis showed that expression levels for these mutants were comparable to levels in the cell line expressing wild-type hβ1 and approximately 15-fold higher than levels in the β1-null cell ($p<0.001$) (Fig. 3B). Antibodies against hβ1 integrin completely blocked adhesion to FN for hβ1- and hβ1-D759A-expressing cells ($p<0.01$), whereas antibodies against mβ1 or mβ3 had no effect (Fig. 3C). Adhesion of β1-null cells to FN was completely mediated by mβ3 integrin ($p<0.01$), whereas mβ3 integrin partially contributed to the adhesion of hβ1-tr-expressing cells to FN ($p<0.05$).

Significant differences in cell shape, spread area, and FA assembly were evident among the cell lines cultured on FN-coated glass (Fig. 4). β1-null cells spread to compact shapes with high circularity and exhibited well-defined actin stress fibers terminating at vinculin-containing FAs. hβ1-expressing cells had larger spread areas ($p<0.001$) and were elongated with long projections that contained large, well-defined FAs. Cells expressing the truncated β1 mutant spread more than β1-null cells ($p<0.001$) but to similar levels as hβ1-expressing cells. hβ1-tr-expressing cells had fewer and smaller FAs and less defined stress fibers than hβ1-expressing cells ($p<0.01$). Cells expressing the constitutively active D759A mutant exhibited the highest spread area and were more circular than hβ1-expressing cells ($p<0.01$). Interestingly, hβ1-D759A-expressing cells had a higher number of vinculin-containing FAs compared with

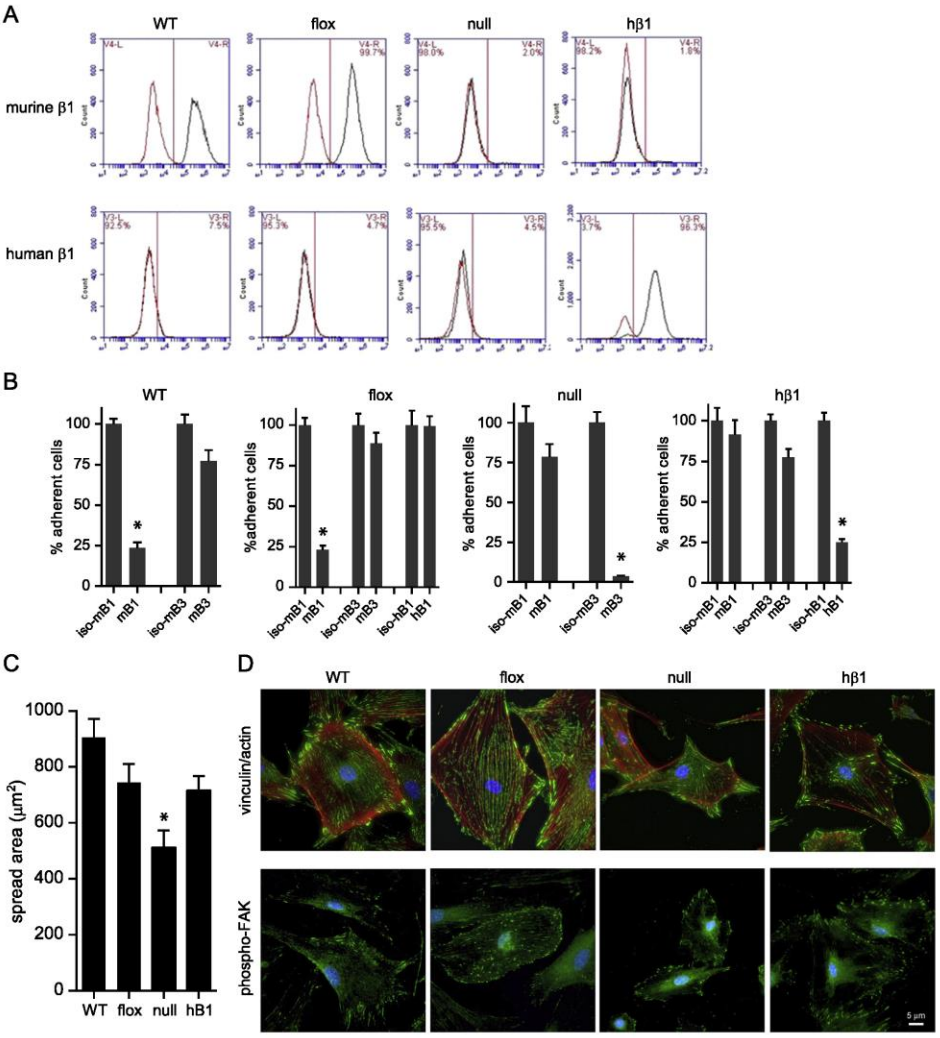

Fig. 1 – Deletion of mβ1 and expression of hβ1 in cells. (A) Flow cytometry histograms (black: integrin antibody, red: isotype control) for mβ1 (top) and hβ1 (bottom) in wild-type (WT), β1-floxed (flox), β1-null (null), and hβ1-expressing (hβ1) cells. (B) Cell adhesion to FN in the presence of blocking antibodies. Cell counts are normalized to counts for cells incubated in isotype control. * $p<0.01$ vs. isotype control. (C) Cell spreading area on FN. * $p<0.01$ vs. all other cell types. (D) Immunostained images for FA components (top) vinculin (green) and actin (red) and (bottom) phosphoY397 FAK (green). Scale bar, 5 μm.

hβ1-expressing cells ($p<0.001$), but the FAs were significantly smaller although the total focal adhesion areas were equivalent. These results demonstrate that the β1 integrin tail regulates cell spreading and shape as well as the number and size of FAs. In addition, the differences between hβ1- and hβ1-D759A-expressing cells indicate that regulation of integrin activation contributes to cell spreading, morphology and FA assembly.

The β1 integrin tail is essential for β1 integrin-FN binding and adhesion strength

We next quantified binding of these integrin tail mutants to FN using a cross-linking and detergent extraction method to selectively retain integrin-FN complexes in cells adhering to micropatterned FN islands [24,32]. Fig. 5A presents images of immunostained β1

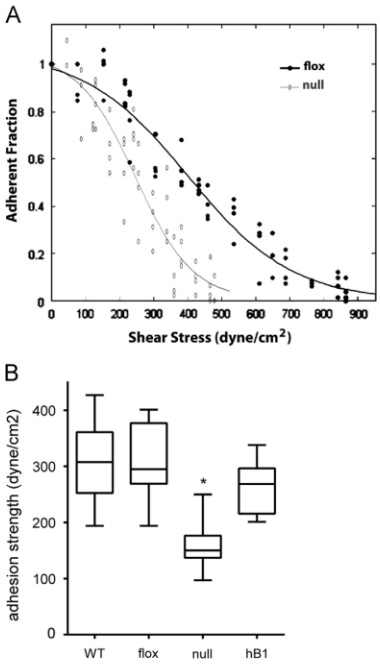

Fig. 2 – hβ1 reconstitutes adhesion strength to FN in β1-null cells. (A) Detachment profiles showing the fraction of adherent cells (f) vs. surface shear stress (τ) for β1-null and β1-floxed cells. (B) Cell adhesion strength, box-whisker plot (mean, 10th, 25th, 75th, and 90th percentile). * $p<0.001$ vs. all other cell types.

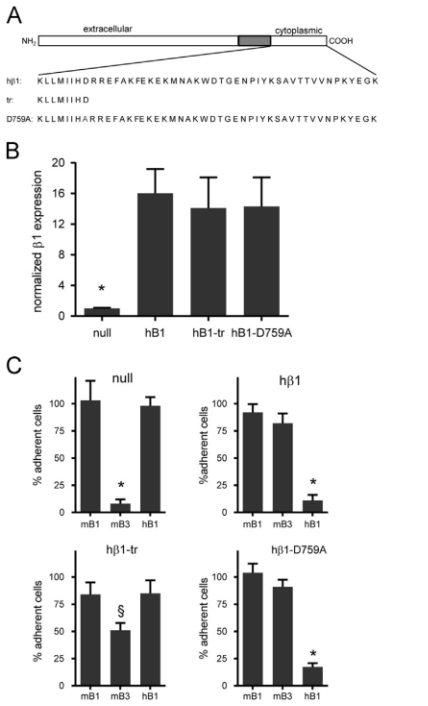

Fig. 3 – Integrin expression and cell adhesion for β1 tail mutants. (A) Schematic of integrin constructs engineered. (B) Flow cytometry analysis for expression levels of hβ1 normalized to expression levels of β1-null cells. * $p<0.001$ vs. all other cell types. (C) Cell adhesion to FN in the presence of blocking antibodies. Cell counts are normalized to counts for cells incubated in isotype control. § $p<0.05$ vs. isotype control, * $p<0.01$ vs. isotype control.

integrin for single cells adhering to 10 μm-diameter FN islands. Fig. 5B presents frequency maps for integrin binding generated by stacking and color coding multiple images; this analysis exploits the spatial arrangement of the FN islands to extract the dominant spatial localization of FN-bound integrins across multiple cells [33]. Fig. 5C and D plots the fraction of the adhesive area occupied by integrin-FN complexes and the mean intensity of integrin staining over the micropatterned area, respectively. β1-null cells had very low levels of bound β1 integrins, consistent with the antibody-blocking results (Fig. 1B). hβ1-expressing cells exhibited punctate integrin-FN clusters localized to the periphery of the FN island that occupied 8-fold higher area ($p<0.001$) and had 2-fold higher mean intensity ($p<0.01$) compared with β1-null cells. Cells expressing the truncated tail mutant had low levels of integrin-FN complexes equivalent to β1-null cells. This result shows that the β1 tail is essential for the formation of stable integrin-FN complexes. Cells expressing the D759A mutant formed robust integrin-FN complexes localized to the periphery of the FN island, and there were no differences in area occupied or mean intensity between hβ1 and hβ1-D759A.

We next analyzed the adhesion strength of these cell lines to FN micropatterned islands (Fig. 6). The adhesion strength of hβ1 was approximately 2.3-fold higher than β1-null cells ($p<0.001$). hβ1-tr-expressing cells had low levels of adhesion strength to FN, equivalent levels as β1-null cells. Adhesion strength for the D759A mutant was not different from wild-type hβ1 but was significantly higher from the null control and truncated tail mutant ($p<0.001$). The differences in adhesion strength among the integrin mutants are consistent with the differences in integrin-FN complex formation. We expect a significant contribution of endogenous β3 integrin to the adhesion strength of β1-null and hβ1-tr-expressing cells to FN as antibodies against this integrin subunit significantly reduced adhesion to FN (Fig. 3B). In contrast, adhesion of hβ1- and hβ1-D759A-expressing cells to FN was completely mediated by integrin β1 ($p<0.01$) (Fig. 3B). Taken together, these results demonstrate that the β1 tail is essential for adhesion strength to FN and the D759A mutation has no effect on integrin-FN complexes or adhesion strength for cells on micropatterned FN islands.

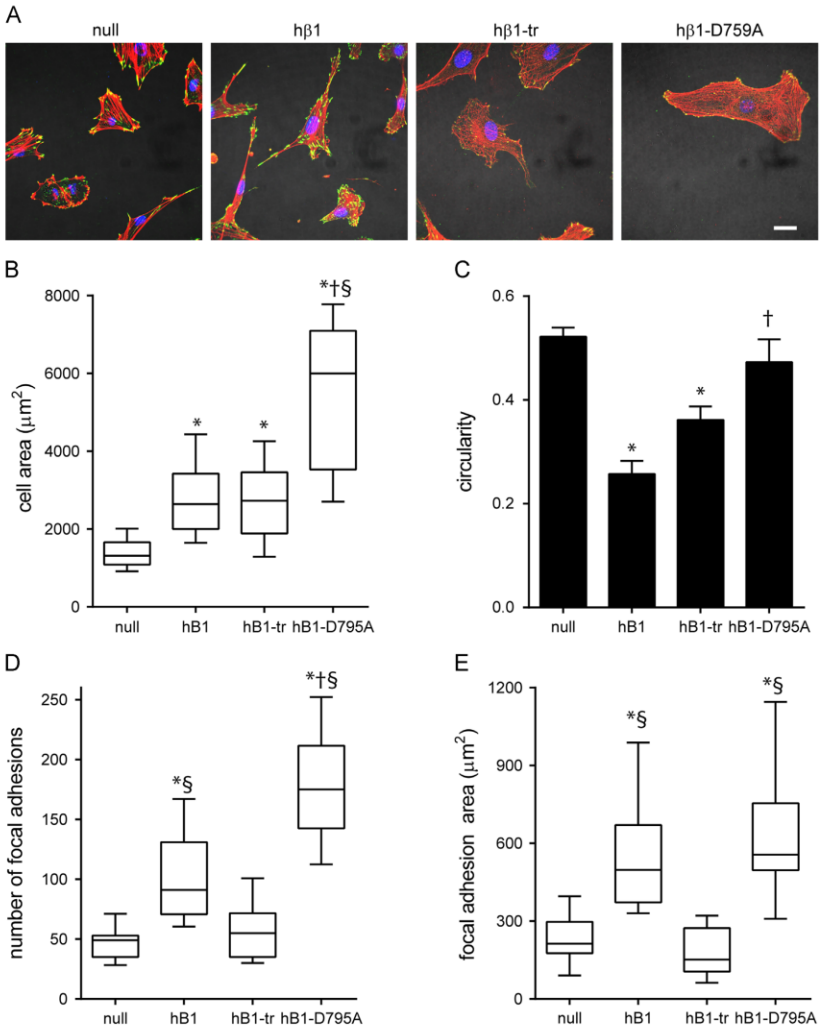

Fig. 4 – β1 tail regulates cell spreading, morphology and FA assembly. (A) Immunostained images for vinculin (green) and actin (red). Scale bar, 10 μm. (B) Cell spread area, box-whisker plot (mean, 10th, 25th, 75th, and 90th percentile). * $p<0.001$ vs. null, § $p<0.001$ vs. hβ1-tr, † $p<0.01$ vs. hβ1. (C) Cell circularity. * $p<0.001$ vs. null, § $p<0.001$ vs. hβ1-tr. (D) Number of FA, box-whisker plot (mean, 10th, 25th, 75th, and 90th percentile). * $p<0.001$ vs. null, § $p<0.01$ vs. hβ1-tr, † $p<0.01$ vs. hβ1. (E) Total FA area, box-whisker plot (mean, 10th, 25th, 75th, and 90th percentile). * $p<0.001$ vs. null, § $p<0.001$ vs. hβ1-tr.

Contributions of the β1 integrin tail to traction forces

We used microfabricated post-array deflection devices (mPADs) to measure traction forces generated by cells expressing these integrins. In this system, traction forces generated by adhering cells deflect the tips of the posts in the array; these deflections can then be used to determine the traction forces because the elastic modulus and geometry of the posts are defined [28,32]. During overnight culture on these devices, all cell lines attached to, spread on the posts, and generated traction forces. Fig. 7A presents images for FN-coated posts (red) with the cell outlined in yellow. Post-deflections were measured and converted into traction forces, and Fig. 7B presents the traction force vectors (cyan). On these deformable substrates, hβ1-expressing cells spread

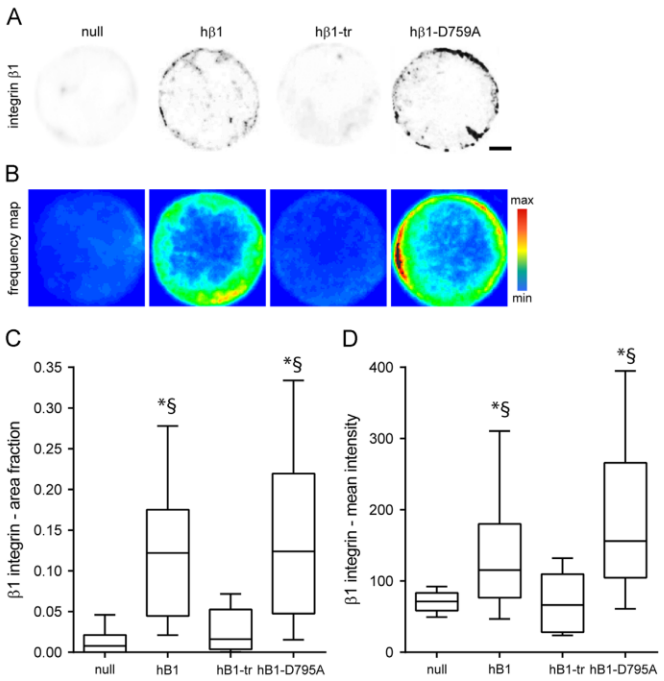

Fig. 5 – : β1 tail is required for integrin β1-FN binding on micropatterned islands. (A) Immunostained images for hβ1 integrin in cell adhering FN islands. Staining is shown as grayscale on white background to facilitate visualization. Scale bar, 2 μm. (B) Frequency maps for stacked images of immunostained hβ1. (C) Fraction of FN island stained for hβ1, box-whisker plot (mean, 10th, 25th, 75th, and 90th percentile). * $p<0.001$ vs. null, § $p<0.001$ vs. hβ1-tr. (D) Mean intensity of hβ1 staining, box-whisker plot (mean, 10th, 25th, 75th, and 90th percentile). * $p<0.01$ vs. null, § $p<0.01$ vs. hβ1-tr.

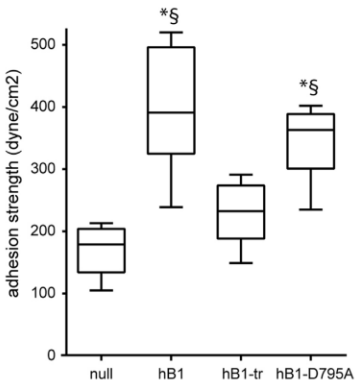

Fig. 6 – : β1 tail is essential for adhesion strength to FN. Cell adhesion strength, box-whisker plot (mean, 10th, 25th, 75th, and 90th percentile). * $p<0.01$ vs. null, § $p<0.01$ vs. hβ1-tr.

considerably more than the other cell lines ($p<0.01$) (Fig. 7C). hβ1-D759A-expressing cells spread to the same extent as β1-null and hβ1-truncated-expressing cells. This result contrasts with our observations for cell spreading on glass (Fig. 4) and may be due to the difference in stiffness between glass and mPADs. The magnitude of traction forces varied significantly across a single cell, with the highest forces at the cell periphery. Fig. 7D presents box-whisker plots for the total traction force per cell, which represents the sum of the magnitudes of the force vectors for each cell. hβ1-expressing cells exerted 3.7-fold higher traction forces compared to β1-null cells ($p<0.001$). Cells expressing the integrin mutant with a truncated tail generated equivalent traction forces as β1-null cells. This result shows that the β1 tail is essential for traction forces on FN. Surprisingly, cells expressing the constitutively activated D759A mutant exerted higher forces than the β1-null cells ($p<0.01$), but the levels were only 33% of the total traction force generated by the hβ1-expressing cells.

Because there are significant differences in cell spreading and total traction force among the cell lines, we also evaluated the traction force per post (Fig. 7E). Similar to the measurements for total traction force, hβ1-expressing cells generated significantly

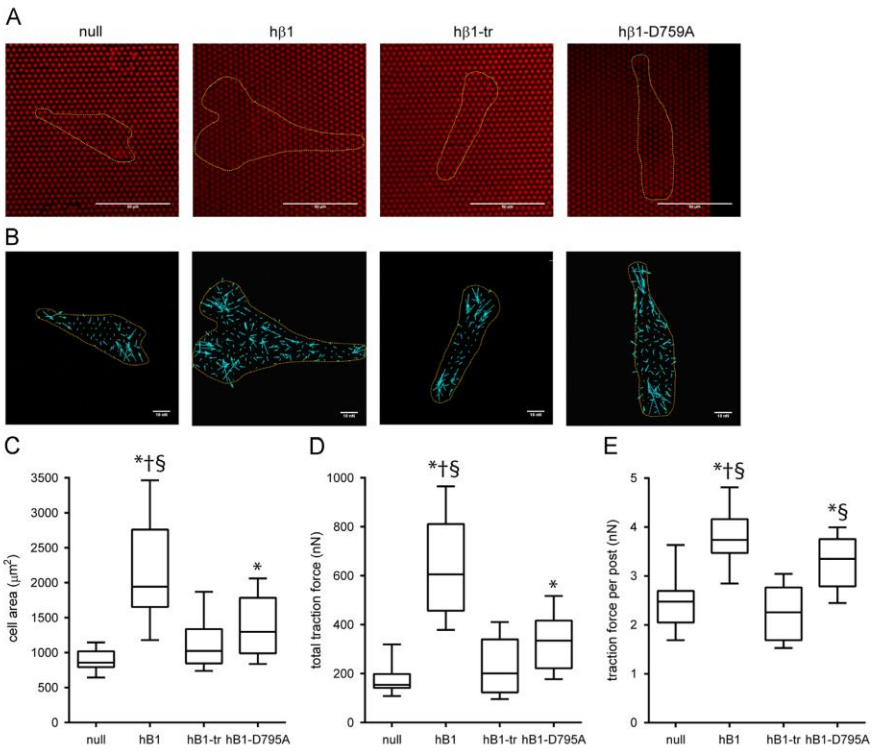

Fig. 7 – : β1 tail and traction force. (A) Cells (yellow outline) spread on mPADs (posts labeled red). Scale bar, 50 μm. (B) Traction force vectors (cyan) with cell outline (yellow). Scale bar, 10 nN. (C) Cell spread area, box-whisker plot (mean, 10th, 25th, 75th, and 90th percentile). * $p<0.001$ vs. null, § $p<0.001$ vs. hβ1-tr, † $p<0.05$ vs. hβ1-D759A. (D) Total traction force per cell, box-whisker plot (mean, 10th, 25th, 75th, and 90th percentile). * $p<0.001$ vs. null, § $p<0.001$ vs. hβ1-tr, † $p<0.01$ vs. hβ1-D759A. (E) Traction force per post, box-whisker plot (mean, 10th, 25th, 75th, and 90th percentile). * $p<0.001$ vs. null, § $p<0.001$ vs. hβ1-tr, † $p<0.01$ vs. hβ1-D759A.

higher traction force per post compared with β1-null and hβ1-tr-expressing cells ($p<0.001$). There was no difference in traction force per post between β1-null and hβ1-tr-expressing cells, confirming our conclusion from the total traction force analysis. Cells expressing the hβ1-D759A mutant generated higher traction forces per post than β1-null and hβ1-tr-expressing cells ($p<0.001$), but these forces were approximately 40% lower than forces exerted by hβ1-expressing cells ($p<0.01$).

Finally, we examined the relationship between cell area and traction force because we previously showed that cell area-traction force coupling represents a robust metric to analyze the role of FA components on force transfer [32]. Fig. S3 plots cell area and the corresponding traction force for individual cells. Linear regression analyses revealed a strong correlation between cell area and traction force for each cell line ($p<0.0001$). There was no difference in regression slope among cell lines, indicating that the integrin β1 tail does not alter cell area-traction force coupling. Taken together, these results demonstrate that the β1 tail is required for the generation of traction forces and D759 is important for high traction force generation.

Discussion

In this study, we generated stable cell lines expressing wild-type and tail mutant β1 integrins in β1-null fibroblasts to analyze the contributions of the β1 tail to adhesive forces. A major advantage of this system is the lack of endogenous, wild-type murine β1 integrins that could confound interpretation of the data. Deletion of β1 integrin significantly reduced cell spreading, focal adhesion assembly, and adhesive forces, and expression of hβ1 integrin in these cells restored adhesive functions to the levels of control wild-type and floxed cells. Cells expressing the truncated tail mutant had impaired spreading, fewer and smaller FAs, reduced integrin binding to FN, and significantly lower adhesion strength and traction forces compared to hβ1-expressing cells. All these

metrics were equivalent to those for β1-null cells, demonstrating that the β1 tail is essential to these adhesive functions. Expression of the constitutively-active D759A mutant restored many of these adhesive functions in β1-null cells, although with important differences when compared to wild-type β1. Even though there were no differences in integrin-FN binding and adhesion strength to FN between hβ1- and hβ1-D759A-expressing cells, hβ1-D759A-expressing cells assembled more but smaller FAs and the spread area and shape were different from hβ1-expressing cells. Importantly, hβ1-D759A-expressing cells generated considerably lower traction forces compared to hβ1-expressing cells.

Previous studies have established that truncations at different locations along the β1 tail impair cell spreading, integrin recruitment to FAs, FA assembly, and signaling [16,18,30,34]. Our results confirm the critical importance of the β1 tail domain to these adhesive functions. Furthermore, we demonstrate that the β1 tail is essential for integrin-FN binding and the transmission of adhesive forces related to adhesion strength and traction force. Our previous analyses of adhesion strength to FN indicated that binding of β1 integrin to FN in the absence of FA assembly provided the major contribution to adhesion strength [24]. Based on this result, we expected that the truncated β1 mutant would provide partial adhesion strength. However, the lack of any adhesion strength for this mutant can be explained by the abrogation of β1 integrin binding to FN in this mutant.

The effects of the D759A mutation on adhesive functions are not well understood and appear to be cell context-dependent. Expression of this mutant in β1-deficient GD25 fibroblastic cells results in a constitutively active β1 integrin with high binding affinity for FN, increased cell adhesion and motility, and more numerous and larger FAs [9,35]. In contrast, mice carrying the D759A mutation had no overt phenotype, and keratinocytes isolated from these mice exhibit normal integrin activation levels, adhesion and migration [12]. In the present study, we observed significant reductions in spread area and traction forces on deformable substrates for hβ1-D759A-expressing cells compared to hβ1-expressing cells, indicating a defect in traction force generation. This defect in traction force generation accounts for the reduced cell spreading on the deformable substrates as there are no differences in traction force-area coupling between hβ1- and hβ1-D759A-expressing cells. Indeed, the traction force per post was reduced in hβ1-D759A-expressing cells compared to hβ1-expressing cells. However, it is not clear whether the reduced traction force arises from a defect in force transmission at the single receptor level. Alternatively, the reduced traction force generation could be a consequence of altered receptor clustering/FA assembly or interactions with cytoskeletal partners due to the inability of this receptor to regulate its affinity. The smaller FAs assembled by hβ1-D759A-expressing cells could account for the reduced adhesive force [28,33,36]. These differences between hβ1- and hβ1-D759A-expressing cells suggest that regulation of integrin activation is important for fine-tuning cell spreading, FA assembly, and traction force generation.

Acknowledgments

Funding was provided by the National Institutes of Health (R01-GM065918). J.R.G. was partially supported by the National Science Foundation IGERT program on Stem Cell Biomanufacturing (DGE 0965945). The pMSCV-puro gateway vector was kindly provided by Jing Chen (Emory University School of Medicine). No conflicts of interest are declared.

Appendix A. Supporting information

Supplementary data associated with this article can be found in the online version at http://dx.doi.org/10.1016/j.yexcr.2014.11.008.

REFERENCES

[1] R.O. Hynes, Integrins: bidirectional, allosteric signaling machines, Cell 110 (2002) 673–687.
[2] S.A. Wickstrom, K. Radovanac, R. Fassler, Genetic analyses of integrin signaling, Cold Spring Harb. Perspect. Biol. 3 (2011) a005116.
[3] R.O. Hynes, The extracellular matrix: not just pretty fibrils, Science 326 (2009) 1216–1219.
[4] R. Fassler, M. Meyer, Consequences of lack of beta 1 integrin gene expression in mice, Genes Dev. 9 (1995) 1896–1908.
[5] L.E. Stephens, A.E. Sutherland, I.V. Klimanskaya, A. Andrieux, J. Meneses, R.A. Pedersen, C.H. Damsky, Deletion of beta 1 integrins in mice results in inner cell mass failure and peri-implantation lethality, Genes Dev. 9 (1995) 1883–1895.
[6] D.A. Calderwood, I.D. Campbell, D.R. Critchley, Talins and kindlins: partners in integrin-mediated adhesion, Nat. Rev. Mol. Cell Biol. 14 (2013) 503–517.
[7] S. Liu, D.A. Calderwood, M.H. Ginsberg, Integrin cytoplasmic domain-binding proteins, J. Cell Sci. 113 (2000) 3563–3571.
[8] D.S. Harburger, D.A. Calderwood, Integrin signalling at a glance, J. Cell Sci. 122 (2009) 159–163.
[9] T. Sakai, Q. Zhang, R. Fassler, D.F. Mosher, Modulation of beta1A integrin functions by tyrosine residues in the beta1 cytoplasmic domain, J. Cell Biol. 141 (1998) 527–538.
[10] E. Hirsch, L. Barberis, M. Brancaccio, O. Azzolino, D. Xu, J.M. Kyriakis, L. Silengo, F.G. Giancotti, G. Tarone, R. Fassler, F. Altruda, Defective Rac-mediated proliferation and survival after targeted mutation of the beta1 integrin cytodomain, J. Cell Biol. 157 (2002) 481–492.
[11] K. Wennerberg, A. Armulik, T. Sakai, M. Karlsson, R. Fassler, E.M. Schaefer, D.F. Mosher, S. Johansson, The cytoplasmic tyrosines of integrin subunit beta1 are involved in focal adhesion kinase activation, Mol. Cell Biol. 20 (2000) 5758–5765.
[12] A. Czuchra, H. Meyer, K.R. Legate, C. Brakebusch, R. Fassler, Genetic analysis of beta1 integrin "activation motifs" in mice, J. Cell Biol. 174 (2006) 889–899.
[13] B. Nieves, C.W. Jones, R. Ward, Y. Ohta, C.G. Reverte, S.E. LaFlamme, The NPIY motif in the integrin beta1 tail dictates the requirement for talin-1 in outside-in signaling, J. Cell Sci. 123 (2010) 1216–1226.
[14] C. Margadant, M. Kreft, D.J. de Groot, J.C. Norman, A. Sonnenberg, Distinct roles of talin and kindlin in regulating integrin alpha5-beta1 function and trafficking, Curr. Biol. 22 (2012) 1554–1563.
[15] S.E. LaFlamme, S.K. Akiyama, K.M. Yamada, Regulation of fibronectin receptor distribution, J. Cell Biol. 117 (1992) 437–447.
[16] A. Kaapa, K. Peter, J. Ylanne, Effects of mutations in the cytoplasmic domain of integrin beta(1) to talin binding and cell spreading, Exp. Cell Res. 250 (1999) 524–534.
[17] L.D. Finkelstein, P.J. Reynolds, S.W. Hunt 3rd, Y. Shimizu, Structural requirements for beta1 integrin-mediated tyrosine phosphorylation in human T cells, J. Immunol. 159 (1997) 5355–5363.
[18] A.A. Reszka, Y. Hayashi, A.F. Horwitz, Identification of amino acid sequences in the integrin beta 1 cytoplasmic domain implicated in cytoskeletal associations, J. Cell Biol. 117 (1992) 1321–1330.

[19] P.E. Hughes, F. Diaz-Gonzalez, L. Leong, C. Wu, J.A. McDonald, S.J. Shattil, M.H. Ginsberg, Breaking the integrin hinge. A defined structural constraint regulates integrin signaling, J. Biol. Chem. 271 (1996) 6571–6574.
[20] M.S. Maginnis, B.A. Mainou, A. Derdowski, E.M. Johnson, R. Zent, T.S. Dermody, NPXY motifs in the beta1 integrin cytoplasmic tail are required for functional reovirus entry, J. Virol. 82 (2008) 3181–3191.
[21] J.A. Green, A.L. Berrier, R. Pankov, K.M. Yamada, beta1 integrin cytoplasmic domain residues selectively modulate fibronectin matrix assembly and cell spreading through talin and Akt-1, J. Biol. Chem. 284 (2009) 8148–8159.
[22] A. Meves, T. Geiger, S. Zanivan, J. DiGiovanni, M. Mann, R. Fassler, Beta1 integrin cytoplasmic tyrosines promote skin tumorigenesis independent of their phosphorylation, Proc. Natl. Acad. Sci. USA 108 (2011) 15213–15218.
[23] B.A. Byers, G.K. Pavlath, T.J. Murphy, G. Karsenty, A.J. Garcia, Cell-type-dependent up-regulation of in vitro mineralization after overexpression of the osteoblast-specific transcription factor Runx2/Cbfal, J. Bone Miner. Res. 17 (2002) 1931–1944.
[24] N.D. Gallant, K.E. Michael, A.J. García, Cell adhesion strengthening: contributions of adhesive area, integrin binding, and focal adhesion assembly, Mol. Biol. Cell 16 (2005) 4329–4340.
[25] A.J. García, F. Huber, D. Boettiger, Force required to break alpha5beta1 integrin-fibronectin bonds in intact adherent cells is sensitive to integrin activation state, J. Biol. Chem. 273 (1998) 10988–10993.
[26] A.J. García, M.D. Vega, D. Boettiger, Modulation of cell proliferation and differentiation through substrate-dependent changes in fibronectin conformation, Mol. Biol. Cell 10 (1999) 785–798.
[27] B.G. Keselowsky, A.J. García, Quantitative methods for analysis of integrin binding and focal adhesion formation on biomaterial surfaces, Biomaterials 26 (2005) 413–418.
[28] J. Fu, Y.K. Wang, M.T. Yang, R.A. Desai, X. Yu, Z. Liu, C.S. Chen, Mechanical regulation of cell function with geometrically modulated elastomeric substrates, Nat. Methods 7 (2010) 733–736.
[29] S. Raghavan, C. Bauer, G. Mundschau, Q. Li, E. Fuchs, Conditional ablation of beta1 integrin in skin. Severe defects in epidermal proliferation, basement membrane formation, and hair follicle invagination, J. Cell Biol. 150 (2000) 1149–1160.
[30] Y. Hayashi, B. Haimovich, A. Reszka, D. Boettiger, A. Horwitz, Expression and function of chicken integrin beta 1 subunit and its cytoplasmic domain mutants in mouse NIH 3T3 cells, J. Cell Biol. 110 (1990) 175–184.
[31] L. Vignoud, C. Albiges-Rizo, P. Frachet, M.R. Block, NPXY motifs control the recruitment of the alpha5beta1 integrin in focal adhesions independently of the association of talin with the beta1 chain, J. Cell Sci. 110 (1997) 1421–1430.
[32] D.W. Dumbauld, T.T. Lee, A. Singh, J. Scrimgeour, C.A. Gersbach, E.A. Zamir, J. Fu, C.S. Chen, J.E. Curtis, S.W. Craig, A.J. Garcia, How vinculin regulates force transmission, Proc. Natl. Acad. Sci. USA 110 (2013) 9788–9793.
[33] S.R. Coyer, A. Singh, D.W. Dumbauld, D.A. Calderwood, S.W. Craig, E. Delamarche, A.J. Garcia, Nanopatterning reveals an ECM area threshold for focal adhesion assembly and force transmission that is regulated by integrin activation and cytoskeleton tension, J. Cell Sci. 125 (2012) 5110–5123.
[34] E.E. Marcantonio, J.L. Guan, J.E. Trevithick, R.O. Hynes, Mapping of the functional determinants of the integrin beta 1 cytoplasmic domain by site-directed mutagenesis, Cell Regul. 1 (1990) 597–604.
[35] A. Millon-Fremillon, D. Bouvard, A. Grichine, S. Manet-Dupe, M.R. Block, C. Albiges-Rizo, Cell adaptive response to extracellular matrix density is controlled by ICAP-1-dependent beta1-integrin affinity, J. Cell Biol. 180 (2008) 427–441.
[36] N.Q. Balaban, U.S. Schwarz, D. Riveline, P. Goichberg, G. Tzur, I. Sabanay, D. Mahalu, S. Safran, A. Bershadsky, L. Addadi, B. Geiger, Force and focal adhesion assembly: a close relationship studied using elastic micropatterned substrates, Nat. Cell Biol. 3 (2001) 466–472.

Parallel droplet microfluidics for high throughput cell encapsulation and synthetic microgel generation **Microsystems and Nanoengineering**

OPEN

Microsystems & Nanoengineering (2018) 4, 17076; doi:10.1038/micronano.2017.76
www.nature.com/micronano

ARTICLE

Parallel droplet microfluidics for high throughput cell encapsulation and synthetic microgel generation

Devon M. Headen[1,2], José R. García[1,2] and Andrés J. García[1,2]

Cells can be microencapsulated in synthetic hydrogel microspheres (microgels) using droplet microfluidics, but microfluidic devices with a single droplet generating geometry have limited throughput, especially as microgel diameter decreases. Here we demonstrate microencapsulation of human mesenchymal stem cells (hMSCs) in small (< 100 µm diameter) microgels utilizing parallel droplet generators on a two-layer elastomer device, which has 600% increased throughput vs. single-nozzle devices. Distribution of microgel diameters were compared between products of parallel vs. single-nozzle configurations for two square nozzle widths, 35 and 100 µm. Microgels produced on parallel nozzles were equivalent to those produced on single nozzles, with substantially the same polydispersity. Microencapsulation of hMSCs was compared for parallel nozzle devices of each width. Thirty five micrometer wide nozzle devices could be operated at twice the cell concentration of 100 µm wide nozzle devices but produced more empty microgels than predicted by a Poisson distribution. Hundred micrometer wide nozzle devices produced microgels as predicted by a Poisson distribution. Polydispersity of microgels did not increase with the addition of cells for either nozzle width. hMSCs encapsulated on 35 µm wide nozzle devices had reduced viability (~70%) and a corresponding decrease in vascular endothelial growth factor (VEGF) secretion compared to hMSCs cultured on tissue culture (TC) plastic. Encapsulating hMSCs using 100 µm wide nozzle devices mitigated loss of viability and function, as measured by VEGF secretion.

Keywords: droplets; microencapsulation; microgel; multilayer; parallel

Microsystems & Nanoengineering (2018) **4,** 17076; doi:10.1038/micronano.2017.76; Published online: 15 January 2018

INTRODUCTION

Delivery of encapsulated proteins and cells in hydrogel microspheres, or microgels, has emerged as a promising therapeutic strategy for the treatment of various diseases[1]. Synthetic polymers provide tuneable release rates of encapsulated proteins that can be tailored based on diffusion through the hydrogel network or hydrolytic/enzymatic degradation of microgels[2–4]. These injectable microgels can be implanted in a minimally invasive manner for extended local delivery of therapeutic proteins, such as growth factors and cytokines. In addition, microgel delivery of proteins could allow for 'mosaic' injections, in which multiple microgel populations with individually validated release profiles are combined to provide more complex release profiles or multi-protein delivery.

Encapsulation of cells in microgels provides several key benefits in transplantation settings. By controlling mesh size of microgels, immune infiltration of transplanted cells can be mitigated while transport of oxygen and cellular waste products is maintained. Because potential sources of therapeutic cells are often allogeneic or xenogeneic, immunoisolation has been extensively investigated for reducing systemic immunosuppression requirements after transplantation[5,6]. Microgels can also function to immobilize cells at a desired transplant site by entrapping them in gels, an important consideration since many cell therapies currently rely on systemic administration of cells[7]. In addition to isolating transplanted cells from the host, synthetic microgels permit engineering of encapsulated cell microenvironment, including matrix stiffness and adhesive ligand interactions, which influence differentiation and secretory function of encapsulated stem cells[8,9]. Bulk hydrogel constructs can provide these benefits as well, but the microgel form factor enables applications for which bulk gels are not well suited, such as injection. In addition, thick polymer coatings are a barrier to nutrients and oxygen, so hypoxic death is frequently observed in bulk gels, and even in large microgels, especially when high cell concentrations are used[10]. Therefore, microgel size should be minimized in order to maximize transport of oxygen to encapsulated cells and to enable novel, minimally invasive transplantation schemes. Encapsulation of cells in microgels with diameters < 100 µm enables immobilization of cells in small blood vessels, including arterioles and larger capillaries. Alternatively, larger microgels may occlude larger vessels, restricting blood flow, and unencapsulated cells are difficult to localize[7].

Alginate has been extensively explored for cell microencapsulation because rapid crosslinking allows for facile gelation in cationic aqueous solutions[11]. However, only limited control of cellular microenvironment is possible with alginate. We have previously developed a microfluidic droplet strategy for generating size-controlled crosslinked synthetic microgels based on 4-arm polyethylene glycol (PEG-4MAL) macromers, which are terminated with maleimides[12]. Maleimides efficiently react with free thiols to form covalent bonds, allowing any cysteine containing peptide or thiolated ligand to be tethered to microgels. This versatile chemistry enables local and sustained presentation of bioactive

[1]Woodruff School of Mechanical Engineering, Georgia Institute of Technology, Atlanta, GA 30332, USA and [2]Petit Institute for Bioengineering and Biosciences, Georgia Institute of Technology, Atlanta, GA 30332, USA
Correspondence: Andrés J. García (andres.garcia@me.gatech.edu)
Received: 28 May 2017; revised: 23 August 2017; accepted: 29 August 2017

molecules in microgels, as well as enzyme-mediated active release of therapeutic proteins when microgels are crosslinked with protease-sensitive crosslinks[2]. Crosslinking PEG-4MAL macromers can be accomplished with dithiol molecules and does not require free radical initiators, which are detrimental to encapsulated cell health[13]. Similar microfluidic schemes for producing microgels[14–16] and encapsulating cells[17–19] have recently been reported for widely varying applications, including wound healing, stem cell culture and fundamental studies of cell biology. The versatility of microfluidic cell encapsulation extends to other polymers, including Matrigel[20], agarose[21] and even multilayer core-shell composites such as collagen cores with alginate shells[22].

Minimization of microgel diameter maximizes transport of oxygen and nutrients to encapsulated cells, enables applications for which larger microgels are not suited (such as injection) and potentially reduces transplant graft volume. Microfluidics provide precise control of size and polydispersity of droplets[23] and can be used to make very small cell laden microgels, including those with membranes as thin as 6 μm[24]. Unfortunately, volumetric throughput of macromer on flow focusing nozzles decreases with the cube of droplet diameter, so volumetric throughput can be severely limited when very small microgels are being produced. Furthermore, cells suspended at high concentrations ($>10^6$ cells per mL) tend to aggregate, which can lead to incomplete cell encapsulation as well as increased microgel diameters. Therefore, low concentration cell suspensions (10^4–10^5 cells per mL) are typically used, often resulting in a high percentage of empty microgels according to the Poisson distribution[25], which is undesirable for *in vivo* efficacy and limits applications of encapsulation. Microgels containing cells can be purified by sorting or can be selectively crosslinked[7,24,26,27], but encapsulating clinically relevant numbers of cells in these very small microgels is highly challenging, since several tens of millions of cells may be required for therapeutic efficacy[28,29]. Long processing times associated with encapsulation or sorting are likely to decrease cell viability, so faster cell microencapsulation rates are desirable not just for convenience, but also to maintain cell potency.

To maximize cell encapsulation rate, both the concentration of cells in suspension and the volumetric throughput of macromer in microfluidic devices must be maximized. One way to increase flow rate of macromer in a microfluidic droplet generating device is to utilize a parallel flow focusing nozzle configuration. However, coupled inlet and outlet flow paths present significant challenges to maintaining size control and low polydispersity of droplet diameter, due to propagation of pressure fluctuations between nozzles. Nonetheless, uniform droplet production has been shown on parallel droplet generators with a variety of configurations[30–34]. Parallel microfluidics have been used to produce microgels through light-initiated free-radical polymerization on single layer microfluidics, and the nature of crosstalk between parallel droplet generators has been studied in this context[35]. Furthermore, in an impressive display of microfluidic control, even uniform double emulsion polymerosomes were formed on parallel geometries[36,37], and robust, massively parallel droplet production has been demonstrated[38]. However, suspensions containing high density cell suspensions complicate fluid behavior and may cause non-uniform distribution of fluid to focusing nozzles. Likely because of these hurdles, parallel droplet generators have not been utilized to date for suspension of cells in droplets, much less their encapsulation in polymer microspheres.

Here we report a process for the high-throughput encapsulation of cells in sub-100 μm diameter microgels, which utilizes a novel two-layer microfluidic device with six parallel flow focusing nozzles. Devices with two different nozzle widths, 35 and 100 μm, were developed, each with benefits and disadvantages. Thirty five micrometer wide nozzle devices produce smaller microgels and can break up droplets from precursors with twice the cell concentration as 100 μm wide nozzle devices. However, encapsulation on 35 μm wide nozzle devices reduces viability of human mesenchymal stem cells (hMSCs), and reduces their ability to secrete vascular endothelial growth factor (VEGF) in proportion to this loss of viability. On the other hand, following encapsulation on 100 μm wide nozzle devices, hMSCs have >90% viability and only minimal reduction of VEGF secretion vs. hMSCs cultured on tissue culture (TC) plastic. Although only six parallel channels are utilized in order to maintain robust operation, this parallelization of 100 μm wide nozzles could reduce total encapsulation time by sixfold compared to a single-nozzle device. Microgels with sub-100 μm diameters are ideal for many applications, due to their relatively low polymer content, but encapsulating clinically relevant numbers of cells in small microgels poses unique challenges. The scheme presented here addresses these challenges in a practical but novel way, through simultaneously maximizing cell concentration and effectively parallelizing encapsulation on flow focusing nozzles.

MATERIALS AND METHODS

Microfluidic fabrication

Photolithography was used to pattern microfluidic masters after spin coating SU-8 2050 photoresist (MicroChem, Westborough, MA, USA) onto silicon wafers, then masters were developed and treated with vapor phase trichloro(1H,1H,2H,2H-perfluorooctyl) silane (Sigma, St. Louis, MO, USA) to reduce sticking. Devices with 35 and 100 μm wide nozzles had focusing layer patterns that were 35 and 100 μm tall, respectively, and their corresponding top layer patterns were 80 and 140 μm tall. PDMS (Sylgard 184) was mixed according to manufacturer specifications and was molded on the SU-8 master to make microfluidic channel replicas (Figure 1a). After curing for 11 min at 110 °C, crosslinker inlet and outlet holes were punched in the top layer, and inter-layer vias were punched in the bottom layer. Relevant surfaces were exposed to air plasma for 20 s in a PlasmaPreen (North Brunswick, NJ, USA) system, and layers were aligned and pressed together by hand before being cured at 110 °C for 5 min. After PDMS to PDMS bond was stabilized, oil and macromer inlets were punched through both layers. These elastomer constructs were sonicated, along with glass substrates, in 200 proof ethanol, and then were dried with compressed nitrogen. Cleaned components were quickly treated with 12 s of plasma and PDMS was bonded to a glass slide, sealing the lower layer flow channels. Devices were cured overnight at 60 °C before being used.

Microgel synthesis and characterization

Microfluidic devices were primed with light mineral oil (Sigma) containing 2% SPAN80 (Sigma), which was also used as the continuous phase fluid. The crosslinker emulsion was comprised of 30 mg mL^{-1} dithiothreitol (DTT; Sigma) emulsified at a 1:15 ratio in the continuous phase. The macromer solution consisted of 6.5% (w/v) PEG-4MAL (20 kDa, Laysan Bio, Arab, AL, USA), which had been reacted with a cell adhesive peptide (1.0 mM, Genscript, Piscataway, NJ, USA) that was pre-conjugated to AlexaFluor594 (Thermo Fisher, Waltham, MA, USA) to enable imaging and for consistency with cell encapsulation experiments. Also motivated by consistency with subsequent cell encapsulation experiments, this reaction was performed in a buffer which had additives to address challenges associated with cell encapsulation. Particularly, the buffer contained OptiPrep density gradient (Sigma) and PBS in a 1:4 ratio to match the density of cells and minimize settling of cells. The buffer also contained 0.1% Pluronic F108, which reduces cell sticking to glass or PDMS. After connecting the outlet and all inlets, fluid flows were driven at the flow rates prescribed in Table 1 by Hamilton gastight syringes on Harvard Apparatus Elite syringe pumps. To prevent unwanted gelation of polymer precursor on chip and minimize polydispersity due to transient

doi:10.1038/micronano.2017.76

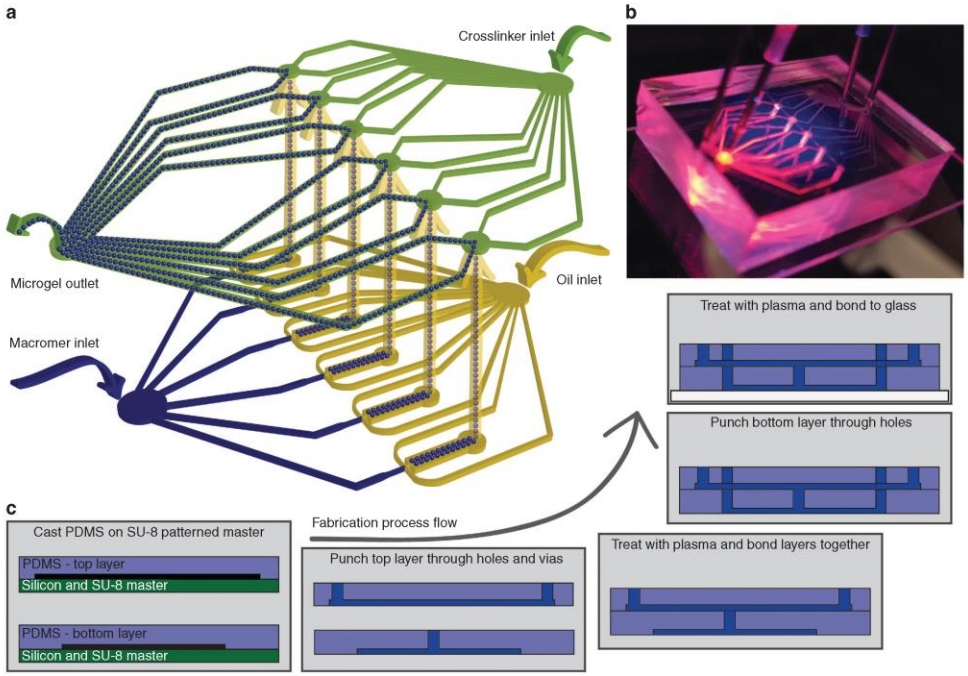

Figure 1 Schematic and representative images demonstrating parallel microfluidic device operation and fabrication are shown. (**a**) Droplets containing macromer precursor (and optionally cells) are emulsified in oil on the lower layer of the device when these immiscible fluids are co-flowed through a flow focusing geometry. The droplets produced on all six flow focusing nozzles are carried up to the top layer where they are exposed to crosslinker and are pooled before exiting the device at a single outlet. (**b**) Fluorescent label facilitates visualization of microfluidic device operation, as seen in this photograph of microgel generation in progress. (**c**) The two-layer microfluidic device requires several steps for fabrication. First, PDMS is molded from SU-8 and silicon masters, and then holes that go through one layer only are punched. PDMS layers are exposed to air plasma and are aligned and bonded to each other. Inlets for the bottom layer are punched through both layers, and the device is completed by bonding the two-layer PDMS construct to a glass substrate after plasma exposure.

Table 1 Microfluidic devices with parallel nozzle configuration have 600% increased macromer throughput rate over single-nozzle configurations

	Flow rate (μL min^{-1})		
	Macromer	Oil	Crosslinker
35 μm width			
Single nozzle	0.2	1.0	2.0
Parallel nozzles	1.2	6.0	15.0
100 μm width			
Single nozzle	1.67	12.5	15.0
Parallel nozzles	10.0	75.0	40.0

Flow rates shown were used for all experiments discussed herein.

flows, first oil, then crosslinker fluid flows were initiated and allowed to stabilize. Only after flows stabilized was macromer precursor flow initiated. After at least 20 min of generation, microgels were collected in phosphate buffered saline containing 2% bovine serum albumin (to reduce microgel sticking). Most of the oil was removed by aspiration after centrifugation (600 g for 5 min), after which microgels were washed three more times by centrifugation in a new 15 mL conical tube to remove any mineral oil residue from microgels. Microgels were imaged using a Nikon Ti-E microscope with C2-Plus Confocal System, and diameter was determined using 'Analyze Particles' on binarized images in ImageJ. Output of three independent microgel generations were characterized for all four device designs tested, with a minimum of 163 microgels counted per device.

Human MSC microencapsulation and characterization

A similar protocol was used to encapsulate hMSCs, with a few modifications. First, hMSCs were trypsinized for 10 min in 0.25% trypsin/EDTA, which minimized cell clumping and homogenized cell morphology compared to shorter trypsinization times. A macromer solution was made containing twice the desired final concentrations—that is, 13 wt% PEG-4MAL, 2.0 mM RGD, 0.2% Pluronic F108, in a buffer comprised of 1:2 OptiPrep in PBS. This precursor was mixed with an equal volume of cells suspended at twice their desired concentration. The resulting solution contained gel precursor concentrations consistent with those used for microgel synthesis and contained the desired concentration of cells in suspension (2×10^7 cells per mL for 35 μm wide nozzle or 10^7 cells per mL for 100 μm wide nozzle). This suspension was mixed thoroughly by pipetting and was used as quickly as

possible to generate microgels in parallel nozzle microfluidic devices, using the same protocol described for empty microgels. Three independent encapsulations were performed on both the 35 and 100 μm wide nozzles for at least 20 min each, and the resulting microgels were washed with culture media four times by centrifugation. Live and dead cells were then stained with Calcein-AM and TOTO-3 iodide, respectively (Thermo Fisher). Microgels containing cells were imaged on a confocal microscope and were measured in ImageJ. The number of cells per microgel was determined by manual counting due to cell clustering. At least 425 microgels were characterized from each encapsulation.

Human MSC viability in culture

Viability of microencapsulated hMSC was monitored over time for cells encapsulated on parallel microfluidic devices with both 35 and 100 μm wide nozzles. Cell viability on day 0 was calculated by dividing the number of Calcein-AM positive cells by the total number of cells counted. Some encapsulated cells were not stained on day 0 and were instead cultured with media changes every three days. On days 1, 3 and 7 post encapsulation, encapsulated cells were removed from culture and were stained and imaged to determine cell viability. As a control, viability was also determined over time for hMSCs grown on TC plastic. Day 0 viability of cells in microgels was compared for cells encapsulated on 35 μm vs 100 μm wide nozzle devices using Mann–Whitney test in GraphPad (La Jolla, CA, USA).

VEGF secretion

Twenty four hours following encapsulation, ~10^5 hMSCs, microencapsulated using either 35 μm or 100 μm nozzle devices, were suspended in 1.0 mL growth media in a 24-well plate. Unencapsulated hMSCs were also seeded onto a 24-well plate at an equal concentration. After incubation for 48 h, conditioned media from all samples was collected and frozen at −80 °C. At the time of analysis, conditioned media was thawed and concentrations of VEGF were quantified using ELISA (Biolegend, San Diego, CA, USA). DNA was quantified from each sample using CyQUANT assay following the manufacturer's instructions (Thermo Fisher). VEGF secretion was normalized to DNA content, and normalized values were compared between groups using ANOVA with a Tukey *post hoc* test. $P < 0.05$ was considered significant.

RESULTS AND DISCUSSION

Microfluidic design and fabrication

Our target application during device development was intravascular cell delivery for extended local VEGF secretion and mitigation of inflammation. Therefore, the goals of our iterative design were to maximize encapsulation throughput as well as viability and function of encapsulated cells while simultaneously minimizing microgel size as well as the number of empty microgels. During the course of preliminary experiments with devices comprised of single square flow focusing nozzles, nozzle widths smaller than 30 μm did not consistently encapsulate cells, especially hMSCs, which were relatively large cells with heterogeneous morphology. Therefore, 35 μm wide nozzles were determined to be the smallest nozzle appropriate for encapsulation of hMSCs. Also during these preliminary experiments, we observed that cell viability was reduced in these very small microgels, which might limit their potency. Cells encapsulated on 100 μm wide nozzles had higher viability, and therefore therapeutic potential, but encapsulation of clinically relevant cell numbers was still challenging. For example, encapsulation of 30 million cells would require ~30 h.

Therefore, we determined that parallel flow focusing geometries and very high cell suspension concentrations were essential for encapsulating clinically relevant cell numbers in a practical time frame. Several different two-layer parallel nozzle flow focusing microfluidic devices were designed and fabricated (for both 35 and 100 μm widths) using soft lithography, in an iterative design process. However, at high cell loading ($> 5 \times 10^6$ per mL), all devices tested which had more than six channels produced extremely heterogeneous microgel sizes due to increased clogging of nozzles with cells. On the six-nozzle device, clogs with deformable particles frequently cleared themselves due to increasing local pressure; however, on devices with more than six nozzles, sustained clogs were frequently observed, likely because there were channels with lower resistance through which flow could be diverted. These nozzle obstructions would cause oil to divert upstream into the aqueous phase distribution, which perturbed droplet production at multiple nozzles. On the final design (Figure 1), all flow channels on the top layer are relatively large and open (80 μm tall for devices with 35 μm wide nozzles; 140 μm tall for devices with 100 μm wide nozzles), to reduce the pressure stressing the PDMS to PDMS bond. The six nozzle designs represent a compromise achieved through extensive trial and error to balance (a) high cell loading, (b) low empty microgel rate and (c) high cell throughput.

Maximum flow rates of macromer phase resulting in consistent microencapsulation and low polydispersity were determined in previous experiments utilizing mineral oil as the continuous phase. Fluorinated oils produce lower capillary number flow relative to mineral oil, and so can be operated with higher macromer phase flow rates while maintaining dripping flow. We attempted to increase throughput even further by utilizing one such oil, Fluorinert FC40, along with a nonionic fluorinated surfactant purchased from RAN biotechnologies (008) (Beverly, MA, USA). Unfortunately, nozzle-to-nozzle variability in droplet breakup was much greater with fluorinated oils than with mineral oil when utilizing parallel flow focusing nozzle geometries, resulting in more polydispersed droplet diameters. Because of this increased variability and difficulty of maintaining crosslinker emulsion in fluorinated oils, mineral oil was used as the continuous phase for all subsequent experiments.

Parallel encapsulation allows for 600% increased throughput while maintaining size control of microgels

A major benefit of synthesizing microgels with droplet microfluidics is the ability to precisely control microgel size and polydispersity. However, maintaining low polydispersity is challenging in parallel nozzle devices, because any variation in fluidic resistance between flow focusers (or respective distribution/collection channels) results in variation of droplet size produced at each nozzle. We synthesized PEG-4MAL microgels on both single- and parallel nozzle devices in order to characterize any increase in polydispersity due to parallel synthesis (Figure 2). Parallel nozzle devices were operated with six times the flow rate of single-nozzle devices (Table 1). Three separate synthesis runs were performed on three separate devices of each design. Representative histograms of microgel size are shown for each synthesis run (Figures 2a and b) along with representative fluorescent images of microgels. Although Kruskal-Wallis tests indicate differences in median microgel size across devices of the same design ($P < 0.05$ for all four devices), this is likely due to the small variances and large sample sizes. No gross differences in size distribution were seen between microgels generated on multiple devices of the same design (Figure 2), and mean microgel size was highly consistent between devices of the same design (Table 2). For practical purposes, we conclude that microgel production is repeatable on all four microfluidic designs. Microgels analyzed from all three encapsulations were pooled for each device so that comparisons could be made between single and parallel devices with the same nozzle size. For the 35 μm wide nozzle

doi:10.1038/micronano.2017.76

device, a *t*-test revealed statistical differences ($P = 0.012$; Figure 2c) in mean diameter of microgels produced on parallel vs. single nozzles, but the magnitude of this difference was small (< 1.8%)—average diameter was 65.1 ± 8.2 μm for parallel nozzle devices vs. 64.0 ± 6.3 μm for single-nozzle devices (Table 2). The mean diameter was equivalent for pooled microgels produced on 100 μm nozzles (104.5 μm), whether single or parallel configurations were used, and no differences in mean diameter were found ($P = 0.97$). *F*-tests revealed differences in variance of microgel diameter for parallel vs. single-nozzle production for both nozzle widths tested ($P < 0.0001$ in each case). For 35 μm nozzle width, the parallel configuration resulted in higher standard deviations than the single configuration, as expected. Surprisingly, the single 100 μm nozzle produced microgel diameters with higher standard deviations (±9.6 μm) than those produced on the parallel configuration (±7.5 μm). Whereas statistically significant differences were found between diameters of microgels produced on single vs. parallel nozzle configurations, the differences are small and are unlikely to matter for practical applications. Taken together, these results demonstrate that our parallel microfluidic device is capable of increasing microgel production rate by 600%, while having minimal impact on the size or polydispersity of resulting microgels.

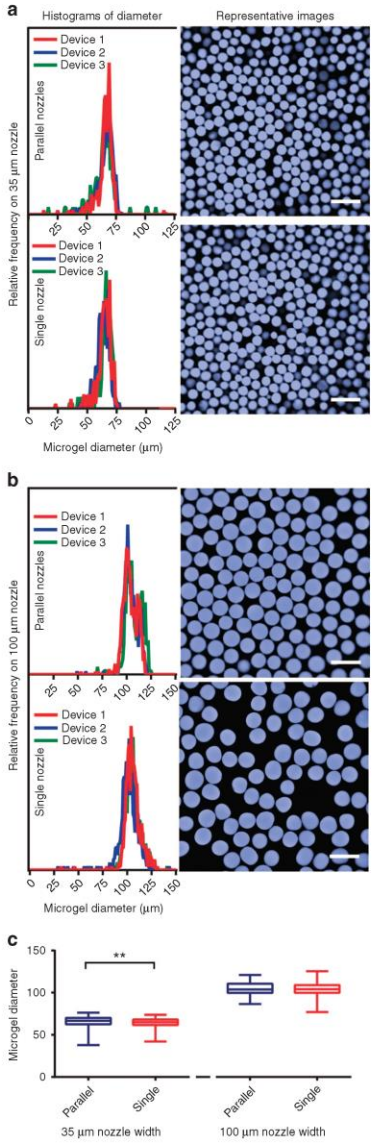

Figure 2 Microfluidic devices with parallel nozzles can produce microgels with controlled size, and with polydispersities comparable to microgels produced on a single nozzle. (**a** and **b**) Representative histograms of microgel diameter frequency and representative fluorescent images of microgels show similar output from single and parallel nozzles for both nozzle widths tested. (**c**) Consistency in diameter distribution is further demonstrated by comparing pooled microgels produced from each device. Significant differences were found between parallel and single configurations of 35 μm nozzles ($P = .0012$), but the magnitude of differences was not practically relevant. 100 μm nozzles did not produce different sized microgels with parallel vs. single configurations ($P = 0.97$).

Table 2 Statistics for microgel populations produced on different microfluidic devices, with or without cells

	Device 1	Device 2	Device 3	Pooled microgels
35 μm width				
Single nozzle (−cell)				
Mean diameter (μm)	64.2	62.9	64.7	64.0
± s.d. (μm)	6.0	5.3	6.8	6.3
CV (%)	9.3	8.4	10.6	9.9
Parallel nozzles (−cell)				
Mean diameter (μm)	65.6	65.1	64.2	65.1
± s.d. (μm)	7.9	8.5	8.8	8.2
CV (%)	12.1	13.0	13.7	12.7
Parallel nozzles (+cell)				
Mean diameter (μm)	77.2	76.4	75.9	76.5
± s.d. (μm)	6.3	5.7	7.5	6.6
CV (%)	8.2	7.5	9.9	8.6
100 μm width				
Single nozzle (−cell)				
Mean diameter (μm)	106.0	102.0	105.5	104.5
± s.d. (μm)	12.2	12.7	8.4	10.1
CV (%)	11.5	12.5	7.9	9.6
Parallel nozzles (−cell)				
Mean diameter (μm)	103.6	104.0	107.1	104.5
± s.d. (μm)	7.0	6.6	7.3	7.9
CV (%)	6.7	6.3	6.8	7.5
Parallel nozzles (+cell)				
Mean diameter (μm)	97.8	98.1	98.3	98.1
± s.d. (μm)	7.6	7.2	6.6	7.1
CV (%)	7.8	7.3	6.7	7.3

Results are shown for three independent syntheses for each process. Measured values from all three syntheses are pooled in the right most column to facilitate comparison between designs.

Human MSCs can be encapsulated on parallel nozzle microfluidic device with high loading density

The design criteria of maximum cell throughput and the desire for reduced transplant graft volume and microgel size both motivate a minimization of empty microgels and a maximization of cell loading in each microgel. Increasing the cell concentration in macromer solution exacerbates several challenges that may prevent successful encapsulation. High concentrations of hMSCs tend to aggregate in solution, which often result in many empty microgels and a relatively few, large microgels that contain clusters of cells. The tendency of hMSCs to aggregate was reduced by increasing trypsin exposure from 5 min to 10 min while harvesting cells, without notable deleterious effects on cell viability. Cells, especially when aggregating, tended to stick in microfluidic channels, forming sieves that prevent successful encapsulation. The addition of 0.1% Pluronic F108 eliminated this problem, along with further reducing cell aggregation. Cells also tended to settle in microfluidic tubing because their density is higher than a 6.5% PEG-4MAL solution in PBS, which results in increased cell aggregation and many empty microgels. After adding the cytocompatible density gradient media OptiPrep at a 1:4 ratio in cell suspensions, encapsulation runs up to 30 min were completed without noticeable cell settling. These three process improvements enabled microencapsulation of hMSCs with relatively high loading densities, as shown by fluorescent images in Figure 3a. In these images, green indicates live cells (stained with Calcein-AM), red indicates dead cells (stained with TOTO-3 iodide) and blue indicates the outline of microgels (obtained using 'Find Edges' in ImageJ). Histograms showing the frequency of microgels containing a given number of cells are shown in Figure 3b, along with the frequencies predicted by a Poisson distribution, using the measured average value as the expected value. Measured frequencies for number of cells per microgel closely matched those predicted by a Poisson distribution for microencapsulation on both 35 and 100 μm wide nozzles, except that approximately two times more empty microgels are produced than expected on 35 μm wide nozzles. Fewer empty microgels are produced when 100 μm wide nozzles are used rather than 35 μm wide nozzles ($P = 0.02$, Figure 3c), which may lead to more uniform cell spacing in packed microgel arrays.

The diameters of microgels that encapsulate hMSCs were measured from three separate parallel microfluidic devices for both 35 and 100 μm nozzle widths (Table 2). Cell-laden microgels produced on 100 μm wide nozzles had significantly smaller diameter than cell-free microgels, with a modest decrease in mean diameter of 6.4 μm, or 6.1%. Microgels produced on 35 μm wide nozzles were significantly larger when they contained cells than when no cells were present ($P < 0.0001$), with an increase in mean diameter of 11.4 μm, or 18%. Whereas aggregation of cells could explain the larger size of microgels produced on 35 μm wide nozzles, increased polydispersity would be expected if this was the case. Surprisingly, the addition of cells decreased microgel polydispersity when compared to microgels with no cells, as seen by the lower coefficient of variation on 35 μm wide nozzles when cells were present. The presence of cells did not meaningfully impact polydispersity of microgels from 100 μm wide nozzles, although the *F*-test shows statistically significant differences in variance between cell-laden and cell-free microgels ($P < 0.0001$ for both nozzle sizes; data in Table 2).

Microgels support hMSC viability and VEGF secretion, but the microencapsulation process reduces cell viability in a nozzle size–dependent fashion

Human MSCs were encapsulated in microgels utilizing three separate devices in independent encapsulations, for both 35 and 100 μm nozzle widths with parallel configurations. These microgels were functionalized with a peptide that contained the cell adhesive sequence RGD to support adhesive signaling of encapsulated cells. On days 0, 1, 3 and 7 after encapsulation, live and dead cells were labeled with Calcein-AM and TOTO-3 iodide, respectively, before being imaged, and viable cell fractions were calculated as the fraction of live cells over the total number of cells counted for each sample (Figure 4a). Cells encapsulated on 100 μm wide nozzles had excellent initial viability of $< 90\%$ on the day of encapsulation, and viability remained high ($< 75\%$) on day 3 post encapsulation, indicating that microgels support cell health. In contrast, cells encapsulated on 35 μm wide nozzles average only 71% viability on the day of encapsulation, implicating the smaller dimensions of the device as damaging to cells. This damage could be due to increased probability of cells being exposed to membrane-disrupting mineral oil during encapsulation, which has been shown to decrease encapsulated cell viability[39].

To further elucidate the effects of encapsulation on hMSCs, secretion of VEGF was measured 48 h after encapsulation, and was compared with secretion from hMSCs on TC plastic. Secretion of VEGF, which is known to promote angiogenesis[40], was reduced in a nozzle size–dependent manner consistent with viability after encapsulation (Figure 4b). This result suggests that the ability of encapsulated cells to secrete VEGF is not negatively impacted, since reduction of VEGF secretion is explained by reduction in viability.

Parallel nozzle microfluidic devices enable encapsulation of clinically relevant numbers of hMSC within practical time constraints

Maintaining cell viability during long encapsulation or sorting processes is challenging, so processing time needs to be minimized. Clinical human and preclinical large animal studies indicate that tens of million cells will likely be required for efficacy of some cell therapies[28,29]. The parallelized device discussed herein increases throughput by 600% without reductions in cell viability or VEGF secretion. This reduction overcomes a practical limitation of synthetic microgel encapsulation by allowing clinically relevant cell doses to be encapsulated within a standard workday.

CONCLUSIONS

Synthetic hydrogels used to deliver cells *in vivo* can be engineered to provide important biochemical signals to encapsulated cells and host tissue, and tuneable pore size allows for immunoisolation of encapsulated cells from host tissue. Bulk hydrogel constructs limit mass transport around encapsulated cells and are often prohibitively large when many cells are required. Microencapsulation, or the encapsulation of cells in microgels, can reduce mass transport limitations and large graft sizes associated with bulk encapsulation of cells and enables injectable delivery of cells within controlled microenvironments. All of these benefits are enhanced as microgel diameter is decreased, but volumetric throughput decreases with the cube of nozzle width, so it can be difficult to encapsulate clinically relevant numbers of cells in very small microgels. The parallel microfluidic device presented here increases microgel throughput six-fold with minimal change in polydispersity while maintaining high cell viability and secretory functions. Microencapsulation on 35 μm wide nozzle devices can be done at very high cell loading (2×10^7 cells per mL), which results in relatively small microgels (76.5 ± 6.6 μm), minimizing graft volume and transport limitations. The lower cell densities required to maintain uniform droplet breakup on 100 μm wide nozzles would result in increased graft volumes, but associated increases in cell viability and throughput may outweigh these concerns. Secretion of VEGF is reduced by hMSC encapsulation proportionally to the nozzle size–dependent loss of viability,

doi:10.1038/micronano.2017.76

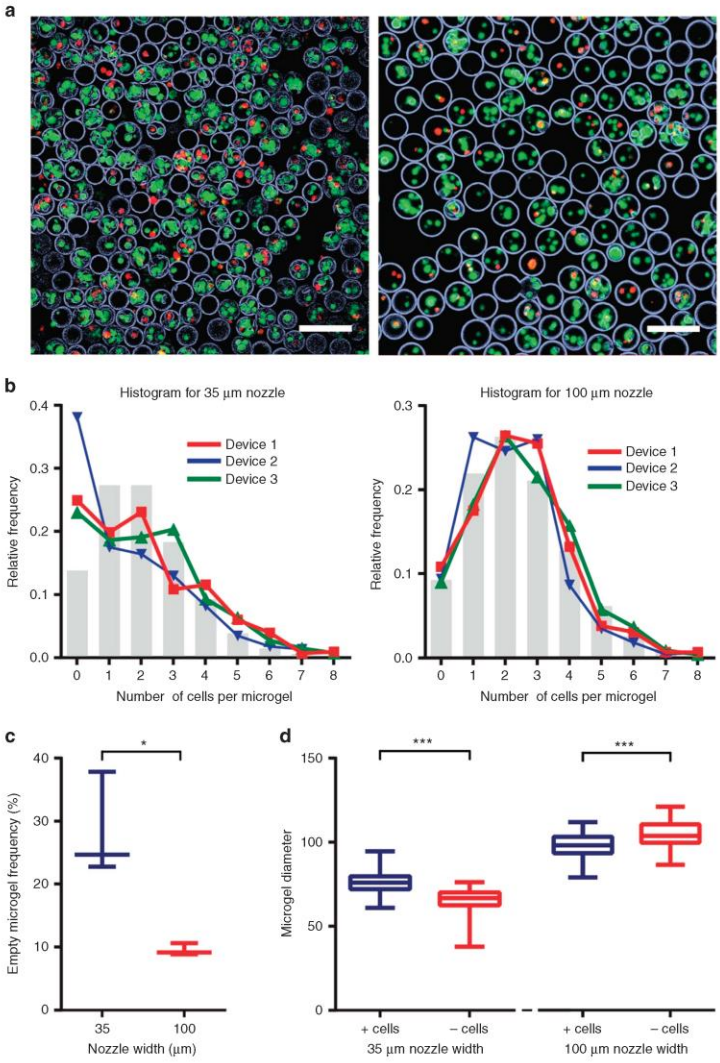

Figure 3 Parallel nozzle microfluidic devices provide high-throughput encapsulation of human mesenchymal stem cells (hMSCs) with high loading density. (**a**) Representative images are shown for cells microencapsulated on both 35 μm (left) and 100 μm (right) nozzle widths (scale bar 200 μm). Microgels encapsulating hMSCs were functionalized with a fluorescently labeled peptide containing the cell adhesive sequence RGD in order to support cell health and aid microgel visualization (outline of microgels was traced in blue using ImageJ). Live cells were stained with Calcein-AM (green) and dead cells with TOTO-3 iodide (red). (**b**) The number of cells per microgel was recorded for three independent encapsulations for each size nozzle, and their relative frequencies were plotted on histograms, along with the frequencies predicted by a Poisson distribution (gray bars). Number of cells in microgels produced on 100 μm wide nozzles closely matched the frequencies predicted by a Poisson distribution, but microgels produced on 35 μm wide nozzle devices contained more empty microgels than predicted. (**c**) Microencapsulation on 100 μm wide nozzles produces significantly fewer empty microgels than devices with 35 μm wide nozzles ($P = 0.02$). (**d**) Addition of cells has significant effects on distributions of microgel diameter vs. cell-free microgels for both 35 μm width, where average microgel size increases, and 100 μm width, where average microgel size decreases ($P < 0.0001$ for both widths).

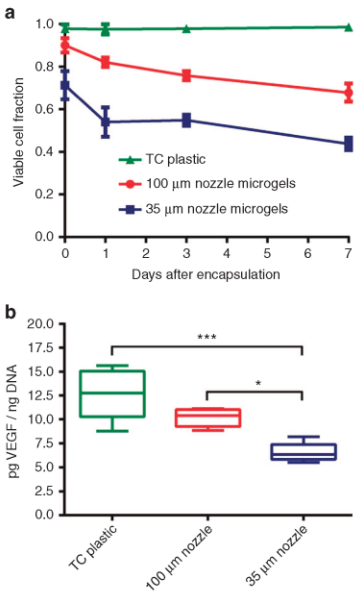

Figure 4 Microencapsulation in PEG-4MAL microgels has nozzle size–dependent effects on hMSC viability and VEGF secretion. (**a**) Viable cell fraction was determined over time in culture to measure the ability of microgels produced on each nozzle width to support hMSC health. Cells encapsulated on 100 µm wide nozzles had good viability on the day of encapsulation, and maintained adequate viability for seven days in culture. Cells encapsulated on 35 µm wide nozzles had significantly reduced viability on the day of encapsulation versus cells encapsulated on 100 µm wide nozzles ($P = 0.01$), after which cell viability decreased at similar rates to cells encapsulated on 100 µm wide nozzles. (**b**) VEGF secretion from encapsulated hMSCs followed similar nozzle size–dependent trends to viability, suggesting that VEGF secretion per viable cell remains unchanged following encapsulation. ($^{*}P < 0.05$; $^{***}P < 0.001$; $^{****}P < 0.0001$). hMSCs, human mesenchymal stem cells' (hMSCs); TC, tissue culture; VEGF, vascular endothelial growth factor.

which indicates that viable cells maintain capacity to promote angiogenesis. Each nozzle width has been designed prioritizing differently the particular challenges associated with high-throughput cell encapsulation in small microgels, but both of these devices utilize similar, novel approaches to solve limited cell throughput. By using high concentration cell suspensions and parallel flow focusing nozzles, clinically relevant cell numbers can be rapidly encapsulated in small microgels.

ACKNOWLEDGEMENTS

This work was funded by NIH (Grant No. R21EB020107) and the Juvenile Diabetes Research Foundation (Grant No. 2-SRA-2014-287-Q-R).

COMPETING INTERESTS

DMH and AJG are inventors in a patent associated with polyethylene microgels for cell encapsulation (U.S. Patent 9,381,217). The remaining authors declare no conflict of interest.

REFERENCES

1 Liu AL, Garcia AJ. Methods for generating hydrogel particles for protein delivery. *Annals of Biomedical Engineering* 2016; **44**: 1946–1958.
2 Foster GA, Headen DM, González-García C *et al.* Protease-degradable microgels for protein delivery for vascularization. *Biomaterials* 2017; **113**: 170–175.
3 Lutolf MP, Hubbell JA. Synthetic biomaterials as instructive extracellular micro-environments for morphogenesis in tissue engineering. *Nature Biotechnology* 2005; **23**: 47–55.
4 Alge DL, Azagarsamy MA, Donohue DF *et al.* Synthetically tractable click hydrogels for three-dimensional cell culture formed using tetrazine-norbornene chemistry. *Biomacromolecules* 2013; **14**: 949–953.
5 Vegas AJ, Veiseh O, Gurtler M *et al.* Long-term glycemic control using polymer-encapsulated human stem cell-derived beta cells in immune-competent mice. *Nature Medicine* 2016; **22**: 306–311.
6 Tomei AA, Manzoli V, Fraker CA *et al.* Device design and materials optimization of conformal coating for islets of Langerhans. *Procedings of the National Academies of Sciences USA* 2014; **111**: 10514–10519.
7 Mao AS, Shin J-W, Utech S *et al.* Deterministic encapsulation of single cells in thin tunable microgels for niche modelling and therapeutic delivery. *Nature Materials* 2016; **16**: 236–243.
8 Park JS, Chu JS, Tsou AD *et al.* The effect of matrix stiffness on the differentiation of mesenchymal stem cells in response to TGF-beta. *Biomaterials* 2011; **32**: 3921–3930.
9 García JR, Clark AY, García AJ. Integrin-specific hydrogels functionalized with VEGF for vascularization and bone regeneration of critical-size bone defects. *Journal of Biomedical Materials Research Part A* 2016; **104**: 889–900.
10 Johnson AS, O'Sullivan E, D'Aoust LN *et al.* Quantitative assessment of islets of langerhans encapsulated in alginate. *Tissue Engineering Part C: Methods* 2011; **17**: 435–449.
11 Lim F, Sun AM. Microencapsulated islets as bioartificial endocrine pancreas. *Science* 1980; **210**: 908–910.
12 Headen DM, Aubry G, Lu H *et al.* Microfluidic-based generation of size-controlled, biofunctionalized synthetic polymer microgels for cell encapsulation. *Advanced Materials* 2014; **26**: 3003–3008.
13 Williams CG, Malik AN, Kim TK *et al.* Variable cytocompatibility of six cell lines with photoinitiators used for polymerizing hydrogels and cell encapsulation. *Biomaterials* 2005; **26**: 1211–1218.
14 Allazetta S, Hausherr TC, Lutolf MP. Microfluidic synthesis of cell-type-specific artificial extracellular matrix hydrogels. *Biomacromolecules* 2013; **14**: 1122–1131.
15 Kesselman LRB, Shinwary S, Selvaganapathy PR *et al.* Synthesis of monodisperse, covalently cross-linked, degradable 'smart' microgels using microfluidics. *Small* 2012; **8**: 1092–1098.
16 Griffin DR, Weaver WM, Scumpia PO *et al.* Accelerated wound healing by injectable microporous gel scaffolds assembled from annealed building blocks. *Nature Materials* 2015; **14**: 737–744.
17 Allazetta S, Kolb L, Zerbib S *et al.* Cell-instructive microgels with tailor-made physicochemical properties. *Small* 2015; **11**: 5647–5656.
18 Siltanen C, Yaghoobi M, Haque A *et al.* Microfluidic fabrication of bioactive microgels for rapid formation and enhanced differentiation of stem cell spheroids. *Acta Biomaterialia* 2016; **34**: 125–132.
19 Velasco D, Tumarkin E, Kumacheva E. Microfluidic encapsulation of cells in polymer microgels. *Small* 2012; **8**: 1633–1642.
20 Dolega ME, Abeille F, Picollet-D'hahan N *et al.* Controlled 3D culture in Matrigel microbeads to analyze clonal acinar development. *Biomaterials* 2015; **52**: 347–357.
21 Tumarkin E, Tzadu L, Csaszar E *et al.* High-throughput combinatorial cell co-culture using microfluidics. *Integrative Biology* 2011; **3**: 653–662.
22 Agarwal P, Choi JK, Huang H *et al.* A biomimetic core-shell platform for miniaturized 3D cell and tissue engineering. *Particle & Particle Systems Characterization* 2015; **32**: 809–816.
23 Anna SL, Bontoux N, Stone HA. Formation of dispersions using 'flow focusing' in microchannels. *Applied Physics Letters* 2003; **82**: 364–366.
24 Lienemann PS, Rossow T, Mao AS *et al.* Single cell-laden protease-sensitive microniches for long-term culture in 3D. *Lab on a Chip* 2017; **17**: 727–737.
25 Collins DJ, Neild A, deMello A *et al.* The Poisson distribution and beyond: Methods for microfluidic droplet production and single cell encapsulation. *Lab on a Chip* 2015; **15**: 3439–3459.
26 Kim J, Won J, Song S. Dual-mode on-demand droplet routing in multiple microchannels using a magnetic fluid as carrier phase. *Biomicrofluidics* 2014; **8**: 054105.
27 Agresti JJ, Antipov E, Abate AR *et al.* Ultrahigh-throughput screening in drop-based microfluidics for directed evolution. *Proceedings of the National Academy of Sciences of United States of America* 2010; **107**: 4004–4009.
28 Strauer BE, Brehm M, Zeus T *et al.* Repair of infarcted myocardium by autologous intracoronary mononuclear bone marrow cell transplantation in humans. *Circulation* 2002; **106**: 1913–1918.

 doi:10.1038/micronano.2017.76

29 Golpanian S, Schulman IH, Ebert RF *et al.* Concise review: Review and perspective of cell dosage and routes of administration from preclinical and clinical studies of stem cell therapy for heart disease. *Stem Cells Translational Medicine* 2016; **5**: 186–191.
30 Tetradis-Meris G, Rossetti D, de Torres CP *et al.* Novel parallel integration of microfluidic device network for emulsion formation. *Industrial & Engineering Chemistry Research* 2009; **48**: 8881–8889.
31 Bardin D, Kendall MR, Dayton PA *et al.* Parallel generation of uniform fine droplets at hundreds of kilohertz in a flow-focusing module. *Biomicrofluidics* 2013; **7**: 13.
32 Jeong H-H, Yelleswarapu VR, Yadavali S *et al.* Kilo-scale droplet generation in three-dimensional monolithic elastomer device (3D MED). *Lab on a Chip* 2015; **15**: 4387–4392.
33 Mulligan MK, Rothstein JP. Scale-up and control of droplet production in coupled microfluidic flow-focusing geometries. *Microfluidics and Nanofluidics* 2012; **13**: 65–73.
34 Muluneh M, Issadore D. Hybrid soft-lithography/laser machined microchips for the parallel generation of droplets. *Lab on a Chip* 2013; **13**: 4750–4754.
35 Li W, Greener J, Voicu D *et al.* Multiple modular microfluidic (M 3) reactors for the synthesis of polymer particles. *Lab on a Chip* 2009; **9**: 2715–2721.
36 Kim SH, Kim JW, Kim DH *et al.* Enhanced-throughput production of polymersomes using a parallelized capillary microfluidic device. *Microfluidics and Nanofluidics* 2013; **14**: 509–514.
37 Romanowsky MB, Abate AR, Rotem A *et al.* High throughput production of single core double emulsions in a parallelized microfluidic device. *Lab on a Chip* 2012; **12**: 802–807.
38 Amstad E, Chemama M, Eggersdorfer M *et al.* Robust scalable high throughput production of monodisperse drops. *Lab on a Chip* 2016; **16**: 4163–4172.
39 Kim S, Oh J, Cha C. Enhancing the biocompatibility of microfluidics-assisted fabrication of cell-laden microgels with channel geometry. *Colloids and Surfaces B: Biointerfaces* 2016; **147**: 1–8.
40 Ferrara N, Gerber HP, LeCouter J. The biology of VEGF and its receptors. *Nature Medicine* 2003; **9**: 669–676.

REFERENCES

1. Squillaro, T., G. Peluso, and U. Galderisi, *Clinical Trials With Mesenchymal Stem Cells: An Update.* Cell Transplant, 2016. **25**(5): p. 829-48.

2. Castro-Manrreza, M.E. and J.J. Montesinos, *Immunoregulation by mesenchymal stem cells: biological aspects and clinical applications.* J Immunol Res, 2015. **2015**: p. 394917.

3. Pittenger, M.F., et al., *Multilineage potential of adult human mesenchymal stem cells.* Science, 1999. **284**(5411): p. 143-7.

4. Doorn, J., et al., *Therapeutic applications of mesenchymal stromal cells: paracrine effects and potential improvements.* Tissue Eng Part B Rev, 2012. **18**(2): p. 101-15.

5. Corn, D.J., et al., *Imaging early stage osteogenic differentiation of mesenchymal stem cells.* J Orthop Res, 2013. **31**(6): p. 871-9.

6. Gohil, S.V., et al., *Evaluation of the donor cell contribution in rhBMP-2 mediated bone formation with chitosan thermogels using fluorescent protein reporter mice.* J Biomed Mater Res A, 2016. **104**(4): p. 928-41.

7. Rai, B., et al., *Differences between in vitro viability and differentiation and in vivo bone-forming efficacy of human mesenchymal stem cells cultured on PCL-TCP scaffolds.* Biomaterials, 2010. **31**(31): p. 7960-70.

8. Yanez, R., et al., *Adipose tissue-derived mesenchymal stem cells have in vivo immunosuppressive properties applicable for the control of the graft-versus-host disease.* Stem Cells, 2006. **24**(11): p. 2582-91.

9. Panchalingam, K.M., et al., *Bioprocessing strategies for the large-scale production of human mesenchymal stem cells: a review.* Stem Cell Res Ther, 2015. **6**: p. 225.

10. Mastri, M., H. Lin, and T. Lee, *Enhancing the efficacy of mesenchymal stem cell therapy.* World J Stem Cells, 2014. **6**(2): p. 82-93.

11. Garcia, J.R. and A.J. Garcia, *Biomaterial-mediated strategies targeting vascularization for bone repair.* Drug Deliv Transl Res, 2015.

12. Friedenstein, A.J., R.K. Chailakhjan, and K.S. Lalykina, *The development of fibroblast colonies in monolayer cultures of guinea-pig bone marrow and spleen cells.* Cell Tissue Kinet, 1970. **3**(4): p. 393-403.

13. Friedenstein, A.J., *Stromal mechanisms of bone marrow: cloning in vitro and retransplantation in vivo.* Haematol Blood Transfus, 1980. **25**: p. 19-29.

14. Friedenstein, A.J., et al., *Stromal cells responsible for transferring the microenvironment of the hemopoietic tissues. Cloning in vitro and retransplantation in vivo.* Transplantation, 1974. **17**(4): p. 331-40.

15. Dominici, M., et al., *Minimal criteria for defining multipotent mesenchymal stromal cells. The International Society for Cellular Therapy position statement.* Cytotherapy, 2006. **8**(4): p. 315-7.

16. Jaiswal, N., et al., *Osteogenic differentiation of purified, culture-expanded human mesenchymal stem cells in vitro.* J Cell Biochem, 1997. **64**(2): p. 295-312.

17. Liechty, K.W., et al., *Human mesenchymal stem cells engraft and demonstrate site-specific differentiation after in utero transplantation in sheep.* Nat Med, 2000. **6**(11): p. 1282-6.

18. Hass, R., et al., *Different populations and sources of human mesenchymal stem cells (MSC): A comparison of adult and neonatal tissue-derived MSC.* Cell Commun Signal, 2011. **9**: p. 12.

19. Lee, O.K., et al., *Isolation of multipotent mesenchymal stem cells from umbilical cord blood.* Blood, 2004. **103**(5): p. 1669-75.

20. In 't Anker, P.S., et al., *Isolation of mesenchymal stem cells of fetal or maternal origin from human placenta.* Stem Cells, 2004. **22**(7): p. 1338-45.

21. Shi, S. and S. Gronthos, *Perivascular niche of postnatal mesenchymal stem cells in human bone marrow and dental pulp.* J Bone Miner Res, 2003. **18**(4): p. 696-704.

22. Zuk, P.A., et al., *Human adipose tissue is a source of multipotent stem cells.* Mol Biol Cell, 2002. **13**(12): p. 4279-95.

23. Minteer, D., K.G. Marra, and J.P. Rubin, *Adipose-derived mesenchymal stem cells: biology and potential applications.* Adv Biochem Eng Biotechnol, 2013. **129**: p. 59-71.

24. Kern, S., et al., *Comparative analysis of mesenchymal stem cells from bone marrow, umbilical cord blood, or adipose tissue.* Stem Cells, 2006. **24**(5): p. 1294-301.

25. Puissant, B., et al., *Immunomodulatory effect of human adipose tissue-derived adult stem cells: comparison with bone marrow mesenchymal stem cells.* Br J Haematol, 2005. **129**(1): p. 118-29.

26. Yoo, K.H., et al., *Comparison of immunomodulatory properties of mesenchymal stem cells derived from adult human tissues.* Cell Immunol, 2009. **259**(2): p. 150-6.

27. Bishop, J.A., et al., *Assessment of compromised fracture healing.* J Am Acad Orthop Surg, 2012. **20**(5): p. 273-82.

28. Buza, J.A., 3rd and T. Einhorn, *Bone healing in 2016.* Clin Cases Miner Bone Metab, 2016. **13**(2): p. 101-105.

29. Akiyama, H., et al., *The transcription factor Sox9 has essential roles in successive steps of the chondrocyte differentiation pathway and is required for expression of Sox5 and Sox6.* Genes Dev, 2002. **16**(21): p. 2813-28.

30. Mackie, E.J., et al., *Endochondral ossification: how cartilage is converted into bone in the developing skeleton.* Int J Biochem Cell Biol, 2008. **40**(1): p. 46-62.

31. Baek, W.Y., et al., *Positive regulation of adult bone formation by osteoblast-specific transcription factor osterix.* J Bone Miner Res, 2009. **24**(6): p. 1055-65.

32. Tsumaki, N., et al., *Bone morphogenetic protein signals are required for cartilage formation and differently regulate joint development during skeletogenesis.* J Bone Miner Res, 2002. **17**(5): p. 898-906.

33. Majumdar, M.K., E. Wang, and E.A. Morris, *BMP-2 and BMP-9 promotes chondrogenic differentiation of human multipotential mesenchymal cells and overcomes the inhibitory effect of IL-1.* J Cell Physiol, 2001. **189**(3): p. 275-84.

34. Carlevaro, M.F., et al., *Vascular endothelial growth factor (VEGF) in cartilage neovascularization and chondrocyte differentiation: auto-paracrine role during endochondral bone formation.* J Cell Sci, 2000. **113 (Pt 1)**: p. 59-69.

35. Zelzer, E., et al., *VEGFA is necessary for chondrocyte survival during bone development.* Development, 2004. **131**(9): p. 2161-71.

36. Gerber, H.P., et al., *VEGF couples hypertrophic cartilage remodeling, ossification and angiogenesis during endochondral bone formation.* Nat Med, 1999. **5**(6): p. 623-8.

37. Ohbayashi, N., et al., *FGF18 is required for normal cell proliferation and differentiation during osteogenesis and chondrogenesis.* Genes Dev, 2002. **16**(7): p. 870-9.

38. Liu, Z., et al., *Coordination of chondrogenesis and osteogenesis by fibroblast growth factor 18.* Genes Dev, 2002. **16**(7): p. 859-69.

39. Clarke, B., *Normal bone anatomy and physiology.* Clin J Am Soc Nephrol, 2008. **3 Suppl 3**: p. S131-9.

40. Ornitz, D.M. and P.J. Marie, *FGF signaling pathways in endochondral and intramembranous bone development and human genetic disease.* Genes Dev, 2002. **16**(12): p. 1446-65.

41. Sorrell, J.M., *Development of arteries in embryonic chick bone marrow with special reference to the appearance of periarterial granulopoietic sheaths.* Anat Rec, 1988. **221**(3): p. 730-6.

42. Percival, C.J. and J.T. Richtsmeier, *Angiogenesis and intramembranous osteogenesis.* Dev Dyn, 2013. **242**(8): p. 909-22.

43. Bruder, S.P., et al., *Bone regeneration by implantation of purified, culture-expanded human mesenchymal stem cells.* J Orthop Res, 1998. **16**(2): p. 155-62.

44. Bruder, S.P., et al., *The effect of implants loaded with autologous mesenchymal stem cells on the healing of canine segmental bone defects.* J Bone Joint Surg Am, 1998. **80**(7): p. 985-96.

45. Arinzeh, T.L., et al., *Allogeneic mesenchymal stem cells regenerate bone in a critical-sized canine segmental defect.* J Bone Joint Surg Am, 2003. **85-A**(10): p. 1927-35.

46. Kon, E., et al., *Autologous bone marrow stromal cells loaded onto porous hydroxyapatite ceramic accelerate bone repair in critical-size defects of sheep long bones.* J Biomed Mater Res, 2000. **49**(3): p. 328-37.

47. Koob, S., et al., *Bone formation and neovascularization mediated by mesenchymal stem cells and endothelial cells in critical-sized calvarial defects.* Tissue Eng Part A, 2011. **17**(3-4): p. 311-21.

48. Dupont, K.M., et al., *Human stem cell delivery for treatment of large segmental bone defects.* Proc Natl Acad Sci U S A, 2010. **107**(8): p. 3305-10.

49. Vila, O.F., et al., *Bioluminescent and micro-computed tomography imaging of bone repair induced by fibrin-binding growth factors.* Acta Biomater, 2014. **10**(10): p. 4377-89.

50. Niemeyer, P., et al., *Transplantation of human mesenchymal stem cells in a non-autogenous setting for bone regeneration in a rabbit critical-size defect model.* Acta Biomater, 2010. **6**(3): p. 900-8.

51. Seebach, C., et al., *Endothelial progenitor cells and mesenchymal stem cells seeded onto beta-TCP granules enhance early vascularization and bone healing in a critical-sized bone defect in rats.* Tissue Eng Part A, 2010. **16**(6): p. 1961-70.

52. Zou, D., et al., *Repair of critical-sized rat calvarial defects using genetically engineered bone marrow-derived mesenchymal stem cells overexpressing hypoxia-inducible factor-1alpha.* Stem Cells, 2011. **29**(9): p. 1380-90.

53. Niemeyer, P., et al., *Comparison of mesenchymal stem cells from bone marrow and adipose tissue for bone regeneration in a critical size defect of the sheep tibia and the influence of platelet-rich plasma.* Biomaterials, 2010. **31**(13): p. 3572-9.

54. Dickson, K.F., S. Katzman, and G. Paiement, *The importance of the blood supply in the healing of tibial fractures.* Contemp Orthop, 1995. **30**(6): p. 489-93.

55. Lu, C., et al., *Ischemia leads to delayed union during fracture healing: a mouse model.* J Orthop Res, 2007. **25**(1): p. 51-61.

56. Becquart, P., et al., *Ischemia is the prime but not the only cause of human multipotent stromal cell death in tissue-engineered constructs in vivo.* Tissue Eng Part A, 2012. **18**(19-20): p. 2084-94.

57. Degano, I.R., et al., *Bioluminescence imaging of calvarial bone repair using bone marrow and adipose tissue-derived mesenchymal stem cells.* Biomaterials, 2008. **29**(4): p. 427-37.

58. Allen, A.B., et al., *In vivo bioluminescent tracking of mesenchymal stem cells within large hydrogel constructs.* Tissue Eng Part C Methods, 2014. **20**(10): p. 806-16.

59. Bian, L., et al., *Enhanced MSC chondrogenesis following delivery of TGF-beta3 from alginate microspheres within hyaluronic acid hydrogels in vitro and in vivo.* Biomaterials, 2011. **32**(27): p. 6425-34.

60. Park, H., et al., *Injectable biodegradable hydrogel composites for rabbit marrow mesenchymal stem cell and growth factor delivery for cartilage tissue engineering.* Biomaterials, 2007. **28**(21): p. 3217-27.

61. Kim, M., et al., *Transient exposure to TGF-beta3 improves the functional chondrogenesis of MSC-laden hyaluronic acid hydrogels.* J Mech Behav Biomed Mater, 2012. **11**: p. 92-101.

62. Kim, H., et al., *In vivo bone formation by human marrow stromal cells in biodegradable scaffolds that release dexamethasone and ascorbate-2-phosphate.* Biochem Biophys Res Commun, 2005. **332**(4): p. 1053-60.

63. Na, K., et al., *Osteogenic differentiation of rabbit mesenchymal stem cells in thermo-reversible hydrogel constructs containing hydroxyapatite and bone morphogenic protein-2 (BMP-2).* Biomaterials, 2007. **28**(16): p. 2631-7.

64. Nuttelman, C.R., M.C. Tripodi, and K.S. Anseth, *Dexamethasone-functionalized gels induce osteogenic differentiation of encapsulated hMSCs.* J Biomed Mater Res A, 2006. **76**(1): p. 183-95.

65. Martino, M.M., et al., *Engineering the growth factor microenvironment with fibronectin domains to promote wound and bone tissue healing.* Sci Transl Med, 2011. **3**(100): p. 100ra89.

66. Engler, A.J., et al., *Matrix elasticity directs stem cell lineage specification.* Cell, 2006. **126**(4): p. 677-89.

67. Discher, D.E., D.J. Mooney, and P.W. Zandstra, *Growth factors, matrices, and forces combine and control stem cells.* Science, 2009. **324**(5935): p. 1673-7.

68. Boonen, K.J., et al., *Essential environmental cues from the satellite cell niche: optimizing proliferation and differentiation.* Am J Physiol Cell Physiol, 2009. **296**(6): p. C1338-45.

69. Garcia, J.R. and A.J. Garcia, *Cellular mechanotransduction: sensing rigidity.* Nat Mater, 2014. **13**(6): p. 539-40.

70. Elosegui-Artola, A., et al., *Rigidity sensing and adaptation through regulation of integrin types.* Nat Mater, 2014. **13**(6): p. 631-7.

71. del Rio, A., et al., *Stretching single talin rod molecules activates vinculin binding.* Science, 2009. **323**(5914): p. 638-41.

72. Dumbauld, D.W., et al., *How vinculin regulates force transmission.* Proc Natl Acad Sci U S A, 2013. **110**(24): p. 9788-93.

73. Folkman, J. and A. Moscona, *Role of cell shape in growth control.* Nature, 1978. **273**(5661): p. 345-9.

74. Chen, C.S., et al., *Geometric control of cell life and death.* Science, 1997. **276**(5317): p. 1425-8.

75. Chen, C.S., et al., *Micropatterned surfaces for control of cell shape, position, and function.* Biotechnol Prog, 1998. **14**(3): p. 356-63.

76. Andersson, A.S., et al., *The effects of continuous and discontinuous groove edges on cell shape and alignment.* Exp Cell Res, 2003. **288**(1): p. 177-88.

77. Stevens, M.M. and J.H. George, *Exploring and engineering the cell surface interface.* Science, 2005. **310**(5751): p. 1135-8.

78. McBeath, R., et al., *Cell shape, cytoskeletal tension, and RhoA regulate stem cell lineage commitment.* Dev Cell, 2004. **6**(4): p. 483-95.

79. Dalby, M.J., et al., *The control of human mesenchymal cell differentiation using nanoscale symmetry and disorder.* Nat Mater, 2007. **6**(12): p. 997-1003.

80. Humphries, M.J., *Integrin structure.* Biochem Soc Trans, 2000. **28**(4): p. 311-39.

81. Hynes, R.O., *Integrins: bidirectional, allosteric signaling machines.* Cell, 2002. **110**(6): p. 673-87.

82. Kling, D., J. Fingerle, and J.M. Harlan, *Inhibition of leukocyte extravasation with a monoclonal antibody to CD18 during formation of experimental intimal thickening in rabbit carotid arteries.* Arterioscler Thromb, 1992. **12**(9): p. 997-1007.

83. Schenkel, A.R., Z. Mamdouh, and W.A. Muller, *Locomotion of monocytes on endothelium is a critical step during extravasation.* Nat Immunol, 2004. **5**(4): p. 393-400.

84. Plow, E.F., et al., *Ligand binding to integrins.* J Biol Chem, 2000. **275**(29): p. 21785-8.

85. Bershadsky, A.D., N.Q. Balaban, and B. Geiger, *Adhesion-dependent cell mechanosensitivity.* Annu Rev Cell Dev Biol, 2003. **19**: p. 677-95.

86. Qin, J., O. Vinogradova, and E.F. Plow, *Integrin bidirectional signaling: a molecular view.* PLoS Biol, 2004. **2**(6): p. e169.

87. Law, D.A., L. Nannizzi-Alaimo, and D.R. Phillips, *Outside-in integrin signal transduction. Alpha IIb beta 3-(GP IIb IIIa) tyrosine phosphorylation induced by platelet aggregation.* J Biol Chem, 1996. **271**(18): p. 10811-5.

88. Miranti, C.K. and J.S. Brugge, *Sensing the environment: a historical perspective on integrin signal transduction.* Nat Cell Biol, 2002. **4**(4): p. E83-90.

89. Shimaoka, M., J. Takagi, and T.A. Springer, *Conformational regulation of integrin structure and function.* Annu Rev Biophys Biomol Struct, 2002. **31**: p. 485-516.

90. Giancotti, F.G. and E. Ruoslahti, *Integrin signaling.* Science, 1999. **285**(5430): p. 1028-32.

91. Tran, H., et al., *Integrin clustering induces kinectin accumulation.* J Cell Sci, 2002. **115**(Pt 10): p. 2031-40.

92. Calderwood, D.A., S.J. Shattil, and M.H. Ginsberg, *Integrins and actin filaments: reciprocal regulation of cell adhesion and signaling.* J Biol Chem, 2000. **275**(30): p. 22607-10.

93. Carisey, A. and C. Ballestrem, *Vinculin, an adapter protein in control of cell adhesion signalling.* Eur J Cell Biol, 2011. **90**(2-3): p. 157-63.

94. Katsumi, A., et al., *Integrins in mechanotransduction.* J Biol Chem, 2004. **279**(13): p. 12001-4.

95. Goksoy, E., et al., *Structural basis for the autoinhibition of talin in regulating integrin activation.* Mol Cell, 2008. **31**(1): p. 124-33.

96. Moser, M., et al., *The tail of integrins, talin, and kindlins.* Science, 2009. **324**(5929): p. 895-9.

97. Tadokoro, S., et al., *Talin binding to integrin beta tails: a final common step in integrin activation.* Science, 2003. **302**(5642): p. 103-6.

98. Moser, M., et al., *Kindlin-3 is essential for integrin activation and platelet aggregation.* Nat Med, 2008. **14**(3): p. 325-30.

99. Li, H., et al., *Structural basis of kindlin-mediated integrin recognition and activation.* Proc Natl Acad Sci U S A, 2017. **114**(35): p. 9349-9354.

100. Das, M., et al., *Mechanisms of talin-dependent integrin signaling and crosstalk.* Biochim Biophys Acta, 2014. **1838**(2): p. 579-88.

101. Vial, D. and P.J. McKeown-Longo, *Epidermal growth factor (EGF) regulates alpha5beta1 integrin activation state in human cancer cell lines through the p90RSK-dependent phosphorylation of filamin A.* J Biol Chem, 2012. **287**(48): p. 40371-80.

102. Ridley, A.J. and A. Hall, *The small GTP-binding protein rho regulates the assembly of focal adhesions and actin stress fibers in response to growth factors.* Cell, 1992. **70**(3): p. 389-99.

103. Beauvais, D.M. and A.C. Rapraeger, *Syndecan-1 couples the insulin-like growth factor-1 receptor to inside-out integrin activation.* J Cell Sci, 2010. **123**(Pt 21): p. 3796-807.

104. Li, Q., et al., *Reinforcement of integrin-mediated T-Lymphocyte adhesion by TNF-induced Inside-out Signaling.* Sci Rep, 2016. **6**: p. 30452.

105. Somanath, P.R., N.L. Malinin, and T.V. Byzova, *Cooperation between integrin alphavbeta3 and VEGFR2 in angiogenesis.* Angiogenesis, 2009. **12**(2): p. 177-85.

106. De, S., et al., *VEGF-integrin interplay controls tumor growth and vascularization.* Proc Natl Acad Sci U S A, 2005. **102**(21): p. 7589-94.

107. Soldi, R., et al., *Role of alphavbeta3 integrin in the activation of vascular endothelial growth factor receptor-2.* EMBO J, 1999. **18**(4): p. 882-92.

108. Borges, E., Y. Jan, and E. Ruoslahti, *Platelet-derived growth factor receptor beta and vascular endothelial growth factor receptor 2 bind to the beta 3 integrin through its extracellular domain.* J Biol Chem, 2000. **275**(51): p. 39867-73.

109. Garces, C.A., et al., *Vascular endothelial growth factor receptor-3 and focal adhesion kinase bind and suppress apoptosis in breast cancer cells.* Cancer Res, 2006. **66**(3): p. 1446-54.

110. Farris, A.L., A.N. Rindone, and W.L. Grayson, *Oxygen Delivering Biomaterials for Tissue Engineering.* J Mater Chem B, 2016. **4**(20): p. 3422-3432.

111. Li, Z., X. Guo, and J. Guan, *An oxygen release system to augment cardiac progenitor cell survival and differentiation under hypoxic condition.* Biomaterials, 2012. **33**(25): p. 5914-23.

112. Ma, T., et al., *The effect of synthetic oxygen carrier-enriched fibrin hydrogel on Schwann cells under hypoxia condition in vitro.* Biomaterials, 2013. **34**(38): p. 10016-27.

113. Pedraza, E., et al., *Preventing hypoxia-induced cell death in beta cells and islets via hydrolytically activated, oxygen-generating biomaterials.* Proc Natl Acad Sci U S A, 2012. **109**(11): p. 4245-50.

114. Kimelman-Bleich, N., et al., *The use of a synthetic oxygen carrier-enriched hydrogel to enhance mesenchymal stem cell-based bone formation in vivo.* Biomaterials, 2009. **30**(27): p. 4639-48.

115. Bai, Y., et al., *Localized delivery of growth factors for angiogenesis and bone formation in tissue engineering.* Int Immunopharmacol, 2013. **16**(2): p. 214-23.

116. Ferrara, N., H.P. Gerber, and J. LeCouter, *The biology of VEGF and its receptors.* Nat Med, 2003. **9**(6): p. 669-76.

117. Street, J., et al., *Vascular endothelial growth factor stimulates bone repair by promoting angiogenesis and bone turnover.* Proc Natl Acad Sci U S A, 2002. **99**(15): p. 9656-61.

118. Ozawa, C.R., et al., *Microenvironmental VEGF concentration, not total dose, determines a threshold between normal and aberrant angiogenesis.* J Clin Invest, 2004. **113**(4): p. 516-27.

119. Karvinen, H., et al., *Long-term VEGF-A expression promotes aberrant angiogenesis and fibrosis in skeletal muscle.* Gene Ther, 2011. **18**(12): p. 1166-72.

120. Wernike, E., et al., *VEGF incorporated into calcium phosphate ceramics promotes vascularisation and bone formation in vivo.* Eur Cell Mater, 2010. **19**: p. 30-40.

121. Leach, J.K., et al., *Coating of VEGF-releasing scaffolds with bioactive glass for angiogenesis and bone regeneration.* Biomaterials, 2006. **27**(17): p. 3249-55.

122. Bao, P., et al., *The role of vascular endothelial growth factor in wound healing.* J Surg Res, 2009. **153**(2): p. 347-58.

123. Ravanti, L. and V.M. Kahari, *Matrix metalloproteinases in wound repair (review).* Int J Mol Med, 2000. **6**(4): p. 391-407.

124. Lutolf, M.P., et al., *Repair of bone defects using synthetic mimetics of collagenous extracellular matrices.* Nat Biotechnol, 2003. **21**(5): p. 513-8.

125. Mariner, P.D., et al., *Synthetic hydrogel scaffold is an effective vehicle for delivery of INFUSE (rhBMP2) to critical-sized calvaria bone defects in rats.* J Orthop Res, 2013. **31**(3): p. 401-6.

126. Zisch, A.H., et al., *Cell-demanded release of VEGF from synthetic, biointeractive cell ingrowth matrices for vascularized tissue growth.* FASEB J, 2003. **17**(15): p. 2260-2.

127. Lee, T.T., et al., *Light-triggered in vivo activation of adhesive peptides regulates cell adhesion, inflammation and vascularization of biomaterials.* Nat Mater, 2014.

128. Leslie-Barbick, J.E., J.J. Moon, and J.L. West, *Covalently-immobilized vascular endothelial growth factor promotes endothelial cell tubulogenesis in poly(ethylene glycol) diacrylate hydrogels.* J Biomater Sci Polym Ed, 2009. **20**(12): p. 1763-79.

129. Phelps, E.A., et al., *Bioartificial matrices for therapeutic vascularization.* Proc Natl Acad Sci U S A, 2010. **107**(8): p. 3323-8.

130. Salimath, A.S., et al., *Dual delivery of hepatocyte and vascular endothelial growth factors via a protease-degradable hydrogel improves cardiac function in rats.* PLoS One, 2012. **7**(11): p. e50980.

131. Phelps, E.A., et al., *Vasculogenic bio-synthetic hydrogel for enhancement of pancreatic islet engraftment and function in type 1 diabetes.* Biomaterials, 2013. **34**(19): p. 4602-11.

132. Zieris, A., et al., *FGF-2 and VEGF functionalization of starPEG-heparin hydrogels to modulate biomolecular and physical cues of angiogenesis.* Biomaterials, 2010. **31**(31): p. 7985-94.

133. Fujita, M., et al., *Vascularization in vivo caused by the controlled release of fibroblast growth factor-2 from an injectable chitosan/non-anticoagulant heparin hydrogel.* Biomaterials, 2004. **25**(4): p. 699-706.

134. Hettiaratchi, M.H., et al., *Heparin microparticle effects on presentation and bioactivity of bone morphogenetic protein-2.* Biomaterials, 2014. **35**(25): p. 7228-38.

135. Freeman, I., A. Kedem, and S. Cohen, *The effect of sulfation of alginate hydrogels on the specific binding and controlled release of heparin-binding proteins.* Biomaterials, 2008. **29**(22): p. 3260-8.

136. Martino, M.M., et al., *Growth factors engineered for super-affinity to the extracellular matrix enhance tissue healing.* Science, 2014. **343**(6173): p. 885-8.

137. Tayalia, P. and D.J. Mooney, *Controlled growth factor delivery for tissue engineering.* Adv Mater, 2009. **21**(32-33): p. 3269-85.

138. Nguyen, T.H., et al., *A heparin-mimicking polymer conjugate stabilizes basic fibroblast growth factor.* Nat Chem, 2013. **5**(3): p. 221-7.

139. McCall, J.D., J.E. Luoma, and K.S. Anseth, *Covalently tethered transforming growth factor beta in PEG hydrogels promotes chondrogenic differentiation of encapsulated human mesenchymal stem cells.* Drug Deliv Transl Res, 2012. **2**(5): p. 305-312.

140. Hood, J.D., et al., *Differential alphav integrin-mediated Ras-ERK signaling during two pathways of angiogenesis.* J Cell Biol, 2003. **162**(5): p. 933-43.

141. Mizuno, M., R. Fujisawa, and Y. Kuboki, *Type I collagen-induced osteoblastic differentiation of bone-marrow cells mediated by collagen-alpha2beta1 integrin interaction.* J Cell Physiol, 2000. **184**(2): p. 207-13.

142. Pierschbacher, M.D. and E. Ruoslahti, *Cell attachment activity of fibronectin can be duplicated by small synthetic fragments of the molecule.* Nature, 1984. **309**(5963): p. 30-3.

143. Emsley, J., et al., *Structure of the integrin alpha2beta1-binding collagen peptide.* J Mol Biol, 2004. **335**(4): p. 1019-28.

144. Reyes, C.D. and A.J. Garcia, *Engineering integrin-specific surfaces with a triple-helical collagen-mimetic peptide.* J Biomed Mater Res A, 2003. **65**(4): p. 511-23.

145. Sephel, G.C., et al., *Laminin A chain synthetic peptide which supports neurite outgrowth.* Biochem Biophys Res Commun, 1989. **162**(2): p. 821-9.

146. Wojtowicz, A.M., et al., *Coating of biomaterial scaffolds with the collagen-mimetic peptide GFOGER for bone defect repair.* Biomaterials, 2010. **31**(9): p. 2574-82.

147. Brooks, P.C., R.A. Clark, and D.A. Cheresh, *Requirement of vascular integrin alpha v beta 3 for angiogenesis.* Science, 1994. **264**(5158): p. 569-71.

148. Sipkins, D.A., et al., *Detection of tumor angiogenesis in vivo by alphaVbeta3-targeted magnetic resonance imaging.* Nat Med, 1998. **4**(5): p. 623-6.

149. Mullamitha, S.A., et al., *Phase I evaluation of a fully human anti-alphav integrin monoclonal antibody (CNTO 95) in patients with advanced solid tumors.* Clin Cancer Res, 2007. **13**(7): p. 2128-35.

150. Gutheil, J.C., et al., *Targeted antiangiogenic therapy for cancer using Vitaxin: a humanized monoclonal antibody to the integrin alphavbeta3.* Clin Cancer Res, 2000. **6**(8): p. 3056-61.

151. Mahabeleshwar, G.H., et al., *Mechanisms of integrin-vascular endothelial growth factor receptor cross-activation in angiogenesis.* Circ Res, 2007. **101**(6): p. 570-80.

152. Caplan, A.I., *Adult mesenchymal stem cells for tissue engineering versus regenerative medicine.* J Cell Physiol, 2007. **213**(2): p. 341-7.

153. Toma, C., et al., *Human mesenchymal stem cells differentiate to a cardiomyocyte phenotype in the adult murine heart.* Circulation, 2002. **105**(1): p. 93-8.

154. Oswald, J., et al., *Mesenchymal stem cells can be differentiated into endothelial cells in vitro.* Stem Cells, 2004. **22**(3): p. 377-84.

155. Baraniak, P.R. and T.C. McDevitt, *Stem cell paracrine actions and tissue regeneration.* Regen Med, 2010. **5**(1): p. 121-43.

156. Taguchi, K., et al., *The role of bone marrow-derived cells in bone fracture repair in a green fluorescent protein chimeric mouse model.* Biochem Biophys Res Commun, 2005. **331**(1): p. 31-6.

157. Gebler, A., O. Zabel, and B. Seliger, *The immunomodulatory capacity of mesenchymal stem cells.* Trends Mol Med, 2012. **18**(2): p. 128-34.

158. Ma, S., et al., *Immunobiology of mesenchymal stem cells.* Cell Death Differ, 2014. **21**(2): p. 216-25.

159. Kean, T.J., et al., *MSCs: Delivery Routes and Engraftment, Cell-Targeting Strategies, and Immune Modulation.* Stem Cells Int, 2013. **2013**: p. 732742.

160. Taylor, M.W. and G.S. Feng, *Relationship between interferon-gamma, indoleamine 2,3-dioxygenase, and tryptophan catabolism.* FASEB J, 1991. **5**(11): p. 2516-22.

161. Shimizu, T., et al., *Indoleamine 2,3-dioxygenase. Purification and some properties.* J Biol Chem, 1978. **253**(13): p. 4700-6.

162. Hwu, P., et al., *Indoleamine 2,3-dioxygenase production by human dendritic cells results in the inhibition of T cell proliferation.* J Immunol, 2000. **164**(7): p. 3596-9.

163. Munn, D.H., et al., *Potential regulatory function of human dendritic cells expressing indoleamine 2,3-dioxygenase.* Science, 2002. **297**(5588): p. 1867-70.

164. Meisel, R., et al., *Human bone marrow stromal cells inhibit allogeneic T-cell responses by indoleamine 2,3-dioxygenase-mediated tryptophan degradation.* Blood, 2004. **103**(12): p. 4619-21.

165. Glennie, S., et al., *Bone marrow mesenchymal stem cells induce division arrest anergy of activated T cells.* Blood, 2005. **105**(7): p. 2821-7.

166. Di Nicola, M., et al., *Human bone marrow stromal cells suppress T-lymphocyte proliferation induced by cellular or nonspecific mitogenic stimuli.* Blood, 2002. **99**(10): p. 3838-43.

167. Yang, S.H., et al., *Soluble mediators from mesenchymal stem cells suppress T cell proliferation by inducing IL-10.* Exp Mol Med, 2009. **41**(5): p. 315-24.

168. Spaggiari, G.M., et al., *Mesenchymal stem cells inhibit natural killer-cell proliferation, cytotoxicity, and cytokine production: role of indoleamine 2,3-dioxygenase and prostaglandin E2.* Blood, 2008. **111**(3): p. 1327-33.

169. Ren, G., et al., *Mesenchymal stem cell-mediated immunosuppression occurs via concerted action of chemokines and nitric oxide.* Cell Stem Cell, 2008. **2**(2): p. 141-50.

170. Sato, K., et al., *Nitric oxide plays a critical role in suppression of T-cell proliferation by mesenchymal stem cells.* Blood, 2007. **109**(1): p. 228-34.

171. Su, J., et al., *Phylogenetic distinction of iNOS and IDO function in mesenchymal stem cell-mediated immunosuppression in mammalian species.* Cell Death Differ, 2014. **21**(3): p. 388-96.

172. Krampera, M., et al., *Role for interferon-gamma in the immunomodulatory activity of human bone marrow mesenchymal stem cells.* Stem Cells, 2006. **24**(2): p. 386-98.

173. Ryan, J.M., et al., *Interferon-gamma does not break, but promotes the immunosuppressive capacity of adult human mesenchymal stem cells.* Clin Exp Immunol, 2007. **149**(2): p. 353-63.

174. Chinnadurai, R., et al., *IDO-independent suppression of T cell effector function by IFN-gamma-licensed human mesenchymal stromal cells.* J Immunol, 2014. **192**(4): p. 1491-501.

175. Francois, M., et al., *Human MSC suppression correlates with cytokine induction of indoleamine 2,3-dioxygenase and bystander M2 macrophage differentiation.* Mol Ther, 2012. **20**(1): p. 187-95.

176. Kalinski, P., *Regulation of immune responses by prostaglandin E2.* J Immunol, 2012. **188**(1): p. 21-8.

177. Wang, D. and R.N. Dubois, *Prostaglandins and cancer.* Gut, 2006. **55**(1): p. 115-22.

178. Nakanishi, M. and D.W. Rosenberg, *Multifaceted roles of PGE2 in inflammation and cancer.* Semin Immunopathol, 2013. **35**(2): p. 123-37.

179. Kozak, K.R., et al., *Metabolism of prostaglandin glycerol esters and prostaglandin ethanolamides in vitro and in vivo.* J Biol Chem, 2001. **276**(40): p. 36993-8.

180. Sugimoto, Y. and S. Narumiya, *Prostaglandin E receptors.* J Biol Chem, 2007. **282**(16): p. 11613-7.

181. Chen, K., et al., *Human umbilical cord mesenchymal stem cells hUC-MSCs exert immunosuppressive activities through a PGE2-dependent mechanism.* Clin Immunol, 2010. **135**(3): p. 448-58.

182. Hegyi, B., et al., *Activated T-cells and pro-inflammatory cytokines differentially regulate prostaglandin E2 secretion by mesenchymal stem cells.* Biochem Biophys Res Commun, 2012. **419**(2): p. 215-20.

183. Hsu, W.T., et al., *Prostaglandin E2 potentiates mesenchymal stem cell-induced IL-10+IFN-gamma+CD4+ regulatory T cells to control transplant arteriosclerosis.* J Immunol, 2013. **190**(5): p. 2372-80.

184. Duffy, M.M., et al., *Mesenchymal stem cell inhibition of T-helper 17 cell-differentiation is triggered by cell-cell contact and mediated by prostaglandin E2 via the EP4 receptor.* Eur J Immunol, 2011. **41**(10): p. 2840-51.

185. Sotiropoulou, P.A., et al., *Interactions between human mesenchymal stem cells and natural killer cells.* Stem Cells, 2006. **24**(1): p. 74-85.

186. Spaggiari, G.M., et al., *MSCs inhibit monocyte-derived DC maturation and function by selectively interfering with the generation of immature DCs: central role of MSC-derived prostaglandin E2.* Blood, 2009. **113**(26): p. 6576-83.

187. Brandau, S., et al., *Tissue-resident mesenchymal stem cells attract peripheral blood neutrophils and enhance their inflammatory activity in response to microbial challenge.* J Leukoc Biol, 2010. **88**(5): p. 1005-15.

188. Jiang, X.X., et al., *Human mesenchymal stem cells inhibit differentiation and function of monocyte-derived dendritic cells.* Blood, 2005. **105**(10): p. 4120-6.

189. Nauta, A.J., et al., *Mesenchymal stem cells inhibit generation and function of both CD34+-derived and monocyte-derived dendritic cells.* J Immunol, 2006. **177**(4): p. 2080-7.

190. Deng, Y., et al., *Umbilical Cord-derived Mesenchymal Stem Cells Instruct Monocytes Towards an IL10-producing Phenotype by Secreting IL6 and HGF*. Sci Rep, 2016. **6**: p. 37566.

191. Ushach, I. and A. Zlotnik, *Biological role of granulocyte macrophage colony-stimulating factor (GM-CSF) and macrophage colony-stimulating factor (M-CSF) on cells of the myeloid lineage.* J Leukoc Biol, 2016. **100**(3): p. 481-9.

192. Italiani, P. and D. Boraschi, *From Monocytes to M1/M2 Macrophages: Phenotypical vs. Functional Differentiation.* Front Immunol, 2014. **5**: p. 514.

193. Hamilton, J.A., *Colony-stimulating factors in inflammation and autoimmunity.* Nat Rev Immunol, 2008. **8**(7): p. 533-44.

194. Haynesworth, S.E., M.A. Baber, and A.I. Caplan, *Cytokine expression by human marrow-derived mesenchymal progenitor cells in vitro: effects of dexamethasone and IL-1 alpha.* J Cell Physiol, 1996. **166**(3): p. 585-92.

195. Rafei, M., et al., *Mesenchymal stromal cell-derived CCL2 suppresses plasma cell immunoglobulin production via STAT3 inactivation and PAX5 induction.* Blood, 2008. **112**(13): p. 4991-8.

196. Krampera, M., et al., *Bone marrow mesenchymal stem cells inhibit the response of naive and memory antigen-specific T cells to their cognate peptide.* Blood, 2003. **101**(9): p. 3722-9.

197. Selmani, Z., et al., *Human leukocyte antigen-G5 secretion by human mesenchymal stem cells is required to suppress T lymphocyte and natural killer function and to induce CD4+CD25highFOXP3+ regulatory T cells.* Stem Cells, 2008. **26**(1): p. 212-22.

198. Sheng, H., et al., *A critical role of IFNgamma in priming MSC-mediated suppression of T cell proliferation through up-regulation of B7-H1*. Cell Res, 2008. **18**(8): p. 846-57.

199. Cras, A., et al., *Update on mesenchymal stem cell-based therapy in lupus and scleroderma.* Arthritis Res Ther, 2015. **17**: p. 301.

200. He, X.W., et al., *Systemic infusion of bone marrow-derived mesenchymal stem cells for treatment of experimental colitis in mice.* Dig Dis Sci, 2012. **57**(12): p. 3136-44.

201. Gao, F., et al., *Mesenchymal stem cells and immunomodulation: current status and future prospects.* Cell Death Dis, 2016. **7**: p. e2062.

202. Liang, L., et al., *Human umbilical cord mesenchymal stem cells ameliorate mice trinitrobenzene sulfonic acid (TNBS)-induced colitis.* Cell Transplant, 2011. **20**(9): p. 1395-408.

203. Gonzalez, M.A., et al., *Treatment of experimental arthritis by inducing immune tolerance with human adipose-derived mesenchymal stem cells.* Arthritis Rheum, 2009. **60**(4): p. 1006-19.

204. Jurewicz, M., et al., *Congenic mesenchymal stem cell therapy reverses hyperglycemia in experimental type 1 diabetes.* Diabetes, 2010. **59**(12): p. 3139-47.

205. Amorin, B., et al., *Mesenchymal stem cell therapy and acute graft-versus-host disease: a review.* Hum Cell, 2014. **27**(4): p. 137-50.

206. Zeiser, R. and B.R. Blazar, *Acute Graft-versus-Host Disease - Biologic Process, Prevention, and Therapy.* N Engl J Med, 2017. **377**(22): p. 2167-2179.

207. Le Blanc, K., et al., *Mesenchymal stem cells for treatment of steroid-resistant, severe, acute graft-versus-host disease: a phase II study.* Lancet, 2008. **371**(9624): p. 1579-86.

208. Resnick, I.B., et al., *Treatment of severe steroid resistant acute GVHD with mesenchymal stromal cells (MSC).* Am J Blood Res, 2013. **3**(3): p. 225-38.

209. Introna, M., et al., *Treatment of graft versus host disease with mesenchymal stromal cells: a phase I study on 40 adult and pediatric patients.* Biol Blood Marrow Transplant, 2014. **20**(3): p. 375-81.

210. Galipeau, J., *The mesenchymal stromal cells dilemma--does a negative phase III trial of random donor mesenchymal stromal cells in steroid-resistant graft-versus-host disease represent a death knell or a bump in the road?* Cytotherapy, 2013. **15**(1): p. 2-8.

211. Lightner, A.L., *Stem Cell Therapy for Inflammatory Bowel Disease.* Clin Transl Gastroenterol, 2017. **8**(3): p. e82.

212. Dalal, J., K. Gandy, and J. Domen, *Role of mesenchymal stem cell therapy in Crohn's disease.* Pediatr Res, 2012. **71**(4 Pt 2): p. 445-51.

213. Duijvestein, M., et al., *Autologous bone marrow-derived mesenchymal stromal cell treatment for refractory luminal Crohn's disease: results of a phase I study.* Gut, 2010. **59**(12): p. 1662-9.

214. Forbes, G.M., et al., *A phase 2 study of allogeneic mesenchymal stromal cells for luminal Crohn's disease refractory to biologic therapy.* Clin Gastroenterol Hepatol, 2014. **12**(1): p. 64-71.

215. Panes, J., et al., *Expanded allogeneic adipose-derived mesenchymal stem cells (Cx601) for complex perianal fistulas in Crohn's disease: a phase 3 randomised, double-blind controlled trial.* Lancet, 2016. **388**(10051): p. 1281-90.

216. Polchert, D., et al., *IFN-gamma activation of mesenchymal stem cells for treatment and prevention of graft versus host disease.* Eur J Immunol, 2008. **38**(6): p. 1745-55.

217. Ryu, D.B., et al., *Induction of Indoleamine 2,3-dioxygenase by Pre-treatment with Poly(I:C) May Enhance the Efficacy of MSC Treatment in DSS-induced Colitis.* Immune Netw, 2016. **16**(6): p. 358-365.

218. Fan, H., et al., *Pre-treatment with IL-1beta enhances the efficacy of MSC transplantation in DSS-induced colitis.* Cell Mol Immunol, 2012. **9**(6): p. 473-81.

219. Szabo, E., et al., *Licensing by Inflammatory Cytokines Abolishes Heterogeneity of Immunosuppressive Function of Mesenchymal Stem Cell Population.* Stem Cells Dev, 2015. **24**(18): p. 2171-80.

220. Zimmermann, J.A., M.H. Hettiaratchi, and T.C. McDevitt, *Enhanced Immunosuppression of T Cells by Sustained Presentation of Bioactive Interferon-gamma Within Three-Dimensional Mesenchymal Stem Cell Constructs.* Stem Cells Transl Med, 2017. **6**(1): p. 223-237.

221. Chen, Y., et al., *Gene delivery with IFN-gamma-expression plasmids enhances the therapeutic effects of MSCs on DSS-induced mouse colitis.* Inflamm Res, 2015. **64**(9): p. 671-81.

222. Garcia, J.R., A.Y. Clark, and A.J. Garcia, *Integrin-specific hydrogels functionalized with VEGF for vascularization and bone regeneration of critical-size bone defects.* J Biomed Mater Res A, 2016. **104**(7): p. 1845.

223. Rao, R.R. and J.P. Stegemann, *Cell-based approaches to the engineering of vascularized bone tissue.* Cytotherapy, 2013. **15**(11): p. 1309-22.

224. Nguyen, L.H., et al., *Vascularized bone tissue engineering: approaches for potential improvement.* Tissue Eng Part B Rev, 2012. **18**(5): p. 363-82.

225. Zhou, Z., et al., *Impaired endochondral ossification and angiogenesis in mice deficient in membrane-type matrix metalloproteinase I.* Proc Natl Acad Sci U S A, 2000. **97**(8): p. 4052-7.

226. Carano, R.A. and E.H. Filvaroff, *Angiogenesis and bone repair.* Drug Discov Today, 2003. **8**(21): p. 980-9.

227. Giannoudis, P.V., H. Dinopoulos, and E. Tsiridis, *Bone substitutes: an update.* Injury, 2005. **36 Suppl 3**: p. S20-7.

228. Finkemeier, C.G., *Bone-grafting and bone-graft substitutes.* J Bone Joint Surg Am, 2002. **84-A**(3): p. 454-464.

229. Frohlich, M., et al., *Tissue engineered bone grafts: biological requirements, tissue culture and clinical relevance.* Curr Stem Cell Res Ther, 2008. **3**(4): p. 254-64.

230. Patel, Z.S., et al., *Dual delivery of an angiogenic and an osteogenic growth factor for bone regeneration in a critical size defect model.* Bone, 2008. **43**(5): p. 931-40.

231. Young, S., et al., *Dose effect of dual delivery of vascular endothelial growth factor and bone morphogenetic protein-2 on bone regeneration in a rat critical-size defect model.* Tissue Eng Part A, 2009. **15**(9): p. 2347-62.

232. Hernandez, A., et al., *In vivo osteogenic response to different ratios of BMP-2 and VEGF released from a biodegradable porous system.* J Biomed Mater Res A, 2012. **100**(9): p. 2382-91.

233. Geuze, R.E., et al., *A differential effect of bone morphogenetic protein-2 and vascular endothelial growth factor release timing on osteogenesis at ectopic and orthotopic sites in a large-animal model.* Tissue Eng Part A, 2012. **18**(19-20): p. 2052-62.

234. De la Riva, B., et al., *Local controlled release of VEGF and PDGF from a combined brushite-chitosan system enhances bone regeneration.* J Control Release, 2010. **143**(1): p. 45-52.

235. Senger, D.R., et al., *The alpha(1)beta(1) and alpha(2)beta(1) integrins provide critical support for vascular endothelial growth factor signaling, endothelial cell migration, and tumor angiogenesis.* Am J Pathol, 2002. **160**(1): p. 195-204.

236. Senger, D.R., et al., *Angiogenesis promoted by vascular endothelial growth factor: regulation through alpha1beta1 and alpha2beta1 integrins.* Proc Natl Acad Sci U S A, 1997. **94**(25): p. 13612-7.

237. Silva, R., et al., *Integrins: the keys to unlocking angiogenesis.* Arterioscler Thromb Vasc Biol, 2008. **28**(10): p. 1703-13.

238. Liu, Z., F. Wang, and X. Chen, *Integrin alpha(v)beta(3)-Targeted Cancer Therapy.* Drug Dev Res, 2008. **69**(6): p. 329-339.

239. Buerkle, M.A., et al., *Inhibition of the alpha-nu integrins with a cyclic RGD peptide impairs angiogenesis, growth and metastasis of solid tumours in vivo.* Br J Cancer, 2002. **86**(5): p. 788-95.

240. Alghisi, G.C., L. Ponsonnet, and C. Ruegg, *The integrin antagonist cilengitide activates alphaVbeta3, disrupts VE-cadherin localization at cell junctions and enhances permeability in endothelial cells.* PLoS One, 2009. **4**(2): p. e4449.

241. Maubant, S., et al., *Blockade of alpha v beta3 and alpha v beta5 integrins by RGD mimetics induces anoikis and not integrin-mediated death in human endothelial cells.* Blood, 2006. **108**(9): p. 3035-44.

242. Brooks, P.C., et al., *Integrin alpha v beta 3 antagonists promote tumor regression by inducing apoptosis of angiogenic blood vessels.* Cell, 1994. **79**(7): p. 1157-64.

243. Danhier, F., A. Le Breton, and V. Preat, *RGD-based strategies to target alpha(v) beta(3) integrin in cancer therapy and diagnosis.* Mol Pharm, 2012. **9**(11): p. 2961-73.

244. Reyes, C.D. and A.J. Garcia, *Alpha2beta1 integrin-specific collagen-mimetic surfaces supporting osteoblastic differentiation.* J Biomed Mater Res A, 2004. **69**(4): p. 591-600.

245. Reyes, C.D., et al., *Biomolecular surface coating to enhance orthopaedic tissue healing and integration.* Biomaterials, 2007. **28**(21): p. 3228-35.

246. Shekaran, A., et al., *Bone regeneration using an alpha 2 beta 1 integrin-specific hydrogel as a BMP-2 delivery vehicle.* Biomaterials, 2014. **35**(21): p. 5453-61.

247. Phelps, E.A., et al., *Engineered VEGF-releasing PEG-MAL hydrogel for pancreatic islet vascularization.* Drug Deliv Transl Res, 2015. **5**(2): p. 125-36.

248. dela Paz, N.G. and P.A. D'Amore, *Arterial versus venous endothelial cells.* Cell Tissue Res, 2009. **335**(1): p. 5-16.

249. Gnecchi, M., et al., *Paracrine mechanisms in adult stem cell signaling and therapy.* Circ Res, 2008. **103**(11): p. 1204-19.

250. Kumar, S., et al., *Mesenchymal stem cells expressing osteogenic and angiogenic factors synergistically enhance bone formation in a mouse model of segmental bone defect.* Mol Ther, 2010. **18**(5): p. 1026-34.

251. Wang, X., et al., *Role of mesenchymal stem cells in bone regeneration and fracture repair: a review.* Int Orthop, 2013. **37**(12): p. 2491-8.

252. Kretlow, J.D. and A.G. Mikos, *Review: mineralization of synthetic polymer scaffolds for bone tissue engineering.* Tissue Eng, 2007. **13**(5): p. 927-38.

253. Krishnan, L., N.J. Willett, and R.E. Guldberg, *Vascularization strategies for bone regeneration.* Ann Biomed Eng, 2014. **42**(2): p. 432-44.

254. Avraamides, C.J., B. Garmy-Susini, and J.A. Varner, *Integrins in angiogenesis and lymphangiogenesis.* Nat Rev Cancer, 2008. **8**(8): p. 604-17.

255. Frokjaer, S. and D.E. Otzen, *Protein drug stability: a formulation challenge.* Nat Rev Drug Discov, 2005. **4**(4): p. 298-306.

256. Steiner, D., et al., *Effects of endothelial cells on proliferation and survival of human mesenchymal stem cells and primary osteoblasts.* J Orthop Res, 2012. **30**(10): p. 1682-9.

257. Grellier, M., et al., *The effect of the co-immobilization of human osteoprogenitors and endothelial cells within alginate microspheres on mineralization in a bone defect.* Biomaterials, 2009. **30**(19): p. 3271-8.

258. Grellier, M., et al., *Role of vascular endothelial growth factor in the communication between human osteoprogenitors and endothelial cells.* J Cell Biochem, 2009. **106**(3): p. 390-8.

259. Robinson, S.D. and K.M. Hodivala-Dilke, *The role of beta3-integrins in tumor angiogenesis: context is everything.* Curr Opin Cell Biol, 2011. **23**(5): p. 630-7.

260. Reynolds, L.E., et al., *Enhanced pathological angiogenesis in mice lacking beta3 integrin or beta3 and beta5 integrins.* Nat Med, 2002. **8**(1): p. 27-34.

261. Mahabeleshwar, G.H., et al., *Integrin signaling is critical for pathological angiogenesis.* J Exp Med, 2006. **203**(11): p. 2495-507.

262. Kaur, S., et al., *{beta}3-integrin expression on tumor cells inhibits tumor progression, reduces metastasis, and is associated with a favorable prognosis in patients with ovarian cancer.* Am J Pathol, 2009. **175**(5): p. 2184-96.

263. Masson-Gadais, B., et al., *Integrin alphavbeta3, requirement for VEGFR2-mediated activation of SAPK2/p38 and for Hsp90-dependent phosphorylation of focal adhesion kinase in endothelial cells activated by VEGF.* Cell Stress Chaperones, 2003. **8**(1): p. 37-52.

264. Maes, C., et al., *Impaired angiogenesis and endochondral bone formation in mice lacking the vascular endothelial growth factor isoforms VEGF164 and VEGF188.* Mech Dev, 2002. **111**(1-2): p. 61-73.

265. Kaigler, D., et al., *VEGF scaffolds enhance angiogenesis and bone regeneration in irradiated osseous defects.* J Bone Miner Res, 2006. **21**(5): p. 735-44.

266. Kempen, D.H., et al., *Effect of local sequential VEGF and BMP-2 delivery on ectopic and orthotopic bone regeneration.* Biomaterials, 2009. **30**(14): p. 2816-25.

267. Bruder, S.P., D.J. Fink, and A.I. Caplan, *Mesenchymal stem cells in bone development, bone repair, and skeletal regeneration therapy.* J Cell Biochem, 1994. **56**(3): p. 283-94.

268. Aggarwal, S. and M.F. Pittenger, *Human mesenchymal stem cells modulate allogeneic immune cell responses.* Blood, 2005. **105**(4): p. 1815-22.

269. Wang, Y., et al., *Plasticity of mesenchymal stem cells in immunomodulation: pathological and therapeutic implications.* Nat Immunol, 2014. **15**(11): p. 1009-16.

270. Corcione, A., et al., *Human mesenchymal stem cells modulate B-cell functions.* Blood, 2006. **107**(1): p. 367-72.

271. Auletta, J.J., et al., *Human mesenchymal stromal cells attenuate graft-versus-host disease and maintain graft-versus-leukemia activity following experimental allogeneic bone marrow transplantation.* Stem Cells, 2015. **33**(2): p. 601-14.

272. Wang, X., et al., *Human ESC-derived MSCs outperform bone marrow MSCs in the treatment of an EAE model of multiple sclerosis.* Stem Cell Reports, 2014. **3**(1): p. 115-30.

273. Gonzalez, M.A., et al., *Adipose-derived mesenchymal stem cells alleviate experimental colitis by inhibiting inflammatory and autoimmune responses.* Gastroenterology, 2009. **136**(3): p. 978-89.

274. Lee, M.W., et al., *Strategies to improve the immunosuppressive properties of human mesenchymal stem cells.* Stem Cell Res Ther, 2015. **6**: p. 179.

275. Liang, C., et al., *Interferon-gamma mediates the immunosuppression of bone marrow mesenchymal stem cells on T-lymphocytes in vitro.* Hematology, 2018. **23**(1): p. 44-49.

276. Jin, P., et al., *Interferon-gamma and Tumor Necrosis Factor-alpha Polarize Bone Marrow Stromal Cells Uniformly to a Th1 Phenotype.* Sci Rep, 2016. **6**: p. 26345.

277. Bernardo, M.E. and W.E. Fibbe, *Mesenchymal stromal cells: sensors and switchers of inflammation.* Cell Stem Cell, 2013. **13**(4): p. 392-402.

278. Shi, Y., et al., *How mesenchymal stem cells interact with tissue immune responses.* Trends Immunol, 2012. **33**(3): p. 136-43.

279. Duijvestein, M., et al., *Pretreatment with interferon-gamma enhances the therapeutic activity of mesenchymal stromal cells in animal models of colitis.* Stem Cells, 2011. **29**(10): p. 1549-58.

280. Heathman, T.R., et al., *The translation of cell-based therapies: clinical landscape and manufacturing challenges.* Regen Med, 2015. **10**(1): p. 49-64.

281. Tarnowski, J., et al., *Delivering advanced therapies: the big pharma approach.* Gene Ther, 2017. **24**(9): p. 593-598.

282. Dodson, B.P. and A.D. Levine, *Challenges in the translation and commercialization of cell therapies.* BMC Biotechnol, 2015. **15**: p. 70.

283. Enam, S.F., et al., *Enrichment of endogenous fractalkine and anti-inflammatory cells via aptamer-functionalized hydrogels.* Biomaterials, 2017. **142**: p. 52-61.

284. Caiazzo, M., et al., *Defined three-dimensional microenvironments boost induction of pluripotency.* Nat Mater, 2016. **15**(3): p. 344-52.

285. Benoit, D.S., et al., *Small functional groups for controlled differentiation of hydrogel-encapsulated human mesenchymal stem cells.* Nat Mater, 2008. **7**(10): p. 816-23.

286. Fam, C.M., et al., *PEGylation improves the pharmacokinetic properties and ability of interferon gamma to inhibit growth of a human tumor xenograft in athymic mice.* J Interferon Cytokine Res, 2014. **34**(10): p. 759-68.

287. Grohmann, U., F. Fallarino, and P. Puccetti, *Tolerance, DCs and tryptophan: much ado about IDO.* Trends Immunol, 2003. **24**(5): p. 242-8.

288. Zhang, Q., et al., *Mesenchymal stem cells derived from human gingiva are capable of immunomodulatory functions and ameliorate inflammation-related tissue destruction in experimental colitis.* J Immunol, 2009. **183**(12): p. 7787-98.

289. Cruz-Acuna, R., et al., *Synthetic hydrogels for human intestinal organoid generation and colonic wound repair.* Nat Cell Biol, 2017. **19**(11): p. 1326-1335.

290. Croitoru-Lamoury, J., et al., *Interferon-gamma regulates the proliferation and differentiation of mesenchymal stem cells via activation of indoleamine 2,3 dioxygenase (IDO).* PLoS One, 2011. **6**(2): p. e14698.

291. Mao, F., et al., *Mesenchymal stem cells and their therapeutic applications in inflammatory bowel disease.* Oncotarget, 2017. **8**(23): p. 38008-38021.

292. Klinker, M.W. and C.H. Wei, *Mesenchymal stem cells in the treatment of inflammatory and autoimmune diseases in experimental animal models.* World J Stem Cells, 2015. **7**(3): p. 556-67.

293. Wang, L.T., et al., *Human mesenchymal stem cells (MSCs) for treatment towards immune- and inflammation-mediated diseases: review of current clinical trials.* J Biomed Sci, 2016. **23**(1): p. 76.

294. Krampera, M., *Mesenchymal stromal cell 'licensing': a multistep process.* Leukemia, 2011. **25**(9): p. 1408-14.

295. Reinke, S., et al., *Terminally differentiated CD8(+) T cells negatively affect bone regeneration in humans.* Sci Transl Med, 2013. **5**(177): p. 177ra36.

296. Mizoguchi, A., *Animal models of inflammatory bowel disease.* Prog Mol Biol Transl Sci, 2012. **105**: p. 263-320.